

Aus der
Urologischen Klinik und Poliklinik
des LMU Klinikums der
Ludwig-Maximilians-Universität München
Direktor: Prof. Dr. med. Christian G. Stief

**Methodische Entwicklungen
zur interstitiellen photodynamischen Therapie
solider Tumore**



Kumulativie Habilitationsschrift
zur Erlangung der Venia Legendi
für das Fach
Translationale Laser-Medizinische Forschung

vorgelegt von

Dr. rer. nat. Adrian Rühm
aus München

2025

Inhaltsverzeichnis

1. Einleitung - Behandlungsmethoden für solide Tumore	2
2. Status Quo der Behandlung von Hirntumoren mittels photodynamischer Therapie	3
3. Ziel und Einordnung des Habilitationsprojekts	5
4. Fragestellungen und Untersuchungen	6
4.1 Methodische Entwicklungen und präklinische Untersuchungen	7
4.1.1 Fluoreszenz-basierte Methoden zur Erhöhung der Sicherheit bei der stereotaktischen Biopsie	7
4.1.2 Methoden zur laser-basierten Herstellung zylindrischer Lichtdiffusoren mit frei wählbaren Abstrahlprofilen	8
4.1.3 Optische Analyse der Zusammensetzung von humanem Blut als Basis für die Erkennung PDT-induzierter photochemischer Veränderungen optischer Gewebeeigenschaften in vivo	9
4.1.4 Entwicklung dualer Gewebe-Phantome mit simultan variabel einstellbaren optischen und NMR-Eigenschaften	10
4.2 Klinische Umsetzung und Analysen zur interstitiellen photodynamischen Therapie (iPDT) an Hirntumoren	11
4.2.1 Durchführung und Auswertung von iPDT-Behandlungen von Rezidiven maligner Gliome und unbehandelten Glioblastomen	11
4.2.2 Untersuchung von Relationen zwischen SOM-Daten und MRT-Daten sowie deren zeitlicher Entwicklung im Verlauf bzw. im Nachgang von iPDT-Behandlungen an Hirntumor-Patienten	13
5. Ausblick - Mögliche Weiterentwicklungen und andere Anwendungsbereiche	15
6. Bibliographie	16
7. Danksagung	19
8. Originalarbeiten der kumulativen Habilitationsleistung	21

1. Einleitung – Behandlungsmethoden für solide Tumore

Solide Tumore stellen eine erhebliche Belastung für Patienten und die Gesundheitssysteme dar. In vielen Fällen ist die Resektion solcher Tumore nicht möglich oder mit erheblichen Risiken und Beeinträchtigungen für den Patienten verbunden. Die Bedeutung alternativer, insbesondere minimalinvasiver Verfahren nimmt im Zuge anhaltender weltweiter Forschungsaktivitäten stetig zu. Wichtige Ziele sind hierbei, Risiken und Nebenwirkungen zu minimieren, die Funktion des betroffenen Körperareals zu erhalten, sowie möglichst auch die Kosten des Eingriffs für Patienten und die Gesundheitssysteme zu reduzieren.

Zum Teil können diese Ziele durch mittlerweile etablierte minimalinvasive Methoden zur lokalen Tumorentfernung mittels Mikrochirurgie, Thermoablation oder thermischer Laseranwendungen bereits erreicht werden. Diese Therapieansätze werden häufig ergänzt durch externe oder (bei der Brachytherapie mittels radioaktiver Seeds [1]) interne Bestrahlung mit ionisierender Strahlung und/oder systemisch durch Chemotherapie (inkl. Hormontherapie). Darüber hinaus werden zunehmend weitere Behandlungsansätze erforscht und verfügbar. Hierzu zählen beispielsweise Tumor-Treating Fields (TTF), mit denen die Zellteilung von Tumorzellen verhindert oder verlangsamt werden soll [2]. Trotz kontroverser Diskussionen ist dieses Verfahren inzwischen in den USA im Rahmen der Behandlung primärer und rezidivierender Glioblastome zugelassen [3]. Verschiedene andere in der Entwicklung befindliche Verfahren stützen sich auf die intrazelluläre Erzeugung reaktiver Sauerstoffspezies und deren zytotoxische Wirkung. Hier sind als subthermische laserbasierte Verfahren die bereits recht weitreichend verfügbare photodynamische Therapie (PDT) zu nennen, welche einen Photosensibilisator erfordert, ferner als noch in der Exploration befindliche Methoden die direkte optische 2-Photonen-Anregung von reaktiven Sauerstoffspezies ohne Photosensibilisator [4], die Röntgenbestrahlung von Nanopartikeln [5], sowie die Chemolumineszenzbasierte PDT [6]. Im Unterschied hierzu sind bei der noch nicht sehr ausführlich erforschten Sonodynamischen Therapie (SDT) [7-10], welche einen Sonosensibilisator erfordert, thermische Prozesse wie Kavitation, Pyrolyse und Sonolumineszenz involviert. Einen chronologischen Überblick über die Einführung dieser Behandlungsmethoden am Beispiel des Glioblastoms gibt [11].

Die für verschiedene Anwendungsfelder bereits ausgereifte und zugelassene photodynamische Therapie (PDT) zielt auf eine photochemische Zerstörung von Tumorzellen ab und induziert mutmaßlich zusätzlich eine Reaktivierung des Immunsystems gegen die Tumorzellen. Sehr vorteilhaft ist, dass es hierbei nicht zu einer Hitze-Entwicklung im Gewebe kommt, was prinzipiell eine selektive Zerstörung von Tumorzellen unter weitgehender Schonung von gesunden Zellen und somit einen zumindest teilweisen Funktionserhalt des behandelten Körperareals ermöglicht. Eine solche Selektivität der Laserbehandlung wird in der Regel in Kombination mit Licht absorbierenden Molekülen (Photosensibilisatoren) erreicht, die in oder an der Tumorzelle lokalisiert bzw. angereichert sind. Hierbei kann die Laserenergie in vielen Fällen sehr einfach minimalinvasiv über dünne Lichtleiter in die betroffene Körperregion geführt und sowohl oberflächlich als auch intraluminal oder interstitiell appliziert werden. Ferner kann der Therapieeffekt über die Wahl der Laserleistung, der Wellenlänge und der Zeitstruktur der Lichtanwendung gezielt eingestellt werden, so dass Risiken, Verträglichkeit und Nebenwirkungen der Therapie gut kontrolliert und begrenzt werden können. Die Methode verspricht damit generell eine sehr gute Kompatibilität mit den Anforderungen an eine moderne medizinische Versorgung, für die insbesondere die Nachhaltigkeit des Behandlungserfolgs, die Minimierung von unerwünschten Nebeneffekten der Therapie sowie die Erhaltung der Lebensqualität entscheidend sind, bei gleichzeitiger Beachtung wirtschaftlicher Aspekte und Rahmenbedingungen.

Die vorliegende kumulative Arbeit befasst sich mit dem Einsatz der interstitiellen photodynamischen Therapie (iPDT) bei der Behandlung von Hirntumoren sowie den für den Transfer einschlägiger Forschungsergebnisse in die klinische Praxis erforderlichen methodischen Entwicklungen.

2. Status Quo der Behandlung von Hirntumoren mittels photodynamischer Therapie

Im Jahr 1904 prägte Herrmann von Tappeiner den Begriff „Photodynamische Reaktion“ [12], basierend auf Untersuchungen seines Studenten Oscar Raab, insbesondere der Beobachtung von Fluoreszenz, die er als potenziell ausschlaggebend für den Erfolg licht-therapeutischer Behandlungen von Infektionen und Hauttumoren ansah. Auch wenn es sich bei der Fluoreszenz tatsächlich nur um ein parallel zur therapeutisch wirksamen photochemischen Reaktion auftretendes Phänomen handelt, waren somit photodynamische Effekte faktisch bereits Ende des 19. Jahrhunderts untersucht und bekannt. Dennoch blieben medizinische Anwendungen bei Tumorerkrankungen am menschlichen Gehirn zunächst noch für viele Jahrzehnte aus, da die Blut-Hirn-Schranke (blood-brain barrier, BBB) einen Übertritt von systemisch verabreichten Photosensibilisatoren ins Hirngewebe verhindert [13]. Nach Verabreichung von Hematoporphyrin derivative (HpD) konnte jedoch in Hirntumor-Gewebe letztlich eine selektive Anreicherung des Photosensibilisators nachgewiesen werden [14], da zumindest in hochgradigen Hirntumoren die BBB nicht vollständig intakt ist. Hieraus entwickelte sich durch die Arbeiten von Prof. Walter Stummer (Neurochirurgie, Klinikum der Universität München) die Methode der fluoreszenz-gestützten Resektion (FGR) auf Basis der tumor-selektiven Anreicherung von Protoporphyrin IX (PpIX) nach systemischer Verabreichung von 5-Aminolävulin-Säure (5-ALA) [15], die heute fester Bestandteil des Standard-of-Care für die Behandlung von Glioblastomen ist. Hierfür hat 5-ALA unter dem Handelsnamen Gliolan® die Zulassung durch die Europäische Arzneimittel-Agentur (EMA) für die intraoperative Verwendung bei malignen Gliomen erhalten, sowie im Jahr 2017 unter dem Handelsnamen Gleolan® durch die US Food and Drug Administration (FDA) für die intraoperative optische Bildgebung in Patienten mit Verdacht auf ein hochgradiges Gliom.

Erste Veröffentlichungen über klinische In-vivo-Anwendungen der PDT an Hirntumoren erschienen ab 1980 [16,17]. Aufgrund der seither verzeichneten Behandlungserfolge von PDT laufen inzwischen prospektive multizentrische klinische Studien, mit denen im weiteren Verlauf die Zulassung erwirkt wurde [18] oder angestrebt wird [19,20]. Wesentliche Motivation ist hierbei, einerseits die Prognose nach FGR hinsichtlich Lebenszeit und Lebensqualität verbessern zu können, sowie andererseits auch Patienten mit nicht resektablem Hirntumor eine Behandlungsoption mit ähnlich guter Prognose anbieten zu können.

Die Anwendung der PDT auf Hirntumore entwickelte sich von einer oberflächlichen intrakavitären Nachbestrahlung des Resektionsbetts [16,18] über eine Nachbestrahlung über (zur Erhöhung der Wirtktiefe) ins Gewebe eingebrachte Lichtdiffusoren [16,21] bis hin zur rein minimalinvasiven Variante, der stereotaktisch geführten interstitiellen PDT (iPDT) ohne Resektion [17,22-24], wobei alle Konzepte noch weiterentwickelt werden. Für die Behandlung des Glioblastoms stellt die FGR nebst Temozolomid-basierter Radiochemotherapie gemäß Stupp-Protokoll [25] den Standard-of-Care dar [26]. In Anlehnung an diesen Standard wird auch die iPDT zur Behandlung des Glioblastoms analog durch Radiochemotherapie ergänzt [22,24].

Angesichts der generell sehr schlechten Überlebensprognose nach Auftreten hochgradiger Hirntumore, insbesondere von Glioblastomen und Hirntumor-Rezidiven, ist hier das zentrale Ziel der iPDT, ebenso wie aller anderen Therapieansätze, ein möglichst langes progressionsfreies Überleben. Hierbei bietet die iPDT auf Basis bisheriger Ergebnisse die Perspektive, das in einigen Fällen beobachtete Langzeitüberleben (> 2 Jahre [27]) prinzipiell auf einen größeren Anteil an Behandlungen erweitern zu können. Diese Hoffnung stützt sich auf die Hypothese, dass durch den Verbleib der nach der iPDT untergehenden Tumormasse im Körper eine im Vergleich zur Resektion beträchtliche Aktivierung des Immunsystems stattfindet [28-31]. Hierdurch kann die PDT indirekt auch außerhalb des beleuchteten Gewebeareals wirken, indem anschließend vitale Tumorzellen auch in anderen Körperregionen vom Immunsystem erkannt und angegriffen werden. In diesem Zusammenhang sind insbesondere in Kombination mit Immuntherapien auf der Basis von Checkpoint-Inhibitoren weitere Fortschritte zu erwarten [29,32,33]. Auch Kombinationen mit Hyperthermie [34] sowie mit adjuvanter Medikation (z.B. Methadon [35] oder Phytopharmaka [36])

wurden und werden weiterhin zumindest präklinisch untersucht, mit dem Ziel, die Wirkung der PDT zu erhöhen. Zusätzlich ist zu erwähnen, dass der therapeutische Effekt der PDT teilweise auch ohne Photosensibilisator durch eine direkte optische Anregung von intrazellulärem Sauerstoff zu reaktiven Sauerstoffspezies (ROS) ausgelöst werden kann, was im Rahmen eines aktuellen EU-Projekts näher untersucht werden soll [4]. Dieser Ansatz könnte es ermöglichen, das Anwendungsspektrum der PDT auf niedriggradige Hirntumore zu erweitern.

Bei der iPDT von Hirntumoren fokussiert sich die weitere klinische Erforschung derzeit weitestgehend auf nicht resezierbare Glioblastome und Hirntumor-Rezidive, da einerseits eine beeinträchtigte Blut-Hirn-Schranke für die PS-Anreicherung erforderlich ist und andererseits bei Nicht-Resezierbarkeit (z.B. aufgrund einer Lokalisation im Sprachzentrum) keine anderen vielversprechenden Therapieformen zur Verfügung stehen. Insgesamt waren die mittels iPDT erzielten Ergebnisse hinsichtlich Gesamt- und Progressionsfreiem Überleben sowohl bei zuvor unbehandelten Glioblastomen wie auch bei Hirntumor-Rezidiven vergleichbar mit dem Standard-of-Care bei resezierbaren Tumoren dieser Art [24,27,37]. Allerdings waren die mittels iPDT behandelten Tumore selektiert in Bezug auf ihre Größe (Durchmesser < 2 cm) und Form (gut umschrieben, nicht diffus infiltrierend).

Bislang konnte mit keiner Methode eine Heilung des Glioblastoms nachgewiesen werden. Allerdings wurden nach iPDT-Anwendung am Glioblastom in Einzelfällen sehr lange Überlebenszeiten beobachtet [23,27], und auch eine Rezidiv-Bildung blieb in vielen dieser Fälle ganz oder lange Zeit aus. Ein besseres/vollständigeres Verständnis der Ursachen für die unterschiedlichen Behandlungserfolge wäre wünschenswert, um darauf aufbauend letztlich das Behandlungsergebnis für alle Patienten verbessern zu können.

Zusammenfassend ist festzustellen, dass die iPDT ein effektives Verfahren zur Behandlung des Glioblastoms und Hirntumor-Rezidiven darstellt, dass jedoch die Nachhaltigkeit des Behandlungserfolges (entsprechend dem Charakter dieser Tumore und der technischen Komplexität der Behandlung) noch nicht zufriedenstellend ist und eine Erweiterung der Anwendbarkeit auf weniger maligne Hirntumore wünschenswert wäre, um zum Wohle der Patienten einem breiteren Einsatz der Methodik zum Durchbruch zu verhelfen.

3. Ziel und Einordnung des Habilitationsprojekts

Übergeordnetes Ziel des Habilitationsprojekts war es, bei der Anwendung minimalinvasiver optischer Therapieverfahren durch Nutzung messtechnisch zugänglicher Daten und Zusammenführung der Ergebnisse verschiedener Untersuchungsmethoden ein besseres Verständnis von für den Therapieerfolg entscheidenden Mechanismen, Einflussgrößen und Randbedingungen zu entwickeln, um dadurch die Behandlungserfolge zu optimieren und die Auswahl der jeweils individuell geeigneten Therapieanwendung zu unterstützen. Einbezogen wurden hierfür Untersuchungen im Zusammenhang mit der interstitiellen PDT von Glioblastomen.

Einen zentralen Aspekt der Arbeiten stellen licht-dosimetrische Berechnungen und Simulationen in Relation zur Tumorgeometrie auf Basis von medizinischen Bildgebungsdaten (MRT, CT, PET) dar, ferner spektral aufgelöste optische Messungen über im Tumorbereich platzierte faserbasierte Licht-Diffusoren, sowie Beobachtungen von Gewebeveränderungen im Zeitverlauf, unmittelbar vor und nach der Intervention bis hin zum eventuellen Auftreten eines Rezidivs. Im Zusammenhang mit ersten klinischen Anwendungen zeigte sich, dass an selektierten, de facto inoperablen Tumoren bereits gute Behandlungserfolge bei sehr geringem Risiko erzielt werden [24,37], dass aber nicht zu unterschätzendes weiteres Verbesserungspotenzial besteht, das durch methodische Optimierung genutzt werden kann [27,38]. Die im Rahmen der klinischen Anwendung gewonnenen Ergebnisse wurden durch entsprechende präklinische Untersuchungen an Gewebe und artifiziellen Gewebe-Phantomen ergänzt. Zudem wurden methodische Konzepte und Protokolle für die klinische Anwendung erarbeitet und getestet.

Als weitere Untersuchungen bieten sich, neben der Auswertung der bereits laufenden kontrollierten klinischen Studien, Vergleiche zwischen iPDT und anderen oben erwähnten Therapieansätzen bzw. entsprechenden Kombinationsverfahren in Bezug auf Therapieeffekt und Langzeitverlauf an. Wünschenswert wäre langfristig eine Erweiterung des Anwendungsspektrums der iPDT auf weitere Tumorarten (z.B. auch niedriggradige Gliome).

4. Fragestellungen und Untersuchungen

Die im Folgenden zusammengefassten Arbeiten zum Habilitationsprojekt wurden am LIFE-Zentrum des LMU Klinikums unter anderem in Kooperation mit der Neurochirurgischen Klinik und den Kliniken für Neuroradiologie und Radiologie durchgeführt und, wie aus dem beigefügten Schriftenverzeichnis hervorgeht, weitestgehend publiziert.

Die nachfolgend beschriebenen Fragestellungen und Untersuchungen sind ihrem Charakter nach in zwei Gruppen unterteilt. Die erste Gruppe umfasst methodische Entwicklungen und präklinische Untersuchungen, die keine direkte Anwendung am Menschen beinhalten (Abschnitt 4.1). Die zweite Gruppe umfasst Fragestellungen und Untersuchungen, die eine klinische Umsetzung im Rahmen von iPDT-Behandlungen an Hirntumoren von Patienten sowie daran geknüpfte Analysen beinhalten (Abschnitt 4.2).

4.1 Methodische Entwicklungen und präklinische Untersuchungen

Vorbereitend wurden auf Basis bestehender Erkenntnisse zu iPDT-Behandlungen an Hirntumorpatienten grundlegende Untersuchungen zu relevantem Teilsystemen und -methodiken durchgeführt.

4.1.1 Fluoreszenz-basierte Methoden zur Erhöhung der Sicherheit bei der stereotaktischen Biopsie

Für die stereotaktische Biopsie im Vorfeld einer iPDT wurde ein Konzept für eine optisch geführte Biopsie-Nadel erarbeitet und an Labormustern erprobt (Abb. 1). Hiermit soll die Sicherheit der Biopsieentnahme erhöht werden, indem größere Blutgefäße erkannt und deren Beschädigung, z.B. durch geeignete axiale Rotation der Biopsienadel vor der Gewebe-Abscherung, vermieden werden kann.

Platzhalter für Abb. 1, Bildquelle einsehbar unter:

Markwardt NA, Stepp H, Franz G, Sroka R, Goetz M, Zelenkov P, Rühm A. Remission spectrometry for blood vessel detection during stereotactic biopsy of brain tumors. J Biophotonics. 2017 Aug;10(8):1080-1094. doi: 10.1002/jbio.201600193. Epub 2016 Oct 7. PMID: 27714967.

Aus urheberrechtlichen Gründen nicht in dieser elektronischen Publikation enthalten.

Abb. 1: Biopsie-Nadel mit Blutgefäß-Erkennung für die optisch geführte Biopsie. **(a)** Schematischer Aufbau der Biopsie-Nadel mit seitlicher Öffnung zur Abscherung von Gewebe sowie zwei integrierten, fixierten optischen Seitblick-Fasern mit verspiegelten Faser-Enden, die mit einer Lichtquelle bzw. einem Spektrometer verbunden sind. Dargestellt sind ferner Querschnitte von Blutgefäßen in drei verschiedenen Abständen zur Biopsie-Nadel. **(b)** Detektiertes Remissionssignal als Funktion der Position des Blutgefäßes entlang der Längsrichtung der Biopsie-Nadel für die drei verschiedenen Blutgefäß-Abstände von der Biopsie-Nadel. Bei axialer Bewegung der Biopsie-Nadel ist durch den starken Abfall des Remissionssignals klar erkennbar, wenn sich das Blutgefäß sehr nahe oder gar innerhalb des Abscher-Bereichs der Biopsie-Nadel befindet. Hierdurch wird eine Blutgefäß-Erkennung während der Biopsie ermöglicht.

Adaptiert aus [O1].

Originalarbeiten:

[O1] Markwardt NA, Stepp H, Franz G, Sroka R, Goetz M, Zelenkov P, Rühm A. Remission spectrometry for blood vessel detection during stereotactic biopsy of brain tumors. J Biophotonics. 2017 Aug;10(8):1080-1094. doi: 10.1002/jbio.201600193. Epub 2016 Oct 7. PMID: 27714967

[O2] Markwardt NA, Haj-Hosseini N, Hollnburger B, Stepp H, Zelenkov P, Rühm A. 405 nm versus 633 nm for protoporphyrin IX excitation in fluorescence-guided stereotactic biopsy of brain tumors. J Biophotonics. 2016 Sep;9(9):901-12. doi: 10.1002/jbio.201500195. Epub 2015 Nov 13. PMID: 26564058

4.1.2 Methoden zur laser-basierten Herstellung zylindrischer Lichtdiffusoren mit frei wählbaren Abstrahlprofilen

In Zusammenarbeit mit der Fachhochschule Vorarlberg (Dornbirn, Österreich) wurden Messungen und Simulationen zur Abstrahlcharakteristik von zylindrischen Lichtdiffusoren durchgeführt (Abb. 2), die darauf abzielen, Inhomogenitäten im Abstrahlprofil zu ermitteln und künftig mittels laser-basierter Herstellungsverfahren zu vermeiden, um eine präzisere Licht-Dosimetrie für die i PDT zu ermöglichen. Die erhaltenen Erkenntnisse werden in einem durch das Zentrale Innovationsprogramm Mittelstand (ZIM) des Bundesministeriums für Wirtschaft und Klimaschutz geförderten Projekt verwertet und für die weitere klinische Anwendungen wie die Endovenöse Lasertherapie weiterentwickelt.

Platzhalter für Abb. 2, Bildquelle einsehbar unter:

Ströbl S, Domke M, Rühm A, Sroka R. Investigation of non-uniformly emitting optical fiber diffusers on the light distribution in tissue. Biomed Opt Express. 2020 Jun 8;11(7):3601-3617. doi: 10.1364/BOE.394494. eCollection 2020 Jul 1. PMID: 33014554

Aus urheberrechtlichen Gründen nicht in dieser elektronischen Publikation enthalten.

Abb. 2: Methoden zur Untersuchung der Abstrahlcharakteristik von zylindrischen Lichtdiffusoren sowie exemplarische Ergebnisse. **(a)** Kamera-basiertes Verfahren zur Abbildung der Intensitätsverteilung auf der Diffusor-Oberfläche. **(b)** Kamera-basiertes Nah-Feld-Verfahren zur nicht-abbildenden Erfassung der Winkelverteilung der Abstrahlung von der Diffusor-Oberfläche. **(c)** Verfahren zur Vermessung der Lichtverteilung in einem artifiziellen optischen Gewebephantom mit eingebettetem zylindrischer Lichtdiffusor. Hierzu wird der Lichtdiffusor parallel zur Oberfläche in verschiedenen Abständen (hier: 2 mm, 5 mm, 10 mm und 15 mm) platziert und die Lichtverteilung an der Oberfläche des Phantoms bildgebend erfasst. **(d)** Schematische Darstellung des Simulationsmodells zum Messaufbau (c). Zugrunde gelegt wird in der Simulation das mit dem Messaufbau (a) bestimmte Emissionsprofil entlang der Diffusor-Achse sowie von jedem Punkt der Diffusor-Oberfläche eine konische Emission. Der volle Öffnungswinkel des Konus beträgt 2°, der Neigungswinkel des Konus ist ein freier Modellparameter. Die Lichtverteilung wird in virtuellen Empfangsebenen in den entsprechenden Abständen von der Diffusor-Oberfläche bestimmt. **(e)** Intensitätsprofile parallel zur Diffusor-Achse gemessen mit Messaufbau (a) (schwarze gepunktete Linie) an der Diffusor-Oberfläche sowie mit Messaufbau (c) an der Phantom-Oberfläche für vier Diffusor-Abstände von der Oberfläche.

Adaptiert aus [O3].

Originalarbeiten:

[O3] Ströbl S, Domke M, Rühm A, Sroka R. Investigation of non-uniformly emitting optical fiber diffusers on the light distribution in tissue. Biomed Opt Express. 2020 Jun 8;11(7):3601-3617. doi: 10.1364/BOE.394494. eCollection 2020 Jul 1. PMID: 33014554

[O4] Ströbl S, Wäger F, Domke M, Rühm A, Sroka R. Homogeneously Emitting, Mechanically Stable, and Efficient fs-Laser-Machined Fiber Diffusers for Medical Applications. Lasers Surg Med. 2022 Apr;54(4):588-599. doi: 10.1002/lsm.23365. Epub 2020 Dec 8. PMID: 33616996

4.1.3 Optische Analyse der Zusammensetzung von humanem Blut als Basis für die Erkennung PDT-induzierter photochemischer Veränderungen optischer Gewebeeigenschaften in vivo

Um ein besseres Verständnis von in vivo während der iPDT beobachteten Veränderungen optischer Transmissionsspektren zu entwickeln, z.B. aufgrund einer Umwandlung von Oxyhämoglobin zu Methämoglobin, wurden Absorptionsspektren einfacher Mischungen verschiedener Hämoglobin-Varianten genau analysiert (Abb. 3). Es zeigte sich, dass durch die genaue Bestimmung der Position des Maximums im gewichteten Summenspektrum auf die Anteile der beiden Hämoglobin-Varianten geschlossen werden kann. Störende glatte Untergrundsignale mussten dabei durch eine Modellanpassung auf Basis der 2. Ableitung des Rohsignals ausgeblendet werden.

Platzhalter für Abb. 3, Bildquelle einsehbar unter:

Heckl C, Lang A, Rühm A, Sroka R, Duffield T, Vogeser M, Paal M. Spectrophotometric evaluation of hemolysis in plasma by quantification of free oxyhemoglobin, methemoglobin, and methemalbumin in presence of bilirubin. J Biophotonics. 2021 May;14(5):e202000461. doi: 10.1002/jbio.202000461. Epub 2021 Feb 13. PMID: 33527705

Aus urheberrechtlichen Gründen nicht in dieser elektronischen Publikation enthalten.

Abb. 3: Optische Analyse der Zusammensetzung von humanem Blut.

Oben: Prinzip des second-derivative-Fit-Algorithmus: Spektren von Referenz-Komponenten (Oxyhämoglobin: gestrichelte Linie; Methämoglobin/Methämalbumin: strichpunktierte Linie) werden mit iterativ angepasster Gewichtung vom Ausgangsspektrum der Probe (durchgezogene Linie) subtrahiert, so dass der Mittelwert der zweiten Ableitung (nicht gezeigt) des Residual-Spektrums (gepunktete Linie) minimal wird.

Unten: Mittels second-derivative-Fit-Algorithmus untergrund-bereinigte Spektren: Im Bereich der Soret-Banden verschiedener Häm-Pigment-Mischungen ist eine Verschiebung des Absorptionsmaximums erkennbar, hier von 415 nm für pures Oxyhämoglobin (fette schwarze Linie) bis zu 405 nm mit wachsendem Methämoglobin-Anteil (Linien mit abnehmendem Grauton).

Adaptiert aus [O5].

Originalarbeiten:

[O5] Heckl C, Lang A, **Rühm A**, Sroka R, Duffield T, Vogeser M, Paal M. Spectrophotometric evaluation of hemolysis in plasma by quantification of free oxyhemoglobin, methemoglobin, and methemalbumin in presence of bilirubin. J Biophotonics. 2021 May;14(5):e202000461. doi: 10.1002/jbio.202000461. Epub 2021 Feb 13. PMID: 33527705

4.1.4 Entwicklung dualer Gewebe-Phantome mit simultan variabel einstellbaren optischen und NMR-Eigenschaften

Für eine individualisierte licht-dosimetrische PDT-Therapieplanung ist eine Kenntnis der 3-dimensionalen Verteilung der optischen Eigenschaften im zu behandelnden Hirnareal wünschenswert. Als Modellsystem für kontrollierte Untersuchungen, ob, mit welchen Methoden und mit welcher Präzision diese optischen Eigenschaften aus MRT-Aufnahmen ableitbar sein könnten, wurden duale Gewebe-Phantome entwickelt, deren optische und NMR-Eigenschaften simultan variabel einstellbar sind (Abb. 4).

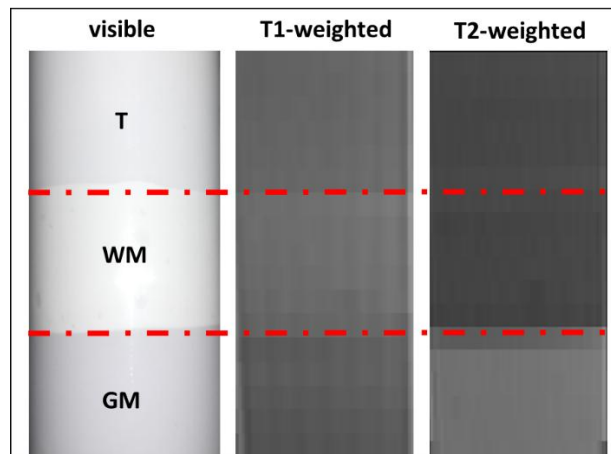


Abb. 4: Erscheinungsbilder eines dualen Phantoms, visuell bzw. in T1- und T2-gewichteter NMR-Bildgebung. Das Phantom besteht aus drei Zonen, die drei Arten von humanem Hirngewebe bzgl. relevanter optischer und NMR-Eigenschaften nachbilden: malignes Gliom/Hirntumor (T), weiße Substanz (WM) und graue Substanz (GM). Die roten Linien markieren die Grenzflächen-Positionen zwischen den drei Zonen. Der Grauwert in den NMR-Bildern entspricht der Signalintensität in der entsprechenden Bildgebungsmodalität. Eine kürzere T1-Zeit erscheint im T1-gewichteten Bild heller, während eine kürzere T2-Zeit im T2-gewichteten Bild dunkler erscheint [39].

Aus [O6].

Originalarbeiten:

- [O6] Aumiller M, Arazar A, Sroka R, Dietrich O, Rühm A. Investigations on correlations between changes of optical tissue properties and NMR relaxation times. Photodiagnosis Photodyn Ther. 2024 Feb;45:103968. doi: 10.1016/j.pdpdt.2024.103968. Epub 2024 Jan 10. PMID: 38215958

4.2 Klinische Umsetzung und Analysen zur interstitiellen photodynamischen Therapie (iPDT) an Hirntumoren

Im Rahmen des Habilitationsprojekts wurden klinische Daten zu iPDT-Behandlungen an Hirntumoren auf Basis bestehender Konzepte ausgewertet und das Potenzial neuer Planungs-, Behandlungs-, Monitoring- und Auswertungskonzepte für klinische Zulassungsstudien geprüft. Basierend auf den daraus abgeleiteten Erkenntnissen wurden geeignete Methoden und Studienprotokolle für kontrollierte klinische Studien erarbeitet und zusammen mit klinischen und industriellen Partnern sowie Experten aus anderen medizinischen Fachrichtungen multizentrisch umgesetzt.

Aus iPDT-Behandlungen an Patienten mit Glioblastomen oder Hirntumor-Rezidiven verfügbare Daten waren auszuwerten und Korrelationen von Behandlungsparametern bzw. von Messergebnissen sind mit dem Überleben der Patienten in Beziehung zu setzen, um daraus Prädiktoren für einen Behandlungserfolg (insbes. Progressionsfreies Überleben (Progression-free Survival, PFS) und Gesamtüberleben (Overall Survival, OS)) ableiten zu können. Hierbei handelt es sich um dosimetrische Parameter in Zusammenhang mit MRT-Daten sowie Ergebnisse von Spectral online monitoring (SOM) vor, nach und ggf. während der iPDT. Im weiteren Verlauf wurden Daten aus der medizinischen Bildgebung im Verlauf analysiert, um mögliche Ursachen für ein Therapieversagen (wie z.B. Bildung eines Rezidivs aufgrund nicht ausreichender Bestrahlung) erkennen zu können. Von Bedeutung ist hier auch die Morphologie des Tumors vor der Bestrahlung (z.B. blutiger Tumor) sowie die Reaktion der bestrahlten Hirngewebe-region auf die Lichteinwirkung. Auch klinische Parameter, insbesondere der Methylierungsstatus des O6-Methylguanin-DNA-Methyltransferase (MGMT) - Promotors, das Alter des Patienten etc., sollten mit berücksichtigt werden. Der beobachtete Therapie-Outcome nach iPDT wurde statistisch mit dem nach dem Standard-of-Care verglichen.

4.2.1 Durchführung und Auswertung von iPDT-Behandlungen von Rezidiven maligner Gliome und unbehandelten Glioblastomen

In Zusammenarbeit mit der Neurochirurgischen Klinik und den Kliniken für Neuroradiologie und Radiologie wurden klinische Daten zu PDT-Behandlungen an Rezidiven maligner Gliome sowie an unbehandelten de-novo-Glioblastomen (jeweils nicht resezierbar, meist aufgrund ihrer Lokalisierung im Bereich des Sprachzentrums) retrospektiv ausgewertet. Hierbei ergaben sich sehr vielversprechende klinische Ergebnisse. Im Falle der Rezidive wurden Kaplan-Meier-Verläufe wie bei resezierbaren Rezidiven erreicht (Abb. 5), im Fall der de-novo-Glioblastome waren die Verläufe sogar vorteilhaft verglichen mit dem Standard-of-Care (Abb. 6). Im de-novo-Fall wurden bei nicht-methyliertem MGMT-Promotor ebenfalls Werte wie bei resezierbaren MGMT-negativen Glioblastomen erreicht (Abb. 7a). Bei methyliertem MGMT-Promotor scheint die iPDT sogar einen deutlichen Überlebensvorteil gegenüber Resektion zu versprechen (Abb. 7b), was allerdings noch in größeren Studien und für weniger stark selektierte Patientenkollektive verifiziert werden muss.

Im Rahmen dieser Untersuchungen wurden auch medizinische Bildgebungsdaten vor und nach iPDT sowie im weiteren Verlauf bis zum Auftreten eines Rezidivs und darüber hinaus ausgewertet, indem verschiedene Gewebeareale im Bereich des Tumors segmentiert und dem Volumen nach quantitativ erfasst und analysiert wurden (Abb. 8). Aus den bisherigen Analysen hierzu konnten allerdings keine zweifelsfreien Prädiktoren für den Behandlungserfolg abgeleitet werden.

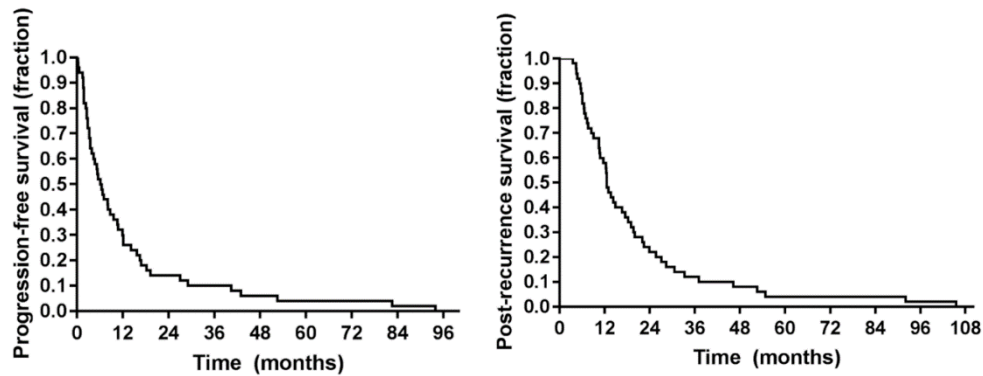


Abb. 5: Kaplan-Meier-Kurven der Überlebenszeit nach iPDT an 44 Patienten mit lokalen malignen Gliom-Rezidiven.

Links: Progressionsfreies Überleben nach iPDT. **Rechts:** Gesamtüberleben nach iPDT. Adaptiert aus [07].

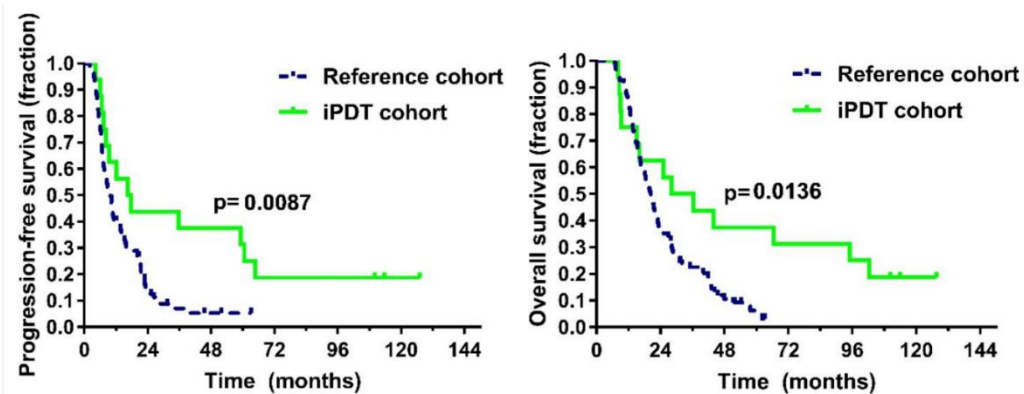


Abb. 6: Kaplan-Meier-Kurven der Überlebenszeit nach iPDT an 16 Patienten mit neu diagnostizierten, klein-volumigen, nicht sicher resezierbaren Glioblastomen.

Links: Progressionsfreies Überleben nach iPDT. **Rechts:** Gesamtüberleben nach iPDT. Beide Überlebenszeiten waren bei der iPDT-Kohorte signifikant länger als bei einer Referenz-Kohorte ($n = 110$), die an der Neurochirurgischen Klinik der Universität München bestmöglich gemäß der an dieser Klinik üblichen Protokolle behandelt wurde.

Aus [08].

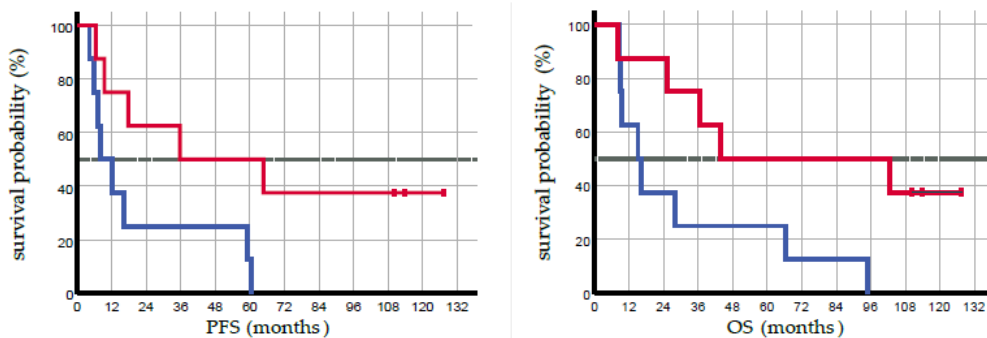


Abb. 7: Kaplan-Meier-Kurven der Überlebenszeit nach iPDT an derselben Kohorte von 16 Patienten mit neu diagnostizierten, klein-volumigen, nicht sicher resezierbaren Glioblastomen (entsprechend Abb. 6), hier jedoch stratifiziert nach dem Methylierungsstatus des MGMT-Promoters (rot: methyliert, blau: nicht-methyliert).

Links: Progressionsfreies Überleben nach iPDT. **Rechts:** Gesamtüberleben nach iPDT. Adaptiert aus [09].

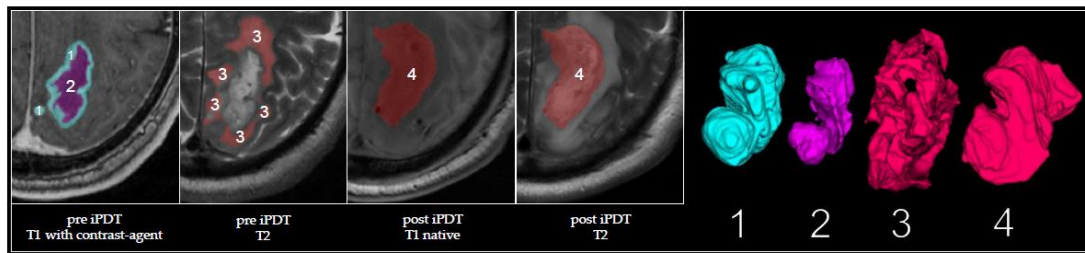


Abb. 8: Auf Basis von MRT-Bilddaten (T1- und T2-Sequenzen) segmentierte Gehirnregionen eines aus den 16 de-novo-GBM-Fällen (entsprechend Abb. 6) exemplarisch ausgewählten Patienten.

Links: Farbliche Hervorhebung mittels Overlay im 2D-Schnitt.

Rechts: 3D-Darstellung der segmentierten Volumina.

(1) T1-Kontrast-verstärkendes Volumen. **(2)** Nekrose. **(1+2)** Tumorumfassen.

(3) Ödem. **(4)** iPDT-Relikt (iPDT remnant).

Adaptiert aus [09].

Originalarbeiten:

- [07] Lietke S, Schmutzer M, Schwartz C, Weller J, Siller S, Aumiller M, Heckl C, Forbrig R, Niyazi M, Egensperger R, Stepp H, Sroka R, Tonn JC, **Rühm A**, Thon N. Interstitial Photodynamic Therapy Using 5-ALA for Malignant Glioma Recurrences. *Cancers (Basel)*. 2021 Apr 7;13(8):1767. doi: 10.3390/cancers13081767. PMID: 33917116
- [08] Quach S, Schwartz C, Aumiller M, Foglar M, Schmutzer M, Katzendobler S, El Fahim M, Forbrig R, Bochmann K, Egensperger R, Sroka R, Stepp H, **Rühm A**, Thon N. Interstitial photodynamic therapy for newly diagnosed glioblastoma. *J Neurooncol*. 2023 Mar;162(1):217-223. doi: 10.1007/s11060-023-04284-9. Epub 2023 Mar 16. PMID: 36928699
- [09] Foglar M, Aumiller M, Bochmann K, Buchner A, El Fahim M, Quach S, Sroka R, Stepp H, Thon N, Forbrig R, **Rühm A**. Interstitial Photodynamic Therapy of Glioblastomas: A Long-Term Follow-up Analysis of Survival and Volumetric MRI Data. *Cancers (Basel)*. 2023 May 4;15(9):2603. doi: 10.3390/cancers15092603. PMID: 37174068

4.2.2 Untersuchung von Relationen zwischen SOM-Daten und MRT-Daten sowie deren zeitlicher Entwicklung im Verlauf bzw. im Nachgang von iPDT-Behandlungen an Hirntumor-Patienten

Um PpIX-Fluoreszenz im Tumoreal nachzuweisen, wurden im Rahmen der durchgeführten iPDT-Behandlungen an Hirntumoren optische Signale am laserseitigen Ende der optischen Zuleitungsfaser eines im Tumor platzierten zylindrischen Lichtdiffusors mit einem Spektrometer abgegriffen während ein einzelner zweiter Lichtdiffusor Behandlungslicht der Wellenlänge 635 nm ins Tumorgewebe emittierte. Die gewonnenen Spektren (Abb. 9a) wiesen zum Teil deutliche Unterschiede auf, sowohl für verschiedene Diffuser-Paare zu Beginn der iPDT als auch im Hinblick auf ihre zeitliche Entwicklung im Verlauf der (laut Protokoll stets 1-stündigen) iPDT. Auf Basis dieser Beobachtungen wurde ein automatisiert ablaufendes, systematisch alle Diffuser-Paare umfassendes „Spectral Online Monitoring (SOM)“-Verfahren etabliert, das auch in zukünftige klinische Studien Eingang finden könnte (z.B. um Annahmen über die optischen Gewebeeigenschaften zu überprüfen oder deren Veränderungen während der Therapie zu erfassen, um im Bedarfsfall das Therapieschema geeignet anzupassen). Als potenziell relevant für den Behandlungserfolg wurde insbesondere ein Rückgang der Transmission des 635nm-Therapielichts durch das Tumorgewebe während der iPDT angesehen (Abb. 9a), da sich hierdurch die Ausleuchtung des Tumors gegenüber der dosimetrischen Therapieplanung verschlechtert. Bei Einbeziehung von MRT-Daten, in die die Diffusoren in 3D eingebettet sind (Abb. 9b), ergab sich eine statistisch signifikant höhere Transmissionsreduktion zwischen Diffuser-Paaren zwischen denen auch eine Hyperintensität im T1-gewichteten

postoperativen MRT-Datensatz zu erkennen war (Abb. 9c). Diese T1-Hyperintensität wird vorläufig auf die Bildung von Methämoglobin zurückgeführt, welches gegenüber Oxy- und Desoxyhämoglobin eine höhere Absorption bei der Therapiewellenlänge 635nm aufweist.

Aus den bisherigen Analysen von optischen SOM-Messungen vor und nach iPDT sowie von medizinischen Bildgebungsdaten vor und nach iPDT, sodann im weiteren Verlauf bis zum Auftreten eines Rezidivs und darüber hinaus, konnten bislang keine zweifelsfreien Prädiktoren für den Behandlungserfolg abgeleitet werden. Detailliertere Analysen auf Basis der Bildgebungsdaten (Abb. 8 in Abschnitt 4.2.1) sowie verfeinerter licht-dosimetrischer Simulationen unter Berücksichtigung von Inhomogenitäten, insbesondere der Gewebemorphologie, scheinen geboten, um mögliche Zusammenhänge zwischen der Überlebenszeit einerseits und der Ausgangskonstellation im Tumor sowie der Behandlungsdurchführung auf den Grund zu gehen.

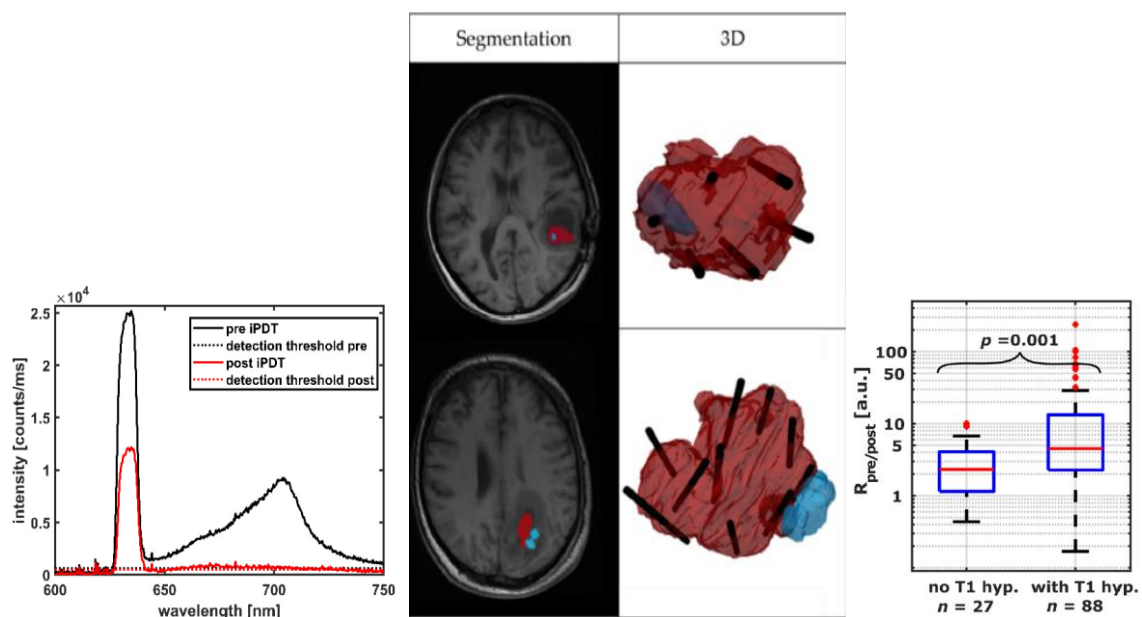


Abb. 9: Exemplarische Ergebnisse der Analyse von SOM- und MRT-Daten, die im Zuge von iPDT-Behandlungen an 11 de-novo-GBM-Patienten gewonnen wurden.

(a) SOM-Spektren vor und nach iPDT. **(b)** Segmentierte Gewebeareale mit eingebetteten zylindrischen Lichtdiffusoren. **(c)** Boxplots der zwischen allen einbezogenen Diffusor-Paaren mittels SOM gemessenen Transmissionsreduktionsverhältnisse für Diffusor-Paare mit und ohne T1-Hyperintensität im Bereich zwischen den beiden Einzel-Diffusoren.

Adaptiert aus [O10].

Originalarbeiten:

[O10] Aumiller M, Heckl C, Quach S, Stepp H, Ertl-Wagner B, Sroka R, Thon N, **Rühm A**. Interrelation between Spectral Online Monitoring and Postoperative T1-Weighted MRI in Interstitial Photodynamic Therapy of Malignant Gliomas. *Cancers* (Basel). 2021 Dec 27;14(1):120. doi: 10.3390/cancers14010120. PMID: 35008284

5. Ausblick - Mögliche Weiterentwicklungen und andere Anwendungsbereiche

Die vorgestellten Konzepte, Methoden und Instrumente können prinzipiell auch auf andere Tumorarten angewendet werden. Im Bereich der Neurochirurgie wäre eine Kombination mit Methoden zur partiellen Öffnung der Blut-Hirn-Schranke wünschenswert, um auch niedriggradige Tumore mittel 5-ALA/PpIX-basierter iPDT behandeln zu können. Darüber hinaus könnten andere Methoden zur Sauerstoff-Aktivierung in den Tumorzellen untersucht und erprobt werden, die ohne Photosensibilisator auskommen, dennoch aber möglichst eine gewisse Tumor-Selektivität im Hinblick auf die Zellschädigung aufweisen sollten. Auch der Ausbau grundlegender Untersuchungen zur PDT könnte das Verständnis der Methodik und ihrer Wechselwirkungen fördern und dadurch Wege zu neuen Behandlungsmöglichkeiten, z.B. in Form von Kombinationstherapien, eröffnen. Hier sind einige aktuelle Projekte zu nennen:

- a) Hendrik Scherer, „Evaluation of the Effects of 5-Aminolevulinic Acid mediated Photodynamic Therapy on Temozolomide Resistant Glioblastoma Cells“ (Bachelorarbeit 2023).
- b) Eva Schneble, „The Effect of Lapatinib on Photodynamic Therapy in Glioblastoma Multiforme“ (Bachelorarbeit 2024).
- c) Lena Katzenstein, „Influence of calcitriol on the effect of photodynamic therapy in glioblastoma“ (Bachelorarbeit 2024).
- d) Direkte Anregung von $^1\text{O}_2$ durch Anregung bei 1270 nm (EU-Projekt „Next Generation Glioma Treatments using Direct Light Therapy (GlioLight)“, 2024-2026).

In anderen soliden Organen, wie Prostata und Niere, können geringfügig adaptierte Verfahren zur Tumorbekämpfung bei gleichzeitiger Erhaltung der Organ-Funktion führen. (Die Leber ist hierbei auszunehmen, da die PpIX-Anreicherung dort nicht tumor-selektiv ist.) Das TOOKAD-Verfahren ist bereits für die Prostata-Behandlung ohne Resektion zugelassen, ist allerdings als vaskulär wirkendes Verfahren nicht inhärent tumor-selektiv und steht auch mit anderen Verfahren in Konkurrenz. In der Harnblase wurde die Effektivität der PDT nach Instillation von 5-ALA bereits nachgewiesen, jedoch hat sich hier die fluoreszenz-gestützte chirurgische Entfernung tumor-befallener Schleimhaut-Areale als schmerzärmer erwiesen. Im Bereich Gastroenterologie ist PDT ein häufig zur Reduzierung der Tumormasse eingesetztes Verfahren, durch das eine spätere Entfernung des den Gallengang umschließenden (Klatskin-)Tumors deutlich vereinfacht wird. In der Dermatologie ist die PDT ein etabliertes Verfahren. Hier gibt es Bestrebungen, die Effektivität oder Verträglichkeit der PDT durch adjuvante Verabreichung geeigneter Substanzen (z.B. Methadon, Shikonin etc.) zu erhöhen.

Zusammenfassend lässt sich feststellen, dass die PDT auf viele Erkrankungen erfolgreich angewendet werden kann. Derzeit erscheint der durch weitere Forschung und Entwicklung erzielbare Fortschritt im Bereich der Neurochirurgie besonders groß.

6. Bibliographie

- [1] Gerbaulet A, Pötter R, Mazeron J, Meertens H, Limbergen EV, eds. (2002). The GEC ESTRO handbook of brachytherapy. Leuven, Belgium: European Society for Therapeutic Radiology and Oncology. OCLC 52988578
- [2] Stupp R, Taillibert S, Kanner A, Read W, Steinberg D, Lhermitte B, Toms S, Idhahbi A, Ahluwalia MS, Fink K, Di Meo F, Lieberman F, Zhu JJ, Stragliotto G, Tran D, Brem S, Hottinger A, Kirson ED, Lavy-Shahaf G, Weinberg U, Kim CY, Paek SH, Nicholas G, Bruna J, Hirte H, Weller M, Palti Y, Hegi ME, Ram Z. Effect of Tumor-Treating Fields Plus Maintenance Temozolomide vs Maintenance Temozolomide Alone on Survival in Patients with Glioblastoma: A Randomized Clinical Trial. JAMA. 2017 Dec 19;318(23):2306-2316. doi: 10.1001/jama.2017.18718. Erratum in: JAMA. 2018 May 1;319(17):1824. PMID: 29260225; PMCID: PMC5820703.
- [3] "FDA approves expanded indication for medical device to treat a form of brain cancer" (Press release). U.S. Food and Drug Administration. October 5, 2015. <https://web.archive.org/web/20151008012814/https://www.fda.gov/NewsEvents/Newsroom/PressAnnouncements/ucm465744.htm>
- [4] Das Projekt „GlioliGHT - Next Generation Glioma Treatments using Direct Light Therapy“ wird im EU-Rahmenprogramm „Horizont Europa“ mit dem zukunftsorientierten EIC-Pathfinder gefördert.
- [5] Ghosh R, Mondal S, Mukherjee D, Adhikari A, Bhattacharyya M, Pal SK. Inorganic-organic Synergy in Nano-hybrids Makes a New Class of Drug with Targeted Delivery: Glutamate Functionalization of Iron Nanoparticles for Potential Bone Marrow Delivery and X-ray Dynamic Therapy. Curr Drug Deliv. 2022;19(10):991-1000. doi: 10.2174/1567201819666220328142620. PMID: 35346006.
- [6] The „Lumiblast“ project has received funding from the European Union's Horizon 2020 framework programme for research and innovation under grant agreement No 712921.
- [7] sonALAsens, „Study of Sonodynamic Therapy in Participants With Recurrent High-Grade Glioma.“, <https://www.clinicaltrials.gov/study/NCT04559685>
- [8] sonALAsens, „A Phase 2 Study of Sonodynamic Therapy Using SONALA-001 and Exablate 4000 Type 2.0 in Patients With DIPG.“, <https://www.clinicaltrials.gov/study/NCT04559685>
- [9] Bunevicius A, Pikis S, Padilla F, Prada F, Sheehan J. Sonodynamic therapy for gliomas. J Neurooncol. 2022 Jan;156(1):1-10. doi: 10.1007/s11060-021-03807-6. Epub 2021 Jul 12. PMID: 34251601.
- [10] Marcus SL, de Souza MP. Theranostic Uses of the Heme Pathway in Neuro-Oncology: Protoporphyrin IX (PpIX) and Its Journey from Photodynamic Therapy (PDT) through Photodynamic Diagnosis (PDD) to Sonodynamic Therapy (SDT). Cancers (Basel). 2024 Feb 10;16(4):740. doi: 10.3390/cancers16040740. PMID: 38398131
- [11] Foo CY, Munir N, Kumaria A, Akhtar Q, Bullock CJ, Narayanan A, Fu RZ. Medical Device Advances in the Treatment of Glioblastoma. Cancers (Basel). 2022 Oct 29;14(21):5341. doi: 10.3390/cancers14215341. PMID: 36358762; PMCID: PMC9656148.
- [12] von Tappeiner H, Jodlbauer A. Über die Wirkung der photodynamischen (fluoreszierenden) Stoffe auf Infusorien. Dtsch Arch Klin Med. 1904; 80: 427-487
- [13] Wise BL, Taxdal DR. Studies of the blood-brain barrier utilizing hematoporphyrin. Brain Res. 1967 Apr;4(4):387-9. doi: 10.1016/0006-8993(67)90171-0. PMID: 6033811.

- [14] Diamond I, Granelli SG, McDonagh AF, Nielsen S, Wilson CB, Jaenicke R. Photodynamic therapy of malignant tumours. *Lancet* 1972 Dec 2;2(7788):1175-7. doi: 10.1016/s0140-6736(72)92596-2, PMID: 4117595 DOI: 10.1016/s0140-6736(72)92596-2
- [15] Stummer W, Stocker S, Wagner S, et al: Intraoperative detection of malignant gliomas by 5-aminolaevulinic acid-induced porphyrin fluorescence. *Neurosurgery* 42:518–526, 1998.
- [16] Perria C, Capuzzo T, Cavagnaro G, Datti R, Francaviglia N, Rivano C, Tercero VE. Fast attempts at the photodynamic treatment of human gliomas. *J Neurosurg Sci.* 1980 Jul-Dec;24(3-4):119-29. PMID: 6267229.
- [17] Laws ER Jr, Cortese DA, Kinsey JH, Eagan RT, Anderson RE. Photoradiation therapy in the treatment of malignant brain tumors: a phase I (feasibility) study. *Neurosurgery.* 1981 Dec;9(6):672-8. doi: 10.1227/00006123-198112000-00010. PMID: 7322332.
- [18] Vermandel M, Dupont C, Lecomte F, Leroy HA, Tuleasca C, Mordon S, Hadjipanayis CG, Reyns N. Standardized intraoperative 5-ALA photodynamic therapy for newly diagnosed glioblastoma patients: a preliminary analysis of the INDYGO clinical trial. *J Neurooncol.* 2021 May;152(3):501-514. doi: 10.1007/s11060-021-03718-6. Epub 2021 Mar 20. PMID: 33743128.
- [19] GL01, „PD L 506 for Stereotactic Interstitial Photodynamic Therapy of Newly Diagnosed Supratentorial IDH Wild-type Glioblastoma.“, <https://clinicaltrials.gov/ct2/show/NCT03897491>
- [20] NOA-11, „Controlled Clinical Trial to Evaluate the Safety and Efficacy of Stereotactical Photodynamic Therapy With 5-aminolevulinic Acid (Gliolan®) in Recurrent Glioblastoma.“, <https://clinicaltrials.gov/ct2/show/NCT04469699>
- [21] Kostron H. Photodynamic diagnosis and therapy and the brain. *Methods Mol Biol.* 2010;635:261-80. doi: 10.1007/978-1-60761-697-9_17. PMID: 20552352.
- [22] Beck, T.J.; Kreth, F.W.; Beyer, W.; Mehrkens, J.H.; Obermeier, A.; Stepp, H.; Stummer, W.; Baumgartner, R. Interstitial photodynamic therapy of nonresectable malignant glioma recurrences using 5-aminolevulinic acid induced protoporphyrin IX. *Lasers Surg. Med.* 2007, 39, 386–393.
- [23] Johansson, A.; Faber, F.; Kniebühler, G.; Stepp, H.; Sroka, R.; Egensperger, R.; Beyer, W.; Kreth, F.-W. Protoporphyrin IX Fluorescence and Photobleaching during Interstitial Photodynamic Therapy of Malignant Gliomas for Early Treatment Prognosis. *Laser Surg. Med.* 2013, 45, 225–234.
- [24] Quach S, Schwartz C, Aumiller M, Foglar M, Schmutzer M, Katzendobler S, El Fahim M, Forbrig R, Bochmann K, Egensperger R, Sroka R, Stepp H, Rühm A, Thon N. Interstitial photodynamic therapy for newly diagnosed glioblastoma. *J Neurooncol.* 2023 Mar;162(1):217-223. doi: 10.1007/s11060-023-04284-9. Epub 2023 Mar 16. PMID: 36928699; PMCID: PMC10050060.
- [25] Stupp R, Mason WP, van den Bent MJ, Weller M, Fisher B, Taphoorn MJ, Belanger K, Brandes AA, Marosi C, Bogdahn U, Curschmann J, Janzer RC, Ludwin SK, Gorlia T, Allgeier A, Lacombe D, Cairncross JG, Eisenhauer E, Mirimanoff RO; European Organisation for Research and Treatment of Cancer Brain Tumor and Radiotherapy Groups; National Cancer Institute of Canada Clinical Trials Group. Radiotherapy plus concomitant and adjuvant temozolomide for glioblastoma. *N Engl J Med.* 2005 Mar 10;352(10):987-96. doi: 10.1056/NEJMoa043330. PMID: 15758009.
- [26] Leroy, H.-A.; Baert, G.; Guerin, L.; Delhem, N.; Mordon, S.; Reyns, N.; Vignion-Dewalle, A.-S. Interstitial Photodynamic Therapy for Glioblastomas: A Standardized Procedure for Clinical Use. *Cancers* 2021, 13, 5754. <https://doi.org/10.3390/cancers13225754>
- [27] Foglar M, Aumiller M, Bochmann K, Buchner A, El Fahim M, Quach S, Sroka R, Stepp H, Thon N, Forbrig R, Rühm A. Interstitial Photodynamic Therapy of Glioblastomas: A Long-Term Follow-up Analysis of Survival and Volumetric MRI Data. *Cancers (Basel).* 2023 May 4;15(9):2603. doi: 10.3390/cancers15092603. PMID: 37174068; PMCID: PMC10177153.

- [28] Nkune NW, Simelane NWN, Montaseri H, Abrahamse H. Photodynamic Therapy-Mediated Immune Responses in Three-Dimensional Tumor Models. *Int J Mol Sci.* 2021 Nov 23;22(23):12618. doi: 10.3390/ijms222312618. PMID: 34884424; PMCID: PMC8657498.
- [29] Hamblin MR, Abrahamse H. Factors Affecting Photodynamic Therapy and Anti-Tumor Immune Response. *Anticancer Agents Med Chem.* 2021;21(2):123-136. doi: 10.2174/1871520620666200318101037. PMID: 32188394.
- [30] Donohoe C, Senge MO, Arnaut LG, Gomes-da-Silva LC. Cell death in photodynamic therapy: From oxidative stress to anti-tumor immunity. *Biochim Biophys Acta Rev Cancer.* 2019 Dec;1872(2):188308. doi: 10.1016/j.bbcan.2019.07.003. Epub 2019 Aug 8. PMID: 31401103.
- [31] Nath S, Obaid G, Hasan T. The Course of Immune Stimulation by Photodynamic Therapy: Bridging Fundamentals of Photochemically Induced Immunogenic Cell Death to the Enrichment of T-Cell Repertoire. *Photochem Photobiol.* 2019 Nov;95(6):1288-1305. doi: 10.1111/php.13173. Epub 2019 Nov 10. PMID: 31602649; PMCID: PMC6878142.
- [32] Cramer GM, Moon EK, Cengel KA, Busch TM. Photodynamic Therapy and Immune Checkpoint Blockade†. *Photochem Photobiol.* 2020 Sep;96(5):954-961. doi: 10.1111/php.13300. Epub 2020 Jul 14. PMID: 32573787.
- [33] Kleinovink JW, Ossendorp F. Combination of Photodynamic Therapy and Immune Checkpoint Blockade. *Methods Mol Biol.* 2022;2451:589-596. doi: 10.1007/978-1-0716-2099-1_30. PMID: 35505035.
- [34] Bienia A, Wiecheć-Cudak O, Murzyn AA, Krzykawska-Serda M. Photodynamic Therapy and Hyperthermia in Combination Treatment-Neglected Forces in the Fight against Cancer. *Pharmaceutics.* 2021 Jul 27;13(8):1147. doi: 10.3390/pharmaceutics13081147. PMID: 34452108; PMCID: PMC8399393.
- [35] Shi L, Buchner A, Pohla H, Pongratz T, Rühm A, Zimmermann W, Gederaas OA, Zhang L, Wang X, Stepp H, Sroka R. Methadone enhances the effectiveness of 5-aminolevulinic acid-based photodynamic therapy for squamous cell carcinoma and glioblastoma in vitro. *J Biophotonics.* 2019 Oct;12(10):e201800468. doi: 10.1002/jbio.201800468. Epub 2019 Jul 4. PMID: 31140754.
- [36] Werner M, Lyu C, Stadlbauer B, Schrader I, Buchner A, Stepp H, Sroka R, Pohla H. The role of Shikonin in improving 5-aminolevulinic acid-based photodynamic therapy and chemotherapy on glioblastoma stem cells. *Photodiagnosis Photodyn Ther.* 2022 Sep;39:102987. doi: 10.1016/j.pdpdt.2022.102987. Epub 2022 Jun 26. PMID: 35760350.
- [37] Lietke S, Schmutzer M, Schwartz C, Weller J, Siller S, Aumiller M, Heckl C, Forbrig R, Niyazi M, Egensperger R, Stepp H, Sroka R, Tonn JC, Rühm A, Thon N. Interstitial Photodynamic Therapy Using 5-ALA for Malignant Glioma Recurrences. *Cancers (Basel).* 2021 Apr 7;13(8):1767. doi: 10.3390/cancers13081767. PMID: 33917116
- [38] Aumiller M, Heckl C, Quach S, Stepp H, Ertl-Wagner B, Sroka R, Thon N, Rühm A. Interrelation between Spectral Online Monitoring and Postoperative T1-Weighted MRI in Interstitial Photodynamic Therapy of Malignant Gliomas. *Cancers (Basel).* 2021 Dec 27;14(1):120. doi: 10.3390/cancers14010120. PMID: 35008284
- [39] Axel L. Relaxation times and NMR signals. *Magn Reson Imaging.* 1984;2(2):121-30. doi: 10.1016/0730-725x(84)90066-3. PMID: 6530921.

7. Danksagung

Zur Entstehung dieser Habilitationsschrift haben unzählige Personen direkt oder indirekt beigetragen. Ich bedanke mich herzlich bei ihnen allen.

Speziell danke ich Herrn Prof. Dr. med. Christian Stief für die Unterstützung dieses Habilitationsvorhabens, das mir entgegengebrachte Vertrauen, sowie schnelle, pragmatische Lösungen zu allen Anliegen. Die mir gewährten Möglichkeiten, am LIFE-Zentrum der Urologischen Klinik am LMU Klinikum interdisziplinäre Forschung mit biomedizinischen optischen Methoden mit direkter Klinik-Anbindung zu betreiben, mit großen Freiheiten für Kooperationen aller Art, sind einzigartig.

Meinem Mentor Prof. Dr. rer. biol. hum. Ronald Sroka bin ich zu größtem Dank verpflichtet. Ohne seine fortwährende Motivation und Unterstützung wäre dieses Habilitationsvorhaben nicht begonnen, geschweige denn beendet worden. Sein Vertrauen, sein Zuspruch, seine teamorientierte Arbeitsweise, sowie seine Menschlichkeit waren für mich sehr beflügelnd. Seine unermüdliche Energie, den „Tanker“ voranzutreiben, und seine Impulse zur Beschreitung neuer Wege waren mit ausschlaggebend für den Erfolg dieses Unterfangens. Für die Möglichkeit, langfristig weitgehend sorgenfrei am LIFE-Zentrum mitarbeiten zu können, bin ich ihm unendlich verbunden.

Für die langjährige gute und erfolgreiche abteilungsübergreifende Zusammenarbeit am LMU Klinikum danke ich allen beteiligten Kollegen und Kolleginnen, insbesondere Prof. Dr. med. Friedrich-Wilhelm Kreth, Prof. Dr. med. Niklas Thon, MBA, und Dr. med. Stefanie Quach (ehemals Lietke) sowie weiteren Kollegen und Kolleginnen aus der Neurochirurgischen Klinik, der HNO-Klinik und der Urologischen Klinik, sowie dem exzellenten OP-Personal.

Meinen langjährigen Kollegen Dr. rer. biol. hum. Herbert Stepp und Dr. rer. nat. Wolfgang Beyer danke ich für ihre inspirierende Art und die Vermittlung ihres enormen theoretischen und praktischen Wissens im Bereich Biophotonik, biomedizinische Optik und licht-basierte medizinische Diagnostik und Therapie. Sie führten mich als Quereinsteiger in die spannende Tätigkeit im Operationssaal ein und machten mich mit allen erdenklichen Fallstricken und Tricks vertraut. Es machte so viel Freude, mit ihnen zu arbeiten, dass ich stets das Gefühl hatte, genau am richtigen Platz zu sein.

Meinem Kollegen Dr. rer. biol. hum. Maximilian Aumiller bin ich sehr dankbar für die jahrelange gute Zusammenarbeit, seine Verlässlichkeit und sein vielfältiges intensives Engagement, unter anderem bei der Betreuung von Studenten, in der Lehre, im Labor-Management, sowie in wissenschaftlichen Projekten und klinischen Studien. Ich habe durch ihn kontinuierlich und insbesondere in der Endphase zur Komplettierung dieser Habilitationsschrift eine enorme Entlastung erfahren. Sein Wirken im Team ist von unschätzbarem Wert.

Besonders geschätzt habe ich das enzyklopädische Wissen von Dr. rer. biol. hum. Christian Freymüller in nahezu allen technischen Bereichen sowie seine Zuverlässigkeit, Begeisterungsfähigkeit und humorvolle Art.

Sehr dankbar bin ich Dr. rer. biol. hum. Katharina Thomsen (ehemals Kromer) für die Einführung und Einarbeitung in biomedizinische Optik und Physiologie zu Beginn meiner Arbeiten auf diesem Gebiet. Diese Phase war als Grundlage für dieses Habilitationsvorhaben sehr bedeutsam. Sehr profitiert habe ich auch von der langjährigen freundschaftlichen Zusammenarbeit mit Dr. rer. nat. Angelika Rück und ihrer leider verstorbenen Mitarbeiterin Dr. rer. nat. Sviatlana Kalinina von der Core Facility Confocal and Multiphoton Microscopy der Universität Ulm, für die ich mich herzlich bedanke. Auch die erhellenden fachlichen Diskussionen mit Prof. Dr. rer. nat. Wolfgang Zimmermann und PD Dr. rer. nat. Heike Pohla sind in diesem Zusammenhang zu nennen. Ganz besonders dankbar bin ich Prof. Dr. med. Alexander Buchner, einerseits für seinen kompetenten Rat zu biologischen und medizinischen Fragestellungen, andererseits für seine kollegiale Unterstützung bezüglich IT und hausinterner Abläufe.

Bei Dipl.-Ing. (FH) Thomas Pongratz möchte ich mich ganz herzlich für seine unverzichtbare technische Beratung und Unterstützung sowie seine vielen zuverlässigen Lösungen bei technischen Problemen aller Art bedanken, sowie darüber hinaus für seine für das Labor sehr wertvollen Arbeiten im Rahmen wissenschaftlicher Projekte. Ebenso danke ich unserer Sekretärin Kornelia Eberle für ihre kompetente Unterstützung und Entlastung bei allen Organisations- und Verwaltungsaufgaben, ihre Beratung bezüglich der vielfältigen hausinternen Abläufe, sowie für Hilfestellungen im Verlauf dieses Habilitationsvorhabens.

Meinem früheren Mentor Prof. Dr. Dr. h.c. Helmut Dosch bin ich dankbar für die verantwortungsvolle innere Haltung, die er mir als stabiles Fundament für meine wissenschaftliche Arbeit vermittelt hat. Er hat meine Begeisterung für die Wissenschaft ausschlaggebend befördert. Für seine Menschlichkeit und Unterstützung in verschiedenen Phasen meiner Laufbahn bin ich ihm sehr dankbar. Eine wichtige Stütze waren auch PD Dr. rer. nat. Janos Major, Prof. Hyunjung Kim, PhD, und Prof. Dr. rer. nat. Wolfgang Donner, durch die ich wesentliche Impulse für die spätere Entscheidung zur Habilitation erfahren habe. Die freundschaftliche Zusammenarbeit mit ihnen im Team war für mich prägend und hat mir viel Freude bereitet.

Ich bedanke mich bei meiner Familie für die Unterstützung und Bestärkung bei allen Unterfangen und in allen Lebenslagen, insbesondere meiner Mutter, meinem Stiefvater, meiner Schwester und ihrem Freund, sowie meinem leider verstorbenen Vater. Letzterem bin ich auch für die frühe Vermittlung physikalischer Zusammenhänge im Alltag dankbar, die meine Faszination für Physik befördert hat, sowie für sein Beispiel von Verantwortungsbewusstsein gegenüber der Schöpfung und der Welt.

Besonders wichtig waren für mich stets Zerstreuung, Lebensfreude und emotionaler Rückhalt durch Freunde, die mir ein kontinuierliches Arbeiten über lange Jahre und auch Durststrecken hinweg ermöglicht haben. Hierfür danke ich meinem leider verstorbenen besten Freund Dr. rer. nat. Michael Schmid („Boe“), der als Wissenschaftler auch alle Aspekte, Probleme und gelegentlichen Skurrilitäten einer Tätigkeit in diesem Bereich aus eigener Erfahrung kannte, sowie Iris, Tom, Michi, Denise, Nati und vielen weiteren. Zusätzlich danke ich meiner Freundin Gabi für ihr Verständnis und die Unterstützung, die sie mir trotz aller Entbehrungen und Schwierigkeiten insbesondere während der Endphase zur Komplettierung dieser Habilitationsschrift entgegengebracht hat.

8. Originalarbeiten der kumulativen Habilitationsleistung

Liste der in diesem Kapitel inkludierten Originalarbeiten dieser kumulativen Habilitationsschrift gemäß ihrer Referenzierung in Kapitel 4:

4.1 Methodische Entwicklungen und präklinische Untersuchungen

4.1.1 Fluoreszenz-basierte Methoden zur Erhöhung der Sicherheit bei der stereotaktischen Biopsie

- [O1] Markwardt NA, Stepp H, Franz G, Sroka R, Goetz M, Zelenkov P, **Rühm A**. Remission spectrometry for blood vessel detection during stereotactic biopsy of brain tumors. J Biophotonics. 2017 Aug;10(8):1080-1094. doi: 10.1002/jbio.201600193. Epub 2016 Oct 7. PMID: 27714967
- [O2] Markwardt NA, Haj-Hosseini N, Hollnburger B, Stepp H, Zelenkov P, **Rühm A**. 405 nm versus 633 nm for protoporphyrin IX excitation in fluorescence-guided stereotactic biopsy of brain tumors. J Biophotonics. 2016 Sep;9(9):901-12. doi: 10.1002/jbio.201500195. Epub 2015 Nov 13. PMID: 26564058

4.1.2 Methoden zur laser-basierten Herstellung zylindrischer Lichtdiffusoren mit frei wählbaren Abstrahlprofilen

- [O3] Ströbl S, Domke M, **Rühm A**, Sroka R. Investigation of non-uniformly emitting optical fiber diffusers on the light distribution in tissue. Biomed Opt Express. 2020 Jun 8;11(7):3601-3617. doi: 10.1364/BOE.394494. eCollection 2020 Jul 1. PMID: 33014554
- [O4] Ströbl S, Wäger F, Domke M, **Rühm A**, Sroka R. Homogeneously Emitting, Mechanically Stable, and Efficient fs-Laser-Machined Fiber Diffusers for Medical Applications. Lasers Surg Med. 2022 Apr;54(4):588-599. doi: 10.1002/lsm.23365. Epub 2020 Dec 8. PMID: 33616996

4.1.3 Optische Analyse der Zusammensetzung von humanem Blut als Basis für die Erkennung PDT-induzierter photochemischer Veränderungen optischer Gewebeeigenschaften in vivo

- [O5] Heckl C, Lang A, **Rühm A**, Sroka R, Duffield T, Vogeser M, Paal M. Spectrophotometric evaluation of hemolysis in plasma by quantification of free oxyhemoglobin, methemoglobin, and methemalbumin in presence of bilirubin. J Biophotonics. 2021 May;14(5):e202000461. doi: 10.1002/jbio.202000461. Epub 2021 Feb 13. PMID: 33527705

4.1.4 Entwicklung dualer Gewebe-Phantome mit simultan variabel einstellbaren optischen und NMR-Eigenschaften

- [O6] Aumiller M, Arazar A, Sroka R, Dietrich O, **Rühm A**. Investigations on correlations between changes of optical tissue properties and NMR relaxation times. Photodiagnosis Photodyn Ther. 2024 Feb;45:103968. doi: 10.1016/j.pdpdt.2024.103968. Epub 2024 Jan 10. PMID: 38215958

4.2 Klinische Umsetzung und Analysen zur interstitiellen photodynamischen Therapie (iPDT) an Hirntumoren

4.2.1 Durchführung und Auswertung von iPDT-Behandlungen von Rezidiven maligner Gliome und unbehandelten Glioblastomen

- [O7]** Lietke S, Schmutzer M, Schwartz C, Weller J, Siller S, Aumiller M, Heckl C, Forbrig R, Niyazi M, Egensperger R, Stepp H, Sroka R, Tonn JC, **Rühm A**, Thon N. Interstitial Photodynamic Therapy Using 5-ALA for Malignant Glioma Recurrences. *Cancers (Basel)*. 2021 Apr 7;13(8):1767. doi: 10.3390/cancers13081767. PMID: 33917116
- [O8]** Quach S, Schwartz C, Aumiller M, Foglar M, Schmutzer M, Katzendobler S, El Fahim M, Forbrig R, Bochmann K, Egensperger R, Sroka R, Stepp H, **Rühm A**, Thon N. Interstitial photodynamic therapy for newly diagnosed glioblastoma. *J Neurooncol*. 2023 Mar;162(1):217-223. doi: 10.1007/s11060-023-04284-9. Epub 2023 Mar 16. PMID: 36928699
- [O9]** Foglar M, Aumiller M, Bochmann K, Buchner A, El Fahim M, Quach S, Sroka R, Stepp H, Thon N, Forbrig R, **Rühm A**. Interstitial Photodynamic Therapy of Glioblastomas: A Long-Term Follow-up Analysis of Survival and Volumetric MRI Data. *Cancers (Basel)*. 2023 May 4;15(9):2603. doi: 10.3390/cancers15092603. PMID: 37174068

4.2.2 Untersuchung von Relationen zwischen SOM-Daten und MRT-Daten sowie deren zeitlicher Entwicklung im Verlauf bzw. im Nachgang von iPDT-Behandlungen an Hirntumor-Patienten

- [O10]** Aumiller M, Heckl C, Quach S, Stepp H, Ertl-Wagner B, Sroka R, Thon N, **Rühm A**. Interrelation between Spectral Online Monitoring and Postoperative T1-Weighted MRI in Interstitial Photodynamic Therapy of Malignant Gliomas. *Cancers (Basel)*. 2021 Dec 27;14(1):120. doi: 10.3390/cancers14010120. PMID: 35008284

Publikation [O1]

Einsehbar unter:

Markwardt NA, Stepp H, Franz G, Sroka R, Goetz M, Zelenkov P, Rühm A. Remission spectrometry for blood vessel detection during stereotactic biopsy of brain tumors. J Biophotonics. 2017 Aug;10(8):1080-1094. doi: 10.1002/jbio.201600193. Epub 2016 Oct 7. PMID: 27714967.

Aus urheberrechtlichen Gründen kann der Inhalt dieser Publikation an dieser Stelle nicht wiedergegeben werden. Er ist mit Hilfe der bibliographischen Informationen abrufbar.

Publikation [O2]

Einsehbar unter:

Markwardt NA, Haj-Hosseini N, Hollnburger B, Stepp H, Zelenkov P, Rühm A. 405 nm versus 633 nm for protoporphyrin IX excitation in fluorescence-guided stereotactic biopsy of brain tumors. J Biophotonics. 2016 Sep;9(9):901-12. doi: 10.1002/jbio.201500195. Epub 2015 Nov 13. PMID: 26564058

Aus urheberrechtlichen Gründen kann der Inhalt dieser Publikation an dieser Stelle nicht wiedergegeben werden. Er ist mit Hilfe der bibliographischen Informationen abrufbar.



Investigation of non-uniformly emitting optical fiber diffusers on the light distribution in tissue

STEPHAN STRÖBL,^{1,2,*} MATTHIAS DOMKE,¹ ADRIAN RÜHM,^{2,3} AND RONALD SROKA^{2,3}

¹Research Centre for Microtechnology, FH Vorarlberg, Dornbirn, Vorarlberg, Austria

²Laser Research Laboratory, LIFE Centre, LMU Munich, Bavaria, Germany

³Department of Urology, University Hospital, LMU Munich, Bavaria, Germany

*stephan.stroebl@fhv.at

Abstract: The influence of inhomogeneities in the emission characteristics of optical fiber diffusers on the light distribution within biological tissue was evaluated by Monte Carlo (MC) simulations and by experiments on optical phantoms. Due to the strong scattering of light within biological tissue, inhomogeneities in the emission profile become blurred within a short light propagation distance, so that the light distribution within the tissue approaches that of a homogeneous diffuser. The degree of feature vanishing in the light distribution is mainly determined by the width of the inhomogeneities. It was shown that the influence of local inhomogeneities on top of a homogeneous light distribution fades away very effectively within 1 mm of tissue depth, which results in a light distribution very close to that for a homogeneously emitting diffuser. Emission profiles composed of multiple narrow peaks distributed over the full diffuser length with a peak-to-peak distance of less than 2 mm result in an almost homogeneous light distribution after approximately 1 mm of tissue depth. While this article is focused on the impact of diffuser inhomogeneities on the light distribution within the tissue, the importance of further investigations on the related thermal effects is also discussed.

© 2020 Optical Society of America under the terms of the [OSA Open Access Publishing Agreement](#)

1. Introduction

Interstitial photodynamic therapy (PDT) is an evolving method for the treatment of malignant brain cancer [1–4]. Much research is currently focussing on the translation from the laboratories to clinical application [5]. The strength of this method is its minimally invasive surgical approach in combination with the selective targeting of individual tumor cells. The selectivity of the tumor treatment is achieved by the increased uptake of aminolevulinic acid (5-ALA) in high-grade brain tumor tissue and the subsequent transformation to protoporphyrin IX (PPIX) as part of the heme-biosynthesis pathway. By illuminating the affected region with light of a wavelength of $\lambda = 635$ nm, the present PPIX molecules become excited. The excited PPIX molecules transfer their energy to the present intracellular oxygen molecules, which triggers the conversion of oxygen into a reactive oxygen species. Reactive oxygen species may cause apoptosis and necrosis in the adjacent regions [6–8]. In order to treat all targeted malignant cells, a sufficiently intense and sufficiently homogenous light distribution within the targeted tumor volume is necessary.

The illumination of such tissue volumes within the human body could be achieved by means of optical fibers with attached cylindrical diffusely scattering fiber tips [9–13]. Depending on the volume to be treated, multiple fiber diffusers may have to be positioned simultaneously within the targeted treatment site. The inter-fiber distance is set to approximately 9 mm in order to avoid thermal side effects between neighbouring fibers, while still retaining a photodynamic response at the outer tumor boundary [14]. Regarding the light intensity limits, it had been determined that the minimal applied photon number per cm^3 to reach a PDT effect in cells is approx. 1.3×10^{18} photons [15]. An upper limit, especially for the brain, is defined by the critical temperature limit of 42°C, where healthy tissue starts to degenerate [16,17].

Cylindrical diffuser tips can be distinguished technically into two groups: volume and surface scattering devices. Volume scatterers are commonly realized by attaching polymer tubes containing scattering particles (e.g. TiO_2) to the end of the light-delivering fiber [18], or by generating internal scattering centers inside the fiber core by laser processing [19–23]. Surface scatterers can be manufactured by roughening the fiber core, which had been proposed to be accomplished with different laser systems (CO_2 , Ultrafast, and Excimer) [24–28], mechanically or by HF-etching techniques [29].

The challenge, which all manufacturing techniques have in common, is to provide homogenous light emission along the complete diffuser length. This is difficult to achieve, and, thus, many diffusers with inhomogeneous emission patterns are on the market. For example, when examined with a laboratory setup, intensity peaks may be present at the distal and/or proximal diffuser end [27,30,31], or the spatial distribution of the scattering elements may lead to alternating intensity maxima and minima along the diffuser [19,25]. This leads to the general question, how intensity variations in the emission profile of fiber diffusers influence the light distribution within the tissue.

This study investigates the impact of intensity inhomogeneities of diffusers on the light distribution within the surrounding tissue. A model based on Monte Carlo ray tracing was developed to simulate the light emission from a cylindrical light diffuser. This model was calibrated by means of the intensity distribution of a diffuser measured on a real cylindrical light diffuser by means of an imaging and a non-imaging camera setup [31]. In addition, the real diffuser was positioned surface-parallel orientation at different depths within an artificial tissue phantom with known optical properties, and the light distribution transmitted to the surface of this phantom was measured and investigated for each diffuser depth. The measurements on the real diffuser were then compared to the respective simulated light distributions in the correspondingly simulated tissue phantom. By varying the modelling parameters of the inhomogeneous emission profiles, the impact of height and width of single intensity peaks, as well as the interplay between two adjacent intensity peaks were investigated regarding depth dependent intensity changes in the modelled surrounding environment.

2. Material and methods

2.1. Experimental Part

As real diffuser with inhomogeneous emission profile, a junk diffuser (based on a CD-403, LifePhotonic GmbH, Bonn, Germany) was selected. It will be termed *reference diffuser* in the following. The emission profile of the reference diffuser is characterized by two local intensity peaks at the distal end, while the radial intensity distribution of the remaining diffuser length is measured to be approximately homogeneous. The diffuser region consists of a 30 mm long polymer tube, filled with TiO_2 polymers acting as scattering centers, attached to the end of a light waveguide with a core diameter of 400 μm . For all subsequently presented measurements and simulations, a diffuser length of 30 mm was used. To reduce the forward transmission of light, a mirror is attached at the distal diffuser end. Thereby, the primary transmitted light is reflected back into the diffuser, which serves to improve the homogeneity of the emission profile.

As sketched in Fig. 1(a), the spatially resolved intensity distribution on the diffuser surface was determined by means of an imaging setup, while the angular resolved emission profile was measured using a non-imaging camera setup as shown in Fig. 1(b). In addition, the light distribution on the surface of an artificial tissue phantom in which the diffuser itself is placed at different depths, as depicted in Fig. 1(c), was measured using the imaging technique. Furthermore, the experiment in Fig. 1(c) was reconstructed and investigated using MC-simulations (Fig. 1(d)).

For all experiments, light of a LED (M625D3, Thorlabs, Newton, NJ, USA) emitting at a wavelength of $\lambda = 635 \text{ nm}$ was coupled into the proximal end of the diffuser fiber. In this way, the whole NA of the fiber was used. The emission power measured at the diffuser end was set to 80

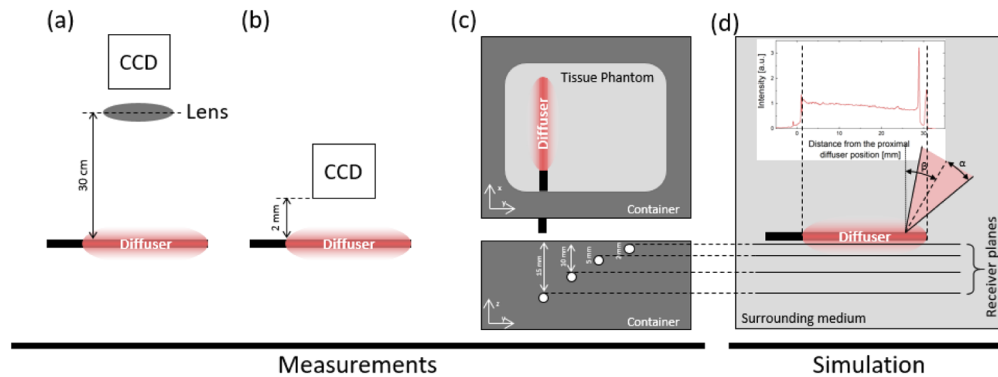


Fig. 1. (a) Imaging camera setup to measure the spatially resolved intensity distribution on the diffuser surface. (b) Non-imaging setup to measure the angular intensity distribution of diffusers. (c) Setup to measure the light distribution in an artificial tissue phantom. The diffuser was placed 2 mm, 5 mm, 10 mm and 15 mm below the surface of the tissue phantom, while an imaging camera recorded the light distribution on the phantom surface. (d) Schematic representation of the simulation model, reconstructing the experiment in (c). The surface emission profile measured with setup (a) was allocated to the modelled surface emitter. A cone-shaped emission was assumed from each spot of the diffuser surface, with full cone opening angle 2α and cone tilt angle β as adjustable model parameters, which were calibrated using the results obtained with setup (b). The resulting light distribution within virtual receiver planes at distances of 2 mm, 5 mm, 10 mm, and 15 mm from the diffuser surface were evaluated.

mW measured by a calibrated integrating sphere (IS200-4, Thorlabs, Newton, NJ, USA). This power level was sufficient to obtain signals from the maximum investigated fiber depth of 15 mm within the tissue phantom.

Emission profiles from cylindrical diffusers and intensity distributions based on subsequent light penetration through tissue were determined experimentally using three setups:

- (a) The *imaging setup* (Fig. 1(a)) for characterization of the emission profile of a cylindrical diffuser consisted of a CCD camera (DMK 41BU02, The Imaging Source Europe GmbH, Bremen, Germany) and a lens ($f = 12$ mm, TCL 1216 5MP, The Imaging Source Europe GmbH, Bremen, Germany). The distance between lens and the diffuser surface was 30 cm while the diffuser was aligned horizontally in the imaging plane. For the determination of the intensity profile along the longitudinal diffuser axis the exposure time of the camera had to be carefully adjusted to avoid oversaturated pixels. Then, an image was captured and the grey-scale values along the diffuser axis were extracted. These intensity values were derived by averaging over 10 adjacent pixels in the direction perpendicular to the diffuser axis. This procedure was used to determine the emission intensity profile in air (Fig. 1(a)) and on the artificial tissue phantom tissue surface (Fig. 1(c)).
- (b) The *non-imaging camera setup* (Fig. 1(b)) [32] for characterization of the emission profile of a cylindrical diffuser consisted of a CCD camera chip (ICX205AL, Sony, Tokyo, Japan, dimension: (4.5×6.0) mm², 1280×960 pixel, pixel size (4.65×4.65) μm²) that was positioned at a distance of 2 mm from the surface of the fiber diffuser. As the diffuser length exceeds the chip sensor's dimension, the sensor was continuously moved by means of a computer controlled stepping motor (LTS300/M, Thorlabs, Newton, NJ, USA) along the diffuser surface with a velocity of 0.1 mm/s, while recording a video-sequence at 15 frames per second. The principle of the raw data acquisition and evaluation is sketched in Fig. 2. Mimicking a line sensor perpendicular to the moving direction, only one pixel line

per frame was evaluated. The analysed pixel line on the sensor is fixed (marked yellow in Fig. 2). Thereby, each frame, with frame number n , corresponds to a distinct position x_n along the longitudinal diffuser axis. Only the intensity value of the brightest pixel within this pixel line (marked by an “X” in Fig. 2) was extracted, as intensity value I_n to build up the emission profile $I_n(x_n)$ along the full diffuser length. By means of this non-imaging method, also forward or backward emitted light could be detected at adjacent pixel positions x_n , which is not possible in the imaging setup.

- (c) The investigation of the *light distribution in tissue* arising from the reference diffuser was performed with the *imaging setup* sketched in Fig. 1(c). The diffuser was submerged in an artificial phantom mimicking the optical properties of human brain tissue. The phantom was prepared using a standard recipe [33]. In brief, 434 ml of water were mixed with 0.6 Vol.-% Agar (3 ml). The solution was heated to 100°C, while continuously stirring. After cooling to 60°C, 12.5 Vol.-% of Lipovenös (Lipovenös MCT 20%, Fresenius Kabi Deutschland GmbH, Bad Homburg, Germany) (62.5 ml) as scatterer and 0.1 Vol.-% of black ink (0.5 ml) as absorber were added to the solution. The scattering and absorption coefficients are defined by the used concentrations of Lipovenös and ink, respectively. The optical properties of this specific artificial phantom were measured to have an absorption coefficient $\mu_a = 0.09 \text{ mm}^{-1}$, a reduced scattering coefficient $\mu_s' = 2.2 \text{ mm}^{-1}$, and an anisotropy factor $g = 0.95$ [33]. After further cooling to 40°C, the liquid phantom was poured into a metal container as illustrated in Fig. 1(c). The container allows for positioning the test diffuser in defined phantom depth positions below the phantom surface by means of pre-drilled lateral horizontal boreholes. The boreholes were set at a depth of 2 mm, 5 mm, 10 mm, and 15 mm below the artificial phantom surface. Preliminary tests revealed that measuring the light distribution for tissue depth smaller than 2 mm was not feasible as rupturing of the artificial phantom surface by the diffuser was not avoidable in this case. After preparation, the artificial phantom was solidified by cooling to room temperature (21°C).

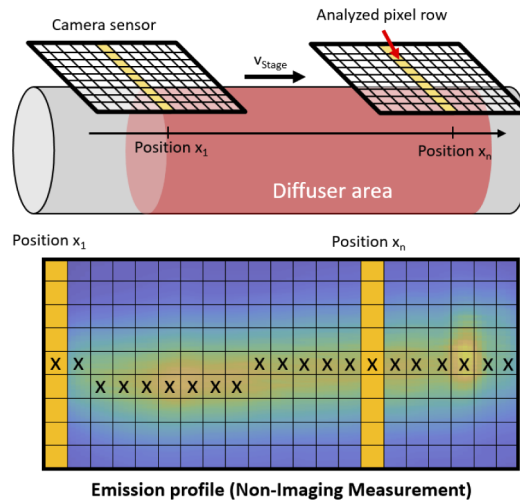


Fig. 2. Acquisition of the emission profile of a cylindrical light diffuser using the non-imaging camera setup. The analysed pixel row per recorded frame is marked in yellow. The brightest pixel per analysed pixel line is marked by an “X” and yields the intensity values building up the emission profile along the longitudinal diffuser axis.

The measurement of the light distribution on the surface of the artificial tissue phantom was performed five times for each depth position as follows: The diffuser was placed through one of the boreholes into the phantom. The phantom surface was imaged using the configuration in Fig. 1(a). The intensity distribution on the phantom surface in the direction parallel to the longitudinal diffuser axis was evaluated in analogy to the abovementioned imaging procedure applied to the diffuser surface in air. This procedure was repeated for diffuser placements in each borehole of the container ($n = 5$) independently and in random order.

2.2. MC-simulation part

Simulation runs were performed using Monte Carlo ray-tracing software (LightTools, Version 8.7.0, Synopsys, Mountain View, CA, USA). In the simulation model, the fiber diffuser is described as cylindrical geometry with a diameter of 1.1 mm and a length of 30 mm. Intensity values were associated to a pixel grid positioned on the cylindrical lateral surface of the modelled diffuser. The grid was composited from 3600 angular pixels (angular resolution: 10 pixel per degree) and 4000 longitudinal pixels (longitudinal resolution: 133 pixel per mm). A rotationally symmetric intensity distribution was assumed, as a worst-case scenario in terms of tissue heating for fixed overall maximum intensity value. For rotationally asymmetric distributions with the same maximum intensity, the overall impact on the surrounding tissue would be reduced. The longitudinal intensity values and the emission direction were adjusted according to the emission profiles measured by the imaging (Fig. 1(a)) and non-imaging setup (Fig. 1(b)), respectively. The emission angle distribution of the light rays was assumed to be Lambertian within limited angular ranges, revealing a good agreement between simulation and experiment in initial testings. As shown in Fig. 1(d), the angles 2α and β define the full opening angle of the respective emission cone and its tilt in relation to the surface normal, respectively. All simulation model runs were carried out with 10^8 rays.

The angles α and β were determined as follows. The emission profile of the reference diffuser measured with the imaging setup (Fig. 1(a)) was imported into the simulation. In analogy to the non-imaging measurement illustrated in Fig. 1(b), in the simulation model, a virtual receiver plane was positioned in the simulation model parallel to the longitudinal diffuser axis at a distance of 2 mm from the diffuser surface, as sketched in Fig. 1(d). The spatial resolution on the virtual receiver plane was defined according to the resolution of the camera sensor with a pixel size of $(4.65 \times 4.65) \mu\text{m}^2$. Simulation runs were performed for $\alpha = 1^\circ, 20^\circ, 25^\circ, 30^\circ$, and 90° and $\beta = 0^\circ$. For $\alpha = 25^\circ$, additional runs were performed to define the fraction of forward and backward emitted rays with $\beta = -35^\circ, 0^\circ$, and 35° . The parameter set of α and β , which provided the best agreement between non-imaging experiment (Fig. 1(b)) and simulation, was selected for all further simulations presented in this study.

Further MC-simulations mimicking the geometries of the phantom experiments (Fig. 1(c)) were performed as illustrated in Fig. 1(d). For this purpose, the simulated cylinder diffuser was embedded in a medium to which the known optical properties of the artificial tissue phantom (brain tissue) were assigned. In analogy to the measurement of the light distributions for different depth positions of the diffuser below the phantom surface (Fig. 1(c)), the light distribution in the simulation model was recorded at the corresponding distances from the diffuser surface (2 mm, 5 mm, 10 mm, 15 mm) using virtual receiver planes. For reasons of simplification, the refractive index mismatch between tissue phantom and air in the experiment was neglected in the simulation. However, initial tests have shown that this only minorly influences the results in the presented setups.

While the knowledge of the light distribution at a few selected distances from the cylindrical diffuser inside a surrounding tissue volume contains valuable information about the light distribution induced in the tissue by the diffuser, it only provides rather coarse information about the continuous evolution of the light distribution as a function of distance to the diffuser surface.

To investigate this evolution with higher resolution in the distance coordinate, an additional virtual receiver plane was introduced, in this case oriented perpendicular to the diffuser axis. In the longitudinal direction, it was placed at the position of the intensity maximum to be investigated. The resolution on the virtual receiver plane was defined by a pixel size of $(100 \times 100) \mu\text{m}^2$.

In addition, the impact of height and width of intensity peaks in the emission profile of cylindrical diffusers on the light distribution in tissue, as well as the interplay between two adjacent intensity peaks were studied by modelling the light distribution in tissue for artificially generated emission profiles. To model a single local intensity peak, a homogeneous intensity distribution over the entire diffuser length, $f_{\square}(x)$, was combined with a Gaussian distribution, $f_{\wedge}(x)$. The total emission profile $f(x)$ was described according to Eq. (1).

$$f(x) = f_{\square} + f_{\wedge} = \begin{cases} I_0 & \forall x \in [0, 30 \text{ mm}] \\ 0 & \forall x \notin [0, 30 \text{ mm}] \end{cases} + I_{\max} \cdot e^{-\ln 2 \frac{(x-x_0)^2}{(w_{\text{FWHM}}/2)^2}} \quad (1)$$

I_0 is the background intensity, I_{\max} is the height, x_0 the position, and w_{FWHM} the full width at half maximum of the added inhomogeneity on top. The position of the intensity maximum was set constant at $x_0 = 15 \text{ mm}$. The intensity of the homogeneous emission was set to $I_0 = 1$, the initial maximum intensity I_{\max} was set to $I_{\max} = 1.5, 2.0, 3.0$, and 6.0 , and the width parameter w_{FWHM} to $w_{\text{FWHM}} = 0.2 \text{ mm}$, 1.0 mm , and 5.0 mm .

The impact of two adjacent intensity peaks on the light distribution in tissue was studied combining f_{\square} with two Gaussian distributions f_{\wedge} . The total emission profile was described by Eq. (2).

$$\begin{aligned} f(x) &= f_{\square} + f_{\wedge,1} + f_{\wedge,2} = \\ &= f_{\square} + I_{\max} \cdot e^{-\ln 2 \frac{(x-(x_0-\frac{\Delta x}{2}))^2}{(w_{\text{FWHM}}/2)^2}} + I_{\max} \cdot e^{-\ln 2 \frac{(x-(x_0+\frac{\Delta x}{2}))^2}{(w_{\text{FWHM}}/2)^2}} \end{aligned} \quad (2)$$

The distance between the two maxima was set to $\Delta x = 2 \text{ mm}$, 3 mm , 5 mm , 8 mm , and 10 mm . The Gaussian function parameter were set to $I_R(0) = 2.0$ and $w_{\text{FWHM}} = (0.2 \text{ mm}, 1.0 \text{ mm})$. Thereby, the influence of the width and the distance between the two intensity peaks on the light distribution in tissue was investigated.

2.3. Analysis part

The influence of inhomogeneities in the emission profile of a cylindrical diffuser on the light distribution in the surrounding tissue was analysed by determining the difference between light distributions from homogeneous emission profiles with and without added local intensity peaks at certain longitudinal positions. For this purpose, it is necessary to separate the additional contribution in the light distribution that is due to the local intensity maximum (A) from the one that is due to the perfectly or at least approximately homogeneous baseline emission (B). In this context, different evaluation procedures had to be applied for the light distributions measured in the experiment and those obtained from the simulations.

In case of intensity profiles measured experimentally after penetration through tissue phantom, the following approach was used to separate the fraction (A) attributed to local intensity maxima and the fraction (B) attributed to an approximately homogeneous baseline intensity. The experimentally measured intensity profile was modelled as a sum of five Gaussian curves, where four Gaussian curves were used to describe the slowly varying intensity distribution interpreted as fraction (B) and one Gaussian curve to describe the local intensity peak interpreted as fraction (A). A sum of five Gaussian curves was chosen, because five was the lowest number of Gaussian curves that provided a mean deviation of less than 1% between fit curve and measured curve. The sum of the five Gaussian functions that was finally used to fit the experimentally measured

intensity profile can be written by Eq. (3) as

$$g(x) = \sum_{i=1}^5 a_i \cdot e^{-\frac{x-b_i}{2c_i^2}}, \quad (3)$$

where a denotes the peak height, b the position, and c the width of each Gaussian curve.

In Fig. 3, an example of a fit curve according to Eq. (3) to an experimentally measured emission profile for a diffuser depth position of $d = 5$ mm below the phantom surface is shown. The blue curve describes the composition of four of the five Gaussian curves, fraction (B), attributed to the approximately homogeneous baseline intensity. The fifth Gaussian curve, fraction (A), models a local intensity maximum at the location x with a peak intensity I_{\max} . Dividing the maximal intensity $I_{\max,x}(d)$ of the intensity peak at the location x by the corresponding baseline intensity $I_{0,x}(d)$ at the same location x yields the intensity ratio $I_R(d) = \frac{I_{\max,x}(d)}{I_{0,x}(d)}$, where d denotes the diffuser depth below the phantom surface. In this way, the intensity maximum can be evaluated in comparison to the baseline intensity. Such evaluations of the measured intensity distributions at the phantom surface were performed for four different depth positions d of the reference diffuser below the phantom surface, $d = 2$ mm, 5 mm, 10 mm, and 15 mm below the phantom surface ($n = 5$ measurements each). Average value and standard deviation of the ratios $I_R(d)$ were calculated for each depth value d from the repeated experiments and evaluations. In this way, the fading of such intensity peaks in the experimental intensity distribution with increasing diffuser depth below the phantom surface was analysed.

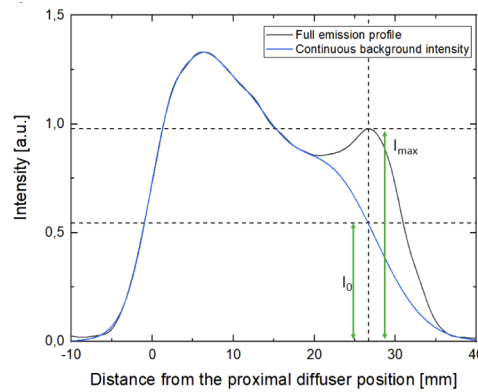


Fig. 3. Measured light distribution (black) of the reference diffuser in a depth of $d = 5$ mm below the surface of an artificial tissue phantom. The intensity contribution I_0 at the peak position $x = 27$ mm that is attributed to an approximately homogeneous baseline emission profile, fraction (B), is determined based on a composition of four Gaussian functions (blue) according to Eq. (3).

In case of intensity profiles, arising from simulated emission profiles after penetration through tissue, the fraction (A) attributable to local intensity peaks in the emission profile on the diffuser surface was separated from the background, fraction (B), by simulating the light distribution after tissue penetration for two scenarios: a perfectly homogeneous emission profile with and without artificially added intensity peaks of Gaussian shape.

For a single intensity peak at the position x , the fading of intensity at the position x with increasing depth d of the diffuser below the phantom surface was evaluated in comparison to the corresponding decrease in intensity at the same position x in the situation without added peak in the emission profile. Dividing the two intensity values at the position x yields the intensity ratio $I_{R,\text{single}}(d) = \frac{I_{\max,x}(d)}{I_{0,x}(d)}$. In Fig. 4, the evaluation process for determining $I_{\max,x}$ and $I_{0,x}$ is

illustrated. A “50% tissue depth” $d_{p,\text{single}}$ at which the excess of the intensity ratio $I_{R,\text{single}}(d)$ over 1 drops to 50% of its initial value was defined by the criterion $\frac{I_{R,\text{single}}(d_{p,\text{single}})-1}{I_{R,\text{single}}(0)-1} = 0.5$. By choosing the value 0.5 instead of the more common value $1/e$ to describe the decay, the corresponding depth value $d_{p,\text{single}}$ could be determined for all measured and simulated scenarios, even for parameter configurations resulting in a rather slow decay.

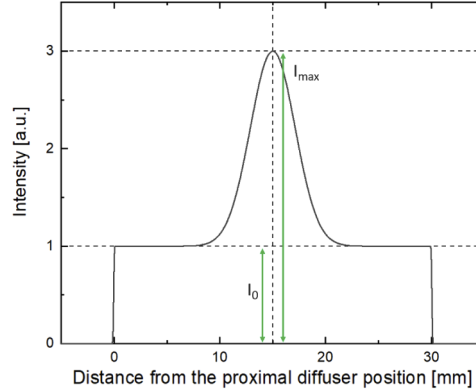


Fig. 4. Illustration of the peak intensity $I_{\max,x}(d)$ at the position of a local peak (here: $x = 15$ mm) in a simulated intensity distribution after light penetration through tissue, in relation to an underlying baseline intensity $I_0(d)$, arising from a simulation with homogeneous emission profile without added intensity peaks. By dividing these intensity values, the intensity ratio $I_{R,\text{single}}(d)$ is calculated, where d is the depth position of the diffuser below the phantom surface.

The possibility to distinguish two neighbouring Gaussian intensity peaks (here always of equal height) on top of a homogeneous emission profile was evaluated by calculating the intensity ratio $I_{R,\text{double}}(d) = \frac{I_{\max}(d)}{I_{\text{center}}(d)}$, as sketched in Fig. 5. For the “peak coalescence tissue depth” $d_{p,\text{double}}$, for which $I_{R,\text{double}}(d_{p,\text{double}}) = 1$ within the precision of the evaluation, the maximum intensity

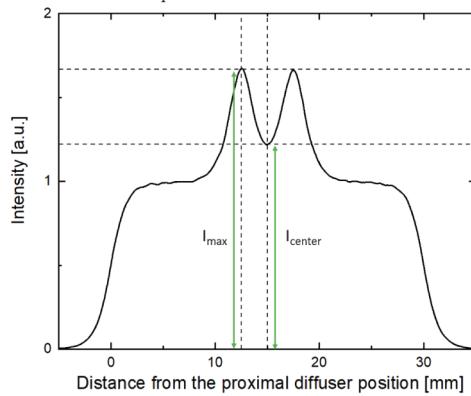


Fig. 5. Illustration of the (here identical) peak intensities $I_{\max,1}(d)$ and $I_{\max,2}(d)$ at two local peaks (here at: $x_1 = 12.5$ mm, $x_2 = 17.5$ mm) in a simulated intensity distribution after light penetration through tissue, in relation to the intensity $I_{\text{center}}(d)$ between the two intensity maxima (here at: $x_c = 15.0$ mm). By dividing these intensity values, the intensity ratio $I_{R,\text{double}}(d)$ is calculated, where d is the depth position of the diffuser below the phantom surface.

$I_{\max}(d_{p,\text{double}})$ becomes identical to $I_{\text{center}}(d_{p,\text{double}})$ and, thus, the two intensity peaks are no longer discernible.

3. Results

In Fig. 6, 7, and 8 the radial emission profile along a diffuser of 30 mm length (0 mm: proximal diffuser part and entrance of light, 30 mm: distal end of diffuser with mirror) is shown for the different experiments on the reference diffuser and corresponding simulations.

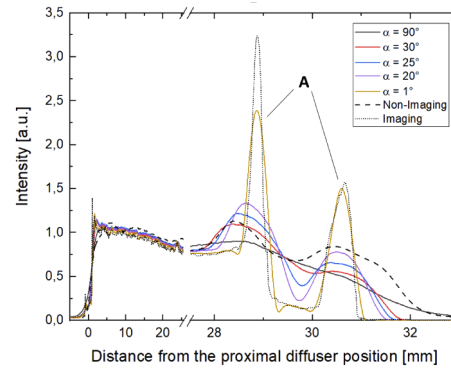


Fig. 6. Simulated emission profiles for a cylindrical light diffuser in air for a cone tilt angle $\beta = 0^\circ$ and five different cone opening angles α ($\alpha = 1^\circ, 20^\circ, 25^\circ, 30^\circ, 90^\circ$). The experimental emission profiles measured on the reference diffuser in air by the non-imaging and imaging setup (Fig. 1(a) and (b)) are shown as black dashed and dotted line, respectively.

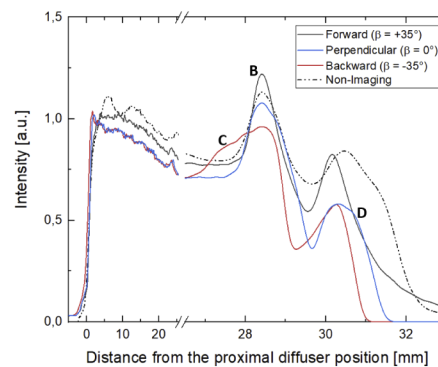


Fig. 7. Simulated emission profile for a cone opening angle $\alpha = 25^\circ$ and three different cone tilt angles β ($\beta = -35^\circ, 0^\circ, +35^\circ$). The experimental emission profile measured on the reference diffuser in air by the non-imaging setup is shown as black dash-dotted line.

The emission profiles at the surface of the reference diffuser measured by the imaging (dotted black line) and non-imaging (dashed black line) method according to Fig. 1(a) and (b) are depicted in Fig. 6. Although, the two intensity decays between the longitudinal positions 0 mm and 25 mm are very similar for the two measurement techniques, the amplitude and shape of the two intensity peaks observed between the longitudinal positions 28 mm and 32 mm differ dramatically. For comparison, five different emission profiles (five solid lines of different colours) were simulated according to Fig. 1(d), for an emission cone perpendicular to the optical axis (i.e.

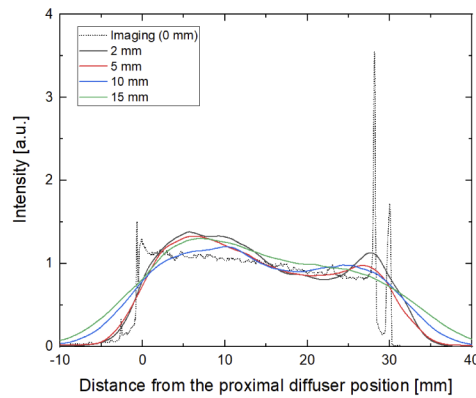


Fig. 8. Experimental intensity profiles measured with the imaging setup on the surface of the reference diffuser (black dotted line, according to Fig. 1(a)) and on the surface of the artificial tissue phantom (colored lines, according to Fig. 1(c)), with the reference diffuser submerged in the tissue phantom at depth positions of 2 mm, 5 mm, 10 mm, and 15 mm.

$\beta = 0^\circ$) and five different cone opening angles α . It can be perceived that the two intensity peaks at the distal diffuser end measured experimentally with the imaging method can be reproduced relatively well by simulation with $\alpha = 1^\circ$ (yellow line), while the measurement result of the non-imaging method can be reproduced better, at least qualitatively, with $\alpha = 25^\circ$ (blue line). By comparing the five solid lines, it becomes obvious, that by increasing the cone opening angle α for fixed cone tilt angle $\beta = 0^\circ$, the intensity peaks broaden and decrease in amplitude.

Further, the influence of the cone tilt angle β on the emission profile was examined for a fixed cone opening angle $\alpha = 25^\circ$. In Fig. 7, the simulated profiles obtained for perpendicular emission ($\beta = 0^\circ$), preferential forward ($\beta = +35^\circ$) and backward ($\beta = -35^\circ$) emission (three solid lines of different colours) are compared to the experimental result of the non-imaging method (dash-dotted black line). The scenario of emission perpendicular to the diffuser surface ($\beta = 0^\circ$, blue line) leads to rather broad intensity peaks. A preferential forward emission ($\beta = +35^\circ$, black line) results in intensity peaks with reduced FWHM and a tiny intensity redistribution into the forward direction in the longitudinal position range 0 - 2 mm, as well as a more pronounced intensity redistribution for positions above 31.5 mm. By contrast, preferential backward emission ($\beta = -35^\circ$, red line) generates a shoulder in the emission profile near the longitudinal position 27 mm, as well as an intensity redistribution into the backward direction at the diffuser end near the longitudinal position 31 mm. It can be deduced that a variation of the cone tilt angle β in the simulation model results in minor influences on the shape of the simulated emission profile. Thus, further simulations were simplified by fixing the tilt angle to $\beta = 0^\circ$, thus mimicking an average emission direction perpendicular to the diffuser surface.

Based on this iterative process, the shape of the emission profile of the reference diffuser can be described by MC-simulations according to Fig. 1(d) with cone tilt angle $\beta = 0^\circ$ and cone opening angle $\alpha = 25^\circ$. In all further investigations, the light distribution generated by the reference diffuser in the surrounding tissue phantom according to Fig. 1(c) was simulated with these fixed values for the simulation parameters α and β .

In Fig. 8 the intensity profile measured on the surface of the tissue phantom with the diffuser placed at a depth of 0 mm (i.e. in air), 2 mm, 5 mm, 10 mm and 15 mm, measured with the imaging method is shown. The results reveal that the intensity distributions at the phantom surface appear more homogeneous than the emission profile of the diffuser in air, and that they become broader with increasing depth of the diffuser below the phantom surface. Characteristic

intensity peaks, like the two intensity peaks at the distal diffuser end, are strongly reduced already for a diffuser position 2 mm below the surface.

In Fig. 9, the simulated (black line) and calculated (blue dots) intensity ratios $I_{R,\text{single}}(d)$ are shown as a function of the diffuser depth d below the phantom surface. The comparison shows a close relationship between measurement and simulation within the error limits of the measurement. The simulation reveals that the excess of intensity ratio $I_{R,\text{single}}(d)$ over 1 drops to 50% (from $I_{R,\text{single}}(0) - 1 = 4.61$ to $I_{R,\text{single}}(d) - 1 = 2.31$) within the first 100 μm in tissue and reaches a value of 10% ($I_{R,\text{single}}(d) - 1 = 0.46$) after about 2 mm. Thus, it can be concluded that local intensity peaks in the emission profile of the diffuser in air fade away quite effectively within the first 1 mm of tissue depth in the case the diffuser is inserted in an artificial brain tissue phantom.

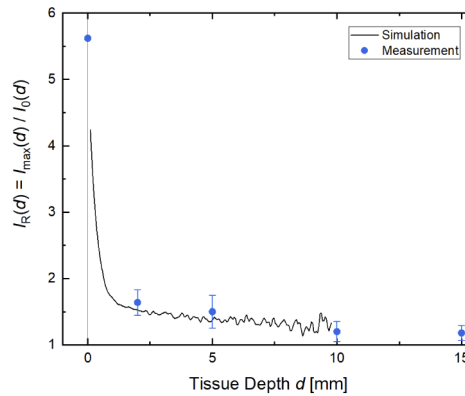


Fig. 9. Simulation results for the intensity ratio $I_{R,\text{single}}(d)$ for the reference diffuser in artificial tissue phantom are shown as black line. Experimentally measured ratios are marked by blue dots.

Simulations for virtual diffusers with artificial emission profiles, placed into an infinite tissue phantom according to Fig. 1(d), were performed to show the influence of height and width of an intensity peak on top of a homogeneous emission profile and the interplay of two adjacent intensity peaks on the light distribution in tissue. For this purpose, artificial emission profiles were generated and implemented into the MC-simulation scenario mimicking the situation of a cylindrical diffuser submerged in an artificial tissue phantom as shown in Fig. 1(c).

First, the width w_{FWHM} and height $I_{R,\text{single}}(0)$ of a single intensity peak in the center position of the diffuser, $x_0 = 15$ mm, were varied. Figure 10 shows the relative peak intensity $I_{R,\text{single}}(d)$ as a function of the tissue depth d from the diffuser for intensity peaks with two different widths of $w_{\text{FWHM}} = 0.2$ mm (Fig. 10(a)), $w_{\text{FWHM}} = 1.0$ mm (Fig. 10(b)) and $w_{\text{FWHM}} = 5.0$ mm (Fig. 10(c)). For each width w_{FWHM} , four scenarios with four different initial values of the relative peak intensity were examined, for $I_{R,\text{single}}(0) = 1.5, 2.0, 3.0$, and 6.0 . All curves are characterised by a steep drop in intensity within the first millimetres. The corresponding “50% tissue depths” $d_{p,\text{single}}$, defined as $\frac{I_{R,\text{single}}(d_p) - 1}{I_{R,\text{single}}(0) - 1} = 0.5$, are shown in Table 1. This comparison shows that the width of the intensity peak, in contrast to the height, has a strong influence on $d_{p,\text{single}}$. $d_{p,\text{single}}$ was below 100 μm for a width of $w_{\text{FWHM}} = 0.2$ mm, while it was determined to be 0.79 mm - 0.91 mm and 1.91 - 2.11 mm at a width of $w_{\text{FWHM}} = 1.0$ mm and $w_{\text{FWHM}} = 5.0$ mm, respectively. This finding suggests that narrow intensity peaks lead to more superficial tissue damage close to the diffuser surface, while broader ones penetrate deeper into tissue.

In Fig. 11(a) simulated intensity profiles are shown for an artificial diffuser with two local intensity peaks of width $w_{\text{FWHM}} = 1.0$ mm separated by a peak-to-peak distance of $\Delta x = 5$ mm. Results are shown for several tissue depths from the diffuser. The diagram shows that the intensity

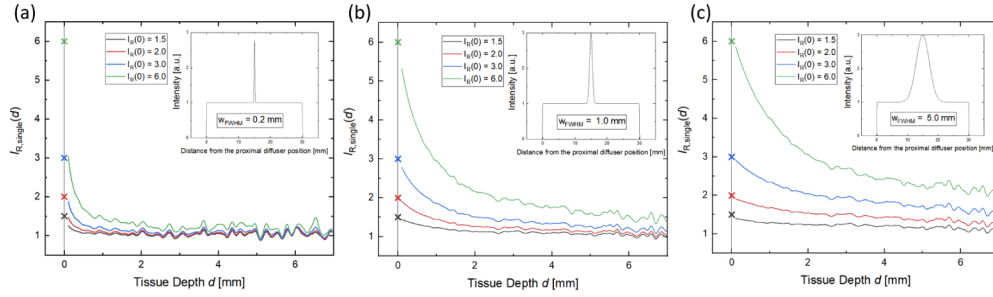


Fig. 10. Evolution of the intensity ratio $I_{R,single}(d)$ with increasing tissue depth for artificially generated emission profiles with one local maximum. The intensity peak was varied in width w_{FWHM} and initial height $I_{R,single}(0)$. Results for a width w_{FWHM} of 0.2 mm, 1.0 mm, and 5.0 mm are illustrated in panels (a), (b), and (c), respectively. For each width, four scenarios with four different initial intensity ratios were simulated, for $I_{R,single}(0) = 1.5, 2.0, 3.0$, and 6.0 .

Table 1. “50% tissue depth” $d_{p,single}$ at which the intensity ratio $I_{R,single}(d)$ drops to 50% of its initial value at the diffuser surface.

“50% tissue depth” $d_{p,single}$ [mm]	$w_{FWHM} = 0.2$ mm	$w_{FWHM} = 1.0$ mm	$w_{FWHM} = 5.0$ mm
$I_{R,single}(0) = 1.5$	<0.10	0.79	1.91
$I_{R,single}(0) = 2.0$	<0.10	0.81	2.00
$I_{R,single}(0) = 3.0$	<0.10	0.83	2.08
$I_{R,single}(0) = 6.0$	<0.10	0.91	2.11

at the positions of both maxima decreases with increasing tissue depth, but the intensity in the center between the two maxima increases. For a tissue depth of $d = 5$ mm, the two intensity peaks have already merged into a single, broad intensity peak.

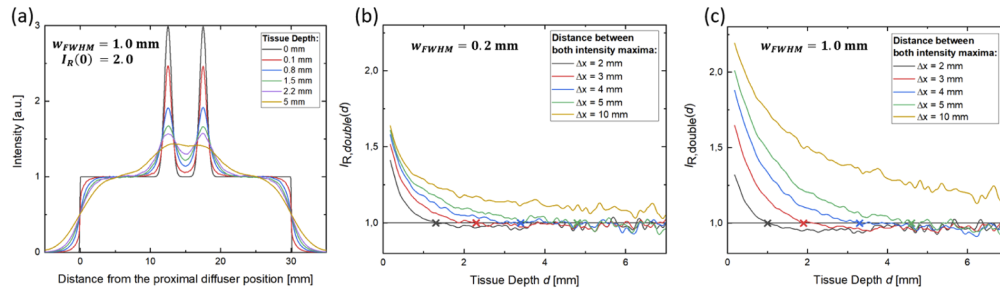


Fig. 11. (a) Emission profile and intensity distributions at a tissue depth from the diffuser surface of $d = 0$ mm, 0.1 mm, 0.8 mm, 1.5 mm, 2.2 mm and 5 mm for two intensity peaks added to a homogeneous emission profile. The peaks were simulated to have a height of $I_{R,double}(0) = 2.0$ and a width of $w_{FWHM} = 1.0$ mm, separated by a peak-to-peak distance of $\Delta x = 5$ mm. The evolution of $I_{R,double}(d)$ with increasing tissue depth d is shown for different initial peak-to-peak distances, $\Delta x = 2$ mm, 3 mm, 4 mm, 5 mm, and 10 mm and for two different fixed peak widths, $w_{FWHM} = 0.2$ mm (b) and 1.0 mm (c).

To provide a deeper insight into the interplay of two adjacent intensity peaks, their distance and width and w_{FWHM} was varied. The intensity ratio $I_{R,double}(d) = \frac{I_{max}(d)}{I_{center}(d)}$ was calculated and plotted as function of the tissue depth d for $w_{FWHM} = 0.2$ mm and 1.0 mm (Fig. 11(b) and (c)). The intensity peaks become indistinguishable when the intensity ratio $I_{R,double}$ reaches 1.

The corresponding “peak coalescence tissue depths” $d_{p,double}$ are listed in Table 2 for different separations Δx of the two peak maxima. It becomes obvious, that for one parameter setting ($w_{FWHM} = 0.2$ mm and $\Delta x = 2$ mm), the two peaks become indistinguishable within 1 mm of tissue depth, while for an initial peak distance of $\Delta x = 10$ mm, the two intensity peaks remain distinguishable over the full range of investigated tissue depths, independently of the initial peak width w_{FWHM} . Comparing the differences between narrower (Fig. 11(b)) and wider intensity peaks (Fig. 11(c)), it can be noted that narrower intensity peaks lead to a faster attenuation of $I_{R,double}$. The tissue depth $d_{p,double}$ at which both peaks merge does not differ for the two different peak width values investigated.

Table 2. “Peak coalescence tissue depth” $d_{p,double}$ at which two intensity peaks become indistinguishable.

“Peak coalescence tissue depth” $d_{p,double}$ [mm]	$\Delta x = 2$ mm	$\Delta x = 3$ mm	$\Delta x = 4$ mm	$\Delta x = 5$ mm	$\Delta x = 10$ mm
$w_{FWHM} = 0.2$ mm	1.3	2.3	3.4	4.8	–
$w_{FWHM} = 1.0$ mm	1.0	1.9	3.3	4.6	–

Overall, it can be suggested that emission profiles consisting of several intensity maxima with a peak-to-peak distance below 2 mm lead to a homogeneous light distribution within the first 1 to 2 mm of tissue depth.

4. Discussion

In this investigation, the influence of local inhomogeneities in the emission profile of fiber diffusers on the light distribution within tissue after interstitial insertion was studied. This was assessed by dedicated MC-simulations based on reproducing experimental measurements.

The experimental measurements were performed using an imaging and a non-imaging camera method [32]. This made it possible to describe the emission behaviour of the diffuser more precisely. While the imaging method could describe the intensity distribution on the surface, the direction of the emission was measured with the non-imaging method. Both measurements were performed in air and the light distribution in tissue was deduced by means of a MC-simulation. Although the simulation was validated by measuring the light distribution in tissue, the question of a measuring method continuously and easily accessing the light distribution in tissue still arises.

Although the MC simulation presented was calibrated and validated by measurements, some assumptions were made. The emission angle was set to $\beta = 0^\circ$. However, this provides a good approximation only for volume-scattering diffusers with a reflecting mirror at the fiber end. The mirror causes light to propagate in both fiber directions, away from and towards the light source. The emission should therefore be almost symmetrical about the angle $\beta = 0^\circ$. For diffusers without mirrors or surface scattering diffusers, this assumption loses its validity and forward directed emission ($\beta > 0^\circ$) must be expected.

Furthermore, the refractive index mismatch between tissue phantom and the surrounding medium air was neglected in the simulation. However, it can be estimated that the angle $\alpha = 25^\circ$ used here would be increased to 33° by a refractive index mismatch. As a consequence, the emission profile, including potential inhomogeneities, would appear broadened. However, the calibration performed in Fig. 6 shows that the intensity distribution for an emission angle of $\alpha = 30^\circ$ deviates only slightly from that for the selected angle $\alpha = 25^\circ$.

Other approaches to air-based measurement include integrating sphere measurement setups [20,32], goniometric approaches [27,34] or photodiode-based measurement methods [35]. A description of the radiation profile by an integrating sphere and photodiode-based method would theoretically lead to similar results as the imaging and non-imaging camera method. An experimental validation will be left to further investigations. A complete description of the light

distribution in air can only be obtained by goniometric imaging of the radiation pattern. In addition to the intensity distribution on the fiber surface, the goniometric representation can also directly measure the directional radiation [34]. The disadvantage of this method is the difficulty in aligning the diffuser in the measurement setup coupled with sophisticated mathematical evaluation procedures [34].

The vanishing of single and multiple intensity maxima during light penetration through a scattering tissue phantom were examined. It was shown, that the light distribution is mainly influenced by the width w_{FWHM} . Intensity peaks with a width in the range of one millimetre have an approximate “50%” and “peak coalescence” tissue depth d_p of one millimetre in tissue. An explanation might lie in the light propagation originating from point and line sources. Since the light intensity flux of point and line sources decreases geometrically by $I \sim \frac{1}{r^2}$ and $I \sim \frac{1}{r}$ [36], respectively, narrow intensity peaks, representing point sources, decay faster with increasing distance to the diffuser surface compared to wide peaks, representing line sources [33,37]. An analytical solution proves to be difficult, as the transition between point source to elongated line source is continuous. The deeper penetration depth of extended light sources is also used in Diffuse Reflectance Spectroscopy [38–40]. Here, light emitted by one fiber is detected by another. If the distance between the fibers, or the fiber radius itself, is increased, deeper tissue regions can be monitored [38–40].

Comparing the simulated results to emission profiles in literature, an evaluation of the profiles with regard to the width w_{FWHM} of the intensity peaks has to be performed. The emission profiles presented in [27,30,31] have pronounced, however, narrow intensity peaks at the distal and/or proximal diffuser end. While the height $I_R(0)$ can reach up to three times the average emitted intensity, the width w_{FWHM} of the intensity peaks does not exceed a width of $w_{FWHM} = 1$ mm. Therefore, it can be concluded, that the influence towards the light distribution is limited to the first millimetre of tissue depth from the diffuser surface.

The light distribution of a diffuser in tissue phantom shown in [41] slightly differs from the results presented here. An emission of a width of 5 mm showed a reduction of the intensity to 50% of the original intensity after only 0.9 mm. The faster decrease might be due to the fact that sinusoidal intensity peaks were used and thus the geometry differs from the here presented Gaussian inhomogeneities.

The investigation on the influence of two narrow peaks in the emission profile on the light distribution within the tissue showed that two peaks with an initial peak-to-peak distance of $\Delta x = 2$ mm become indistinguishable after approximately 1 mm tissue depth. For larger peak-to-peak distances Δx , the two peaks remain separate, and each of them acts as a single intensity peak propagating into the tissue. Applying the gained knowledge to the field of diffuser production, it can be concluded that after only a few millimetres of tissue, an emission profile composed from multiple close intensity peaks over the full diffuser length exhibits an equivalent behavior comparable to homogeneous emission profiles. Other emission profiles, composed from multiple intensity peaks over the full diffuser length, showed a peak-to-peak distance between the intensity maxima of $\Delta x = 0.5$ mm [19,25]. Therefore, the light distribution has a homogeneous intensity distribution after less than 1 mm of tissue depth.

The light distribution in tissue and the attenuation of single and multiple intensity peaks on emission profiles was extensively discussed. While it is difficult to make a statement about the biological influences, a conclusion about spatial allocation of potential tissue damage can be done. The local excess intensity within the tissue induced by local maxima in the emission profile is largest close to the diffuser surface. Thereby, the first cell layers close to the diffuser are affected by strong intensity peaks. This can affect about 2 to 20 cell layers since each cell layer has an approximate size of 5 - 50 μm . However, the simulation model lacks a description of actual damage to tissue or the diffuser itself due to thermal overtreatment. Therefore, the thermal properties of the targeted tissue has to be examined, the calculated light intensities transferred to

temperature, and the thermal diffusion considered. Exceeding 42°C in brain tissue can lead to cellular damage causing side effects to the treatment [17].

While in the present work the influence of inhomogeneities on the light distribution in brain tissue was presented, their influence on other tissue types must be critically discussed, since the optical as well as the thermal properties of different tissue types strongly differ from each other. A decrease in absorption and/or scattering may lead to an enhanced penetration of inhomogeneities to deeper tissue regions, which is the case for skin and prostate tissue at a wavelength of $\lambda = 635$ nm [42]. Furthermore, a variation in thermal properties can influence the temperature distribution in the targeted tissue region. For increased heat capacity, a lower temperature rise is expected, while for increased thermal conductivity, a locally induced temperature rise fades away effectively into the surrounding tissue.

Further investigations will evaluate the effect of certain light doses on the temperature increase in various types of tissue. Mathematical approaches could be built on the solution of Penne's bio-heat equation [16,27,43,44]. Thereby, an applied diffuser power could be defined at which the temperature increase is limited to a total temperature of 42°C. Thus, quality criteria for the homogeneity of diffusers could be defined.

5. Conclusion

Inhomogeneities in the measured emission profile of cylindrical light diffusers in air affect the light distribution in the surrounding tissue. The observed effects are mainly dependent on the width of the local intensity peaks.

Narrow intensity peaks with a width smaller than one millimeter in the emission profile have only a minor effect on the light distribution somewhat deeper within the tissue, while broader or a multitude of intensity maxima can maintain a strong effect also at larger distances from the diffuser. Potential overheating near narrow intensity maxima should be avoided, in particular in case of tissue with strong absorption and scattering and/or low heat capacity and/or low heat conductivity. Clinically, strong local intensity maxima constitute a potential risk factor for sensitive tissue structures in this area.

Funding

Österreichische Forschungsförderungsgesellschaft (855657).

Acknowledgements

This manuscript is part of the inaugural thesis of Stephan Ströbl to be submitted at the Medical Faculty of the Ludwig-Maximilians-Universität, Munich.

Disclosures

The authors declare that there are no conflicts of interest related to this article.

References

1. D. Dolmans, D. Fukumura, and R. K. Jain, "Photodynamic therapy for cancer," *Nat. Rev. Cancer* **3**(5), 380–387 (2003).
2. M. Vermandel, M. Quidet, A.-S. Vignion-Dewalle, H.-A. Leroy, B. Leroux, S. Mordon, and N. Reyns, "Comparison of different treatment schemes in 5-ALA interstitial photodynamic therapy for high-grade glioma in a preclinical model: An MRI study," *Photodiagn. Photodyn. Ther.* **25**, 166–176 (2019).
3. C. Heckl, M. Aumiller, A. Rühm, R. Sroka, and H. Stepp, "Fluorescence and Treatment Light Monitoring for Interstitial Photodynamic Therapy," *Photochem. Photobiol.* **96**(2), 388–396 (2020).
4. H. Stepp, A. Rühm, R. Sroka, and W. Stummer, "Interstitial photodynamic therapy (iPDT) of brain tumours (Conference Presentation)," in *17th International Photodynamic Association World Congress*, T. Hasan, ed. (SPIE, 2019), p. 45.

5. R. Sroka, N. Dominik, M. Eisel, A. Esipova, C. Freymüller, C. Heckl, G. Hennig, C. Homann, N. Hoehne, R. Kammerer, T. Kellerer, A. Lang, N. Markwardt, H. Pohla, T. Pongratz, C.-G. Schmedt, H. Stepp, S. Ströbl, K. Ulaganathan, W. Zimmermann, and A. Ruehm, "Research and developments of laser assisted methods for translation into clinical application," *Front. Optoelectron.* **10**(3), 239–254 (2017).
6. Z. Malik, "Fundamentals of 5-aminolevulinic acid photodynamic therapy and diagnosis: An overview," *Transl. Biophotonics* **2**(1-2), e201900022 (2020).
7. A. P. Castano, T. N. Demidova, and M. R. Hamblin, "Mechanisms in photodynamic therapy: part one—photosensitizers, photochemistry and cellular localization," *Photodiagn. Photodyn. Ther.* **1**(4), 279–293 (2004).
8. A. P. Castano, T. N. Demidova, and M. R. Hamblin, "Mechanisms in photodynamic therapy: part two—cellular signaling, cell metabolism and modes of cell death," *Photodiagn. Photodyn. Ther.* **2**(1), 1–23 (2005).
9. T. J. Beck, F. W. Kreth, W. Beyer, J. H. Mehrkens, A. Obermeier, H. Stepp, W. Stummer, and R. Baumgartner, "Interstitial photodynamic therapy of nonresectable malignant glioma recurrences using 5-aminolevulinic acid induced protoporphyrin IX," *Lasers Surg. Med.* **39**(5), 386–393 (2007).
10. A. Rühm, H. Stepp, W. Beyer, G. Hennig, T. Pongratz, R. Sroka, O. Schnell, J.-C. Tonn, and F.-W. Kreth, "5-ALA based photodynamic management of glioblastoma," in H. Hirschberg, S. J. Madsen, E. D. Jansen, Q. Luo, S. K. Mohanty, and N. V. Thakor, eds. (2014), p. 89280E.
11. R. Sroka, H. Stepp, G. Hennig, G. M. Brittenham, A. Rühm, and L. Lilge, "Medical laser application: translation into the clinics," *J. Biomed. Opt.* **20**(6), 061110 (2015).
12. T. M. Baran and T. H. Foster, "Comparison of flat cleaved and cylindrical diffusing fibers as treatment sources for interstitial photodynamic therapy: Comparing flat cleaved fibers and diffusers for iPDT," *Med. Phys.* **41**(2), 022701 (2014).
13. L. H. P. Murrer, J. P. A. Marijnissen, and W. M. Star, "Light distribution by linear diffusing sources for photodynamic therapy," *Phys. Med. Biol.* **41**(6), 951–961 (1996).
14. A. Johansson, H. Stepp, T. Beck, W. Beyer, T. Pongratz, R. Sroka, T. Meinel, W. Stummer, F.-W. Kreth, J.-C. Tonn, and R. Baumgartner, "ALA-mediated fluorescence-guided resection (FGR) and PDT of glioma," in D. H. Kessel, ed. (2009), p. 73801D.
15. L. Lilge and B. C. Wilson, "Photodynamic Therapy of Intracranial Tissues: A Preclinical Comparative Study of Four Different Photosensitizers," *J. Clin. Laser Med. Surg.* **16**(2), 81–91 (1998).
16. H. H. Pennes, "Analysis of Tissue and Arterial Blood Temperatures in the Resting Human Forearm," *J. Appl. Physiol.* **1**(2), 93–122 (1948).
17. G. C. van Rhoon, T. Samaras, P. S. Yarmolenko, M. W. Dewhirst, E. Neufeld, and N. Kuster, "CEM43°C thermal dose thresholds: a potential guide for magnetic resonance radiofrequency exposure levels?" *Eur. Radiol.* **23**(8), 2215–2227 (2013).
18. W. Stummer, T. Beck, W. Beyer, J. H. Mehrkens, A. Obermeier, N. Etminan, H. Stepp, J.-C. Tonn, R. Baumgartner, J. Herms, and F. W. Kreth, "Long-sustaining response in a patient with non-resectable, distant recurrence of glioblastoma multiforme treated by interstitial photodynamic therapy using 5-ALA: case report," *J. Neuro-Oncol.* **87**(1), 103–109 (2008).
19. V. V. Volkov, V. B. Loshchenov, V. I. Konov, and V. V. Kononenko, "Fibreoptic diffuse-light irradiators of biological tissues," *Quantum Electron.* **40**(8), 746–750 (2010).
20. J. Köcher, V. Knappe, and M. Schwagmeier, "Internal structuring of silica glass fibers: Requirements for scattered light applicators for the usability in medicine," *Photonics Lasers Med.* **5**(1), 1(2016).
21. D. Ashkenasi, A. Rosenfeld, H. Varel, M. Wähmer, and E. E. B. Campbell, "Laser processing of sapphire with picosecond and sub-picosecond pulses," *Appl. Surf. Sci.* **120**(1-2), 65–80 (1997).
22. D. Ashkenasi, A. Rosenfeld, S. B. Spaniol, and A. Terenji, "Ultrashort laser pulse processing of wave guides for medical applications," in J. Neev, A. Ostendorf, and C. B. Schaffer, eds. (2003), p. 180.
23. H. Varel, D. Ashkenasi, A. Rosenfeld, M. Wähmer, and E. E. B. Campbell, "Micromachining of quartz with ultrashort laser pulses," *Appl. Phys. A: Mater. Sci. Process.* **65**(4-5), 367–373 (1997).
24. S. Ströbl, C. Vonach, J. Gratt, M. Domke, and R. Sroka, "Ultrafast-Laser Manufacture of Radially Emitting Optical Fiber Diffusers for Medical Applications," *J. Laser Micro/Nanoeng.* **14**(1), 43–48 (2019).
25. M. Domke, J. Gratt, and R. Sroka, "Fabrication of homogeneously emitting optical fiber diffusers using fs-laser ablation," in A. Heisterkamp, P. R. Herman, M. Meunier, and S. Nolte, eds. (2016), p. 974000.
26. E. U. Şimşek, B. Şimşek, and B. Ortaç, "CO2 laser polishing of conical shaped optical fiber deflectors," *Appl. Phys. B* **123**(6), 176 (2017).
27. T. H. Nguyen, Y. Rhee, J. Ahn, and H. W. Kang, "Circumferential irradiation for interstitial coagulation of urethral stricture," *Opt. Express* **23**(16), 20829 (2015).
28. H. W. Kang, J. Kim, and J. Oh, "Enhanced photocoagulation with catheter-based diffusing optical device," *J. Biomed. Opt.* **17**(11), 118001 (2012).
29. M. A. Kosoglu, R. L. Hood, J. H. Rossmeisl, D. C. Grant, Y. Xu, J. L. Robertson, M. N. Rylander, and C. G. Rylander, "Fiberoptic microneedles: Novel optical diffusers for interstitial delivery of therapeutic light," *Lasers Surg. Med.* **43**(10), 1008–1014 (2011).
30. L. M. Vesselov, W. Whittington, and L. Lilge, "Performance evaluation of cylindrical fiber optic light diffusers for biomedical applications," *Lasers Surg. Med.* **34**(4), 348–351 (2004).

31. L. Lilge, L. Vesselov, and W. Whittington, "Thin cylindrical diffusers in multimode Ge-doped silica fibers," *Lasers Surg. Med.* **36**(3), 245–251 (2005).
32. S. Ströbl, M. Domke, T. Trebst, and R. Sroka, "Radiation profile measurement methods for optical light diffusers: comparison of imaging and non-imaging methods," in *Medical Laser Applications and Laser-Tissue Interactions IX*, L. D. Lilge and C. M. Philipp, eds. (SPIE, 2019), p. 38.
33. N. A. Markwardt, H. Stepp, G. Franz, R. Sroka, M. Goetz, P. Zelenkov, and A. Rühm, "Remission spectrometry for blood vessel detection during stereotactic biopsy of brain tumors," *J. Biophotonics* **10**(8), 1080–1094 (2017).
34. A. Pitzschke, J. Bertholet, B. Lovisa, M. Zellweger, and G. Wagnières, "Determination of the radiance of cylindrical light diffusers: design of a one-axis charge-coupled device camera-based goniometer setup," *J. Biomed. Opt.* **22**(3), 035004 (2017).
35. V. G. Truong, S. Park, V. N. Tran, and H. W. Kang, "Spatial effect of conical angle on optical-thermal distribution for circumferential photocoagulation," *Biomed. Opt. Express* **8**(12), 5663 (2017).
36. D. R. Grimes, C. Robbins, and N. J. O'Hare, "Dose modeling in ultraviolet phototherapy: Dose modeling in ultraviolet phototherapy," *Med. Phys.* **37**(10), 5251–5257 (2010).
37. D. Kobe, S. B. Spaniol, W. Beyer, and W. Ertmer, "Computer modeling of light distributions for diverse PDT applicators," in G. Jori, J. Moan, and W. M. Star, eds. (1994), pp. 4–12.
38. T. Papaioannou, N. W. Preyer, Q. Fang, A. Brightwell, M. Carnohan, G. Cottone, R. Ross, L. R. Jones, and L. Marcu, "Effects of fiber-optic probe design and probe-to-target distance on diffuse reflectance measurements of turbid media: an experimental and computational study at 337 nm," *Appl. Opt.* **43**(14), 2846 (2004).
39. A. Pifferi, J. Swartling, E. Chikoidze, A. Torricelli, P. Taroni, A. Bassi, S. Andersson-Engels, and R. Cubeddu, "Spectroscopic time-resolved diffuse reflectance and transmittance measurements of the female breast at different interfiber distances," *J. Biomed. Opt.* **9**(6), 1143 (2004).
40. R. Hennessy, W. Goth, M. Sharma, M. K. Markey, and J. W. Tunnell, "Effect of probe geometry and optical properties on the sampling depth for diffuse reflectance spectroscopy," *J. Biomed. Opt.* **19**(10), 107002 (2014).
41. M. Sibai, D. J. Wirth, F. Leblond, D. W. Roberts, K. D. Paulsen, and B. C. Wilson, "Quantitative subsurface spatial frequency-domain fluorescence imaging for enhanced glioma resection," *J. Biophotonics* **12**(5), e201800271 (2019).
42. F. Duck, *Physical Properties of Tissues A Comprehensive Reference Book* (Academic Press, 1990).
43. E. H. Wissler, "Pennes' 1948 paper revisited," *J. Appl. Physiol.* **85**(1), 35–41 (1998).
44. T.-C. Shih, P. Yuan, W.-L. Lin, and H.-S. Kou, "Analytical analysis of the Pennes bioheat transfer equation with sinusoidal heat flux condition on skin surface," *Med. Eng. Phys.* **29**(9), 946–953 (2007).

Publikation [O4]

Einsehbar unter:

Ströbl S, Wäger F, Domke M, Rühm A, Sroka R. Homogeneously Emitting, Mechanically Stable, and Efficient fs-Laser-Machined Fiber Diffusers for Medical Applications. Lasers Surg Med. 2022 Apr;54(4):588-599. doi: 10.1002/lsm.23365. Epub 2020 Dec 8. PMID: 33616996

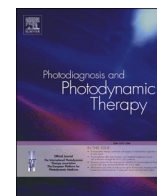
Aus urheberrechtlichen Gründen kann der Inhalt dieser Publikation an dieser Stelle nicht wiedergegeben werden. Er ist mit Hilfe der bibliographischen Informationen abrufbar.

Publikation [05]

Einsehbar unter:

Heckl C, Lang A, Rühm A, Sroka R, Duffield T, Vogeser M, Paal M. Spectrophotometric evaluation of hemolysis in plasma by quantification of free oxyhemoglobin, methemoglobin, and methemalbumin in presence of bilirubin. J Biophotonics. 2021 May;14(5):e202000461. doi: 10.1002/jbio.202000461. Epub 2021 Feb 13. PMID: 33527705

Aus urheberrechtlichen Gründen kann der Inhalt dieser Publikation an dieser Stelle nicht wiedergegeben werden. Er ist mit Hilfe der bibliographischen Informationen abrufbar.



Investigations on correlations between changes of optical tissue properties and NMR relaxation times

Maximilian Aumiller^{a,b,*}, Asmerom Arazar^a, Ronald Sroka^{a,b}, Olaf Dietrich^c, Adrian Rühm^{a,b}

^a Laser-Forschungslabor, LIFE Center, LMU University Hospital, LMU Munich, Planegg 82152, Germany

^b Department of Urology, LMU University Hospital, LMU Munich, Munich 81377, Germany

^c Department of Radiology, LMU University Hospital, LMU Munich, Munich 81377, Germany

ARTICLE INFO

Keywords:

Optical properties
Absorption
Scattering
NMR relaxation times
Interstitial photodynamic therapy

ABSTRACT

Background: Accurate light dosimetry is a complex remaining challenge in interstitial photodynamic therapy (iPDT) for malignant gliomas. The light dosimetry should ideally be based on the tissue morphology and the individual optical tissue properties of each tissue type in the target region. First investigations are reported on using NMR information to estimate changes of individual optical tissue properties.

Methods: Porcine brain tissue and optical tissue phantoms were investigated. To the porcine brain, supplements were added to simulate an edema or high blood content. The tissue phantoms were based on agar, Lipoveneous, ink, blood and gadobutrol (Gd-based MRI contrast agent). The concentrations of phantom ingredients and tissue additives are varied to compare concentration-dependent effects on optical and NMR properties. A 3-tesla whole-body MRI system was used to determine T_1 and T_2 relaxation times. Optical tissue properties, i.e., the spectrally resolved absorption and reduced scattering coefficient, were obtained using a single integrating sphere setup. The observed changes of NMR and optical properties were compared to each other.

Results: By adjusting the NMR relaxation times and optical tissue properties of the tissue phantoms to literature values, recipes for human brain tumor, white matter and grey matter tissue phantoms were obtained that mimic these brain tissues simultaneously in both properties. For porcine brain tissue, it was observed that with increasing water concentration in the tissue, both NMR-relaxation times increased, while μ_a decreased and μ_s' increased at 635 nm. The addition of blood to porcine brain samples showed a constant T_1 , while T_2 shortened and the absorption coefficient at 635 nm increased.

Conclusions: In this investigation, by changing sample contents, notable changes of both NMR relaxation times and optical tissue properties have been observed and their relations examined. The developed dual NMR/optical tissue phantoms can be used in iPDT research, clinical training and demonstrations.

1. Introduction

Interstitial photodynamic therapy (iPDT) for malignant gliomas [1–3] is currently under development and undergoing clinical trials. For this treatment, a precursor is administered to the patient, which leads to accumulation of a photosensitizer in the target tissue. The photosensitizer is excited by light irradiation and creates reactive oxygen species (ROS) via interaction with intracellular oxygen. In case of 5-aminolevulinic acid (5-ALA) mediated iPDT, the photosensitizer is protoporphyrin IX (PpIX), which is excited at a wavelength of 635 nm. [1,2,4]

As part of the treatment planning, the trajectories for the placement

of the light applicators in the brain are defined based on estimates about the light dosimetry [1]. These estimations are based on analytical calculations using diffusion theory under the assumption of homogeneous optical tissue properties [5–7]. In this approximation, the individual optical tissue properties of tumor, white matter, and grey matter are neglected. Currently, more elaborate simulation approaches are under development, using, e.g., Monte Carlo techniques [8]. Here, individual optical tissue properties of different tissue types can be considered and included in the light dosimetry calculations to optimize the light applicator positions in the tissue [8–10].

For the analytical light dosimetry calculations and/or simulations,

* Corresponding author at: Laser-Forschungslabor, LIFE Center, Department of Urology, LMU University Hospital, LMU Munich, Fraunhoferstrasse 20, Planegg 82152, Germany.

E-mail address: max.aumiller@med.uni-muenchen.de (M. Aumiller).

<https://doi.org/10.1016/j.pdpdt.2024.103968>

Received 31 October 2023; Received in revised form 3 January 2024; Accepted 9 January 2024

Available online 10 January 2024

1572-1000/© 2024 The Author(s). Published by Elsevier B.V. This is an open access article under the CC BY-NC-ND license (<http://creativecommons.org/licenses/by-nc-nd/4.0/>).

fixed optical tissue properties may be used, but these properties are actually patient-individual and differ from case to case. In literature, a broad range of optical tissue properties can be found for the same tissue type [11]. This uncertainty can be handled by making worst-case assumptions about the unknown properties or by applying a higher light dose than needed to induce cell death. In case of 5-ALA mediated iPDT, a light overdosage would not affect non-tumor tissue. 5-ALA induced PpIX is mainly selectively accumulating in the tumor tissue and only very low photosensitizer amounts are present in the non tumor tissue [12–14]. Due to destruction of the photosensitizer during the iPDT irradiation (photobleaching process of the photosensitizer), a lethal production of ROS is not reached in the non-tumor tissue and healthy tissue is preserved.

Nevertheless, additional tools are desirable that can provide more insight into the patient's individual optical tissue properties. Spectral online monitoring is highly important, as it provides not only insight into the photosensitizer accumulation by measurement of its fluorescence but also into the actual optical conditions by measurement of the treatment light transmission through the tissue [13,15–17]. Using spectral online monitoring (SOM) measurements between two light applicators, one of which emits treatment light while the other one is connected to a spectrometer and used for light detection, it is possible to analytically calculate the optical attenuation in the tissue region between the light applicators and thus within the entire treated tissue volume [5]. Unfortunately, the inhomogeneity of the tissue and the related optical tissue properties had to be neglected so far [18]. A big advantage of SOM is that it provides insight into processes that may alter the optical tissue properties during the ongoing iPDT irradiation. There are indications that oxygenated hemoglobin is actively deoxygenated by iPDT or directly transmuted into methemoglobin [19–21].

Next to the optical light application and monitoring, medical imaging like X-ray computed tomography (CT) and magnetic resonance imaging (MRI) are an essential part of the iPDT procedure. Currently, these are used for therapy planning, guidance, and follow-up disease monitoring. In particular, the target volume of the therapeutic intervention is defined by these imaging modalities [1,22,23].

For the further development of iPDT procedures, light dosimetry and online monitoring, MRI plays an important role. Based on MRI data, different tissue types in the target region can be identified, and individual optical properties can be assigned to them [24,25].

MRI may not only give insight into the localization of different tissue types. The signal intensities visible in MRI are related to the individual relaxation times of the tissues [26]. Important factors influencing the NMR relaxation times in the brain are the lipid content and the free water content of the tissue [27]. The ratio between free and bound water is individual for each tissue and has a strong effect on the differences in the NMR relaxation times between the different tissue types and within the same tissue type.

Next to NMR relaxation in the brain, optical properties are directly related to the water and lipid content of the tissue. In the visible wavelength range, the water content indirectly affects the concentration of the photon absorbing and scattering substances in the sample with higher water content leading to lower optical absorption and scattering. In addition, the optical scattering is related to the lipid content, as lipids are the dominant optical scatterers in biophotonics [28,29].

In addition to lipids, water and blood content also have an influence on optical tissue properties. Furthermore, both are well known to affect the MRI signal intensities, e.g., in edema or hemorrhage, which are related to changes of the NMR relaxation times in the respective regions [30–32].

This leads to the assumption that changes or differences in MRI signal intensities and relaxation times might be an indicator for changes or differences in optical tissue properties in corresponding tissue regions.

To test this assumption, experiments were conducted on optical tissue phantoms with varying compositions and on porcine brain tissues

with different amounts of additives by measuring the NMR relaxation times T_1 and T_2 along with the optical absorption and reduced scattering coefficient. Out of this, recipes were created for producing tissue phantoms with MRI relaxation times and optical properties similar to those of different types of brain tissue (white matter, grey matter, malignant glioma) encountered in the target zone during iPDT of malignant brain tumors. First indications for a correspondence of changes in NMR relaxation times and optical properties have been found.

2. Material and methods

2.1. Samples

2.1.1. Dual NMR/optical tissue phantoms

Artificial optical tissue phantoms were used as their properties can be easily adjusted by changing the ingredient concentrations, and they are well known and frequently used in research [33]. Solid homogeneous optical tissue phantoms were manufactured based on agar (Agar, A7002, Sigma-Aldrich, St. Louis, Missouri, USA) and gelatin (Gelatin from porcine skin, G2500, Sigma-Aldrich, St. Louis, Missouri, USA). For adjustment of the optical tissue properties, a 20 % lipid emulsion based on Lipoveneous (Lipovenös® MCT 20 %, Fresenius Kabi Deutschland GmbH, Bad Homburg, Germany) and black ink (brilliant black, no. 4001, Pelikan Holding AG, Schindellegi, Switzerland) were used. To further adjust the T_1 relaxation times of the optical tissue phantoms, gadobutrol, a gadolinium-based contrast agent (GBCA, Gadovist® 1.0 mmol/ml, Bayer AG, Leverkusen, Germany) was added to the artificial tissue phantoms.

To manufacture the tissue phantoms, distilled water was boiled to 95 °C with the corresponding amount of agar. In the case of gelatin, the solution was boiled up to 50 °C. The required amount of Lipoveneous was added in small portions into the solution after it cooled down to 38 °C, where the temperature was kept constant. The temperature of the mixture was controlled with a thermocouple during the process. (In case of Lipoveneous, the pure amount of lipid contained in the 20 % lipid emulsion was used to calculate the Lipoveneous fraction in the phantom.)

After the Lipoveneous was stirred entirely into the solution, the black ink was added to adjust the optical absorbance. If needed, after stirring, the black ink was dissolved in the solution of the GBCA, and both were added to the tissue phantom. Before complete hardening, the tissue phantom was split into two parts. The first part was filled into the cuvette for the integrating sphere measurements (filling quantity 3 ml, CM-A130 2 mm ST, Konica Minolta, Japan). The second part was filled into the cuvette used for MRI measurements.

To reduce edge artefacts in the MRI at the cuvette walls, large volumes cuvettes (diameter 2.75 mm; filling quantity 50 ml, Sarstedt AG & Co. Kg, Sarstedt Schrauböhre, Nümbrecht, Germany) were used. Occurring edge artifacts in the MRI, usually affect a distance of up to 1.5–1.75 mm distance from the border zone between two tissues or materials [34]. Using the large volumes cuvettes, in the center of the sample a nearly homogeneous signal is obtained, that is not affected by artefacts.

By varying the agar, Lipoveneous and ink fractions, the effects of these ingredients on the optical tissue properties and NMR relaxation times were determined, and suitable compositions to create brain-mimicking tissue phantoms were derived. The finally developed artificial dual NMR/optical phantoms with brain tissue like properties were manufactured four times and measured to investigate their reproducibility in manufacturing.

2.1.2. Porcine tissue samples

Porcine brain was used as tissue samples to compare the effects of additives on optical properties and NMR relaxation times. The porcine tissue was obtained from the butcher. All samples were mixed using a hand blender until a visually homogeneous tissue sample was obtained.

After this mixing process, additional supplements (water, Lipoveneous, or human blood) were added into the tissue sample so that specific additive volume fractions: $c_{\text{additive}} = V_{\text{additive}} / (V_{\text{tissue}} + V_{\text{additive}})$ were obtained and the overall volume of the measured sample remained constant.

In case of Lipoveneous, V_{additive} was defined as the volume of the lipid emulsion added to the tissue, not the volume of the pure lipid contained therein. For each supplement concentration, the sample was split and filled into the corresponding cuvettes for the optical and NMR measurements.

The usage of human blood was approved by the Ethics Committee of Ludwig-Maximilians-University, Munich, Germany (reference number 18-144). For the usage of porcine tissues, no ethical approval was required as tissues of animals from the food industry were used.

2.2. MRI measurement and analysis

2.2.1. MRI sample mount and protocol

To determine the T_1 and T_2 relaxation times of the samples, a clinical 3-tesla whole-body MRI system (Magnetom Prisma, Siemens Healthineers AG, Erlangen, Germany) was used. A 32-channel head coil (Siemens Healthineers AG, Erlangen, Germany) was used for all MRI measurements. The samples were positioned in the isocenter of the coil using a self-made sample holder. The sample holder consisted of a box in which the 50 ml sample cuvettes were placed and held in a frame at the bottom and top of the box. The box was filled with water doped with 1 % GBCA to remove artefacts from the surrounding air. The sample holder was placed in the isocenter of the scanner to obtain the best possible sample signals.

To determine parameter maps of the longitudinal relaxation time constant, T_1 , a standard inversion recovery half-Fourier-acquired single-shot turbo spin-echo (HASTE) pulse sequence was utilized. This inversion sequence was recorded in 2D slices with single-slice acquisition mode, using a repetition time $T_R = 8420$ ms and an echo time $T_E = 80$ ms. Inversion recovery measurements were performed with 13 different inversion times, T_I , from 50 ms to 8000 ms (50, 150, 250, 500, 750, 1000, 1500, 2000, 3000, 4000, 5000, 6000, 8000 ms). The image resolution of the inversion sequences was $0.6875 \times 0.6875 \times 4.4$ mm³.

To determine parameter maps of the transverse relaxation time constant, T_2 , T_2 -weighting HASTE acquisitions with $T_R = 3100$ ms and a total of 20 echo times, T_E , from 25 ms to 500 ms in steps of 25 ms, were used. The image resolution of the T_2 -mapping sequences was $0.2083 \times 0.2083 \times 6$ mm³. The MRI sequences for the determination of T_1 and T_2 were set in such a way, that the best possible image resolution was achieved to identify inhomogeneities in the samples, while highest possible signal to noise ratio for this resolution is maintained.

For comparison, the finally developed tissue-like dual NMR/optical phantoms were additionally measured with clinical T_1 -weighted (T_1 TSE; $T_E = 6.4$ ms; $T_R = 600$ ms; $0.351 \times 0.351 \times 3.6$ mm³) and T_2 -weighted (T_2 TSE; $T_E = 89$ ms; $T_R = 5000$ ms; $0.4688 \times 0.4688 \times 3.3$ mm³) pulse sequences.

2.2.2. NMR relaxation time evaluation

The image intensities required in the fit procedure were determined from the MRI images using the software ITK-Snap (version 3.8, University of Pennsylvania, Philadelphia, USA) [35]. For this purpose, the sample volume visible in the MRI image in the isocenter of the scanner was segmented manually for each sample (segmentation volumes 5.1 cm³/~2500 voxels for T_1 determination and 4.9 cm³/~19,000 voxels for T_2 determination). The segmentation was done manually to exclude possible sample inhomogeneities from the following intensity analysis. The mean MRI intensity (I_{mean}) and the standard deviation (I_{STD}) were calculated for each sample based on the segmentation. The MRI T_1 -mapping and T_2 -mapping sequences were analyzed based on this procedure. Based on the inversion recovery acquisitions, for each T_I , an

individual intensity value $I_{\text{mean}}(T_I)$ was obtained. Similarly, based on the T_2 -mapping acquisitions, mean intensity values $I_{\text{mean}}(T_E)$ were obtained.

To determine T_1 from the intensities $I_{\text{mean}}(T_I)$, the following model function was used [36,37]:

$$I_{\text{mean}}(T_I) = \left| a - b e^{\left(-\frac{T_I}{T_1} \right)} \right| \quad (1)$$

Eq. (1) describes a 3-parameter model that is fitted to $I_{\text{mean}}(T_I)$ of each sample with free parameters a , b , and T_1 .

To determine T_2 from the intensities $I_{\text{mean}}(T_E)$, the following equation from T_2 -relaxometry was utilized [38,39].

$$I_{\text{mean}}(T_E) = S_0 e^{\left(-\frac{T_E}{T_2} \right)} \quad (2)$$

The mono-exponential model curve given by eq. (2) describes the decrease of the spin-echo signal intensity with increasing T_E , depending on T_2 and the proton density signal, S_0 , as free fit parameters. The data fitting procedures were implemented in Matlab (Matlab R2018b, MathWorks Inc., Natick, MA, USA). A non-linear least-square model with the iteratively reweighted least squares method was used for the curve fitting procedure, and the individual signal intensities I_{mean} were weighted by their variance calculated from the corresponding I_{STD} . The statistical errors of the obtained values of T_1 and T_2 were derived from the confidence interval (95 %) of the fit.

2.3. Measurement of optical tissue properties

The optical tissue properties of the used samples, i.e. the absorption coefficient $\mu_a(\lambda)$ and the reduced scattering coefficient $\mu_s'(\lambda)$, were characterized using an integrating sphere setup [40]. By measurement of the diffuse reflection and diffuse transmission of the sample, its optical tissue properties were determined via the inverse adding doubling (IAD) procedure [41].

The sample cuvette containing the sample was placed in front of one port (port diameter 25.5 mm) of the integrating sphere (sphere diameter 101.6 mm, Labsphere, North Sutton, USA) and irradiated with a collimated light beam of a xenon arc lamp (D-light 201,332 20, Karl Storz, Tuttlingen, Germany). The spectral data were collected with a detection fibre (core diameter 400 μ m, NA: 0.37) inserted into the integrating sphere through the detection port (diameter 3.2 mm). The detection fibre was connected to a spectrometer (S2000, Ocean Optics/Ocean Insight, Ostfildern, Germany). The spectral measurements consisted of three parts. The first part was the measurement of the diffuse transmission signal, $T_{\text{Sig}}(\lambda)$: the sample faced the incident light beam under perpendicular irradiation. The collimated, un-scattered part of the light transmitted through the sample leaves the integrating sphere through the exit port (diameter 25.5 mm) opposite the sample. Only the scattered and finally transmitted light, $T_{\text{Sig}}(\lambda)$, was detected, without the unscattered transmitted light. The second part was the measurement of the diffuse reflection signal, $R_{\text{Sig}}(\lambda)$: the sphere was turned by 180° compared to the diffuse transmission, so only the light scattered and finally reflected by the sample, $R_{\text{Sig}}(\lambda)$, was recorded, without the unscattered reflected light. The last part was the recording of the reference signal of the light source, $\text{Ref}_{\text{Sig}}(\lambda)$, obtained by direct irradiation of the inner surface of the integrating sphere.

From these three spectral datasets, the diffuse transmission $T_d(\lambda)$ and the diffuse reflectance $R_d(\lambda)$ of the sample were calculated using the known reflectivity of the integrating sphere, $R_{\text{IS}}(\lambda)$, with the following formula:

$$T_d(\lambda) = \frac{T_{\text{Sig}}(\lambda)}{\text{Ref}_{\text{Sig}}(\lambda)} R_{\text{IS}}(\lambda) \quad (3)$$

$$R_d(\lambda) = \frac{R_{\text{Sig}}(\lambda)}{R_{\text{Ref}}(\lambda)} R_{\text{IS}}(\lambda) \quad (4)$$

The two spectral datasets calculated by Eqs. (3) and (4) were further evaluated with the IAD procedure [41,42], which allows to iteratively determine the spectrally resolved optical parameters $\mu_a(\lambda)$ and $\mu_s'(\lambda)$ of the artificial sample for the wavelength array from 400 to 700 nm.

The mean and error of the optical tissue properties were determined by three separate measurements and evaluation procedures.

2.4. Reference data from literature

The optical tissue properties as well as the NMR relaxation times of the dual NMR/optical tissue phantoms were compared to the literature values seen in Table 1. The optical tissue properties, used for the comparison, were taken for the wavelength 635 nm [43,44]. The wavelength 635 nm was selected as it corresponds to the treatment wavelength of clinical 5-ALA-based iPDT of malignant brain tumors [4]. The NMR relaxation times were taken from literature providing a range for the relaxation times of the brain tissues white matter and grey matter [45–47]. The T_1 and T_2 relaxation times for malignant glioma have not been explicitly reported in the literature. However, they can be assumed to be equal to or longer than those of white matter, as observed in clinical images of malignant gliomas and the directly surrounding white matter [48].

2.5. Data analysis and statistics

All further data analysis and plotting was performed using Matlab (Matlab R2018b, MathWorks Inc., Natick, MA, USA). No statistical tests were performed.

3. Results

3.1. Dual NMR/optical tissue phantoms

Based on the concentration-dependent measurements shown in Figs. S1 through S5 in the supplement to this article, the finally chosen phantom mixtures were tuned manually to obtain optical coefficients and NMR relaxation times that are, at least for the present study, sufficiently close to the reference values listed in Table 1. Three phantom recipes for artificial dual NMR/optical brain tissue phantoms were created. These tissue phantoms have optical properties (μ_a and μ_s' at 635 nm) and NMR relaxation times (T_1 and T_2 at 3 T) similar to white matter, grey matter, and malignant glioma tissue. Table 2 lists the recipes of the three artificial tissue phantoms and their properties μ_a , μ_s' at 635 nm wavelength, and NMR relaxation times T_1 and T_2 at 3 T. All three phantoms were produced in four separate manufacturing processes to test the reproducibility. To investigate the contrast, the three tissue phantoms were filled into the measurement cuvettes as multi-layered phantoms composed of the three different tissue phantoms (see Fig. 1 for an example).

The experimentally determined mean values of the optical tissue

Table 1

Reference values for optical tissue properties, μ_a and μ_s' at 635 nm wavelength, and NMR relaxation times, T_1 and T_2 at 3 T, for different types of brain tissue according to literature. These literature values serve as a reference for comparison with the values experimentally obtained within this study [43–47].

tissue	μ_a [mm ⁻¹]	μ_s' [mm ⁻¹]	T_1 [ms]	T_2 [ms]
grey matter	0.02 [<0.01–0.03]	1.00 [0.88–1.20]	1342 [1122–1763]	102 [88–132]
white matter	0.08 [0.07–0.09]	6.00 [5.60–7.04]	818 [699–927]	72 [69–84]
malignant glioma	0.02 [0.01–0.06]	2.00 [1.00–5.80]	>818	>72

coefficients at 635 nm of the three prepared phantoms (Table 2) were all located within the range of the reference values obtained from the literature (Table 1), except for the mean value $\mu_s' = 5.37 \text{ mm}^{-1}$ of the white matter phantom. Here, μ_s' is 11 % smaller than the reference value ($\mu_{s',\text{ref}} = 6.00 \text{ mm}^{-1}$), but the error ranges of these two μ_s' values show a small overlap ([5.6–6.5 mm⁻¹] vs. [4.69–5.78 mm⁻¹]).

The mean value of T_1 measured at 3 T on the grey matter tissue phantom was consistent with the corresponding literature range of T_1 (1122–1763 ms), whereas the mean value of T_2 measured on that tissue phantom was about 20 % higher than the upper boundary of the corresponding literature values. The mean value of T_1 measured on the white matter tissue phantom was 3 % shorter than the corresponding lower boundary of the literature range. In contrast, the mean value of T_2 measured on that tissue phantom was consistent with the corresponding literature range. The mean values of T_1 and T_2 measured in the tumor phantom were 19.4 % and 6.2 %, respectively, larger T_2 than those measured on the white matter phantom.

Reproducibility tests have shown that the optical tissue properties at 635 nm could be reproduced within a maximum deviation of 11 % and the NMR relaxation times within a maximum deviation of 14 % for all three phantoms.

In the representations in Fig. 1, the three different phantom layers can be clearly distinguished when combining the information from both NMR imaging modalities (T_1 -weighted and T_2 -weighted MRI). In T_1 -weighted MRI, the white matter layer and the tumor phantom layer appear brighter than the grey matter due to shorter relaxation time, with the white matter phantom having the highest image intensity of the three phantoms. In the T_2 -weighted MRI, shorter relaxation times lead to a lower image intensity. The grey matter phantom layer has the longest T_2 time, resulting in the highest image intensity, leading to the strong contrast visible in the T_2 -weighted image in Fig. 1. With similar T_2 times, there is only a minimal difference in image intensity between the white matter and tumor phantom layers.

3.2. Porcine tissue samples

To simulate the effects of edema, a haemorrhage and varying lipid content in tissue, measurements have been performed on porcine brain tissue with different amounts of water, human blood, or Lipoveneous added as an additive to the tissue.

The addition of water to porcine brain tissue showed, with increasing volume fraction c_{water} of added water, a decrease of the optical absorption coefficient μ_a at 635 nm. At the same time, both NMR relaxation times T_1 and T_2 at 3 T were prolonged (see Table 3). The reduced scattering coefficient μ_s' at 635 nm showed no clear tendency for increasing c_{water} . In Figure S6 in the supplement, the complete measured wavelength-dependent arrays of the absorption and the reduced scattering coefficient are shown for the different c_{water} values.

The addition of Lipoveneous to porcine brain tissue showed that the absorption coefficient μ_a at 635 nm decreases while the reduced scattering coefficient μ_s' at 635 nm increases with increasing Lipoveneous volume fractions $c_{\text{Lipoveneous}}$ (Table 4). (Figure S7 in the supplement shows the complete measured wavelength-dependent arrays of the absorption and the reduced scattering coefficient for the different values of $c_{\text{Lipoveneous}}$.)

The NMR relaxation times T_1 and T_2 at 3 T show a non-neglectable T_1 and T_2 prolongation only for the highest Lipoveneous volume fractions $c_{\text{Lipoveneous}}$ of 30 %.

In contrast to Lipoveneous, the addition of blood shows, with higher blood volume fraction, an increase of the absorption coefficient μ_a and a decrease of the reduced scattering coefficient μ_s' at 635 nm. In Figure S8 in the supplement, the wavelength dependence of the absorption and reduced scattering coefficient are shown for the different c_{blood} values.

The transverse NMR relaxation time T_2 shortens with higher c_{blood} , whereas the longitudinal relaxation time T_1 does not show any relevant changes (Table 5).

Table 2

Recipes for three brain tissue phantoms with mean optical tissue properties at 635 nm and mean NMR relaxation times at 3 T similar to 3 different types of brain tissue, based on manual analyses of the data from 4 manufacturing processes shown in Figs. S1 through S5 in the supplement of this article. In brackets, the statistical standard error of the corresponding value is shown, determined by four repetitive manufacturing and measurement cycles.

tissue phantom type	agar [%]	Lipoveneous [%]	black ink [%]	gadobutrol [%]	μ_a [mm ⁻¹]	μ_s' [mm ⁻¹]	T_1 [ms]	T_2 [ms]
grey matter	1	1.5	0.01	0.01	0.020 (0.001)	1.34 (0.04)	1194 (46)	158 (19)
white matter	2	10.5	0.08	0.0167	0.087 (0.009)	5.36 (0.51)	680 (16)	81 (12)
Malignant glioma	2	3.5	0.01	0.0167	0.022 (0.002)	2.39 (0.22)	812 (39)	86 (6)

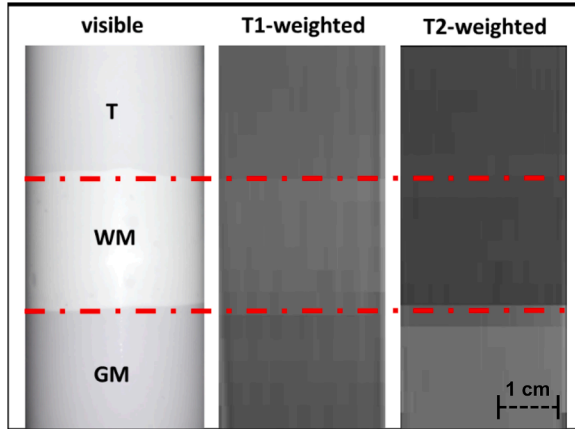


Fig. 1. Visible as well as T_1 - and T_2 -weighted MRI-appearance of phantoms for mimicking the human brain tissue types malignant glioma/tumor (T), white matter (WM) and grey matter (GM). The red dotted lines indicate the interface positions between the different tissue types/phantoms. (The grey value in the NMR images corresponds to the signal intensity in the sample. A shorter T_1 time appears brighter in the T_1 -weighted image, while a shorter T_2 time appears darker in the T_2 -weighted image [26]).

Table 3

Absorption coefficient μ_a and reduced scattering coefficient μ_s' at 635 nm as well as NMR relaxation times T_1 and T_2 shown for different water volume fractions c_{water} .

c_{water} [%]	μ_a [mm ⁻¹]	μ_s' [mm ⁻¹]	T_1 [ms]	T_2 [ms]
0	0.069 ± 0.001	3.77 ± 0.05	1119 ± 71	93 ± 7
5	0.069 ± 0.001	4.32 ± 0.08	1181 ± 62	95 ± 5
10	0.064 ± 0.0006	3.84 ± 0.03	1226 ± 40	102 ± 4
15	0.062 ± 0.001	3.95 ± 0.02	1275 ± 57	109 ± 3
20	0.057 ± 0.002	3.62 ± 0.006	1332 ± 75	115 ± 3
30	0.049 ± 0.001	3.27 ± 0.02	1450 ± 74	132 ± 2

Table 4

Absorption coefficient μ_a and reduced scattering coefficient μ_s' at 635 nm as well as NMR relaxation times T_1 and T_2 shown for different Lipoveneous volume fractions $c_{\text{Lipoveneous}}$. (Here, the Lipoveneous volume fraction corresponds to the ratio of the volume of the added lipid emulsion and the total volume of the final sample).

$c_{\text{Lipoveneous}}$ [%]	μ_a [mm ⁻¹]	μ_s' [mm ⁻¹]	T_1 [ms]	T_2 [ms]
0	0.068 ± 0.001	4.06 ± 0.10	1124 ± 59	91 ± 6
5	0.065 ± 0.002	4.38 ± 0.09	1106 ± 58	87 ± 6
10	0.067 ± 0.002	4.93 ± 0.08	1114 ± 54	91 ± 6
15	0.066 ± 0.003	5.23 ± 0.04	1123 ± 70	94 ± 5
20	0.068 ± 0.002	5.67 ± 0.10	1132 ± 80	97 ± 5
30	0.052 ± 0.004	6.01 ± 0.04	1226 ± 106	105 ± 5

When comparing the water-induced trends observed on the prepared tissue samples regarding the absorption and the reduced scattering coefficient at 635 nm with those regarding the NMR relaxation times T_1 and T_2 at 3 T, it is observed that a prolongation of relaxation times takes

Table 5

Absorption coefficient μ_a and reduced scattering coefficient μ_s' at 635 nm as well as NMR relaxation times T_1 and T_2 shown for different blood volume fractions c_{blood} .

c_{blood} [%]	μ_a [mm ⁻¹]	μ_s' [mm ⁻¹]	T_1 [ms]	T_2 [ms]
0	0.04 ± 0.002	3.95 ± 0.05	1227 ± 100	102 ± 4
2	0.10 ± 0.001	3.92 ± 0.03	1246 ± 55	81 ± 7
4	0.15 ± 0.002	3.90 ± 0.04	1245 ± 127	70 ± 10
6	0.20 ± 0.002	3.86 ± 0.01	1249 ± 125	62 ± 11
8	0.25 ± 0.004	3.69 ± 0.07	1231 ± 119	56 ± 14
10	0.32 ± 0.01	3.74 ± 0.08	1219 ± 102	50 ± 15

place along with a decrease of absorption and scattering (Fig. 2). An increase of the reduced scattering coefficient at 635 nm by the addition of Lipoveneous was accompanied by a prolongation of T_1 and T_2 , when neglecting the sample without added Lipoveneous ($c_{\text{Lipoveneous}}=0$ %) (Fig. 3).

Upon adding human blood, an increase of the absorption coefficient at 635 nm and a decrease of the reduced scattering coefficient were accompanied by a shortening of the NMR relaxation time T_2 at 3 T (Fig. 4).

4. Discussion

4.1. Dual NMR/optical brain tissue phantoms

The central ingredient for solid tissue phantoms is the matrix ingredient. For most solid tissue phantoms, hydrogels such as agar, gelatin or nonionic surfactants are used. It was observed that with increasing hydrogel fraction, μ_s' , T_1 and T_2 decrease (see Figure S1 and Figure S2 in the supplement to this article). It is well known from the manufacturing of optical tissue phantoms that when increasing the hydrogel concentration, additional scattering medium is needed to maintain a specific scattering power [49]. This is related to the increasing water binding capacity and the decreasing fraction of unbound water within the phantom [50], which is further linked with an increasing storage modulus and stiffness. As a result, it is seen that with increasing hydrogel concentration, T_1 and T_2 are reduced due to the lower fraction of unbound water and decreasing diffusion in the tissue phantom [51].

When comparing agar and gelatin, it was observed that agar had a substantially stronger effect on T_2 , which is reduced to 40 ms at 6 % agar, but only to 300 ms at 20 % gelatin (see Figures S1 and S2 in the supplement to this article). For T_1 the effects of agar and gelatin were comparable. The differences between the two hydrogels, e.g. the much higher gelatin fraction required for a given change in NMR relaxation times, may be explained by the different hydrogel mechanisms of agar and gelatin. In agar, the solidification is activated by agarose, a polysaccharide [52]. In contrast, the solidification in gelatin is based on protein chains [53]. In addition, the protein chains are also responsible for the stronger dependence of the resulting phantom properties on the temperature during the manufacturing process [54]. In order to realize the NMR relaxation times T_1 and T_2 in the range 72 - 102 ms listed in Table 1, agar was chosen as matrix for the final tissue phantoms.

Concerning the optical tissue properties, for agar phantoms,

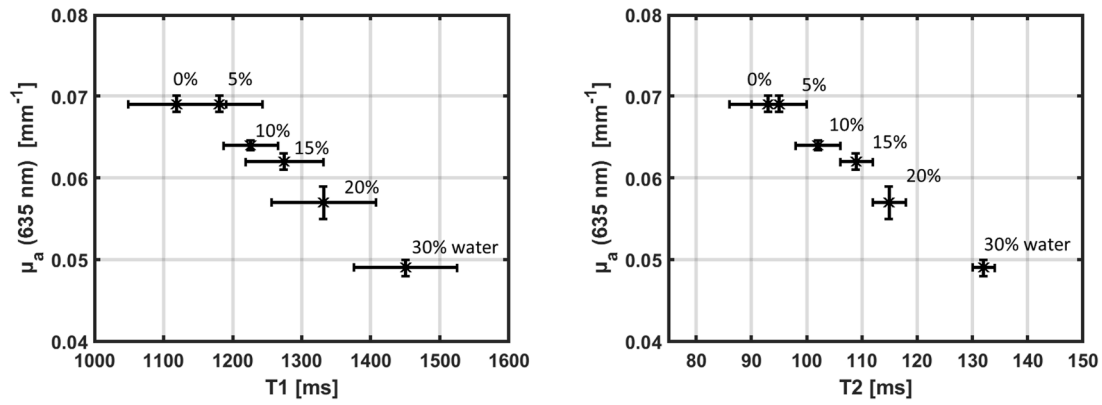


Fig. 2. Absorption coefficient μ_a at 635 nm measured on porcine brain tissue, plotted in relation to the NMR relaxation times T_1 (left) and T_2 (right) for different water volume fractions used to modify the sample properties.

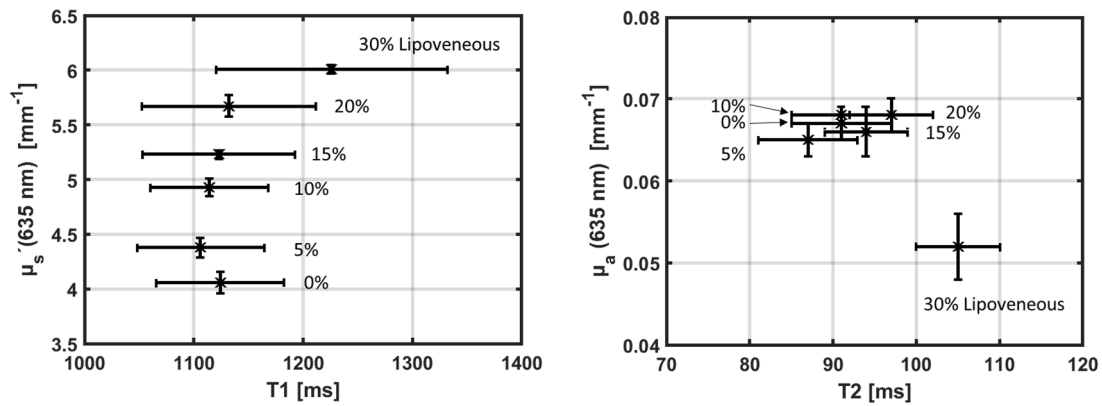


Fig. 3. Absorption coefficient μ_a at 635 nm plotted in relation to the NMR relaxations time T_2 and reduced scattering coefficient μ_s' at 635 nm plotted in relation to the NMR relaxations time T_1 , both measured on porcine brain tissue, for different Lipoveneous volume fractions used to modify the sample properties.

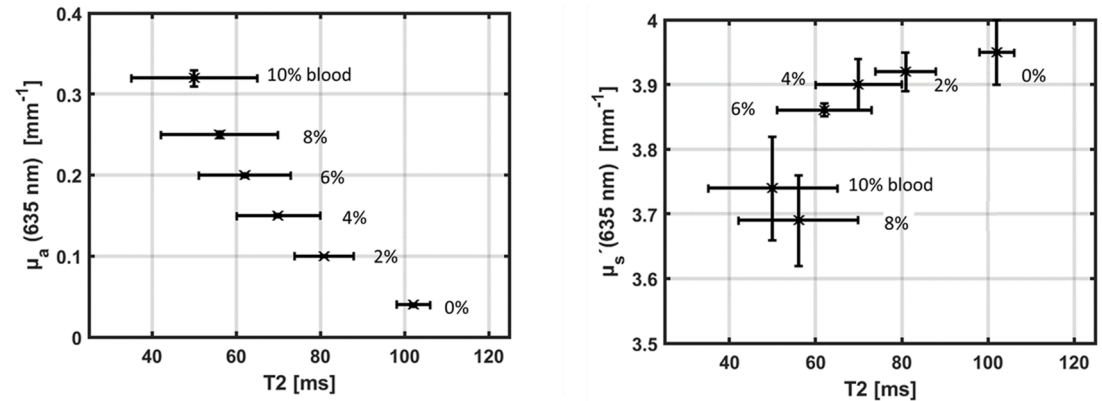


Fig. 4. Absorption coefficient μ_a at 635 nm measured on porcine brain tissue, plotted in relation to the NMR relaxations time T_2 for different human blood volume fractions used to modify the sample properties.

reductions of μ_a were observed when increasing the agar concentration to 4 % and 6 %. At these two concentrations, however, problems in the manufacturing process were observed as the viscosity of the base medium for the tissue phantom is already very high during the cooking process. This problem becomes worse with higher Lipoveneous fractions because the amount of plain water added to the phantom has to be reduced to compensate for the water included in the used 20 % lipid emulsion.

With increasing Lipoveneous fraction in the tissue phantoms, an increase in μ_s' has been observed previously [55]. It is expected that with

increasing Lipoveneous fraction, which is comparable to oil and fat, the NMR relaxation times T_1 and T_2 shorten [27,32]. This was only observed to a minor extent in the solid tissue phantoms based on agar or gelatin. Thus, it can be hypothesized that, regarding T_1 and T_2 the influences of the mechanical properties of the hydrogels agar and gelatine dominate over those of dissolved fats and oils, such as Lipoveneous. This reduces the effect of Lipoveneous on T_1 and T_2 when increasing the hydrogel fraction.

Black ink was used to adjust the absorbance in the tissue phantoms. An increasing concentration of black ink resulted in an increase of μ_a ,

whereas no systematic changes in μ_s' were observed. As the respective measurements were conducted on a gelatin-based hydrogel, the observed changes of μ_s' could be due to the gelatin itself, since preparation of gelatin-based phantoms is highly sensitive to the exact heating procedure, which can strongly affect the resulting optical properties [54]. No effect on the NMR relaxation times was seen using black ink. As the constituents of black ink are unknown, it is unclear if black ink has no effect at all on the NMR relaxation times or if the effect was not notable due to the low concentration of black ink in the tissue phantom.

It was possible to reach T_2 values similar to those of human brain with agar-based phantoms, but not with gelatin-based phantoms. To shorten T_1 while keeping T_2 almost constant, gadobutrol, a gadolinium-based contrast agent, was used. In terms of NMR relaxation times, gadobutrol had similar effects on the hydrogel-based phantoms as on tissue. The used gadobutrol concentration was below 0.01 % - 0.0167 %. This corresponds to gadobutrol weight fractions of 0.073 $\mu\text{g/g}$ - 0.123 $\mu\text{g/g}$ within the phantom, which is in the range of values found for gadobutrol accumulation in tumor tissue (0.034 $\mu\text{g/g}$ - 0.627 $\mu\text{g/g}$) [56].

It has to be noted that the NMR relaxation times T_1 and T_2 of brain tissue observed in individual patients are spread over wide ranges. For the developed tissue phantoms, T_1 and T_2 relaxation times longer than those of white matter were chosen for tumorous tissue, as this is a common finding, but the prolongation is dependent on the presence edema, the level of necrosis, and other factors [57,58]. For tumor regions, that have the ability to take up contrast agent, T_1 values in the range of grey matter have been reported.

The obtained tissue phantoms can easily be reproduced, but for easier manufacturing, experience showed that it is helpful to mix the additional ingredients (gadolinium, Lipoveneous and ink) in a separate beaker and add the mixture in small parts into the agar. When adding one ingredient after the other, problems may occur during preparation of the tumor phantom or white matter phantom as the mixture to be processed has a relatively high viscosity.

In the end, recipes for the preparation of dual phantoms mimicking brain tissue with both optical and MR relaxation times close to literature values are presented. In addition, the measurements and results can easily be adapted to create phantom recipes to mimic other tissues, with individually tunable optical and NMR properties. Each of the added ingredients was used to adjust mainly one property of the artificial phantom, without having a significant effect on the other properties. An exception to this is the hydrogel whose concentration defines the basic properties on which the whole tissue phantom is built on, so this is the first component to be chosen, including its concentration. In this case, the agar concentration was used to adjust the T_2 time of the tissue phantom. Afterwards, with Lipoveneous and ink the optical tissue properties can be adjusted. In the end, the needed amount of gadobutrol is added to reduce T_1 to the desired value. Within the relevant concentration range, T_2 was not significantly affected by the addition of gadobutrol.

Of course, one may also use other ingredients to prepare tissue phantoms. For example instead of Lipoveneous other fat-based scattering media like Intralipid and Lipofundin, metal oxides like Titanium dioxide (TiO_2), Barium sulfate (BaSO_4) or polystyrenes may be used, which are all already being used for manufacturing tissue phantoms [33, 54,55,59-61]. For the adjustment of T_1 and T_2 , also other metal-based contrast agents may be used [62]. The compatibility between the ingredients has to be tested in each case. Thereafter optical characterization measurements and MRI scans have to be performed to characterize and monitor the different effects on relaxation times and optical properties of the artificial tissue phantom.

Overall, artificial phantoms were developed that simultaneously exhibit optical properties and NMR relaxation times of different types of brain tissues relevant during iPDT. These artificial tissue phantoms may be combined to simulate iPDT a realistic inhomogeneous tissue environment and to investigate and develop simultaneous MRI and spectral

online monitoring systems. Furthermore, such artificial phantoms may be used for the development of devices for training and demonstrations.

4.2. Optical properties and NMR relaxation times

In addition to the investigations on artificial tissue phantoms, experiments on porcine brain tissue with different additives were performed to compare their effects on optical properties and NMR relaxation times.

To simulate a tumor-induced edema, water was added to the porcine brain tissue. A brain edema is normally caused by the disruption and leakage of the blood-brain barrier, which causes an accumulation of plasma in the brain parenchyma, which in turn leads to more unbound water in the tissue [58,63]. This causes a prolongation of relaxation times in the edema. This prolongation of T_1 and T_2 was also observed when the water fraction added to the porcine brain tissue was increased. At the same time, a decrease of the absorption coefficient at 635 nm was observed, due to the dilution of tissue constituents strongly absorbing at that wavelength (in particular blood, melanin and lipofuscin). For the reduced scattering coefficient, a systematic decrease was only observed at high water content. The results for the addition of water could indicate that in brain edema surrounding the tumor, the prolongation of relaxation times might be an indicator for a decrease of the absorption coefficient compared to the surrounding tissue not affected by the edema.

Next to the occurrence of edema, it is known that a malignant glioma/glioblastoma also affects the lipid metabolism and the lipid content in the tissue [64,65]. Higher lipid content not only results in a shortening of NMR relaxation times [27,32], it typically also results in an increase of optical scattering [55]. To simulate the reported change of lipid content, Lipoveneous was added to the porcine brain. A shortening of T_1 and T_2 was only seen for 5 % Lipoveneous fraction. With higher fractions, the T_1 and T_2 were prolonged, in contrast to the expectable opposite behaviour just mentioned. This could be because pure Lipoveneous was not available by the manufacturer, but only a diluted 20 % MCT emulsion. Therefore, with the increase of the Lipoveneous fraction, the water fraction in the sample is also increased. This may lead to a domination of the relaxation time prolongation by the higher water content in the sample compared to the effects of the higher lipid content. In conclusion, a systematic increase of optical scattering at 635 nm was observed with increasing Lipoveneous fraction, whereas changes of the optical absorption at that wavelength were negligible and changes of the NMR relaxations times were difficult to interpret. In future experiments, the used Lipoveneous emulsion may be replaced by fat or other lipids without water to simulate changes in lipid content in the tissue more purely.

Next to the tumor-related occurrence of edema or changes in lipid metabolism, the blood content in tissue plays an important role as blood is one of the main optical absorbers in biological tissue [29]. The blood volume in tumor tissue is usually increased due to enhanced angiogenesis. Dependent of the grade of angiogenesis, the relative cerebral blood volume (rCBV) of tumor, i.e. the ratio of the cerebral blood volume between tumor and white matter, lies in the range 0.82 - 6.26 [66,67]. In some cases, an rCBV higher than 16 was measured [68,69]. To simulate this, blood was added to the porcine brain tissue, which lead to a shortening of T_2 while the absorption at 635 nm increased and T_1 stayed approximately constant with increasing blood fraction. So, in case the changes are blood-related, a shortening of T_2 with constant T_1 in the examined tissue region might be an indicator for higher absorption at 635 nm, which would result in a lower optical penetration depth of the iPDT treatment light.

In addition to T_1 and T_2 mapping to monitor the blood content in the brain, perfusion MRI may give more detailed information as it is sensitive to the cerebral blood flow and volume. Differences in the perfusion may then indicate differences in absorption between the different areas of the brain.

In this investigation, results were presented mainly for 635 nm as this wavelength is used for the 5-ALA-mediated iPDT of malignant gliomas. When using another photosensitizer with a different excitation wavelength, the respective absorption and scattering properties must be expected to change. Depending on the wavelength dependencies of the absorption and scattering coefficients of the investigated base tissue and the additives, the optical coefficients of the modified tissue may change in a different manner at different wavelengths (which not only refers to the magnitude of the change, but also the direction of the change with increasing additive fraction). It has also to be noted that the observed changes will differ for different tissue types such as brain, liver and prostate, depending on the individual water/lipid/blood content of the tissue.

Altogether, a direct translation from T_1 and T_2 values to optical properties is not possible, but for the treatment planning it is already of high value to identify regions with differing optical tissue properties, e. g., higher absorption and scattering. Knowledge about these areas could already be included in the treatment planning and irradiation concept. It could be shown as a first step that changes (or differences) of the NMR relaxation times T_1 and T_2 could indicate changes (or differences) in the absorption and scattering properties.

Future work should also investigate the possibility to extract changes of optical tissue properties with increasing additive fraction based on curve fitting. This may also lead to transfer functions and/or parameters that allow for a translation from changes and differences in T_1 and T_2 relaxation times to temporal changes and local differences in optical properties.

A transfer of MRI to assumptions for differences in optical tissue properties would lead to an individualization of iPDT light dosimetry. This could be implemented in light dosimetry concepts that are able to take into account different tissue types and inhomogeneities with different optical properties in the tissues. By incorporating such individual optical tissue properties, areas that do not receive enough light due to high absorption, for example, can be identified and taken into account in light dosimetry planning. This could ensure the optimal distribution of the light dose at the beginning of the irradiation and possibly lead to a better response of the tumor to the therapy and thus may lead to a longer patient survival.

5. Conclusion

Dual NMR/optical tissue phantoms were designed to mimic simultaneously NMR relaxation times and optical tissue properties of different types of brain tissue. The obtained tissue phantoms can be used not only for iPDT research and development, but also for demonstration and training. In addition, the phantom properties can also be easily adjusted by slight changes of the additive concentrations. By addition of fluorophores, the phantoms could also be further developed to mimic the fluorescence observable during 5-ALA-based iPDT irradiation.

Furthermore, the obtained results from the measurements of porcine tissue samples with addition of water, lipid or blood seem to be a promising first step for further developing iPDT treatment planning concepts based on local differences in optical tissue properties extracted from differences in NMR relaxation times. This possibility is confirmed by the measurements carried out and the indications observed. In future research, these indications should be further investigated so that by using look-up tables or parametrized functions, differences in NMR relaxation times within the same tissue type may be used to identify the grade of change in optical absorption or scattering. This information could be included in the light-dosimetric calculations and the treatment planning to further individualize the iPDT concept.

Institutional review board statement

The study was conducted according to the guidelines of the Declaration of Helsinki and approved by the Ethics Committee of Ludwig-

Maximilians-University, Munich, Germany (ref. no. 18–144). For the use of porcine tissue samples ethic approval was not needed as the tissue parts used in this work were all obtained from food production.

Informed consent statement

Informed consent was obtained from all blood donors involved in the study.

Data sharing

Data supporting this study are included within the article and supporting materials.

CRediT authorship contribution statement

Maximilian Aumiller: . **Asmerom Arazar:** Writing – review & editing, Investigation, Formal analysis. **Ronald Sroka:** . **Olaf Dietrich:** Writing – review & editing, Supervision, Methodology, Data curation. **Adrian Rühm:** Writing – review & editing, Validation, Supervision, Software, Project administration, Funding acquisition, Conceptualization.

Declaration of competing interest

The authors declare no conflict of interest. The funders had no role in the design of the study; in the collection, analyses, or interpretation of data; in the writing of the manuscript, or in the decision to publish the results.

Acknowledgments

We thank the Mathias Hübner, Marco Düring and the MRI core facility of the Institute for Stroke and Dementia Research (ISD) at LMU Hospital for their assistance in performing the MRI measurements.

Funding

This research was funded by Deutsche Forschungsgemeinschaft (DFG, German Research Foundation) in terms of the GRK2274 (Project number 299102935). The procurement of the MRI scanner was supported by the DFG grant for major research instrumentation (DFG, INST 409/193–1 FUGG).

Supplementary materials

Supplementary material associated with this article can be found, in the online version, at [doi:10.1016/j.pdpdt.2024.103968](https://doi.org/10.1016/j.pdpdt.2024.103968).

References

- [1] T.J. Beck, et al., Interstitial photodynamic therapy of nonresectable malignant glioma recurrences using 5-aminolevulinic acid induced protoporphyrin IX (in en), *Lasers Surg. Med.* 39 (5) (2007) 386–393, 06/2007.
- [2] S. Lietke, et al., Interstitial photodynamic therapy using 5-ALA for malignant Glioma recurrences, *Cancers* 13 (8) (2021). Apr 7.
- [3] A. Johansson, F.W. Kreth, W. Stummer, H. Stepp, Interstitial Photodynamic Therapy of Brain Tumors, *IEEE J. Selected Topics in Quantum Electronics* 16 (4) (2010) 841–853, July 2010.
- [4] S. Quach, et al., Interstitial photodynamic therapy for newly diagnosed glioblastoma, *J. Neurooncol.* 162 (1) (2023) 217–223, Mar.
- [5] M. Aumiller, et al., Interrelation between spectral online monitoring and postoperative T1-weighted MRI in interstitial photodynamic therapy of malignant Gliomas, *Cancers* 14 (1) (2021). Dec 27.
- [6] F. Martelli, *Light Propagation Through Biological Tissue and Other Diffusive Media: Theory, Solutions, and Software*, SPIE Press, 2010, p. 274.
- [7] F. Martelli, M. Bassani, L. Alianelli, L. Zangheri, G. Zaccanti, Accuracy of the diffusion equation to describe photon migration through an infinite medium: numerical and experimental investigation (in en), *Phys. Med. Biol.* 45 (5) (2000) 1359–1373, 2000-05-01.

- [8] J. Cassidy, L. Lilge, and V. Betz, "FullMonte: a framework for high-performance Monte Carlo simulation of light through turbid media with complex geometry", 2013, p. 85920H.
- [9] E. Oakley, B. Wrazen, D.A. Bellnier, Y. Syed, H. Arshad, G. Shafirstein, A new finite element approach for near real-time simulation of light propagation in locally advanced head and neck tumors, *Lasers Surg. Med.* 47 (1) (2015) 60–67. Jan.
- [10] E. Okada, M. Schweiger, S.R. Arridge, M. Firbank, D.T. Delpy, Experimental validation of Monte Carlo and finite-element methods for the estimation of the optical path length in inhomogeneous tissue, *Appl. Opt.* 35 (19) (1996) 3362–3371. Jul 1.
- [11] V.V. Tuchin, S.o.P.-o.I. Engineers, *Tissue Optics: Light Scattering Methods and Instruments for Medical Diagnosis*, SPIE Press, 2015.
- [12] L. Lilge, B.C. Wilson, Photodynamic therapy of intracranial tissues: a preclinical comparative study of four different photosensitizers, *J. Clin. Laser Med. Surg.* 16 (2) (1998) 81–91. Apr.
- [13] A. Johansson, et al., Protoporphyrin IX fluorescence and photobleaching during interstitial photodynamic therapy of malignant Gliomas for early treatment prognosis: fluorescence for treatment prognosis in Glioma PDT (in en), *Lasers Surg. Med.* 45 (4) (2013) 225–234, 04/2013.
- [14] A. Rühm, et al., 5-ALA based photodynamic management of glioblastoma, in: *Proceedings of the SPIE, Optical Techniques in Neurosurgery, Neurophotonics, and Optogenetics*, San Francisco, CA, USA, International Society for Optics and Photonics, 2014, 8928p. 89280E.
- [15] M. Aumiller, et al., Individualization of interstitial photodynamic therapy for malignant gliomas, in: *Medical Laser Applications and Laser-Tissue Interactions IX*, 11079, International Society for Optics and Photonics, 2019, 110790P.
- [16] A. Johansson, et al., In vivo measurement of parameters of dosimetric importance during interstitial photodynamic therapy of thick skin tumors, *J. Biomed. Opt.* 11 (3) (2006) 34029. May-Jun.
- [17] A. Rühm, et al., 5-ALA based photodynamic management of glioblastoma, in: *Proceedings of the Progress in Biomedical Optics and Imaging - Proceedings of SPIE*, 2014, 892889280E, 02/28.
- [18] L.V. Wang, H.-I. Wu, *Biomedical Optics: Principles and Imaging*, John Wiley & Sons, 2012, p. 379.
- [19] C. Heckl, M. Aumiller, A. Ruhm, R. Sroka, H. Stepp, Fluorescence and treatment light monitoring for interstitial photodynamic therapy, *Photochem. Photobiol.* 96 (2) (2020) 388–396. Mar.
- [20] E.L.P. Larsen, et al., Monitoring of hexyl 5-aminolevulinate-induced photodynamic therapy in rat bladder cancer by optical spectroscopy (in en), *J. Biomed. Opt.* 13 (4) (2008) 044031, 2008.
- [21] E.L.P. Larsen, L.L. Randeberg, O.A. Gederaas, H.E. Krokan, D.R. Hjelm, and L.O. Svaasand, "In vitro study on methemoglobin formation in erythrocytes following hexyl-aminolevulinate induced photodynamic therapy", 2007, p. 642719.
- [22] J.E. Villanueva-Meyer, M.C. Mabray, S. Cha, Current clinical brain tumor imaging, *Neurosurgery* 81 (3) (2017) 397–415. Sep 1.
- [23] B. Karakullukcu, et al., MR and CT based treatment planning for mTHPC mediated interstitial photodynamic therapy of head and neck cancer: description of the method, *Lasers Surg. Med.* 45 (8) (2013) 517–523. Oct.
- [24] S.L. Jacques, How tissue optics affect dosimetry of photodynamic therapy, *J. Biomed. Opt.* 15 (5) (2010), 2010.
- [25] Ed B.C. Wilson, M.S. Patterson, S.T. Flock, D.R. Wyman, Tissue optical properties in relation to light propagation models and in vivo dosimetry, in: B. Chance, MA Boston (Eds.), *Photon Migration in Tissues*, Springer US, 1989, pp. 25–42. Ed.
- [26] L. Axel, Relaxation times and NMR signals, *Magn. Reson. Imaging* 2 (2) (1984) 121–130.
- [27] C. Leuze, et al., The separate effects of lipids and proteins on brain MRI contrast revealed through tissue clearing, *Neuroimage* 156 (2017) 412–422. Aug 1.
- [28] W.F. Cheong, S.A. Prah, A.J. Welch, A review of the optical properties of biological tissues, *IEEE J. Quantum Electron* 26 (12) (1990) 2166–2185. December 1990.
- [29] S.L. Jacques, Optical properties of biological tissues: a review (in en), *Phys. Med. Biol.* 58 (11) (2013) R37–R61, 2013-06-07.
- [30] R. Bansal, X. Hao, F. Liu, D. Xu, J. Liu, B.S. Peterson, The effects of changing water content, relaxation times, and tissue contrast on tissue segmentation and measures of cortical anatomy in MR images, *Magn. Reson. Imaging* 31 (10) (2013) 1709–1730. Dec.
- [31] W.G. Bradley, MR appearance of hemorrhage in the brain (in eng), *Radiology* 189 (1) (1993) 15–26. Oct 1993.
- [32] A. Zimny, L. Zinska, J. Bladowska, M. Neska-Matuszewska, M. Siasidek, Intracranial lesions with high signal intensity on T1-weighted MR images - review of pathologies, *Pol. J. Radiol.* 78 (4) (2013) 36–46. Oct.
- [33] B.W. Pogue, M.S. Patterson, Review of tissue simulating phantoms for optical spectroscopy, imaging and dosimetry, *J. Biomed. Opt.* 11 (4) (2006) 041102. Jul-Aug.
- [34] M.A. Bernstein, J. Huston 3rd, H.A. Ward, Imaging artifacts at 3.0T, *J. Magn. Reson. Imaging* 24 (4) (2006) 735–746. Oct.
- [35] P.A. Yushkevich, et al., User-guided 3D active contour segmentation of anatomical structures: significantly improved efficiency and reliability, *Neuroimage* 31 (3) (2006) 1116–1128. July 1, 2006.
- [36] A. Karakuzu, et al., qMRlab: quantitative MRI analysis, under one umbrella (in en), *J. Open Source Software* 5 (53) (2020) 2343, 2020/09/03.
- [37] J.K. Barral, E. Gudmundson, N. Stikov, M. Etezadi-Amoli, P. Stoica, D. G. Nishimura, A robust methodology for in vivo T1 mapping, *Magn. Reson. Med.* 64 (4) (2010) 1057–1067. Oct.
- [38] S. Bidhult, G. Kantasis, A.H. Aletras, H. Arheden, E. Heiberg, E. Hedström, Validation of T1 and T2 algorithms for quantitative MRI: performance by a vendor-independent software (in en), *BMC Med. Imaging* 16 (1) (2016), 12/2016.
- [39] D. Milford, N. Rosbach, M. Bendszus, S. Heiland, Mono-Exponential fitting in T2-relaxometry: relevance of offset and first echo, *PLoS ONE* 10 (12) (2015), 2015-12-17.
- [40] M. Eisel, S. Strobl, T. Pongratz, H. Stepp, A. Ruhm, R. Sroka, Investigation of optical properties of dissected and homogenized biological tissue, *J. Biomed. Opt.* 23 (9) (2018) 1–9. Sep.
- [41] S.A. Prah, M.J.C. van Gemert, A.J. Welch, Determining the optical properties of turbid media by using the adding-doubling method" (in en), *Appl. Opt.* 32 (4) (1993) 559, 1993-02-01.
- [42] S. Prah, "Optical Property Measurements using the Inverse Adding-Doubling Program", (in en), 2020, p. 53.
- [43] T.J. Beck et al., "Clinical Determination of Tissue Optical Properties in vivo by Spatially Resolved Reflectance Measurements", (in en), 2020, p. 10.
- [44] A.N. Yaroslavsky, P.C. Schulze, I.V. Yaroslavsky, R. Schober, F. Ulrich, H. J. Schwarzaier, Optical properties of selected native and coagulated human brain tissues in vitro in the visible and near infrared spectral range (in en), *Phys. Med. Biol.* 47 (12) (2002) 2059–2073, 2002-6-21.
- [45] J.P. Wansapura, S.K. Holland, R.S. Dunn, W.S. Ball, NMR relaxation times in the human brain at 3.0 tesla (in en), *J. Magn. Reson. Imaging* 9 (4) (1999) 531–538, 04/1999.
- [46] H. Lu, L.M. Nagae-Poetscher, X. Golay, D. Lin, M. Pomper, P.C.M. van Zijl, Routine clinical brain MRI sequences for use at 3.0 Tesla (in en), *J. Magn. Reson. Imaging* 22 (1) (2005) 13–22, 07/2005.
- [47] N. Gelman, J.R. Ewing, J.M. Gorell, E.M. Spickler, E.G. Solomon, Interregional variation of longitudinal relaxation rates in human brain at 3.0 T: relation to estimated iron and water contents, *Magn. Reson. Med.* 45 (1) (2001) 71–79. Jan.
- [48] C. Badve, et al., MR fingerprinting of adult brain tumors: initial experience, *AJNR Am. J. Neuroradiol.* 38 (3) (2017) 492–499. Mar.
- [49] R. Cubeddu, A. Pifferi, P. Taroni, A. Torricelli, G. Valentini, A solid tissue phantom for photon migration studies (in en), *Phys. Med. Biol.* 42 (10) (1997) 1971–1979, 1997-10-01.
- [50] C. Wu, W. Ma, Y. Chen, W. Navicha, D. Wu, M. Du, The water holding capacity and storage modulus of chemical cross-linked soy protein gels directly related to aggregates size, *LWT* 103 (2018), 12/01.
- [51] Z.G. Portakal, et al., Design and characterization of tissue-mimicking gel phantoms for diffusion kurtosis imaging, *Med. Phys.* 45 (6) (2018) 2476–2485. Jun.
- [52] M. Nasrollahzadeh, M. Sajjadi, Z. Nezafat, N. Shafiei, Chapter 3 - Polysaccharide biopolymer chemistry. Biopolymer-Based Metal Nanoparticle Chemistry for Sustainable Applications, M. Nasrollahzadeh, Elsevier, 2021, pp. 45–105. Ed.
- [53] P. Jaiphan, A. Nguyen, R. Narayan, Gelatin-based hydrogels for biomedical applications, *MRS Commun.* 7 (2017) 416–426, 09/01.
- [54] P. Lai, X. Xu, L.V. Wang, Dependence of optical scattering from Intralipid in gelatin-gel based tissue-mimicking phantoms on mixing temperature and time (in en), *J. Biomed. Opt.* 19 (3) (2014) 035002, 2014-03-06.
- [55] R. Michels, F. Foschum, A. Kienle, Optical properties of fat emulsions (in en), *Opt. Express* 16 (8) (2008) 5907, 2008-04-14.
- [56] A. Kiviniemi, M. Gardberg, P. Ek, J. Frantzen, J. Bobacka, H. Minn, Gadolinium retention in gliomas and adjacent normal brain tissue: association with tumor contrast enhancement and linear/macrocyclic agents, *Neuroradiology* 61 (5) (2019) 535–544. May.
- [57] Y. Li, R. Srinivasan, H. Ratiney, Y. Lu, S.M. Chang, S.J. Nelson, Comparison of T(1) and T(2) metabolite relaxation times in glioma and normal brain at 3T, *J. Magn. Reson. Imaging* 28 (2) (2008) 342–350. Aug.
- [58] C.M. Pirk, et al., Accelerated 3D whole-brain T1, T2, and proton density mapping: feasibility for clinical glioma MR imaging, *Neuroradiology* 63 (11) (2021) 1831–1851. Nov.
- [59] L. Cortese, et al., Liquid phantoms for near-infrared and diffuse correlation spectroscopies with tunable optical and dynamic properties, *Biomed. Opt. Express* 9 (5) (2018) 2068–2080. May 1.
- [60] M.S. Durkee, L.D. Nash, F. Nooshabadi, J.D. Cirillo, D.J. Maitland, K.C. Maitland, Fabrication and characterization of optical tissue phantoms containing macrostructure, *J. Vis. Exp.* (132) (2018). Feb 12.
- [61] D. Passos, J.C. Hebden, P.N. Pinto, R. Guerra, Tissue phantom for optical diagnostics based on a suspension of microspheres with a fractal size distribution, *J. Biomed. Opt.* 10 (6) (2005) 064036. Nov-Dec.
- [62] Y.D. Xiao, R. Paudel, J. Liu, C. Ma, Z.S. Zhang, S.K. Zhou, MRI contrast agents: classification and application (Review), *Int. J. Mol. Med.* 38 (5) (2016) 1319–1326. Nov.
- [63] Y. Esquenazi, V.P. Lo, K. Lee, Critical care management of cerebral edema in brain tumors, *J. Intensive Care Med.* 32 (1) (2017) 15–24. Jan.
- [64] H. He, et al., Method for lipidomic analysis: p53 expression modulation of sulfatide, ganglioside, and phospholipid composition of U87 MG glioblastoma cells, *Anal. Chem.* 79 (22) (2007) 8423–8430. Nov 15.
- [65] K. Abdul Rashid, K. Ibrahim, J.H.D. Wong, N. Mohd Ramli, Lipid alterations in glioma: a systematic review, *Metabolites* 12 (12) (Dec 16 2022).
- [66] H.J. Aronen, et al., Cerebral blood volume maps of gliomas: comparison with tumor grade and histologic findings (in en), *Radiology* (1994), 1994-04-01.
- [67] S.J. Lee, et al., Perfusion MR imaging in gliomas: comparison with histologic tumor grade, *Korean J. Radiol.* 2 (1) (2001) 1–7, 2001.
- [68] T. Sugahara, et al., Correlation of MR imaging-determined cerebral blood volume maps with histologic and angiographic determination of vascularity of gliomas, *AJR Am. J. Roentgenol.* 171 (6) (1998) 1479–1486. Dec.
- [69] M. Law, et al., High cerebral blood volume in human gliomas predicts deletion of chromosome 1p: preliminary results of molecular studies in gliomas with elevated perfusion, *J. Magn. Reson. Imaging* 25 (6) (2007) 1113–1119. Jun.

Article

Interstitial Photodynamic Therapy Using 5-ALA for Malignant Glioma Recurrences

Stefanie Lietke ^{1,2,†} , Michael Schmutzer ^{1,2,†} , Christoph Schwartz ^{1,3}, Jonathan Weller ^{1,2} , Sebastian Siller ^{1,2} , Maximilian Aumiller ^{4,5} , Christian Heckl ^{4,5} , Robert Forbrig ⁶, Maximilian Niyazi ^{2,7}, Rupert Egensperger ⁸, Herbert Stepp ^{4,5} , Ronald Sroka ^{4,5} , Jörg-Christian Tonn ^{1,2}, Adrian Rühm ^{4,5,‡} and Niklas Thon ^{1,2,*,‡}

¹ Department of Neurosurgery, University Hospital, LMU Munich, 81377 Munich, Germany

² German Cancer Consortium (DKTK), Partner Site Munich, 81377 Munich, Germany

³ Department of Neurosurgery, University Hospital Salzburg, Paracelsus Medical University Salzburg, 5020 Salzburg, Austria

⁴ Laser-Forschungslabor, LIFE Center, University Hospital, LMU Munich, 81377 Munich, Germany

⁵ Department of Urology, University Hospital, LMU Munich, 81377 Munich, Germany

⁶ Institute for Clinical Neuroradiology, University Hospital, LMU Munich, 81377 Munich, Germany

⁷ Department of Radiation Oncology, University Hospital, LMU Munich, 81377 Munich, Germany

⁸ Center for Neuropathology and Prion Research, University Hospital, LMU Munich, 81377 Munich, Germany

* Correspondence: niklas.thon@med.uni-muenchen.de; Tel.: +49-89-4400-0

† Both authors contributed equally.

‡ This study is guided by AR and NT equally thus both serve as shared last authors.



Citation: Lietke, S.; Schmutzer, M.; Schwartz, C.; Weller, J.; Siller, S.; Aumiller, M.; Heckl, C.; Forbrig, R.; Niyazi, M.; Egensperger, R.; et al. Interstitial Photodynamic Therapy Using 5-ALA for Malignant Glioma Recurrences. *Cancers* **2021**, *13*, 1767. <https://doi.org/10.3390/cancers13081767>

Academic Editors: Giuseppe Lombardi, Emilie Le Rhun, Ahmed Idbaih, Matthias Preusser and Pim French

Received: 23 February 2021

Accepted: 29 March 2021

Published: 7 April 2021

Publisher's Note: MDPI stays neutral with regard to jurisdictional claims in published maps and institutional affiliations.



Copyright: © 2021 by the authors. Licensee MDPI, Basel, Switzerland. This article is an open access article distributed under the terms and conditions of the Creative Commons Attribution (CC BY) license (<https://creativecommons.org/licenses/by/4.0/>).

Simple Summary: Malignant glioma has a poor prognosis, especially in recurrent situations. Interstitial photodynamic therapy (iPDT) uses light delivered by implanted light-diffusing fibers to activate a photosensitizing agent to induce tumor cell death. This study examined iPDT for the treatment of malignant glioma recurrences. Forty-four patients treated at one institution were retrospectively analyzed and patient-, tumor- and treatment-related factors were retrieved from hospital charts. Most of the patients (37) had glioblastomas, the most aggressive type of glioma. Brain swelling or small bleedings caused worsening of symptoms in 18 patients, but only in one case severe symptoms persisted for more than six weeks. After iPDT, tumors recurred after a median of 7.1 months and patients lived for a median of 13.0 months. Two years after iPDT treatment, 25% of the patients were still alive. These promising results should be evaluated further in a prospective study.

Abstract: Interstitial photodynamic therapy (iPDT) using 5-aminolevulinic acid (5-ALA)-induced protoporphyrin IX (PpIX) as a cytotoxic photosensitizer could be a feasible treatment option for malignant gliomas. In a monocentric cohort of consecutive patients treated between 2006 and 2018, a risk profile analysis of salvage iPDT for local malignant glioma recurrences and associated outcome measures are presented here. It was considered indicated in patients with circumscribed biopsy-proven malignant glioma recurrences after standard therapy, if not deemed eligible for safe complete resection. A 3D treatment-planning software was used to determine the number and suitable positions of the cylindrical diffusing fibers placed stereotactically to ensure optimal interstitial irradiation of the target volume. Outcome measurements included the risk profile of the procedure, estimated time-to-treatment-failure (TTF), post-recurrence survival (PRS) and prognostic factors. Forty-seven patients were treated, of which 44 (median age, 49.4 years, range, 33.4–87.0 years, 27 males) could be retrospectively evaluated. Recurrent gliomas included 37 glioblastomas (WHO grade IV) and 7 anaplastic astrocytomas (WHO grade III). Thirty (68.2%) tumors were O-6-methylguanine-DNA methyltransferase (MGMT)-methylated, 29 (65.9%)—isocitrate dehydrogenase (IDH)—wildtype. Twenty-six (59.1%) patients were treated for their first, 9 (20.5%)—for their second, 9 (20.5%)—for the third or further recurrence. The median iPDT target volume was 3.34 cm³ (range, 0.50–22.8 cm³). Severe neurologic deterioration lasted for more than six weeks in one patient only. The median TTF was 7.1 (95% confidence interval (CI), 4.4–9.8) months and the median PRS was 13.0 (95% CI, 9.2–16.8) months. The 2- and 5-year PRS rates were 25.0% and 4.5%, respectively. The treatment response was heterogeneous and not significantly associated with patient characteristics,

treatment-related factors or molecular markers. The promising outcome and acceptable risk profile deserve further prospective evaluation particularly to identify mechanisms and prognostic factors of favorable treatment response.

Keywords: malignant glioma; glioblastoma; recurrence; photodynamic therapy; 5-ALA; stereotactic surgery; outcome

1. Introduction

Despite recent advances in the treatment of malignant glioma, prognosis remains poor with a median overall survival (OS) of less than two years in IDH-wildtype glioblastomas [1,2]. Upon inevitable tumor recurrence, median post-recurrence survival (PRS) is limited to 7–12 months in most recent studies [3–12]. Salvage treatment options include resurgery, reirradiation protocols, chemotherapy and any combination thereof. Each of these treatment options offers specific advantages and limitations. While salvage surgery can be of advantage in selected cases, only complete resection of the contrast-enhancing tumor mass seems to prolong post-recurrence survival [10,13–15]. In the case of eloquent, diffuse and/or multifocal tumor recurrences, reirradiation and/or second-line chemotherapy regimens may be preferable [16,17]. No randomized controlled study, however, has been able to show a relevant survival benefit for any of the treatment regimens tested [18–25]. This also concerns the use of recently introduced tumor-treating fields [6] and some early results from immunotherapy [26]. Accordingly, no standard treatment for progressive/recurrent malignant gliomas exists, and therefore, management has to be optimally tailored to the individual patient [27].

Photodynamic therapy (PDT) has been introduced as a local surgical treatment option which is based on cytotoxic effects induced by a photosensitizing agent that is accumulated within malignant glioma tissue and activated by light of an appropriate wavelength [28]. PDT for malignant glioma was developed alongside fluorescence-guided resection with 5-aminolevulinic acid (5-ALA) [29] which provides highly tumor-specific fluorescence in combination with minimal side effects: in an approval study [29] as well as in a more recent assessment [30], safety concerns with respect to drug application or morbidity caused by fluorescence-guided resection did not exceed the ones of standard surgery. PDT can be applied as surface PDT within a resection cavity [31–33]. At our institution, PDT is applied as interstitial PDT (iPDT) by cylindrical diffusing fibers that are stereotactically inserted to ensure a spatially precise interstitial irradiation of the target tumor volume. In a former iPDT series of 10 patients with local recurrence of a malignant glioma after multimodal therapy, we demonstrated the feasibility and tolerability of iPDT [28]. In addition, cases of remarkably long tumor control have been observed [34]. Here, results of salvage iPDT of patients ($N = 44$) suffering from local malignant glioma recurrences after standard therapy are presented. Special attention is given to the risk profile of iPDT and associated outcome parameters in this selected patient cohort.

2. Patients and Methods

2.1. Patient Selection

At our institution, salvage iPDT was considered in adult patients with a Karnofsky performance score (KPS) of at least 70 who presented with a unifocal circumscribed malignant glioma recurrence after standard multimodal therapy. Local tumor recurrence or progressive disease as suspected by contemporary measurements [35,36] must not exceed a maximum extension of 3 cm defined by the contrast-enhancing tumor volume in gadolinium T1-weighted magnetic resonance imaging (MRI). As part of clinical routine, viable tumor tissue was always histologically verified upfront by minimally invasive stereotactic biopsy procedures [37] to exclude treatment-associated effects or pseudoprogression. Use of iPDT was considered indicated in consensus by the neurooncological tumor board when

other local therapy options such as (re-)resection or (re-)radiotherapy alone were deemed not to be safely feasible or refused by the patient who qualified for novel experimental treatment options.

For this single-center retrospective analysis, all 47 consecutive patients who underwent salvage iPDT for malignant glioma recurrences between 2006 and 2018 were included. In three patients, however, no follow-up data were available. All patients provided written informed consent to treatment. This retrospective investigation was approved by the ethics committee of the Ludwig Maximilian University, Munich, Germany (reference number 19–650).

2.2. Magnetic Resonance Imaging Protocol

Magnetic resonance imaging always included three-dimensional gadolinium-enhanced T1- (1 mm slices) and T2-weighted (2 mm slices) scans preoperatively and thereafter. Early postoperative MRI was routinely performed within 48 h after iPDT treatment and additionally included diffusion-weighted imaging (DWI) and apparent diffusion coefficient (ADC) to assess early treatment effects.

2.3. Neuropathological Analysis

Neuropathological diagnosis of tumor recurrence was performed according to the respective valid WHO classification from the years 2007 and 2016 [38,39]. After 2009, pyrosequencing was performed routinely to determine isocitrate dehydrogenase (IDH) mutational status and microsatellite analysis for 1 p/19 q codeletion status. In all patients for whom materials were available, IDH mutations were analyzed retrospectively. O-6-methylguanine-DNA methyltransferase (MGMT) promoter methylation was analyzed by methylation-specific PCR and sequencing.

2.4. Interstitial PDT Protocol

Interstitial illumination was performed using a diode laser (Ceralas Diode Laser, Biolitec AG, Jena, Germany) and cylindrical diffusing fibers as described before [25]. The target volume was defined after multimodal image fusion of the intraoperative stereotactic CT (contrast-enhanced scans, 0.6 mm axial slices) with the preoperative MRI and, if available, O-(2-[¹⁸F]fluoroethyl)-L-tyrosine (18F-FET)-PET scan. A spatially precise interstitial irradiation of the individual tumor volumes was planned using the @target 1.19 software (Brainlab, Munich, Germany) [29].

The patients were administered 20 mg/kg body weight of 5-ALA three to five hours before the start of iPDT illumination. Depending on tumor geometry, cylindrical diffusing fibers with an active diffuser length of, optionally, 20 mm or 30 mm were selected. The fibers had an outer diameter of 1600 µm (CeramOptec GmbH, Bonn, Germany) (first 26 treatments) and 1560 µm (Light Guide Optics, Rheinbach, Germany) (last 18 treatments), respectively. The fibers were stereotactically inserted with 6 to 12 mm interfiber distances using a modified Riechert stereotactic frame system (Medical High Tech GmbH, Bad-Krozingen-Biengen, Germany). Prior to fiber placement, a mandrin was inserted into the brain along the trajectory to the target to prepare a channel for the fibers and to serve as a reference for an accurate implantation procedure by means of an orthogonal C-arm X-ray evaluation (Siemens Healthineers, Erlangen, Germany). Correct positioning of the light diffusers within the target volume was then ensured using metallic X-ray markers integrated at the distal and proximal ends of the active segment of the cylindrical diffusing fibers. During therapy, patients received mechanical ventilation with 100% oxygen to ensure adequate oxygen supply for the production of free radicals. Interstitial PDT irradiation was performed with a laser light of 635 nm wavelength at the illumination power of 200 mW/cm diffuser length for a treatment time of 60 min. In cases where the treatment plan resulted in small interfiber distances, the illumination power was decreased and the illumination time was prolonged. Illumination was stopped after the scheduled time if no residual fluorescence was observed. Intraoperative spectral online monitoring

was performed prior to and after iPDT illumination as described previously [33,40]. In brief, one after the other, each cylindrical diffusing fiber was used as an emitter, while each of the other fibers sequentially served as an optical detection probe connected to a spectrometer (S2000 or USB2000+, Ocean Optics/Ocean Insight, Ostfildern, Germany) measuring the detected light in the wavelength range of 550 nm to 800 nm. After iPDT irradiation, the cylindrical diffusing fibers were removed.

2.5. Spectral Online Monitoring Analysis

The acquired spectral online monitoring data were analyzed for detectable transmitted treatment light at 635 ± 3 nm and protoporphyrin IX (PpIX) fluorescence signals at 705 ± 3 nm. To distinguish between signal artifacts and the true signal, a signal threshold of three times the signal-to-noise ratio was assumed. In addition, only fiber pairs less than 19 mm apart were used for spectral analyses. If at least 75% of all transmission or fluorescence signals of a patient showed a true signal, the patient was graded as good, otherwise—as poor.

2.6. Perioperative Management and Risk Assessment of iPDT

All iPDT procedures were performed under general anesthesia. In order not to inhibit antitumor immunological effects, no cortisone was administered peri- and postoperatively except in case of uncontrolled edema causing severe neurological deterioration.

Any perioperative sequelae resolving within six weeks were considered transient, all others—as permanent complications of this kind of iPDT treatment. Severity was classified according to the Common Terminology Criteria for Adverse Events Version 5 (CTCAE) [41].

2.7. Treatment after iPDT and Follow-Up Evaluation

The decision to perform iPDT as standalone treatment or in combination with additional salvage treatment was made individually by the interdisciplinary neurooncological tumor board considering each patient's risk profile, previous therapies, as well as molecular tumor characteristics.

Patients were followed in the outpatient clinic for six weeks after therapy and in three-month intervals thereafter. Radiologic tumor recurrence was defined according to MacDonald or after the response assessment in neuro-oncology (RANO) 2010 criteria [35,36]. Once validated FET-PET data had become available [42,43], FET-PET examination was used, partially in combination with rebiopsy, to rule out pseudoprogression in unclear non-palliative cases.

2.8. Statistical Evaluation

The reference point for overall survival (OS) was the date of the initial tumor diagnosis. Time-to-treatment failure (TTF) and post-recurrence survival (PRS) were calculated from the date of iPDT. Patients had been followed until the last patient died. The distribution of continuous (categorical) variables was analyzed by means of the Wilcoxon test (X^2 statistics). Survival was analyzed with the Kaplan–Meier method. A Cox proportional hazards model was used to identify epidemiologic and molecular prognostic factors. Differences between responders and non-responders were analyzed using logistic regression models. The complete statistical analysis was performed with the use of SPSS Statistics 25 (IBM, Armonk, New York, USA). The significance level was set to $p \leq 0.05$.

3. Results

3.1. Patient Characteristics

This study included 44 patients (27 (61.4%) males) (Table 1) between 2006 and 2018. The median age at the time of iPDT was 49.4 years (range, 33.4–87.0 years) and the median KPS was 90 (range, 70–100) (Table 1). The median time between initial tumor diagnosis and salvage iPDT was 16.9 months (range, 3.5–192.4 months). Twenty-six (59.1%) patients were treated for their first, 9 (20.5%)—for their second, 9 (20.5%)—for the third or

further recurrence. Thirty-six (81.8%) patients had undergone open tumor resection, 43 (97.7%) patients had been treated with percutaneous irradiation and 39 (88.6%)—with chemotherapy before salvage iPDT for circumscribed tumor recurrences was considered. At the time of salvage iPDT, 37 (84.1%) of the recurrent tumors were classified as WHO grade IV glioblastomas, 7 (15.9%)—as WHO grade III anaplastic astrocytomas. Six (13.6%) patients suffered from a malignant transformation of an initially diagnosed WHO grade II diffuse astrocytoma. Twenty-nine (65.9%) of the tumors were IDH-wildtype tumors, 9 (20.5%) had an IDH mutation. For six patients, residual tumor material was insufficient for retrospective analysis of the IDH status. A methylated MGMT promoter status was recorded for 30 (68.2%) tumors as part of the integrated histopathological diagnosis.

Table 1. Summary of patients' characteristics.

Characteristics at iPDT	All Patients (N = 44)
Age (years)	
Median	49.4
Range	33.4–87.0
Gender, n (%)	
Male	27 (61.4)
Female	17 (38.6)
KPS, n (%)	
100	3 (6.8)
90	29 (65.9)
80	9 (20.5)
70	3 (6.8)
Symptoms, n (%)	
Seizures	27 (61.4)
Aphasia without paresis	12 (27.3)
Paresis without aphasia	4 (9.1)
Aphasia and paresis	1 (2.3) ¹
Side, n (%)	
Right	20 (45.5)
Left	24 (54.5)
Localization, n (%)	
Deep-seated involvement	31 (70.5)
Eloquent lobar localization	17 (38.6)
Stage of disease, n (%)	
First tumor recurrence	26 (59.1)
Second tumor recurrence	9 (20.5)
Third tumor recurrence	6 (13.6)
Later stages	3 (6.8)
WHO grade, n (%)	
IV	37 (84.1)
III	7 (15.9)

Table 1. Cont.

Characteristics at iPDT	All Patients (N = 44)
WHO grade at initial diagnosis, n (%)	
IV	30 (68.2)
III	8 (18.2)
II	6 (13.6)
MGMT promoter methylation status, n (%)	
Methylated	30 (68.2)
Unmethylated	14 (31.8)
IDH mutation, n (%)	
Wildtype	29 (65.9)
Mutated	9 (20.5)
Unknown (no material left)	6 (13.6)
1 p/19 q codeletion, n (%)	
1 p/19 q codeletion	1 (2.3)
No 1 p/19 q codeletion	20 (45.5)
Not tested	23 (52.3)

¹ Percentages may not total 100.0 due to rounding.

3.2. Interstitial PDT Treatment

The median iPDT target volume was 3.34 cm³ (range, 0.50–22.8 cm³), targeted with a median of 4 (range, 3–8) cylindrical diffusing fibers (Table 2). The minimum irradiation time of 60 min (range, 60–167 min) was received by 29 patients. The median applied light power per cm diffuser length was 200 mW (range, 82–210 mW). The median energy dose applied during iPDT illumination was 8996 J (range, 5760–17,388 J), largely depending on the iPDT target volume and the corresponding adapted number of cylindrical diffusing fibers.

Table 2. Treatment characteristics.

Treatment Algorithms	All Patients (N = 44)
Treatment before iPDT, n (%)	
Tumor resection	36 (81.9)
Irradiation	43 (97.7)
Chemotherapy	39 (88.6)
Interstitial PDT characteristics	
Target volume (cm ³)	
Median	3.34
Range	0.50–22.8
Number of cylindrical diffusing fibers (range)	4 (3–8)
Applied light power per diffuser length (mW/cm)	
Median	200
Range	82–210
Treatment dose (J)	
Median	8883
Range	5760–17,388
Treatment time (minutes)	
Median	60 (N = 29)
Range	60–167
Salvage treatment with iPDT, n (%)	
Chemotherapy	20 (45.4)
Radiotherapy	7 (15.9)
Radiochemotherapy	4 (9.1)
Treatment after iPDT failure, n (%)	
Any chemotherapy	31 (70.5)
Any (re-)radiotherapy	20 (45.5)
Any tumor resection/debulking	4 (9.1)

The bold cells are sub-headlines.

3.3. Imaging after iPDT

Early postoperative imaging within 48 h after iPDT showed a decrease or effacement of contrast enhancement in all cases. Typically, diffusion restriction occurred in the treated area (Figure 1). A transient increase in edema surrounding the tumor treatment volume was seen in 12 cases, six of which caused transient neurological deterioration (two—paresis, four—aphasia).

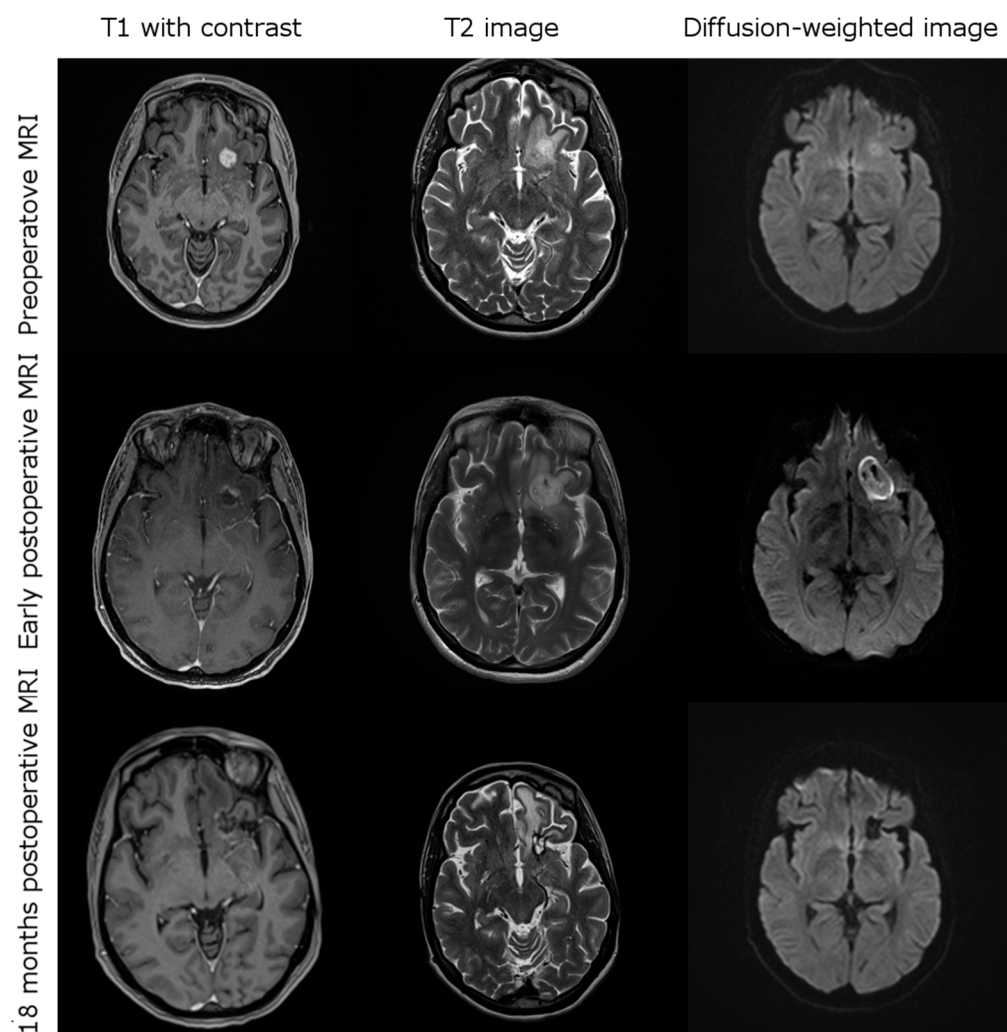


Figure 1. Exemplary case of a 41-year-old female patient suffering from a left frontal glioblastoma recurrence causing mild aphasia. Post-iPDT MRI showing characteristic changes such as disappearance of contrast enhancement, diffusion restriction within the treatment volume and mild perifocal edema. Peri-interventionally, there was transient worsening of aphasia, which then resolved completely in subsequent weeks.

3.4. Complications after iPDT

Complications after iPDT are listed in Table 3. Overall, 18 patients (40.0%) experienced transient worsening of the usually preexistent neurological deficits, i.e., mainly incomplete aphasia and/or hemiparesis. One patient developed malignant edema and underwent emergency decompression within 24 h after iPDT treatment. In this case, only slight word-finding difficulties (CTCAE °2) persisted. After six weeks, most deficits resolved or would not inhibit activities of daily life ($N = 9$, CTCAE °1). Three patients (6.8%) suffered from residual deficits; in one case, self-care was affected (CTCAE °3). Postoperative complications were not found to correlate with the patients' TTF ($p = 0.841$) and PRS ($p = 0.492$).

Table 3. Complications after iPDT.

Complications after iPDT	All Patients (N = 44)
Postoperative CTCAE grade, N (%)	
0	26 (59.1)
1	4 (9.1)
2	10 (22.7)
3	3 (6.8)
4	1 (2.3)
5	0 (0.0)
CTCAE grade at six weeks, N (%)	
0	32 (72.7)
1	9 (20.5)
2	2 (4.5)
3	1 (2.3)
4	0 (0.0)
5	0 (0.0)
Type of complications, N (%)	
Aphasia	7 (15.9)
Paresis	6 (13.6)
Paresis and aphasia	4 (9.1)
Hyp-/dysaesthesia only	1 (2.3)
None	26 (59.1)

The bold cells are sub-headlines.

3.5. Treatment after iPDT

As part of a predefined combined treatment algorithm, iPDT was immediately followed by chemotherapy in 20 cases (45.5%; temozolomide, $N = 14$, 31.8%; procarbazine/lomustine, $N = 6$, 13.6%) and by re-radiotherapy with/without chemotherapy in 11 (25.0%) cases (Table 2). At the time of tumor progression after iPDT treatment, all patients were found eligible for additional multimodal treatment (31 (70.5%) patients were treated with chemotherapy, 20 (45.5%) received re-radiotherapy and 4 (9.1%) underwent open tumor debulking for space-occupying recurrences before salvage chemotherapy was initiated). No immediately palliative case (usually confined to best supportive care only) was observed. Patients with MGMT-methylated tumors did not receive more or less often radiotherapy ($p = 0.81$) or chemotherapy ($p = 0.92$) in the further course of their disease.

3.6. Outcome

The median follow-up duration was 13.0 months (range, 4.7–105.6 months). In three patients, however, no follow-up data were available. Within their individual follow-up duration, all the remaining patients experienced tumor progression and died, with all recorded deaths being tumor-related. Here, the median OS from the first tumor diagnosis was 39.7 months (range, 9.8–199.0 months). The median time between the first diagnosis and salvage iPDT was 16.9 months (range, 3.5–192.4 months), median TTF after iPDT was 7.1 months (range, 0.6–93.9 months; 95% confidence interval (CI), 4.4–9.8) and median PRS was 13.0 months (range, 4.7–105.6 months; CI, 9.2–16.8) (Figure 2). When the three patients lost to follow-up were also included in the analysis (as part of the intended-to-treat population), median TTF was 6.8 months and mean PRS was 12.5 months (Supplementary Figure S1). As can be derived from Figure 2, six- and twelve-months recurrence-free survival rates after salvage iPDT were 59.1% and 34.1%, respectively. Six- and twelve-months survival rates after iPDT were 88.6% and 63.6%, respectively. Two years after iPDT treatment, eleven (25.0%) patients were alive, seven (15.9%) of them recurrence-free.

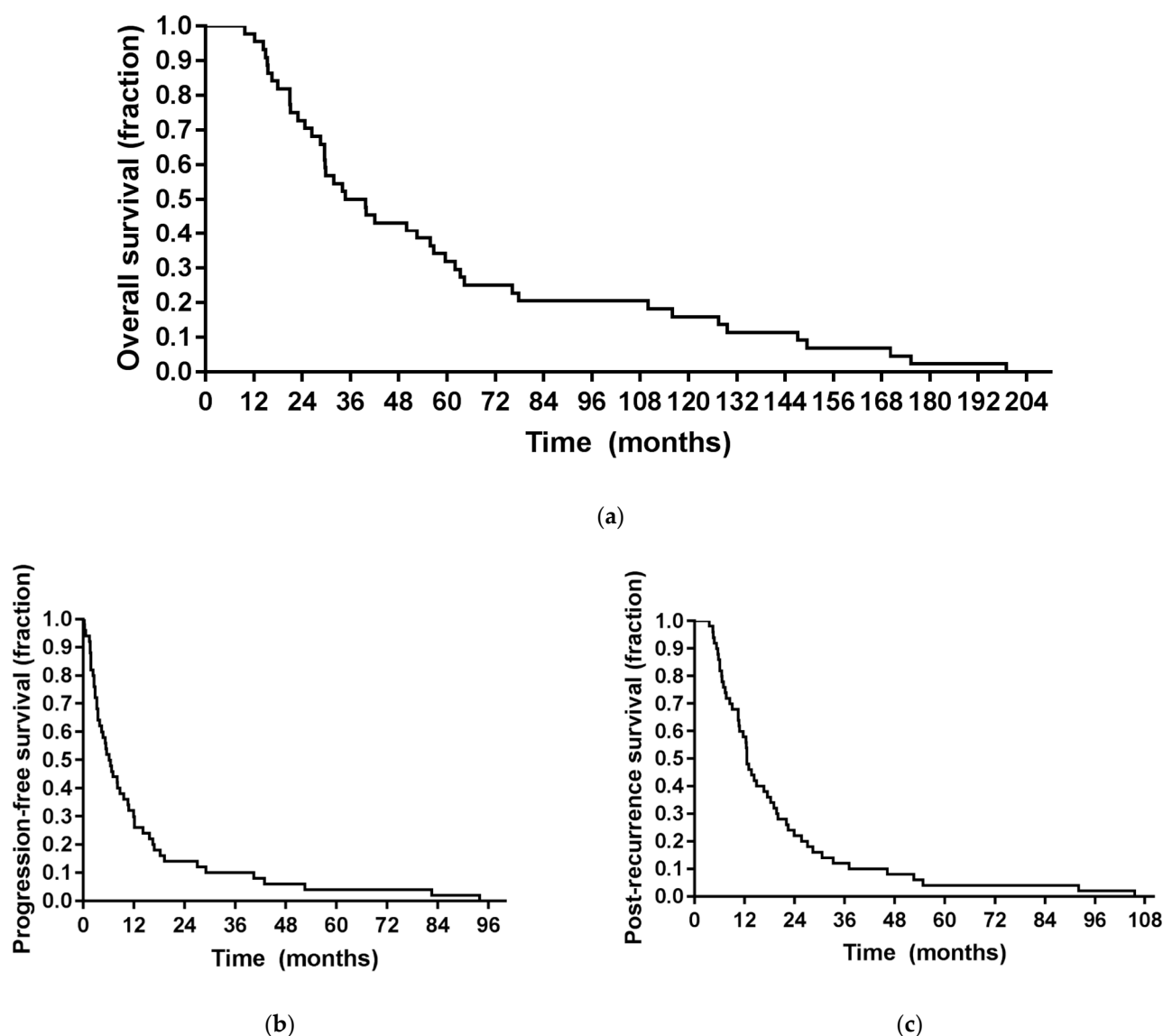


Figure 2. Survival curves. (a) Overall survival of the study population after initial tumor diagnosis; (b) time-to-treatment failure (TTF) of the study population after iPDT treatment; (c) post-recurrence survival (PRS) of the study population after iPDT treatment.

3.7. Prognostic Factors

In Table 4, the correlations of prognostic factors with regard to PRS after iPDT are summarized. Univariate analysis showed a significant influence of KPS on PRS ($p = 0.019$). No significant influence of age, MGMT promoter methylation or IDH mutational status, target volume, time to iPDT treatment or any salvage treatment modality on PRS could be found. Time between initial diagnosis and iPDT did not correlate with PRS (Pearson's coefficient, -0.112 , $p = 0.469$) or TTF (Pearson's coefficient, -0.169 , $p = 0.274$). No salvage treatment regimen was associated with an additional survival benefit, neither in the complete study cohort nor in the subgroup of patients with a methylated MGMT promoter sequence. No known prognostic factor was found to correlate with TTF (Supplementary Table S1). FET-PET imaging before treatment was available for 12 patients (median maximum Standardized Uptake Value (SUVmax), 2.95, range, 2.2–8.2) and after treatment for 15 patients (median SUVmax, 2.7, range, 1.5–7.4). Post-therapeutic decrease in SUVmax was associated with longer TTF ($p = 0.081$).

Table 4. Prognostic factors for PRS after iPDT in uni- and multivariate models; HR—hazard ratio, CI—confidence interval.

Characteristic	HR	Univariate 95% CI	p-Value	HR	Multivariate 95% CI	p-Value
Post-recurrence survival (after iPDT)						
Age at iPDT	1.006	0.981–1.033	0.635	1.023	0.968–1.080	0.424
KPS at iPDT	0.936	0.886–0.989	0.019	1.961	0.755–5.092	0.167
MGMT methylation	0.751	0.392–1.438	0.388	1.000	0.339–2.946	1.000
IDH mutation	0.878	0.405–1.904	0.742	1.018	0.326–3.178	0.976
Target volume	1.019	0.956–1.086	0.557	1.017	0.943–1.096	0.666
Time to iPDT	1.003	0.996–1.010	0.392	1.003	0.992–1.015	0.553
Further chemotherapy	0.811	0.421–1.561	0.530	1.030	0.443–2.392	0.946
Further radiotherapy	0.999	0.540–1.849	0.999	1.005	0.317–3.189	0.994
Further surgery	0.782	0.276–2.212	0.643	1.303	0.258–6.568	0.748

The bold cells are sub-headlines.

3.8. Intraoperative Spectral Online Monitoring

Intraoperative transmission and fluorescence data could be evaluated for 18 patients. A total of 300 pre- and postoperative spectra each were analyzed, with one spectrum recorded for each possible fiber pair. The median number of spectra per patient was 24 (range, 12–84). Overall, insufficient postoperative transmission was detected in 21.7% of the spectra and preoperative fluorescence in 15.8%. Of the 18 patients, 13 (72.2%) showed good postoperative transmission rates between two fibers (of 75% or more), indicating sufficient illumination over the complete duration of treatment. Ten (55.6%) also showed PpIX fluorescence over a threshold of 75%. In three (16.7%) cases, only preoperative fluorescence was graded as good, but not the postoperative transmission. In all patients, no residual PpIX fluorescence could be detected after the iPDT. Good postoperative transmission and preoperative fluorescence were associated with longer TTF and PRS, although the differences were not highly significant (Table 5).

Table 5. Results of statistical tests of the association of intraoperative spectral online monitoring with time-to-treatment failure (TTF) and post-recurrence survival (PRS), including 95% confidence intervals (CI).

Spectral Data (N = 18)	Median TTF (CI) (Months)	p-Value	Median PRS (CI) (Months)	p-Value
Transmission < 75%	9.63 (.978; 18.28)	0.196	12.97 (12.03; 13.92)	0.130
Transmission > 75%	15.73 (4.71; 24.96))		19.70 (4.32; 35.08)	
Fluorescence < 75%	9.63 (4.20; 15.06)	0.427	16.57 (7.83; 25.31)	0.326
Fluorescence > 75%	12.13 (3.84; 20.42)		17.47 (4.20; 30.74)	

4. Discussion

This study's main findings are: (1) iPDT was technically feasible in all patients; (2) iPDT can be performed with acceptable risk even in highly eloquent tumor localizations; (3) iPDT appears to be associated with favorable treatment effects even in heavily pretreated malignant glioma recurrences; (4) iPDT as part of a salvage treatment concept is associated with considerable long-term survival (PRS > 2 years) in a—so far—poorly defined subpopulation of malignant glioma patients; (5) treatment success was not associated with any of the known conventional and molecular prognostic factors of malignant gliomas.

Interstitial PDT is a technically demanding form of local treatment that is used for various tumor diseases [44]. Malignant glioma cells are characterized by a selective and effective uptake of systematically administered 5-ALA with subsequent intracellular conversion into the red fluorescent, phototoxic PpIX by exploiting the enzymatic machinery of heme synthesis [45]. As a photosensitizer, PpIX mediates energy transfer from light photons to oxygen molecules to generate reactive oxygen species that lead to oxidation and destruction of membranes, proteins and other vital intracellular structures [46,47].

Some of the cell death mechanisms initiated in this manner effectively stimulate the immune response, adding an intriguing systemic effect to this otherwise local treatment modality [48,49].

These characteristics of 5-ALA in combination with the possibility of a spatially precise interstitial illumination by means of a stereotactic frame-based installation of the respective light diffusers make iPDT an attractive tool for local malignant glioma recurrences after standard therapy. This minimally invasive procedure might be of advantage over the technical alternative of a surface PDT, in which an illumination source is introduced directly into the resection cavity at the end of surgery to illuminate any residual tumor tissue. The disadvantage of this method is that the extent of the residual tumor tissue cannot be determined with certainty and the penetration depth of illumination is limited to a few millimeters. However, since a spatially precise illumination of the target tumor volume seems to be fundamental to achieve full treatment effects, the image-guided stereotactic iPDT may be preferred. Moreover, iPDT is not limited to resectable tumors. Only few centers, however, have gained some preliminary clinical experience with iPDT in malignant brain tumors so far (yet unpublished personal communications). To date, just one prospective study has been published which suggested 5-ALA-based iPDT to be safe and feasible for a selected patient population with glioblastoma recurrences [28]. No permanent procedure-related morbidity was seen in the 10 patients treated and select patients survived surprisingly long, possibly thanks to immunological effects known from PDT treatment [50].

This manuscript presents clinical experiences in a large cohort of 44 multimodally pretreated patients who underwent iPDT for small, unifocal and circumscribed malignant glioma recurrences with a maximum extension of 3 cm. This size limitation was based on the maximum number of light fibers per laser and the experimental data, which have shown optimal spacing of light diffusers of about 7–9 mm for accurate tissue illumination without causing critical thermal effects [28].

Based upon intense interdisciplinary and collaborative efforts, dedicated equipment had been made available so that treatment planning, diffusing fiber insertion and light application were technically feasible in all intended cases. By means of the intraoperative spectral online monitoring technique, transmission of treatment light between fibers and PpIX fluorescence light could be monitored. During most treatments, PpIX fluorescence was characterized as good before starting the illumination and vanished during irradiation, which, at least in cases with good postoperative light transmission grading, indicates substantial consumption of PpIX as expected due to photobleaching of this photosensitizer. The technique of spectral online monitoring seems to be a promising tool to monitor 5-ALA administration, PpIX accumulation and fiber placement and potentially to estimate treatment effectiveness. In addition, it was observed that the portion of spectral data indicating good treatment light transmission decreased during treatment. This can be used as an indicator that optical tissue properties change such that the light penetration depth is reduced during iPDT illumination, commonly leading to partial and, in some cases, complete transmission signal loss. The reasons for these changes in the *in vivo* situation have not yet been investigated and understood in detail. However, this observation is in accordance with a previous study [51], where a reduction of treatment light transmission during iPDT was already reported.

Transient clinical deterioration was recorded in about 40% of patients and was mainly due to exaggerated edema and/or some hemorrhagic imbibition. The latter observations could not be attributed to direct interference of individual catheter trajectories with intratumoral vascular structures.

Only one patient experienced a grade 3 neurological deterioration persisting for more than six weeks. In this retrospective iPDT study, symptoms usually resolved within six weeks after iPDT even without steroid treatment, which was held back so as not to impede possible immunological effects. The development of perioperative complications was independent of the density of previous tumor treatments, tumor volume and the number

of laser fibers implanted. This may be due to the limitation to tumors not exceeding 3 cm in extension suggested by earlier studies [33].

Comparison of these complication rates to those reported after other local treatments is challenging because of differences in patient selection, especially regarding tumor size and potentially eloquent location. In the *de novo* unselected setting, the current gold standard local treatment, fluorescence-guided resection, has reported adverse events in about 40% of the cases, with grade 3 or worse aphasia in up to 6% and hemiparesis in up to 4% of the treatments [52]. For resection in eloquent location, neurological deterioration in up to 60% of the treatments has been reported [53]. In the recurrent setting, complication rates for open resection have been suggested to even increase sequentially in each recurrence situation [54,55]. As an adjunct or alternative to resection, re-radiotherapy (with/without bevacizumab) emerged as an increasingly used salvage treatment option after 2011. Notably, toxicity rates of grade III or higher aphasia have been described in between 4% [56] and 32% [57] of the treatments. In summary, in an often multimodally pretreated and symptomatic patient population, any local treatment is associated with an increased risk of at least transient morbidity.

The observed median PRS of 13.0 months is in the upper range of the median PRS originated by other treatment modalities, ranging mostly between seven and nine months [17]. In the DIRECTOR study where first glioblastoma recurrences were treated with different temozolomide dose regimens, PRS ranged between 7.9 months for MGMT-unmethylated and 12.5 months for MGMT-methylated tumors [58]. In that cohort, complete resection of contrast enhancement was associated with a more favorable PRS of 12.9 months, compared to incomplete resection (PRS, 6.5 months) and no resection (PRS, 9.8 months), indicating, like the present study, a benefit of local treatment if possible [10].

In the present iPDT cohort, no influence of molecular markers such as MGMT and IDH on response to iPDT with or without adjuvant therapy including temozolomide can be observed. Different numbers and types of pretreatments and a heterogeneous patient population may explain the lack of an observable effect or a still too low total number of cases, as other studies also did not uniformly observe a prognostic effect of MGMT promoter methylation or lack thereof in recurrent situations [58,59]. Due to different treatment groups in different studies, a direct meaningful comparison of outcome data is rather difficult. Interestingly, though, more than 20% of patients in the iPDT series survived more than two years after malignant glioma recurrence irrespective of time to PDT and later salvage treatments and even with MGMT-unmethylated primary glioblastomas. This high percentage of long-term survivors warrants further investigation. As shown, common prognostic factors in malignant glioma patients did not differ between long-term and short-term survivors in this cohort, based on a threshold PRS of two years. Possibly, immunological factors may play a role, as has been suggested in experimental settings [60,61]. One of the key factors stimulating the immune response may be the heat shock protein HSP-70 as it was shown that sublethal 5-ALA PDT upregulated HSP-70 by up to 50-fold in glioma cells [49]. The upregulation of HSP-70 and the fact that 5-ALA PDT on glioma spheroids attracted and matured coincubated dendritic cells was experimentally confirmed [62]. The cell death mechanisms glioblastoma cells in a patient treated with iPDT undergo are expected to be very heterogeneous, as both light distribution and photosensitizer distribution are not homogenous. Therefore, parts of the tumor may undergo direct necrosis, others—apoptotic cell death and some cells in the periphery may survive. However, the plethora of cell death mechanisms initiated may be advantageous for an efficient stimulation of immune response with presentation of damage-associated molecular patterns, production of inflammatory cytokines such as interleukin 6 and attraction and maturation of dendritic cells, altogether leading to recruitment of effector T cells as reviewed in [63]. These authors suggested a combined therapeutic approach of PDT with immune checkpoint blockade. Further research, especially into immunological processes surrounding glioblastoma treatment, is required to gain more detailed and specific knowledge to benefit most from iPDT.

In addition, standard MRI images after iPDT showed loss of contrast and FET enhancement and a change in the diffusion restriction precisely confined to the treatment volume. The interpretation of such findings with regard to mechanisms and clinical relevance will be addressed in future studies. Importantly, data interpretation in this study is not hampered by immunologically induced imaging effects as tumor recurrence was histologically verified in all non-palliative cases.

5. Conclusions

Interstitial PDT of gliomas remains a challenging procedure due to limited light penetration depth in brain tissue, a complex planning and implantation procedure and potential risk of clinical deterioration especially after treatment in eloquent areas. Nevertheless, in experienced hands, iPDT may be a promising treatment option in a high-risk patient population combining acceptable, mostly transient morbidity with the possibility of long-term survival. It does not critically interfere with but may rather complement other treatment options in the recurrent disease such as re-radiotherapy and/or salvage chemotherapy regimens. These data strongly support further investigation in a controlled prospective setting.

Supplementary Materials: The following are available online at <https://www.mdpi.com/article/10.3390/cancers13081767/s1>, Figure S1: Survival curves. (a) Overall survival of the intention to treat population after initial tumor diagnosis; (b) time-to-treatment failure (TTF) of the intention to treat population after iPDT treatment; (c) post-recurrence survival (PRS) of the intention to treat population after iPDT treatment; Table S1: Prognostic factors for TTF after iPDT in uni- and multivariate models HR—Hazard ratio, CI—confidence interval.

Author Contributions: Conceptualization, S.L., R.S., H.S., A.R. and N.T.; methodology, S.L., M.S. and M.A.; validation, C.S., J.W. and H.S.; formal analysis, S.L.; investigation, M.S., S.L.; resources, R.E., R.F.; data curation, M.S., S.L.; writing—original draft preparation, S.L., M.S. and M.A.; writing—review and editing, C.S., J.W., S.S., C.H., R.F., M.N., R.E., H.S., R.S., J.-C.T., A.R. and N.T.; visualization, S.L.; supervision, A.R., N.T. and R.S.; project administration A.R., N.T. and R.S.; funding acquisition, A.R., N.T. and R.S. All authors have read and agreed to the published version of the manuscript.

Funding: We thank the German Research Foundation (DFG) for financial support of the research training group (RTG) GRK2274.

Institutional Review Board Statement: The study was conducted according to the guidelines of the Declaration of Helsinki and approved by the Ethics Committee of Ludwig Maximilian University, Munich, Germany (reference number 19-650).

Informed Consent Statement: Informed consent was obtained from all subjects involved in the study.

Data Availability Statement: No new data were created or analyzed in this study. Data sharing is not applicable to this article.

Acknowledgments: We gratefully acknowledge Christoph Barth and Wolfgang Beyer for technical assistance.

Conflicts of Interest: The authors declare no conflict of interest. The funders had no role in the design of the study; in the collection, analyses, or interpretation of data; in the writing of the manuscript, or in the decision to publish the results.

References

1. Stupp, R.; Taillibert, S.; Kanner, A.A.; Kesari, S.; Steinberg, D.M.; Toms, S.A.; Taylor, L.P.; Lieberman, F.; Silvani, A.; Fink, K.L.; et al. Maintenance Therapy with Tumor-Treating Fields Plus Temozolomide vs Temozolomide Alone for Glioblastoma: A Randomized Clinical Trial. *JAMA* **2015**, *314*, 2535–2543. [\[CrossRef\]](#)
2. Stupp, R.; Taillibert, S.; Kanner, A.; Read, W.; Steinberg, D.M.; Lhermitte, B.; Toms, S.; Idhah, A.; Ahluwalia, M.S.; Fink, K.; et al. Effect of Tumor-Treating Fields Plus Maintenance Temozolomide vs Maintenance Temozolomide Alone on Survival in Patients with Glioblastoma: A Randomized Clinical Trial. *JAMA* **2017**, *318*, 2306–2316. [\[CrossRef\]](#)
3. Nam, J.Y.; Groot, J.F.D. Treatment of Glioblastoma. *J. Oncol. Pract.* **2017**, *13*, 629–638. [\[CrossRef\]](#) [\[PubMed\]](#)

4. Brada, M.; Hoang-Xuan, K.; Rampling, R.; Dietrich, P.Y.; Dirix, L.Y.; Macdonald, D.; Heimans, J.J.; Zonnenberg, B.A.; Bravo-Marques, J.M.; Henriksson, R.; et al. Multicenter phase II trial of temozolomide in patients with glioblastoma multiforme at first relapse. *Ann. Oncol.* **2001**, *12*, 259–266. [[CrossRef](#)] [[PubMed](#)]
5. Lombardi, G.; De Salvo, G.L.; Brandes, A.A.; Eoli, M.; Rudà, R.; Faedi, M.; Lolli, I.; Pace, A.; Daniele, B.; Pasqualetti, F.; et al. Regorafenib compared with lomustine in patients with relapsed glioblastoma (REGOMA): A multicentre, open-label, randomised, controlled, phase 2 trial. *Lancet Oncol.* **2019**, *20*, 110–119. [[CrossRef](#)]
6. Stupp, R.; Wong, E.T.; Kanner, A.A.; Steinberg, D.; Engelhard, H.; Heidecke, V.; Kirson, E.D.; Taillibert, S.; Liebermann, F.; Dbaly, V.; et al. NovoTTF-100A versus physician’s choice chemotherapy in recurrent glioblastoma: A randomised phase III trial of a novel treatment modality. *Eur. J. Cancer (Oxf. Engl. 1990)* **2012**, *48*, 2192–2202. [[CrossRef](#)]
7. Weller, M.; Le Rhun, E. How did lomustine become standard of care in recurrent glioblastoma? *Cancer Treat. Rev.* **2020**, *87*, 102029. [[CrossRef](#)]
8. Desjardins, A.; Gromeier, M.; Herndon, J.E., 2nd; Beaubier, N.; Bolognesi, D.P.; Friedman, A.H.; Friedman, H.S.; McSherry, F.; Muscat, A.M.; Nair, S.; et al. Recurrent Glioblastoma Treated with Recombinant Poliovirus. *N. Engl. J. Med.* **2018**, *379*, 150–161. [[CrossRef](#)] [[PubMed](#)]
9. Puduvalli, V.K.; Wu, J.; Yuan, Y.; Armstrong, T.S.; Vera, E.; Wu, J.; Xu, J.; Giglio, P.; Colman, H.; Walbert, T.; et al. A Bayesian Adaptive Randomized Phase II Multicenter Trial of Bevacizumab with or without Vorinostat in Adults with Recurrent Glioblastoma. *Neuro-Oncology* **2020**, 1505–1515. [[CrossRef](#)] [[PubMed](#)]
10. Suchorska, B.; Weller, M.; Tabatabai, G.; Senft, C.; Hau, P.; Sabel, M.C.; Herrlinger, U.; Ketter, R.; Schlegel, U.; Marosi, C.; et al. Complete resection of contrast-enhancing tumor volume is associated with improved survival in recurrent glioblastoma—results from the DIRECTOR trial. *Neuro-Oncology* **2016**, *18*, 549–556. [[CrossRef](#)]
11. Chiocca, E.A.; Yu, J.S.; Lukas, R.V.; Solomon, I.H.; Ligon, K.L.; Nakashima, H.; Triggs, D.A.; Reardon, D.A.; Wen, P.; Stopa, B.M.; et al. Regulatable interleukin-12 gene therapy in patients with recurrent high-grade glioma: Results of a phase 1 trial. *Sci. Transl. Med.* **2019**, *11*. [[CrossRef](#)]
12. Cloughesy, T.F.; Petrecca, K.; Walbert, T.; Butowski, N.; Salacz, M.; Perry, J.; Damek, D.; Bota, D.; Bettegowda, C.; Zhu, J.J.; et al. Effect of Vocimagene Amiretrorepvec in Combination With Flucytosine vs Standard of Care on Survival Following Tumor Resection in Patients With Recurrent High-Grade Glioma: A Randomized Clinical Trial. *JAMA Oncol.* **2020**, *6*, 1939–1946. [[CrossRef](#)] [[PubMed](#)]
13. Stummer, W.; Reulen, H.J.; Meinel, T.; Pichlmeier, U.; Schumacher, W.; Tonn, J.C.; Rohde, V.; Oppel, F.; Turowski, B.; Woiciechowsky, C.; et al. Extent of resection and survival in glioblastoma multiforme: Identification of and adjustment for bias. *Neurosurgery* **2008**, *62*, 564–576. [[CrossRef](#)] [[PubMed](#)]
14. Lu, V.M.; Jue, T.R.; McDonald, K.L.; Rovin, R.A. The Survival Effect of Repeat Surgery at Glioblastoma Recurrence and its Trend: A Systematic Review and Meta-Analysis. *World Neurosurg.* **2018**, *115*, 453–459. [[CrossRef](#)] [[PubMed](#)]
15. Wann, A.; Tully, P.A.; Barnes, E.H.; Lwin, Z.; Jeffree, R.; Drummond, K.J.; Gan, H.; Khasraw, M. Outcomes after second surgery for recurrent glioblastoma: A retrospective case-control study. *J. Neuro-Oncol.* **2018**, *137*, 409–415. [[CrossRef](#)]
16. Wick, W.; Gorlia, T.; Bendszus, M.; Taphoorn, M.; Sahm, F.; Harting, I.; Brandes, A.A.; Taal, W.; Domont, J.; Idbaih, A.; et al. Lomustine and Bevacizumab in Progressive Glioblastoma. *N. Engl. J. Med.* **2017**, *377*, 1954–1963. [[CrossRef](#)]
17. Seystahl, K.; Wick, W.; Weller, M. Therapeutic options in recurrent glioblastoma—An update. *Crit. Rev. Oncol./Hematol.* **2016**, *99*, 389–408. [[CrossRef](#)]
18. Rosenthal, M.A.; Gruber, M.L.; Glass, J.; Nirenberg, A.; Finlay, J.; Hochster, H.; Muggia, F.M. Phase II Study of Combination Taxol and Estramustine Phosphate in the Treatment of Recurrent Glioblastoma Multiforme. *J. Neuro-Oncol.* **2000**, *47*, 59–63. [[CrossRef](#)]
19. Oudard, S.; Carpentier, A.; Banu, E.; Fauchon, F.; Celerier, D.; Poupon, M.F.; Dutrillaux, B.; Andrieu, J.M.; Delattre, J.Y. Phase II study of lornidamine and diazepam in the treatment of recurrent glioblastoma multiforme. *J. Neuro-Oncol.* **2003**, *63*, 81–86. [[CrossRef](#)] [[PubMed](#)]
20. Puduvalli, V.K.; Yung, W.K.; Hess, K.R.; Kuhn, J.G.; Groves, M.D.; Levin, V.A.; Zwiebel, J.; Chang, S.M.; Cloughesy, T.F.; Junck, L.; et al. Phase II study of fenretinide (NSC 374551) in adults with recurrent malignant gliomas: A North American Brain Tumor Consortium study. *J. Clin. Oncol. Off. J. Am. Soc. Clin. Oncol.* **2004**, *22*, 4282–4289. [[CrossRef](#)]
21. Robe, P.A.; Martin, D.H.; Nguyen-Khac, M.T.; Artesi, M.; Deprez, M.; Albert, A.; Vanbelle, S.; Califice, S.; Bredel, M.; Bours, V. Early termination of ISRCTN45828668, a phase 1/2 prospective, randomized study of sulfasalazine for the treatment of progressing malignant gliomas in adults. *BMC Cancer* **2009**, *9*, 1–8. [[CrossRef](#)] [[PubMed](#)]
22. Rich, J.N.; Reardon, D.A.; Peery, T.; Dowell, J.M.; Quinn, J.A.; Penne, K.L.; Wikstrand, C.J.; Van Duyn, L.B.; Dancey, J.E.; McLendon, R.E.; et al. Phase II trial of gefitinib in recurrent glioblastoma. *J. Clin. Oncol. Off. J. Am. Soc. Clin. Oncol.* **2004**, *22*, 133–142. [[CrossRef](#)] [[PubMed](#)]
23. Sathornsumetee, S.; Desjardins, A.; Vredenburgh, J.J.; McLendon, R.E.; Marcello, J.; Herndon, J.E.; Mathe, A.; Hamilton, M.; Rich, J.N.; Norfleet, J.A.; et al. Phase II trial of bevacizumab and erlotinib in patients with recurrent malignant glioma. *Neuro-Oncology* **2010**, *12*, 1300–1310. [[CrossRef](#)]
24. Wick, W.; Puduvalli, V.K.; Chamberlain, M.C.; van den Bent, M.J.; Carpentier, A.F.; Cher, L.M.; Mason, W.; Weller, M.; Hong, S.; Musib, L.; et al. Phase III study of enzastaurin compared with lomustine in the treatment of recurrent intracranial glioblastoma. *J. Clin. Oncol. Off. J. Am. Soc. Clin. Oncol.* **2010**, *28*, 1168–1174. [[CrossRef](#)] [[PubMed](#)]

25. Filley, A.C.; Henriquez, M.; Dey, M. Recurrent glioma clinical trial, CheckMate-143: The game is not over yet. *Oncotarget* **2017**, *8*, 91779–91794. [[CrossRef](#)] [[PubMed](#)]
26. Lim, M.; Xia, Y.; Bettegowda, C.; Weller, M. Current state of immunotherapy for glioblastoma. *Nat. Rev. Clin. Oncol.* **2018**, *15*, 422–442. [[CrossRef](#)]
27. Stupp, R.; Brada, M.; van den Bent, M.J.; Tonn, J.-C.; Pentheroudakis, G. High-grade glioma: ESMO Clinical Practice Guidelines for diagnosis, treatment and follow-up†. *Ann. Oncol.* **2014**, *25*, iii93–iii101. [[CrossRef](#)]
28. Beck, T.J.; Kreth, F.W.; Beyer, W.; Mehrkens, J.H.; Obermeier, A.; Stepp, H.; Stummer, W.; Baumgartner, R. Interstitial photodynamic therapy of nonresectable malignant glioma recurrences using 5-aminolevulinic acid induced protoporphyrin IX. *Lasers Surg. Med.* **2007**, *39*, 386–393. [[CrossRef](#)]
29. Stummer, W.; Pichlmeier, U.; Meinel, T.; Wiestler, O.D.; Zanella, F.; Reulen, H.J. Fluorescence-guided surgery with 5-aminolevulinic acid for resection of malignant glioma: A randomised controlled multicentre phase III trial. *Lancet. Oncol.* **2006**, *7*, 392–401. [[CrossRef](#)]
30. Schucht, P.; Beck, J.; Abu-Isa, J.; Anderegg, L.; Murek, M.; Seidel, K.; Stieglitz, L.; Raabe, A. Gross total resection rates in contemporary glioblastoma surgery: Results of an institutional protocol combining 5-aminolevulinic acid intraoperative fluorescence imaging and brain mapping. *Neurosurgery* **2012**, *71*, 927–935. [[CrossRef](#)]
31. Stylli, S.S.; Kaye, A.H.; MacGregor, L.; Howes, M.; Rajendra, P. Photodynamic therapy of high grade glioma-long term survival. *J. Clin. Neurosci. Off. J. Neurosurg. Soc. Australas.* **2005**, *12*, 389–398. [[CrossRef](#)]
32. Dupont, C.; Vermandel, M.; Leroy, H.-A.; Quidet, M.; Lecomte, F.; Delhem, N.; Mordon, S.; Reyns, N. INtraoperative photODYnamic Therapy for GliOblastomas (INDYGO): Study protocol for a phase I clinical trial. *Neurosurgery* **2018**. [[CrossRef](#)] [[PubMed](#)]
33. Johansson, A.; Faber, F.; Kniebühler, G.; Stepp, H.; Sroka, R.; Egensperger, R.; Beyer, W.; Kreth, F.-W. Protoporphyrin IX Fluorescence and Photobleaching During Interstitial Photodynamic Therapy of Malignant Gliomas for Early Treatment Prognosis. *Lasers Surg. Med.* **2013**, *45*, 225–234. [[CrossRef](#)] [[PubMed](#)]
34. Stummer, W.; Beck, T.; Beyer, W.; Mehrkens, J.H.; Obermeier, A.; Etminan, N.; Stepp, H.; Tonn, J.C.; Baumgartner, R.; Herms, J.; et al. Long-sustaining response in a patient with non-resectable, distant recurrence of glioblastoma multiforme treated by interstitial photodynamic therapy using 5-ALA: Case report. *J. Neuro-Oncol.* **2008**, *87*, 103–109. [[CrossRef](#)] [[PubMed](#)]
35. Macdonald, D.R.; Cascino, T.L.; Schold, S.C., Jr.; Cairncross, J.G. Response criteria for phase II studies of supratentorial malignant glioma. *J. Clin. Oncol. Off. J. Am. Soc. Clin. Oncol.* **1990**, *8*, 1277–1280. [[CrossRef](#)] [[PubMed](#)]
36. Wen, P.Y.; Macdonald, D.R.; Reardon, D.A.; Cloughesy, T.F.; Sorensen, A.G.; Galanis, E.; Degroot, J.; Wick, W.; Gilbert, M.R.; Lassman, A.B.; et al. Updated response assessment criteria for high-grade gliomas: Response assessment in neuro-oncology working group. *J. Clin. Oncol. Off. J. Am. Soc. Clin. Oncol.* **2010**, *28*, 1963–1972. [[CrossRef](#)]
37. Eigenbrod, S.; Trabold, R.; Brucker, D.; Eros, C.; Egensperger, R.; La Fougere, C.; Gobel, W.; Ruhm, A.; Kretschmar, H.A.; Tonn, J.C.; et al. Molecular stereotactic biopsy technique improves diagnostic accuracy and enables personalized treatment strategies in glioma patients. *Acta Neurochir.* **2014**, *156*, 1427–1440. [[CrossRef](#)]
38. Louis, D.N.; Ohgaki, H.; Wiestler, O.D.; Cavenee, W.K.; Burger, P.C.; Jouvet, A.; Scheithauer, B.W.; Kleihues, P. The 2007 WHO Classification of Tumours of the Central Nervous System. *Acta Neuropathol.* **2007**, *114*, 97–109. [[CrossRef](#)]
39. Louis, D.N.; Perry, A.; Reifenberger, G.; von Deimling, A.; Figarella-Branger, D.; Cavenee, W.K.; Ohgaki, H.; Wiestler, O.D.; Kleihues, P.; Ellison, D.W. The 2016 World Health Organization Classification of Tumors of the Central Nervous System: A summary. *Acta Neuropathol.* **2016**, *131*, 803–820. [[CrossRef](#)]
40. Rühm, A.; Stepp, H.; Beyer, W.; Hennig, G.; Pongratz, T.; Sroka, R.; Schnell, O.; Tonn, J.-C.; Kreth, F.-W. 5-ALA based photodynamic management of glioblastoma. In Proceedings of the SPIE, San Francisco, CA, USA, 24 March 2014.
41. *National Institutes of Health Common Terminology Criteria for Adverse Events (CTCAE)*; National Cancer Institute: Bethesda, MD, USA, 2017.
42. Rachinger, W.; Goetz, C.; Popperl, G.; Gildehaus, F.J.; Kreth, F.W.; Holtmannspotter, M.; Herms, J.; Koch, W.; Tatsch, K.; Tonn, J.C. Positron emission tomography with O-(2-[¹⁸F]fluoroethyl)-L-tyrosine versus magnetic resonance imaging in the diagnosis of recurrent gliomas. *Neurosurgery* **2005**, *57*, 505–511. [[CrossRef](#)]
43. Mehrkens, J.H.; Popperl, G.; Rachinger, W.; Herms, J.; Seelos, K.; Tatsch, K.; Tonn, J.C.; Kreth, F.W. The positive predictive value of O-(2-[¹⁸F]fluoroethyl)-L-tyrosine (FET) PET in the diagnosis of a glioma recurrence after multimodal treatment. *J. Neuro-Oncol.* **2008**, *88*, 27–35. [[CrossRef](#)] [[PubMed](#)]
44. Shafirstein, G.; Bellnier, D.; Oakley, E.; Hamilton, S.; Potasek, M.; Beeson, K.; Parilov, E. Interstitial Photodynamic Therapy-A Focused Review. *Cancers* **2017**, *9*, 12. [[CrossRef](#)] [[PubMed](#)]
45. Collaud, S.; Juzeniene, A.; Moan, J.; Lange, N. On the selectivity of 5-aminolevulinic acid-induced protoporphyrin IX formation. *Curr. Med. Chem. Anti-Cancer Agents* **2004**, *4*, 301–316. [[CrossRef](#)]
46. Agostinis, P.; Berg, K.; Cengel, K.A.; Foster, T.H.; Girotti, A.W.; Gollnick, S.O.; Hahn, S.M.; Hamblin, M.R.; Juzeniene, A.; Kessel, D.; et al. Photodynamic therapy of cancer: An update. *CA A Cancer J. Clin.* **2011**, *61*, 250–281. [[CrossRef](#)]
47. Stepp, H.; Stummer, W. 5-ALA in the management of malignant glioma. *Lasers Surg. Med.* **2018**, *50*, 399–419. [[CrossRef](#)] [[PubMed](#)]
48. Beltrán Hernández, I.; Yu, Y.; Ossendorp, F.; Korbelik, M.; Oliveira, S. Preclinical and Clinical Evidence of Immune Responses Triggered in Oncologic Photodynamic Therapy: Clinical Recommendations. *J. Clin. Med.* **2020**, *9*, 333. [[CrossRef](#)]

49. Kammerer, R.; Buchner, A.; Palluch, P.; Pongratz, T.; Oboukhovskij, K.; Beyer, W.; Johansson, A.; Stepp, H.; Baumgartner, R.; Zimmermann, W. Induction of immune mediators in glioma and prostate cancer cells by non-lethal photodynamic therapy. *PLoS ONE* **2011**, *6*, e21834. [[CrossRef](#)] [[PubMed](#)]
50. Castano, A.P.; Mroz, P.; Hamblin, M.R. Photodynamic therapy and anti-tumour immunity. *Nat. Rev. Cancer* **2006**, *6*, 535–545. [[CrossRef](#)]
51. Heckl, C.; Aumiller, M.; Rühm, A.; Sroka, R.; Stepp, H. Fluorescence and Treatment Light Monitoring for Interstitial Photodynamic Therapy. *Photochem. Photobiol.* **2020**, *96*, 388–396. [[CrossRef](#)]
52. Stummer, W.; Tonn, J.C.; Mehdorn, H.M.; Nestler, U.; Franz, K.; Goetz, C.; Bink, A.; Pichlmeier, U. Counterbalancing risks and gains from extended resections in malignant glioma surgery: A supplemental analysis from the randomized 5-aminolevulinic acid glioma resection study. Clinical article. *J. Neurosurg.* **2011**, *114*, 613–623. [[CrossRef](#)]
53. Magill, S.T.; Han, S.J.; Li, J.; Berger, M.S. Resection of primary motor cortex tumors: Feasibility and surgical outcomes. *J. Neurosurg.* **2018**, *129*, 961–972. [[CrossRef](#)] [[PubMed](#)]
54. Chang, S.M.; Parney, I.F.; McDermott, M.; Barker, F.G., 2nd; Schmidt, M.H.; Huang, W.; Laws, E.R., Jr.; Lillehei, K.O.; Bernstein, M.; Brem, H.; et al. Perioperative complications and neurological outcomes of first and second craniotomies among patients enrolled in the Glioma Outcome Project. *J. Neurosurg.* **2003**, *98*, 1175–1181. [[CrossRef](#)] [[PubMed](#)]
55. Hoover, J.M.; Nwojo, M.; Puffer, R.; Mandrekar, J.; Meyer, F.B.; Parney, I.F. Surgical outcomes in recurrent glioma: Clinical article. *J. Neurosurg.* **2013**, *118*, 1224–1231. [[CrossRef](#)]
56. Flieger, M.; Ganswindt, U.; Schwarz, S.B.; Kreth, F.W.; Tonn, J.C.; la Fougere, C.; Ertl, L.; Linn, J.; Herrlinger, U.; Belka, C.; et al. Re-irradiation and bevacizumab in recurrent high-grade glioma: An effective treatment option. *J. Neuro-Oncol.* **2014**, *117*, 337–345. [[CrossRef](#)] [[PubMed](#)]
57. Lee, J.; Ahn, S.S.; Chang, J.H.; Suh, C.O. Hypofractionated Re-irradiation after Maximal Surgical Resection for Recurrent Glioblastoma: Therapeutic Adequacy and Its Prognosticators of Survival. *Yonsei Med. J.* **2018**, *59*, 194–201. [[CrossRef](#)] [[PubMed](#)]
58. Weller, M.; Tabatabai, G.; Kästner, B.; Felsberg, J.; Steinbach, J.P.; Wick, A.; Schnell, O.; Hau, P.; Herrlinger, U.; Sabel, M.C.; et al. MGMT Promoter Methylation Is a Strong Prognostic Biomarker for Benefit from Dose-Intensified Temozolomide Rechallenge in Progressive Glioblastoma: The DIRECTOR Trial. *Clin. Cancer Res. An Off. J. Am. Assoc. Cancer Res.* **2015**, *21*, 2057–2064. [[CrossRef](#)]
59. Wick, W.; Meisner, C.; Hentschel, B.; Platten, M.; Schilling, A.; Wiestler, B.; Sabel, M.C.; Koeppen, S.; Ketter, R.; Weiler, M.; et al. Prognostic or predictive value of MGMT promoter methylation in gliomas depends on IDH1 mutation. *Neurology* **2013**, *81*, 1515–1522. [[CrossRef](#)] [[PubMed](#)]
60. Li, F.; Cheng, Y.; Lu, J.; Hu, R.; Wan, Q.; Feng, H. Photodynamic therapy boosts anti-glioma immunity in mice: A dependence on the activities of T cells and complement C3. *J. Cell. Biochem.* **2011**, *112*, 3035–3043. [[CrossRef](#)]
61. Hübner, M.; Strauss, G.; Effinger, D.; Pohla, H.; Kreth, F.-W.; Kreth, S. IMPS-15PDT-TREATED GBM CELLS INCREASE EFFECTOR FUNCTIONS OF HUMAN CD8+ T-CELLS. *Neuro-Oncology* **2015**, *17*, v116. [[CrossRef](#)]
62. Etminan, N.; Peters, C.; Lakbir, D.; Bünnemann, E.; Börger, V.; Sabel, M.C.; Hänggi, D.; Steiger, H.J.; Stummer, W.; Sorg, R.V. Heat-shock protein 70-dependent dendritic cell activation by 5-aminolevulinic acid-mediated photodynamic treatment of human glioblastoma spheroids in vitro. *Br. J. Cancer* **2011**, *105*, 961–969. [[CrossRef](#)]
63. Cramer, G.M.; Moon, E.K.; Cengel, K.A.; Busch, T.M. Photodynamic Therapy and Immune Checkpoint Blockade(†). *Photochem. Photobiol.* **2020**, *96*, 954–961. [[CrossRef](#)] [[PubMed](#)]



Interstitial photodynamic therapy for newly diagnosed glioblastoma

Stefanie Quach¹ · Christoph Schwartz^{1,2} · Maximilian Aumiller^{3,4} · Marco Foglar^{3,4} · Michael Schmutzer¹ · Sophie Katzendobler¹ · Mohamed El Fahim^{3,4} · Robert Forbrig⁵ · Katja Bochmann⁶ · Rupert Egensperger⁷ · Ronald Sroka^{3,4} · Herbert Stepp^{3,4} · Adrian Rühm^{3,4} · Niklas Thon^{1,8}

Received: 26 January 2023 / Accepted: 27 February 2023 / Published online: 16 March 2023
© The Author(s) 2023

Abstract

Purpose Innovative, efficient treatments are desperately needed for people with glioblastoma (GBM).

Methods Sixteen patients (median age 65.8 years) with newly diagnosed, small-sized, not safely resectable supratentorial GBM underwent interstitial photodynamic therapy (iPDT) as upfront eradicating local therapy followed by standard chemoradiation. 5-aminolevulinic acid (5-ALA) induced protoporphyrin IX was used as the photosensitizer. The tumors were irradiated with light at 635 nm wavelength via stereotactically implanted cylindrical diffuser fibers. Outcome after iPDT was retrospectively compared with a positively-selected in-house patient cohort (n = 110) who underwent complete tumor resection followed by chemoradiation.

Results Median progression-free survival (PFS) was 16.4 months, and median overall survival (OS) was 28.0 months. Seven patients (43.8%) experienced long-term PFS > 24 months. Median follow-up was 113.9 months for the survivors. Univariate regression revealed MGMT-promoter methylation but not age as a prognostic factor for both OS (p = 0.04 and p = 0.07) and PFS (p = 0.04 and p = 0.67). Permanent iPDT-associated morbidity was seen in one iPDT patient (6.3%). Patients treated with iPDT experienced superior PFS and OS compared to patients who underwent complete tumor removal (p < 0.01 and p = 0.01, respectively). The rate of long-term PFS was higher in iPDT-treated patients (43.8% vs. 8.9%, p < 0.01).

Conclusion iPDT is a feasible treatment concept and might be associated with long-term PFS in a subgroup of GBM patients, potentially via induction of so far unknown immunological tumor-controlling processes.

Keywords 5-aminolevulinic acid · Interstitial photodynamic therapy · Glioblastoma · Overall survival · Postoperative morbidity · Progression-free survival

Introduction

Glioblastoma (GBM) is the most common malignant brain tumor [1]. Current treatment concepts comprise maximal safe resection followed by a combination of radiotherapy and

chemotherapy with temozolomide [2], possibly augmented by tumor-treating fields [3]. Despite this aggressive treatment regimen, median survival is limited to 15–20 months [2–4]. Unfavorable outcome must be particularly expected if the tumor cannot be resected completely due to eloquent

Adrian Rühm and Niklas Thon shared last authorship

✉ Niklas Thon
niklas.thon@med.uni-muenchen.de

¹ Department of Neurosurgery, University Hospital Munich, Ludwig-Maximilians-University, Marchioninistrasse 15, 81377 Munich, Germany

² Department of Neurosurgery, University Hospital Salzburg, Paracelsus Medical University Salzburg, Salzburg, Austria

³ Laser-Forschungslabor, LIFE Center, University Hospital Munich, Ludwig-Maximilians-University, Planegg, Germany

⁴ Department of Urology, University Hospital Munich, Ludwig-Maximilians-University, Munich, Germany

⁵ Department of Neuroradiology, University Hospital Munich, Ludwig-Maximilians-University, Munich, Germany

⁶ Max Planck Institute of Psychiatry, Munich, Germany

⁷ Center for Neuropathology and Prion Research, University Hospital, LMU Munich, 81377 Munich, Germany

⁸ German Cancer Consortium (DKTK), Partner Site Munich, Munich, Germany

location [5, 6], and/or if an unmethylated O6-methylguanine-DNA-methyltransferase (*MGMT*) promoter hampers response to chemotherapy [7]. Thus, alternative treatment concepts need to be evaluated.

Photodynamic therapy (PDT) is a local treatment concept used for a variety of neoplastic [8, 9] and non-neoplastic conditions [10]. It is based on the light-induced activation of a photosensitizer leading to the formation of reactive oxygen species and subsequent apoptosis and necrosis of the affected cells [11]. The photosensitizer protoporphyrin IX is preferentially synthesized within malignant glioma cells after oral application of its precursor 5-aminolevulinic acid (5-ALA). This highly specific accumulation makes 5-ALA a well-suited photosensitizer predrug for PDT [12]. The good tumor-to-background-ratio of protoporphyrin IX synthesis is regularly exploited in fluorescence-guided resection [13]. For tumors unamenable to safe complete resection, interstitial PDT (iPDT) has been explored as a minimally invasive procedure where treatment light is applied through stereotactically implanted optical fibers. IPDT was found to be a feasible salvage treatment option in small malignant glioma case series [14–16]. Recently, a larger series of recurrent malignant gliomas reported a post-recurrence survival longer than 24 months for 25% of the treated patients [17].

Based on these promising results in GBM recurrences, we offered iPDT as an alternative local treatment option upon specific demand to patients with small-sized, unifocal, not safely resectable, newly diagnosed GBM. In here, we share our experiences and outcome data, focusing on progression-free survival (PFS), overall survival (OS), and treatment-associated morbidity in a series of 16 adult patients with untreated GBMs undergoing iPDT as primary treatment. All patients received postoperative standard treatment with radiation therapy plus concomitant and adjuvant temozolomide. Outcome data after iPDT were put into perspective with an in-house cohort of GBM patients having undergone complete tumor resection followed by a complete course of radiochemotherapy according to the EORTC/NCIC protocol [2].

Patients and methods

iPDT patient cohort

All patients were discussed in advance in our local interdisciplinary neurooncological tumor board. The decision to perform iPDT in selected cases was triggered by the patients' specific demand as well as our prior experiences with iPDT treated malignant glioma recurrences. Eligibility criteria for patients undergoing iPDT on specific demand consisted of (1) small-sized (diameter < 4 cm), circumscribed, untreated

GBMs without or moderate midline shift without signs of transtentorial herniation or contact to the ventricular system, (2) unifocal, supratentorial, and (3) patients should rate on the Karnofsky performance scale (KPS) with values ≥ 70 . All patients were informed in detail about the procedure and its associated risks, and about the fact that iPDT is not the established standard treatment for newly diagnosed GBMs and is considered an individual treatment attempt. Written informed consent was obtained from all patients. The institutional review board approved the protocol for the retrospective analysis (ethics approval no. 335–16, Ludwig-Maximilians-University, Munich, Germany).

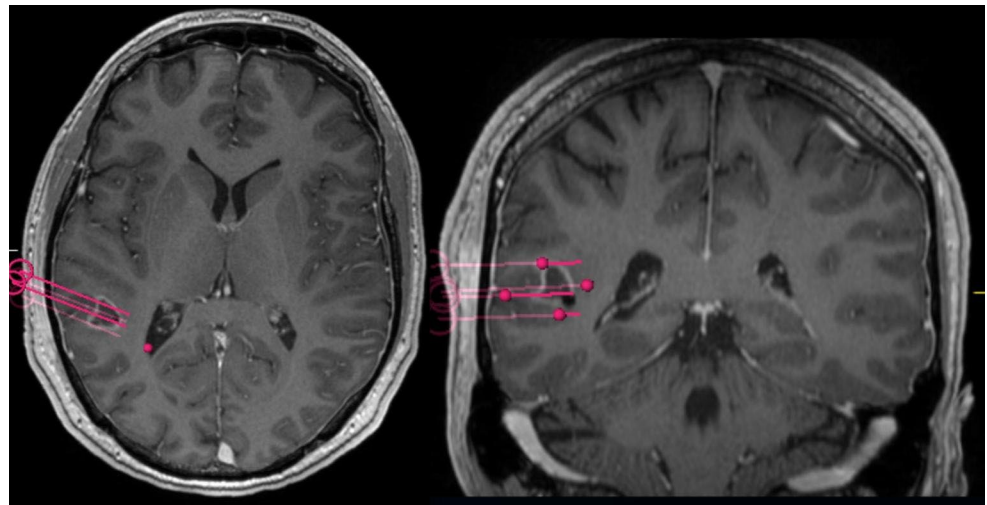
Study cohort for comparative analyses

An in-house patient cohort was used for comparative outcome analyses. This cohort included 110 highly selected patients who had received the optimal available first-line treatment for newly-diagnosed GBMs consisting of complete resection (as proven by early post-operative MRI) followed by a full course of adjuvant radiochemotherapy according to the EORTC/NCIC protocol.

Treatment procedure

All tumors were diagnosed histologically according to the current WHO classification at the time of treatment [18]. *MGMT* methylation status, isocitrate dehydrogenase (*IDH*) mutation status and LOH1p/19q were determined as described previously [19]. Interstitial photodynamic therapy was performed in a standardized fashion as reported in detail before [14, 17]. In brief, a three-dimensional treatment volume was defined using preoperative MRI with contrast-enhanced T1 and, when available, O-2-[^{18}F]fluoroethyl-L-tyrosine-positron emission tomography (FET-PET). These images, together with T2-weighted images and contrast-enhanced MR-angiography, were fused to the intraoperatively acquired stereotactic computerized tomography (CT) to plan the trajectories of the cylindrical light diffusors (CYD 600, Light Guide Optics, Rheinbach, Germany). Figure 1 shows an implantation schematic. Three hours after systemically administering 5-ALA (medac GmbH, Wedel, Germany) at a standard dose of 20 mg/kg bodyweight (maximum: 30 mg/kg), the light diffusors were implanted stereotactically under general anesthesia. Light irradiation was performed at a wavelength of 635 nm (median total dose: 12,240 J, range 7200–20,520 J; median dose per treatment volume: 2.400 J/cm³, range 969–5760 J/cm³; median light power per diffuser length: 200 mW/cm, range: 100–200 mW/cm; Ceralas PDT Diode Laser, biolitec AG, Jena, Germany). The median duration of irradiation was 1.0 h (range: 1.0 to 2.0 h, elongated irradiation times were compensated

Fig. 1 Exemplary case illustrating three-dimensional planning of the light diffusor trajectories. The patient (IPDT 02) presented with seizures and aphasia leading to the diagnosis of glioblastoma in the left angular gyrus



by a reduced radiant flux). Prior to and after the irradiation, intraoperative spectral online monitoring measurements were performed to document the transmission of the treatment light through the tissue and the amount of PpIX fluorescence generated therein as well as to monitor for potential treatment-related or treatment-relevant effects [20, 21].

Adjuvant treatment and follow-up

In accordance with Stupp protocol [2], all but one patient received concomitant radiochemotherapy and adjuvant cycles of temozolomide chemotherapy. One patient (IPDT 11) was treated by adjuvant radiotherapy only because of an unmethylated *MGMT*-promoter status in combination with advanced age > 65 years. Adjuvant treatment was initiated within two weeks after iPDT in all patients. Any treatment-associated morbidity was documented. The last clinical follow-up for this specific cohort was January 12th, 2022.

Evaluation and statistical analyses

The two study endpoints, PFS and OS, were calculated from the date of iPDT or tumor resection (reference cohort). Long-term survival was defined as a PFS of > 24.0 months as calculated by Kaplan-Meier method. Follow-up was assessed by the reverse Kaplan-Meier method. Survival was evaluated with the Kaplan-Meier method and compared by the log-rank test. As potential prognostic factors, *MGMT* methylation status and age were assessed by univariate regression because of the lesser number of events in the iPDT cohort. Categorical variables were analyzed using the χ^2 test and age with Student's t-test. A p-value ≤ 0.05 was considered significant. All calculations were performed using SPSS Statistics 25 (IBM, Armonk, New York, USA).

Results

Patient population

Sixteen patients were consecutively treated with iPDT between 2008 and 2014. Their median age at iPDT was 65.8 years (range 29.7–76.5), and all had a KPS of 90. Clinically, epilepsy (n=12), aphasia (n=3), and hemiparesis (n=1) led to the tumor diagnosis. The treated tumors were localized in the temporal lobe (n=8), the frontal lobe (n=3), the parietal lobe (n=4), and central gyrus and subcentral lobe (n=1). Fourteen tumors were located in the dominant hemisphere. A methylated *MGMT*-promoter status was seen in 8/16 (50.0%) and an *IDH* mutation in 2/16 (12.5%) of iPDT patients. No tumor had a 1p/19q codeletion (LOH1p/19q). The median tumor volume was 6.1 cm³ (range: 1.4–21.8 cm³); the number of implanted light diffusors ranged from three to ten per tumor. Table 1 details histopathological profiles at the time of iPDT and outcome data for the iPDT patient cohort.

Survival after iPDT

Median follow-up for the survivors was 113.9 months. Within this follow-up, 13 patients succumbed to their disease. Median PFS was 16.4 months; median OS was 28.0 months (see Fig. 2). One-year and two-year PFS rates were 56.3% and 43.8%, one-year and two-year OS rates were 75.0% and 62.5%, respectively. Univariate regression revealed *MGMT*-promoter methylation but not age as a prognostic factor for both OS (p=0.04 and p=0.07) and PFS (p=0.04 and p=0.67). At the time of recurrence, the patients received bevacizumab/irinotecan (n=5), re-radiotherapy (n=3), brachytherapy (n=3), temozolomide rechallenge (n=3), procarbazine/lomustine chemotherapy (n=2) or a combination thereof. Four patients presented with

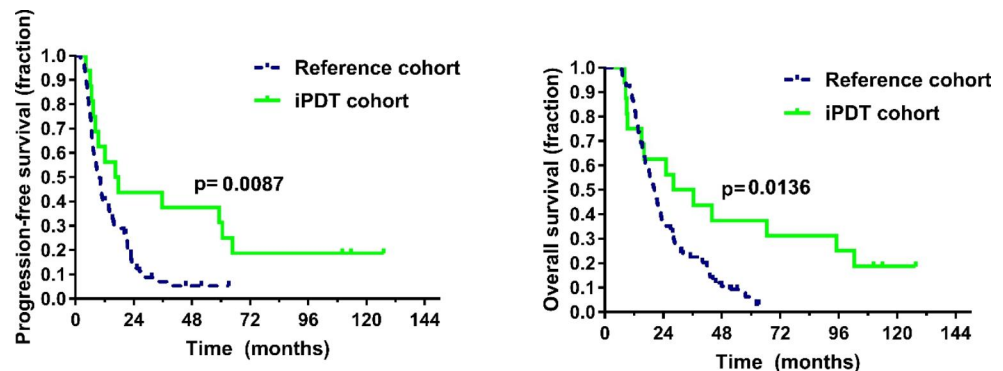
Table 1 Patient characteristics including biomarker status and follow-up

Patient number	sex	Age at iPDT* (years)	<i>MGMT</i> promoter methylated	<i>IDH</i> mutation	Ki67 proliferation index	PFS (months)	OS (months)	status
IPDT 01	m	29,7	yes	yes	?	64,7	102,4	deceased
IPDT 02	m	40,6	no	no	10%	59,2	95,0	deceased
IPDT 03	f	50,3	yes	no	10%	127,1	127,5	alive
IPDT 04	m	69,9	no	no	30%	8,3	15,0	deceased
IPDT 05	m	68,2	no	no	15%	12,0	16,1	deceased
IPDT 06	m	63,7	no	no	20%	4,3	9,0	deceased
IPDT 07	m	70,1	yes	no	25%	110,1	110,3	alive
IPDT 08	f	74,1	no	no	25%	60,6	66,4	deceased
IPDT 09	m	33,3	partially	yes	85%	113,6	113,9	alive
IPDT 10	f	74,3	no	no	30%	16,4	28,0	deceased
IPDT 11	m	68,8	no	no	21%	6,0	8,5	deceased
IPDT 12	m	68,0	yes	no	7%	6,5	8,0	deceased
IPDT 13	f	57,3	partially	no	15%	9,5	25,2	deceased
IPDT 14	m	54,3	yes	no	15%	35,7	43,9	deceased
IPDT 15	m	76,5	no	no	10%	7,4	9,2	deceased
IPDT 16	m	53,4	yes	no	28%	17,8	36,4	deceased

* iPDT = interstitial photodynamic therapy; *MGMT* = O6-methylguanine-DNA-methyltransferase; *IDH* = isocitrate dehydrogenase; PFS = progression-free survival; OS = overall survival; m = male; f = female.

MGMT promoter methylation status was determined as described before [22].

Fig. 2 Progression-free survival and overall survival were significantly longer in the interstitial photodynamic therapy (iPDT) cohort compared to the reference cohort



cognitive deterioration at first recurrence and received best supportive care; no patient underwent open tumor resection.

Comparison to reference population

Patients in the reference cohort resembled iPDT patients with respect to age (median 56.1 years (range: 17.2–86.6 years) vs. 65.9 years, $p=0.21$), *MGMT* promoter methylation (methylation rate: 48/99 (48.5%) vs. 8/16 (50.0%), $p=0.91$), and *IDH* mutation rate (3/40 (7.5%) vs. 2/16 (12.5%), $p=0.55$). KPS was higher in the iPDT treated group (90 for all iPDT patients, median 80, range 60–90 in the reference cohort, $p<0.01$). *MGMT* methylation, but not age were associated with a prolonged OS ($p<0.01$ and $p=0.12$) and PFS ($p<0.01$ and $p=0.07$).

Patients treated with iPDT experienced superior progression-free and overall survival compared to patients who had undergone complete tumor resection ($p<0.01$ and $p=0.01$,

respectively). The rate of patients with long-term PFS (> 24 months) was higher in iPDT treated patients (43.8% vs. 8.9%, $p<0.01$, see also Table 2).

Among patients with *MGMT*-methylated tumors, 62.5% of iPDT treated patients experienced long-term PFS (> 24 months), compared to 16.7% in the reference group ($p<0.01$).

Postoperative morbidity

Perioperative transient morbidity within the first 30 days after iPDT included new aphasia ($n=2$), worsening of a pre-existing aphasia ($n=2$), new hemiparesis ($n=2$), worsening of a preexisting hemiparesis ($n=1$), and pulmonary embolism ($n=1$). Since two patients were affected by multiple postoperative symptoms/complications, a patient-based analysis resulted in a total treatment-associated morbidity rate of 37.5% (6/16 patients). Most neurological symptoms

Table 2 Comparison between iPDT and reference cohort

	iPDT cohort	Reference cohort	p-value
Median age (range)	65.8 years (29.7–76.5 years)	56.1 years (17.2–86.6 years)	0.21
<i>MGMT</i> promoter methylated	8/16 50.0%	48/99* 48.5%	0.91
<i>IDH</i> mutant	2/16 12.5%	3/40* 7.5%	0.55
Median PFS (95% CI)	16.4 months	9.9 months	< 0.01
Median OS (95% CI)	28.0 months (6.0–50.0)	20.4 months (17.9–22.9)	0.01
Long-term PFS (> 24 months)	7/16 (43.8%)	11/110 (8.9%)	< 0.01

* Molecular analyses were unavailable for some patients in the reference cohort.

MGMT=O6-methylguanine-DNA-methyltransferase; *IDH*=isocitrate dehydrogenase; PFS=progression-free survival; CI=confidence interval; OS=overall survival.

were edema-related and improved with oral dexamethasone treatment except for one patient with a permanent new aphasia after iPDT. No long-term steroid treatment or delay of adjuvant treatment was necessary. Thus, a permanent morbidity rate of 6.3% (1/16 of iPDT patients) was recorded over the course of follow-up.

Discussion

Adjuvant radiochemotherapy according to the EORTC/NCIC protocol has shown to improve the outcome of glioblastoma patients with a methylated *MGMT*-promoter status; however, overall survival remains limited [23]. Besides the incremental focus on biomarker profiling leading to more personalized treatment strategies, there remains an increasing need for the evaluation of more effective treatment concepts. One of these possible novel treatment concepts is iPDT for which this study provides a detailed outcome data analysis in comparison to the best available conventional treatment option. It is shown that iPDT, although requiring a careful planning procedure, is a feasible concept with an acceptable side effect profile for patients with untreated, small-sized, unresectable GBMs. A remarkable number of patients, in particular those with a methylated *MGMT*-promoter status, experienced long-term survival after iPDT. Furthermore, iPDT did not interfere with any further adjuvant treatment options.

One iPDT treated patient suffered a permanent treatment-associated morbidity. All other side effects were edema-associated and could be sufficiently treated by oral dexamethasone administration. Whenever possible,

dexamethasone was waived so as to not impair potential immune-modulatory effects. No patient had to undergo long-term anti-edematous therapy and no delay of adjuvant treatment due to treatment-associated complications was recorded.

When assessing the resulting Kaplan-Meier survival curves for PFS and OS, the observed patterns for the iPDT patient cohort were found to reach a plateau indicating long-term PFS and OS for a subgroup of iPDT patients. This favorable course of disease cannot be attributed to additional adjuvant treatment since all patients, with the exception of one case merely receiving radiotherapy, only underwent initial radiochemotherapy in analogy to the EORTC/NCIC protocol with up to nine cycles of TMZ at most. Thereafter, a treatment-free period up to the first sign of tumor recurrence was initiated in all patients. Thus, the burden of adjuvant treatment could be kept to a minimum for a good proportion of these iPDT patients in the initial stages of the disease. No exceptionally aggressive recurrence treatment was noted, either. In this patient series very promising PFS and OS rates one year and two years after iPDT treatment could be recorded. Most surprisingly, a significant proportion of seven patients (43.8%) experienced a PFS > 24.0 months not linked to very aggressive salvage treatment.

Two iPDT-treated patients harbored *IDH*-mutant tumors and would therefore, under the current WHO classification [24], be grouped as astrocytoma, *IDH* mutant, CNS WHO grade 4. Possibly, this molecular profile is in part responsible for the favorable outcome in these cases, although the value of iPDT for this subgroup is not clear. *IDH* mutant tumors were found in the reference group in comparable numbers. Another limitation of our study cohort is the selection of small tumor volumes, so as to minimize the risk of patient harm due to space-occupying increase in edema. Whether this treatment may also benefit the many cases of larger tumors cannot be answered at this point. The patients' excellent clinical status and prompt initiation of adjuvant therapy may have also contributed to the positive result.

A methylated *MGMT*-promoter status was associated with improved outcome parameters in both treatment groups, as is also seen in other treatment settings [7, 25]. The remarkably large survival benefit of iPDT-treated patients with positive *MGMT*-promoter methylation status, however, can most likely not only be explained by the known increased chemosensitivity by itself. Patients with an unmethylated *MGMT*-promoter profile showed outcomes similar to resected patients. Meanwhile the subgroup with methylated *MGMT*-promoter responded even better than resected patients. This response might be mediated through an immune-modulatory effect. The observed outcome improvement may thus be seen as a surrogate marker

of biologically different inflammatory/immunological responses to iPDT.

The precise mechanisms of tumor inactivation by iPDT, reflected in the recorded favorable PFS rate, are not entirely understood yet. Ex vivo experimental data have shown that PDT does have the ability to induce ROS in glioma cell spheroids causing consecutive necrosis [26]. It is now believed that through these events PDT does not only cause a local effect on the directly treated tumor volume but may also trigger a systemic immunological/inflammatory response which significantly contributes to the observed long-term tumor control [11, 27]. In mouse models, following PDT, an immediate infiltration of the tumor tissue by neutrophil granulocytes, mast cells, monocytes, and macrophages has been observed [28]. Preliminary ex vivo studies also suggest that iPDT impacts the adaptive immune system by increasing the cytotoxic potential of human CD8⁺ T-cells by altering the cells' mRNA and protein expression profiles [29]. These findings point to a potential iPDT-related induction of so far unknown tumor-controlling processes possibly overcoming the limitations of other local treatment concepts.

Based on our experiences, we do believe that iPDT is an appealing treatment concept for patients with newly diagnosed small-sized GBMs and deserves further evaluation in prospective clinical trials such as NCT03897491.

Conclusion

We here show that iPDT is a promising local treatment concept for patients with newly diagnosed small-sized GBMs. Notably, despite eloquent tumor localizations, a tolerable risk profile was seen. A considerable proportion of patients, especially those with methylated *MGMT*-promoter status, experienced long-term PFS after iPDT. This might point to the induction of so far, at least in detail, unknown tumor-controlling processes, e.g. inflammatory/immunological responses. Patients treated by iPDT compared favorably in terms of PFS and OS to the cohort of patients who received the optimal conventional treatment, which is an especially impressive finding as the iPDT-treated tumors were not safely resectable. Future clinical and experimental studies should be performed to improve the understanding of the underlying cellular and serological mechanisms and, consequently, to help to identify the subset of patients most suitable for iPDT.

Author contributions SQ, RS, HS, AR, and NT conceptualized the study; CS, MA, MS, SK, RE, RS, and AR investigated the data; SQ, CS, MF, and ME curated the data and aided with methodology; SQ, CS, MA, MF performed the formal analysis; RF, KB, and RE added resources; MF and AR validated the results; SQ and AR visualized the

data; SQ and CS wrote the original draft; RS, HS, AR, and NT edited the draft; AR and NT supervised and administered the project; all authors reviewed the manuscript.

Funding Open Access funding enabled and organized by Projekt DEAL. This study received no external funding. Maximilian Aumiller, Marco Foglar and Mohamed El Fahim have received funding by the Deutsche Forschungsgemeinschaft (GRK2274).

Data Availability Clinical and molecular data on all patients are anonymized and stored in local data bases secured by passwords.

Code Availability Not applicable.

Declarations

Conflicts of interest/Competing interests Stefanie Quach - No disclosures. Christoph Schwartz - No disclosures. Maximilian Aumiller - No disclosures. Marco Foglar - No disclosures. Michael Schmutzer - No disclosures. Sophie Katzendobler - No disclosures. Mohamed El Fahim - No disclosures. Robert Forbrig - No disclosures. Katja Bochrman - No disclosures. Rubert Egensperger - No disclosures. Ronald Sroka - No disclosures. Herbert Stepp - No disclosures. Adrian Rühm - No disclosures. Niklas Thon - No disclosures.

Consent to participate Consent to participate in retrospective studies is given prospectively by all patients treated at the Department of Neurosurgery of the Ludwig Maximilian University of Munich through a local prospective tumor registry.

Additional declarations for articles in life science journals that report the results of studies involving humans and/or animals The present study was conducted retrospectively.

Ethics approval Ethics approval was obtained by the ethics committee of the Ludwig Maximilian University of Munich (project number 335-16).

Consent for publication All authors have consented in submitting this manuscript for publication in the Journal of Neuro-Oncology.

Open Access This article is licensed under a Creative Commons Attribution 4.0 International License, which permits use, sharing, adaptation, distribution and reproduction in any medium or format, as long as you give appropriate credit to the original author(s) and the source, provide a link to the Creative Commons licence, and indicate if changes were made. The images or other third party material in this article are included in the article's Creative Commons licence, unless indicated otherwise in a credit line to the material. If material is not included in the article's Creative Commons licence and your intended use is not permitted by statutory regulation or exceeds the permitted use, you will need to obtain permission directly from the copyright holder. To view a copy of this licence, visit <http://creativecommons.org/licenses/by/4.0/>.

References

1. Ostrom QT et al (2022) CBTRUS Statistical Report: primary brain and other Central Nervous System Tumors diagnosed in the United States in 2015–2019. *Neuro Oncol* 24(Suppl 5):v1–v95
2. Stupp R et al (2005) Radiotherapy plus concomitant and adjuvant temozolomide for glioblastoma. *N Engl J Med* 352(10):987–996

3. Stupp R et al (2017) Effect of Tumor-Treating Fields Plus maintenance temozolomide vs maintenance temozolomide alone on survival in patients with glioblastoma: a Randomized Clinical Trial. *JAMA* 318(23):2306–2316
4. Chinot OL et al (2014) Bevacizumab plus radiotherapy-temozolomide for newly diagnosed glioblastoma. *N Engl J Med* 370(8):709–722
5. Thon N, Tonn JC, Kreth FW (2019) The surgical perspective in precision treatment of diffuse gliomas. *Onco Targets Ther* 12:1497–1508
6. Stummer W, van den Bent MJ, Westphal M (2011) Cytoreductive surgery of glioblastoma as the key to successful adjuvant therapies: new arguments in an old discussion. *Acta Neurochir (Wien)* 153(6):1211–1218
7. Thon N et al (2017) Outcome in unresectable glioblastoma: MGMT promoter methylation makes the difference. *J Neurol* 264(2):350–358
8. Li X et al (2020) Clinical development and potential of photothermal and photodynamic therapies for cancer. *Nat Reviews Clin Oncol* 17(11):657–674
9. Shafirstein G et al (2017) Interstitial Photodynamic Therapy-A Focused Review. *Cancers (Basel)*, 9(2)
10. Pérez C, Zúñiga T, Palavecino CE (2021) Photodynamic therapy for treatment of *Staphylococcus aureus* infections. *Photodiagnosis Photodyn Ther* 34:102285
11. Castano AP, Mroz P, Hamblin MR (2006) Photodynamic therapy and anti-tumour immunity. *Nat Rev Cancer* 6(7):535–545
12. Stepp H, Stummer W (2018) 5-ALA in the management of malignant glioma. *Lasers Surg Med* 50(5):399–419
13. Stummer W et al (2006) Fluorescence-guided surgery with 5-aminolevulinic acid for resection of malignant glioma: a randomised controlled multicentre phase III trial. *Lancet Oncol* 7(5):392–401
14. Beck TJ et al (2007) Interstitial photodynamic therapy of non-resectable malignant glioma recurrences using 5-aminolevulinic acid induced protoporphyrin IX. *Lasers Surg Med* 39(5):386–393
15. Stummer W et al (2008) Long-sustaining response in a patient with non-resectable, distant recurrence of glioblastoma multiforme treated by interstitial photodynamic therapy using 5-ALA: case report. *J Neurooncol* 87(1):103–109
16. Johansson A et al (2013) Protoporphyrin IX fluorescence and photobleaching during interstitial photodynamic therapy of malignant gliomas for early treatment prognosis. *Lasers Surg Med* 45(4):225–234
17. Lietke S et al (2021) Interstitial photodynamic therapy using 5-ALA for malignant glioma recurrences. *Cancers* 13(8):1767
18. Louis DN et al (2007) The 2007 WHO classification of Tumours of the Central Nervous System. *Acta Neuropathol* 114(2):97–109
19. Katzendobler S et al (2022) Diagnostic yield and complication rate of stereotactic biopsies in Precision Medicine of Gliomas. *Frontiers in Neurology*, 13
20. Heckl C et al (2020) Fluorescence and treatment light monitoring for interstitial photodynamic therapy. *Photochem Photobiol* 96(2):388–396
21. Aumiller M et al (2021) Interrelation between Spectral Online monitoring and postoperative T1-Weighted MRI in interstitial photodynamic therapy of malignant gliomas. *Cancers (Basel)*, 14(1)
22. Eigenbrod S et al (2014) Molecular stereotactic biopsy technique improves diagnostic accuracy and enables personalized treatment strategies in glioma patients. *Acta Neurochir (Wien)* 156(8):1427–1440
23. McFaline-Figueroa JR, Wen PY (2023) Negative trials over and over again: how can we do better? *Neurooncology* 25(1):1–3
24. Louis DN et al (2021) The 2021 WHO classification of tumors of the Central Nervous System: a summary. *Neuro Oncol* 23(8):1231–1251
25. Weller M et al (2015) MGMT promoter methylation is a strong prognostic biomarker for benefit from dose-intensified Temozolomide Rechallenge in Progressive Glioblastoma: the DIRECTOR trial. *Clin Cancer Res* 21(9):2057–2064
26. Madsen SJ et al (2000) Photodynamic therapy of human glioma spheroids using 5-aminolevulinic acid. *Photochem Photobiol* 72(1):128–134
27. Wachowska M, Muchowicz A, Demkow U (2015) Immunological aspects of antitumor photodynamic therapy outcome. *Cent Eur J Immunol* 40(4):481–485
28. Kros G, Korbelik M, Dougherty GJ (1995) Induction of immune cell infiltration into murine SCCVII tumour by photofrin-based photodynamic therapy. *Br J Cancer* 71(3):549–555
29. Hübner M et al (2015) IMPS-15-PDT-treated GBM cells increase effector functions of human CD8⁺ T-cells. *Neurooncology* 17(suppl5):v116–v116

Publisher's Note Springer Nature remains neutral with regard to jurisdictional claims in published maps and institutional affiliations.

Springer Nature or its licensor (e.g. a society or other partner) holds exclusive rights to this article under a publishing agreement with the author(s) or other rightsholder(s); author self-archiving of the accepted manuscript version of this article is solely governed by the terms of such publishing agreement and applicable law.

Article

Interstitial Photodynamic Therapy of Glioblastomas: A Long-Term Follow-up Analysis of Survival and Volumetric MRI Data

Marco Foglar ^{1,†} , Maximilian Aumiller ^{1,2} , Katja Bochmann ^{3,4}, Alexander Buchner ² , Mohamed El Fahim ¹, Stefanie Quach ⁵, Ronald Sroka ^{1,2}, Herbert Stepp ^{1,2} , Niklas Thon ⁵, Robert Forbrig ^{4,‡}  and Adrian Rühm ^{1,2,*,‡}

¹ Laser-Forschungslabor, LIFE Center, University Hospital, LMU Munich, 81377 Munich, Germany

² Department of Urology, University Hospital, LMU Munich, 81377 Munich, Germany

³ Max Planck Institute for Psychiatry, Max Planck Society, 80804 Munich, Germany

⁴ Institute of Neuroradiology, University Hospital, LMU Munich, 81377 Munich, Germany

⁵ Department of Neurosurgery, University Hospital, LMU Munich, 81377 Munich, Germany

* Correspondence: adrian.ruehm@med.uni-muenchen.de; Tel.: +49-89-4400-74882

† Part of the inaugural thesis of M.F. is to be submitted to the medical faculty of LMU Munich.

‡ This study is guided by R.F. and A.R. equally; thus both serve as shared last authors.

Simple Summary: Glioblastomas are the most common primary malignant brain tumors, with a devastating survival perspective. The treatment concept of interstitial photodynamic therapy (iPDT) enables the light-induced destruction of tumor cells based on the combination of a photosensitizer that selectively accumulates in the tumor and light to activate the photosensitizer. The tumor region is illuminated by minimally invasively inserted optical fibers. Under this approach, prolonged overall survival was observed. An analysis of the patient characteristics and the evolution of the MRI data before treatment and during follow-up was performed to identify potential predictors of an improved survival outcome. It was found that the methylation status of the DNA-repair enzyme MGMT is an important factor regarding survival. Other commonly assessed parameters, such as the tumor volume, necrosis–tumor ratio, and contrast enhancement after therapy, did not seem to significantly affect survival. Overall, the iPDT-treated patients showed very promising results regarding a sustained absence of their tumors and prolonged overall survival.

Abstract: Background: The treatment of glioblastomas, the most common primary malignant brain tumors, with a devastating survival perspective, remains a major challenge in medicine. Among the recently explored therapeutic approaches, 5-aminolevulinic acid (5-ALA)-mediated interstitial photodynamic therapy (iPDT) has shown promising results. Methods: A total of 16 patients suffering from de novo glioblastomas and undergoing iPDT as their primary treatment were retrospectively analyzed regarding survival and the characteristic tissue regions discernible in the MRI data before treatment and during follow-up. These regions were segmented at different stages and were analyzed, especially regarding their relation to survival. Results: In comparison to the reference cohorts treated with other therapies, the iPDT cohort showed a significantly prolonged progression-free survival (PFS) and overall survival (OS). A total of 10 of 16 patients experienced prolonged OS (≥ 24 months). The dominant prognosis-affecting factor was the MGMT promoter methylation status (methylated: median PFS of 35.7 months and median OS of 43.9 months) (unmethylated: median PFS of 8.3 months and median OS of 15.0 months) (combined: median PFS of 16.4 months and median OS of 28.0 months). Several parameters with a known prognostic relevance to survival after standard treatment were not found to be relevant to this iPDT cohort, such as the necrosis–tumor ratio, tumor volume, and posttreatment contrast enhancement. After iPDT, a characteristic structure (iPDT remnant) appeared in the MRI data in the former tumor area. Conclusions: In this study, iPDT showed its potential as a treatment option for glioblastomas, with a large fraction of patients having prolonged OS. Parameters of prognostic relevance could be derived from the patient characteristics and MRI data, but they may partially need to be interpreted differently compared to the standard of care.



Citation: Foglar, M.; Aumiller, M.; Bochmann, K.; Buchner, A.; El Fahim, M.; Quach, S.; Sroka, R.; Stepp, H.; Thon, N.; Forbrig, R.; et al. Interstitial Photodynamic Therapy of Glioblastomas: A Long-Term Follow-up Analysis of Survival and Volumetric MRI Data. *Cancers* **2023**, *15*, 2603. <https://doi.org/10.3390/cancers15092603>

Academic Editor: Hajime Isomoto

Received: 6 February 2023

Revised: 19 March 2023

Accepted: 20 March 2023

Published: 4 May 2023



Copyright: © 2023 by the authors. Licensee MDPI, Basel, Switzerland. This article is an open access article distributed under the terms and conditions of the Creative Commons Attribution (CC BY) license (<https://creativecommons.org/licenses/by/4.0/>).

Keywords: 5-ALA; glioblastoma; imaging; long term; malignant glioma; MGMT; MRI; photodynamic therapy; recurrence; stereotactic surgery

1. Introduction

Glioblastoma multiforme (2016 WHO CNS, grade IV) is the most frequent primary malignant neoplasia of the CNS [1]. With its devastating median overall survival (OS) of 14.6 months [2], based on a variety of therapeutic resistances [3,4] and its highly invasive growth [5,6], its treatment remains a formidable challenge in modern medicine.

The current standard of care (SOC) involves maximal safe resection followed by chemoradiation [2,7]. Despite the recent advances in resection with fluorescence-guided surgery [8,9], the prognosis remains daunting. Additionally, patients with tumors located in eloquent or deep-seated areas are often excluded from receiving that form of treatment [10]. To address this issue and to potentially prolong survival while preserving an adequate quality of life, several new approaches were explored based on minimally or noninvasive procedures, such as brachytherapy, tumor-treating fields, radiosurgery, and definitive chemoradiation [10–13].

Among these approaches, 5-aminolevulinic acid (5-ALA)-mediated interstitial photodynamic therapy (iPDT) was identified as a promising option building on standard stereotactic procedures [14–17]. Patients receive 5-ALA as a prodrug to achieve the intracellular synthesis of a photosensitizing molecule (protoporphyrin IX, PpIX). Due to an impaired blood–brain barrier within the tumor region and a derailed metabolism in the tumor cells, PpIX accumulates selectively in the malignant cells [18–20]. After the minimally invasive placement of optical diffuser fibers, the target tissue is illuminated with laser light. To activate the photosensitizer, light of a wavelength adopted to the absorption characteristic of the photosensitizer has to be applied. In the case of PpIX, a wavelength of 635 nm is recommended [21]. The light-based excitation of PpIX induces the production of reactive oxygen species (especially singlet oxygen), which damages and, finally, kills the neoplastic cells [22]. In comparison with the SOC, no craniotomy is required. Instead, the devitalized tumor mass remains harmlessly in situ. Another advantage is that the healthy tissue is preserved due to the tumor-selective accumulation of PpIX [18]. After iPDT, prolonged median OS (≥ 24 months) has been observed [14,17,23], although the reasons for this encouraging observation are not yet fully understood.

The effects of iPDT on a tumor and its environment are still under investigation due to the plenitude of involved processes. An immunogenic response may be involved as suggested in a variety of applications of photodynamic therapy (PDT) [24–30].

To understand the complex processes induced by iPDT, the available data need to be assessed and analyzed systematically. In this study, imaging data, patient characteristics, and molecular biological information were collected and evaluated retrospectively. Due to the fundamentally different principle of iPDT compared to the SOC, quite different findings in the imaging data may be expected. Therefore, an inspection of the peculiarities in the MRI data obtained after iPDT was performed. The characteristic differences from the typical imaging findings after performing conventional therapies were described. To determine potentially survival-related factors, various accessible parameters were examined for correlations with the survival data. With this, the study also strived to explore the potential of iPDT, to motivate further research on this important topic, and to lay a foundation for future investigations.

2. Patients and Methods

2.1. Patients

The retrospectively analyzed cohort consisted of 16 patients who underwent 5-ALA-mediated iPDT [17]. This procedure was offered to patients suffering from biopsy-proven de novo glioblastomas for whom an SOC treatment was impossible due to the location

of the tumor or other contraindications. Instead of definitive chemoradiation [10], iPDT combined with a fractionated 60 Gy radiation therapy and temozolomide (according to Stupp [2]) was offered as salvage treatment [17].

These procedures were performed between 2008 and 2014, providing the opportunity to observe the patients' course over the long term. This retrospective analysis of the available data was approved by the institutional review board of the Faculty of Medicine at the Ludwig–Maximilians–Universität München, Munich, Germany (ethics approval No. 335–16).

The presented patient cohort features a median age at diagnosis of 65.8 years (range: [29.7; 76.5] years) and a median tumor volume of 6063 mm³ (range: [1362; 21,825] mm³). The last follow-up date included in the present analysis was 12 January 2022. At that time, there were three survivors with a median follow-up after diagnosis of 113.9 months (range: [110.3; 127.5] months). All three remained progression-free during that period. Patient information and individual outcomes are summarized in Table 1.

Table 1. Patient characteristics and individual outcomes (values rounded, contains selected and, on the other hand, partially extended information in comparison to Table 1 of Quach et al. [17]).

IPDT No. (♂ PFS, † OS)	Sex (m/f)	Age at PDT (Years)	PFS (Months)	OS (Months)	PPS (Months)	Status
IPDT 01 (♂ 65, † 102)	m	29.7	64.7	102.4	37.4	†
IPDT 02 (♂ 59, † 95)	m	40.6	59.2	95.0	35.5	†
IPDT 03 (128)	f	50.3	127.1 *	127.5 *	-	A
IPDT 04 (♂ 8, † 15)	m	69.9	8.3	15.0	6.3	†
IPDT 05 (♂ 12, † 16)	m	68.2	12.0	16.1	3.5	†
IPDT 06 (♂ 4, † 9)	m	63.7	4.3	9.0	3.8	†
IPDT 07 (110)	m	70.1	110.1 *	110.3 *	-	A
IPDT 08 (♂ 61, † 66)	f	74.1	60.6	66.4	5.4	†
IPDT 09 (114)	m	33.3	113.6 *	113.9 *	-	A
IPDT 10 (♂ 16, † 28)	f	74.3	16.4	28.0	10.9	†
IPDT 11 (♂ 6, † 9)	m	68.8	6.0	8.5	2.1	†
IPDT 12 (♂ 7, † 8)	m	68.0	6.5	8.0	1.2	†\REC
IPDT 13 (♂ 10, † 25)	f	57.3	9.5	25.2	15.3	†
IPDT 14 (♂ 36, † 44)	m	54.3	35.7	43.9	7.8	†
IPDT 15 (♂ 7, † 9)	m	76.5	7.4	9.2	1.5	†
IPDT 16 (♂ 18, † 36)	m	53.4	17.8	36.4	18.2	†
Median		65.8	16.4 ^a	28.0 ^a	6.3 ^a	
Average		59.5	43.1 ^a	52.9 ^a	11.5 ^a	
Max		76.5	127.1	127.5	37.4	
Min		29.7	4.3	8.0	1.2	

PFS = ♂ = progression-free survival, OS = † = overall survival, PPS = postprogression survival, m = male, f = female, † = deceased with recurrence, †\REC = deceased without recurrence (palliative discharge), A = alive, * = last follow-up (survivors are still progression-free), and ^a = value calculated through Kaplan–Meier survival analysis in SPSS.

Further clinical aspects regarding these patients can be found in Quach et al. [17]. Details about tumor characteristics and the applied adjuvant therapy are summarized in Table 2.

Table 2. Tumor characteristics and additional therapy regimes (contains selected and, on the other hand, extended information in comparison to Table 1 of Quach et al. [17]).

IPDT No. (⊕ PFS, + OS)	MGMT Methylation ^b	IDH1	IDH2	Ki67	Tumor location	Side	TMZ during Radiation	TMZ Cycles after Radiation
IPDT 01 (⊕ 65, + 102)	yes	yes	no	n/a	frontal supraventricular	right	yes	7
IPDT 02 (⊕ 59, + 95)	no	no	no	10%	temporoparietal	left	partially	2
IPDT 03 (128)	yes	no	no	10%	temporo- occipital	left	yes	9
IPDT 04 (⊕ 8, + 15)	no	no	no	30%	temporal	left	yes	0
IPDT 05 (⊕ 12, + 16)	no	no	no	10–15%	frontal	left	yes	2
IPDT 06 (⊕ 4, + 9)	no	no	no	20%	temporal	right	yes	0
IPDT 07 (110)	yes	no	no	25%	temporal	left	yes	0
IPDT 08 (⊕ 61, + 66)	no	no	no	25%	median frontal gyrus	left	yes	3
IPDT 09 (114)	partially	yes	no	85%	temporal	left	yes	4
IPDT 10 (⊕ 16, + 28)	no	no	no	30%	central gyrus and subcentral lobe	left	yes	0
IPDT 11 (⊕ 6, + 9)	no	no	no	21%	superficial parietal gyrus	left	no	0
IPDT 12 (⊕ 7, + 8)	yes	no	no	7%	parieto-occipital	left	yes	2
IPDT 13 (⊕ 10, + 25)	partially	no	no	15%	temporoparietal	left	partially	4
IPDT 14 (⊕ 36, + 44)	yes	no	no	15%	parieto-occipital	left	partially	8
IPDT 15 (⊕ 7, + 9)	no	no	no	10%	temporal/parietal	left	n/a	n/a
IPDT 16 (⊕ 18, + 36)	yes	no	no	28%	parietal	left	yes	5

PFS = ⊕ = progression-free survival, OS = + = overall survival, n/a = data not available, and ^b = grouping: MGMT unmethylated vs. MGMT methylated (partially and fully).

Glioblastomas show a variety of therapeutic resistances due to their heterogeneous genetic profiles [3,4]. Consequently, new classification criteria were released recently (WHO CNS5) [31]. Since not all tumor characteristics were determined at the time of treatment for the patient cohort reported, the previous classification scheme (2016 CNS WHO) was applied [32], tolerating conceivable changes in classification. The available tumor characteristics of the cohort are shown in Table 2.

Among the regularly recorded MRI scans (in general, every three months), imaging datasets recorded at five specific points of time were selected for this analysis: before treatment, twenty-four hours after treatment, three months after treatment, three months prior to relapse (preceding follow-up, defined retrospectively), and at diagnosis of recurrence. At each instance, the results of three different MRI sequences were analyzed: noncontrast and contrast-enhanced T1-weighted imaging and T2-weighted imaging. Volumes and volume ratios derived from these images are summarized in Supplementary Table S1.

2.2. Methods

2.2.1. Survival Analysis

Progression-free survival (PFS) was defined as the shortest of the three periods from treatment to radiologically identified progression, palliative discharge, or (censored) end of follow-up. Overall survival (OS) was defined as the shortest of the two periods from diagnosis to death (with or without progression) or (censored) end of follow-up. Postprogression survival (PPS) was defined as the period from diagnosis of progression to death or (censored) end of follow-up.

In the literature, no consistent definition of long-term survival for patients with de novo glioblastomas can be found. Suggested values range from 18 to 60 months [33,34]. In numerous publications, the two-year mark is used as a threshold criterion [35–39]. Based on this, the term “prolonged OS” was decided to be used for patients surviving for at least 24 months after diagnosis (OS) or without progression after iPDT (PFS), respectively. The validity of the chosen term was reaffirmed through a meta-analysis reporting a two-year OS for only 18% (95% CI = [0.14; 0.22]) of the treated glioblastomas [40].

Within the iPDT cohort, the patients’ survival, based on their MGMT-methylation status, was examined. In addition, a comparative evaluation was performed with regard to other patient cohorts who, instead of iPDT, received SOC treatment, a sole chemoradiation treatment, CyberKnife® (Accuray, Sunnyvale, CA, USA) surgery, and stereotactic radiosurgery, respectively [2,10–12].

2.2.2. MRI Analysis

Prior to analyzing the images, different preprocessing routines were applied. First, MRI data recorded at different time points were positionally registered to each other. This was performed automatically using the ANTs software package (v2.3.2, University of Pennsylvania, Philadelphia, PA, USA; University of Virginia, Charlottesville, VA, USA; and University of Iowa, Iowa City, IA, USA) [41] followed by manual checks and adjustments. Subsequently, the MRI datasets were semiautomatically segmented using ITK-SNAP (v3.8, University of Pennsylvania, Philadelphia, PA, USA) [42]. All images, adjustments, and segmentations were checked by two experienced neuroradiologists from the Institute of Neuroradiology of the LMU Hospital, Munich (R.F. and K.B.). Volumes of interest are shown exemplarily for one patient (IPDT 14) in Figure 1, such as the tumor volume (consisting of a T1-contrast-enhancing region and a necrotic region), edema, and iPDT remnant. This iPDT remnant appears after treatment and is described and discussed below. For one patient (IPDT 07), the iPDT treatment needed to be performed in two separate sessions, one week apart, due to the tumor’s volume and morphology. Due to this peculiarity, this iPDT treatment did not qualify for the combined analysis of MR images recorded on the first day after treatment. For all other patients, the MR images recorded at this time point could be included in the analysis.

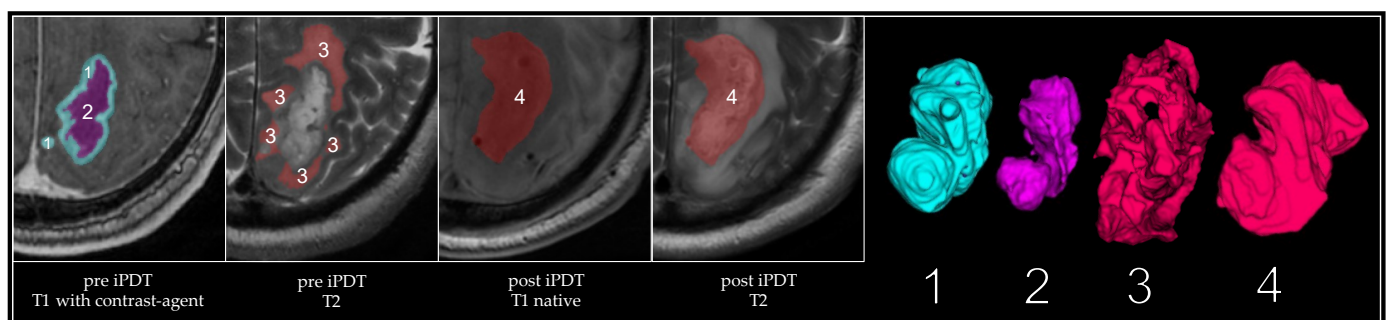


Figure 1. Segmented volumes indicated by color overlays in MR images (T1 and T2 sequences), and separate images indicate 3D volume (1: T1-contrast-enhancing volume) (2: necrotic volume) (1 + 2: tumor volume) (3: edema) (4: iPDT remnant), exemplarily shown for one patient (IPDT 14).

Segmented volumes were rounded to full mm³ since a higher accuracy is not meaningful based on the physical imaging resolution. The necrosis–tumor ratio (NTR) was calculated for the pretreatment situation by dividing necrosis volume by tumor volume, corresponding to Henker et al. [43].

2.2.3. Statistics

Information about the segmented volumes, the patients' individual courses, and clinical parameters was collected in a database. Patients were then divided into subcohorts by recurrence type (local vs. distant) and the methylation status of the MGMT promoter (full/partial methylation vs. no methylation). A double-sided log-rank test was applied to evaluate the statistical significance of differences between each pair of survival curves. Survival analysis was performed using SPSS (v29, IBM Corp., Armonk, NY, USA) [44]. Due to the relatively small number of patients, extensive correlational testing was not feasible. To identify potentially important parameters and relations, the obtained parameters were plotted against survival values using the statistical programming language R (v4.2.1, R Core Team, Vienna, Austria) [45] and the R visualization package GGPlot2 (v3.3.6, Wickham, 2016) [46]. Data plots that seemed to contain an important message were selected for display and further analysis. Univariate Cox regression analysis was performed to investigate the validity of the visually derived conclusions. Along with the *p*-values, the hazard ratios (HR) are shown in Supplementary Table S2.

Since the decease was seen as the most relevant endpoint for the patients, it was decided to restrict the investigations regarding survival-related factors to OS, or PFS in exceptional cases. An analysis primarily focused on PFS and long-term PFS (>24 months) of the iPDT cohort can be found in Quach et al. [17]. For all comparisons, significance level $\alpha = 0.05$ was appointed.

The survival data of some of the compared patient cohorts had to be extracted from published Kaplan–Meier graphs as numeric data using Engauge Digitizer [47] and had to be subsequently reconstructed into a per-patient format using the programming language R [45]. After a plausibility check, a statistical analysis was performed in comparison to the iPDT cohort. A limitation of this approach was that censored survival data could not be identified and included in survival analysis. Hence, the respective *p*-values should be seen as an estimation. A comparison of the published survival parameters and the corresponding parameters recalculated based on reconstructed data can be found in Supplementary Table S3. Besides this limitation, this method enabled a comparison with other patient cohorts for which the detailed original data are unavailable. Whenever original per-patient data of other patient cohorts were available, they were used directly for the comparative analyses.

3. Results

3.1. Survival

The iPDT-treated cohort showed a median PFS of 16.4 months (95% CI: [5.1; 27.6] months) and a median OS of 28.0 months (95% CI: [6.0; 50.0] months) [17]. The median PPS was 6.3 months (95% CI: [1.6; 11.0] months); see Figure 2 and Table 3. Three patients are still alive (IPDT 03: 128 months) (IPDT 07: 110 months) (IPDT 09: 114 months), and none of them have experienced a recurrence [17]. The survival times (OS, PFS, PPS) obtained with iPDT are compared with those of the patient cohorts treated with other methods in Table 3, and the *p*-values obtained through the pairwise log-rank testing of the differences among some of these survival times are listed in Table 4.

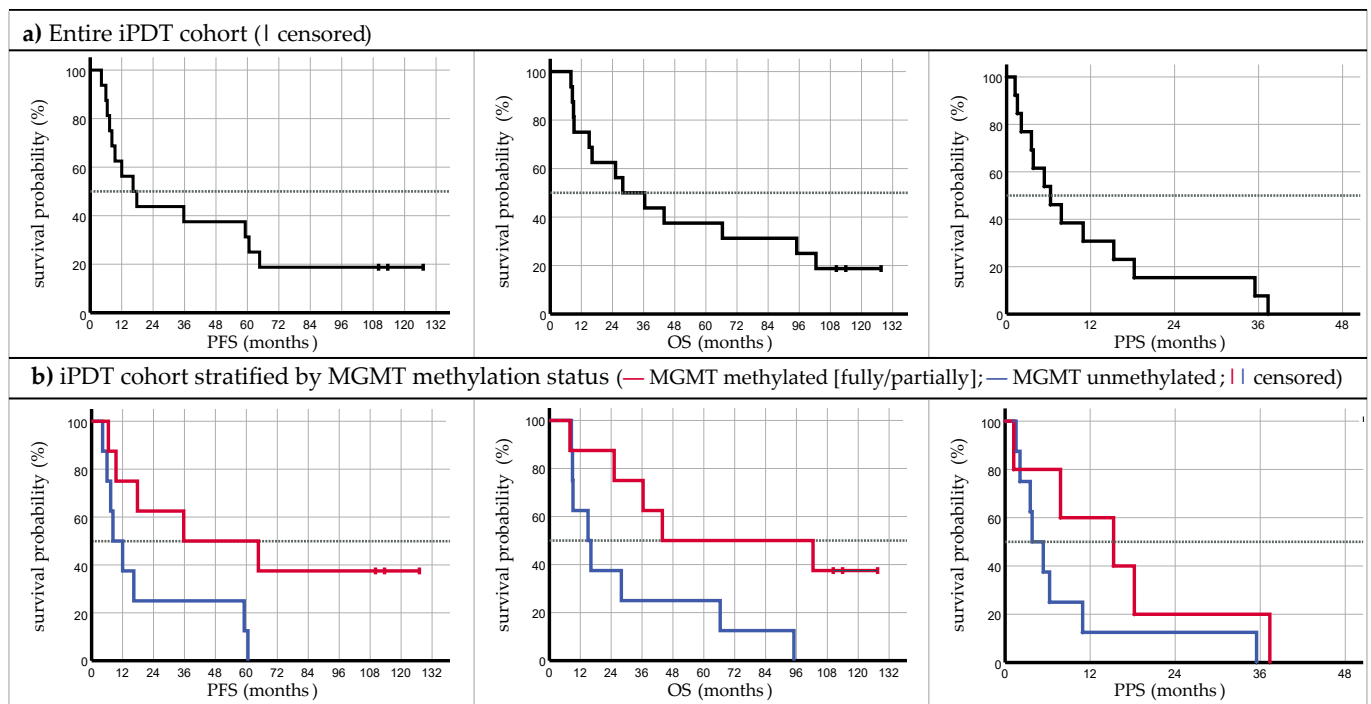


Figure 2. Kaplan–Meier plots related to PFS, OS, and PPS of the (a) iPDT cohort as a whole and (b) stratified by MGMT methylation status.

Table 3. Survival times, OS, PFS, and PPS (median, [95% CI]), obtained for the iPDT cohort in this study, overall and split according to MGMT promoter methylation, in comparison to survival times reported for other therapeutic methods in the literature.

		iPDT All Cases	iPDT MGMT Unmethylated	iPDT MGMT Methylated	Stupp [2] ^c	Chemoradiation [10] ^d	CyberKnife® [12] ^d	Stereotactic Radiosurgery [11] ^c
Subjects (n)		16	8	8	287	56	12	30
PFS (months)	Median [95% CI]	16.4 [5.1; 27.6]	8.3 [1.9; 14.7]	35.7 [0.0; 100.7]	6.9 [5.8; 8.2]	8.0 [5.6; 10.4]	16.0 [10.4; 21.6]	8.2 [4.6; 10.5]
OS (months)	Median [95% CI]	28.0 [6.0; 50.0]	15.0 [5.3; 24.7]	43.9 [0.0; 135.4]	14.6 [13.2; 16.8]	12.0 [9.6; 14.4]	18.0 [10.9; 25.1]	14.8 [10.9; 19.9]
PPS (months)	Median [95% CI]	6.3 [1.6; 11.0]	3.8 [1.3; 6.4]	15.3 [0.0; 31.4]	n/a	4.0 [3.0; 5.0]	3.0 [2.0; 4.0]	n/a

PFS = progression-free survival, OS = overall survival, PPS = postprogression survival, CI = confidence interval, n/a = data not available, ^c = values from publication, and ^d = values calculated.

Table 4. *p*-values according to pairwise log-rank testing (SPSS) of differences among some of the survival times listed in Table 3. Significant differences are highlighted with **boldface** formatting.

	iPDT MGMT Methylated vs. Unmethylated	iPDT vs. Stupp [2]	iPDT vs. Chemoradiation [10]	iPDT vs. CyberKnife® [12]	iPDT vs. Stereotactic Radiosurgery [11]
PFS	0.030	<0.001	0.005	0.341	n/a
OS	0.031	0.017	0.022	0.280	0.036
PPS	0.192	n/a	0.516	0.237	n/a

PFS = progression-free survival, OS = overall survival, and PPS = postprogression survival.

Stratifying the iPDT cohort by the *MGMT promoter methylation status* revealed significantly superior PFS in the case of a methylated *MGMT* promoter (median of methylated *MGMT* of 35.7 months vs. median of unmethylated *MGMT* of 8.3 months; $p = 0.030$). Similarly, OS was significantly longer in the case of a methylated *MGMT* promoter (median of methylated *MGMT* of 43.9 months vs. median of unmethylated *MGMT* of 15.0 months; $p = 0.031$). PPS appeared to be more favorable for the methylated group, but the difference was not statistically significant according to log-rank analysis (median of methylated *MGMT* of 15.3 months vs. median of unmethylated *MGMT* of 3.8 months; $p = 0.192$). Through a univariate Cox regression analysis, as in Quach et al. [17], the *MGMT* status was found to be a potentially survival-related parameter with a significant reduction in the risk of death for patients with a methylated *MGMT* promoter ($p = 0.042$; hazard ratio (HR) = 0.280; 95% CI of HR = [0.082; 0.956]).

When comparing the entire iPDT cohort with the *standard-of-care (SOC)* cohort according to Stupp et al. ($n = 287$) [2], the iPDT cohort showed superior PFS (median of iPDT of 16.4 months vs. median of Stupp of 6.9 months; $p < 0.001$) and OS (median of iPDT of 28.0 months vs. median of Stupp of 14.6 months; $p = 0.017$). For the Kaplan–Meier plots, see Supplementary Figure S1.

A comparison of iPDT with a *sole chemoradiation treatment* ($n = 56$) [10] also revealed superior PFS (median of iPDT of 16.4 vs. median of chemoradiation of 8.0 months; $p = 0.005$) and OS (median of iPDT of 28.0 months vs. median of chemoradiation of 12.0 months; $p = 0.022$) for the iPDT cohort. No significant difference in the PPS values was found (median of iPDT of 6.3 months vs. median of chemoradiation of 4.0 months; $p = 0.516$).

In comparison with the *CyberKnife® surgery* ($n = 12$) [12], no significant differences could be discovered (median PFS of iPDT of 16.4 months vs. median PFS of CyberKnife® surgery of 16.0 months; $p = 0.341$) (median OS of iPDT of 28.0 months vs. median OS of CyberKnife® surgery of 18.0 months; $p = 0.280$) (median PPS of iPDT of 6.3 months vs. median PPS of CyberKnife® surgery of 3.0 months; $p = 0.237$).

Lastly, in comparison with the *stereotactic radiosurgery* ($n = 30$) [11], iPDT featured superior OS (median of iPDT of 28.0 months vs. median of stereotactic radiosurgery of 14.8 months; $p = 0.036$).

Side effects mainly consisted of transient health restrictions such as aphasia. In one case, a pulmonary embolism was seen [17,48]. However, it is important to note that iPDT is not necessarily accountable for the embolism. Brain tumor patients generally bear significant risk factors for thromboembolic events, such as the preexisting malignancy itself, often having an advanced age, and immobilization due to the disease or treatment [49].

3.2. Volumetric Assessments

The time courses of contrast-enhanced T1-weighted MRIs are exemplarily shown for two patients in Figure 3. Both patients experienced prolonged OS and also a PFS of more than 24 months. The first patient (iPDT 02, PFS of 59.2 months, OS of 95.0 months) exhibited a tumor volume of 1362 mm³. Before treatment, the tumor comprised a T1 contrast enhancement (CE) volume of 878 mm³ and a necrosis volume of 484 mm³. At 24 h after iPDT, a small CE volume (22 mm³) remained. Three months after iPDT, no evidence of CE was found. The second patient (iPDT 14, PFS of 35.7 months, OS of 43.9 months) featured a tumor volume of 15,335 mm³ (CE volume of 8929 mm³ and necrosis volume of 6406 mm³). At 24 h after iPDT, a CE volume of 4720 mm³ remained. Three months after iPDT, no evidence of CE was found in this patient.

The statistical information (median, average, minimum, maximum, and standard deviation) on the volumes of these and other distinguishable tissue regions is collected in Table 5. The individual values for each patient are provided in Supplementary Table S1.

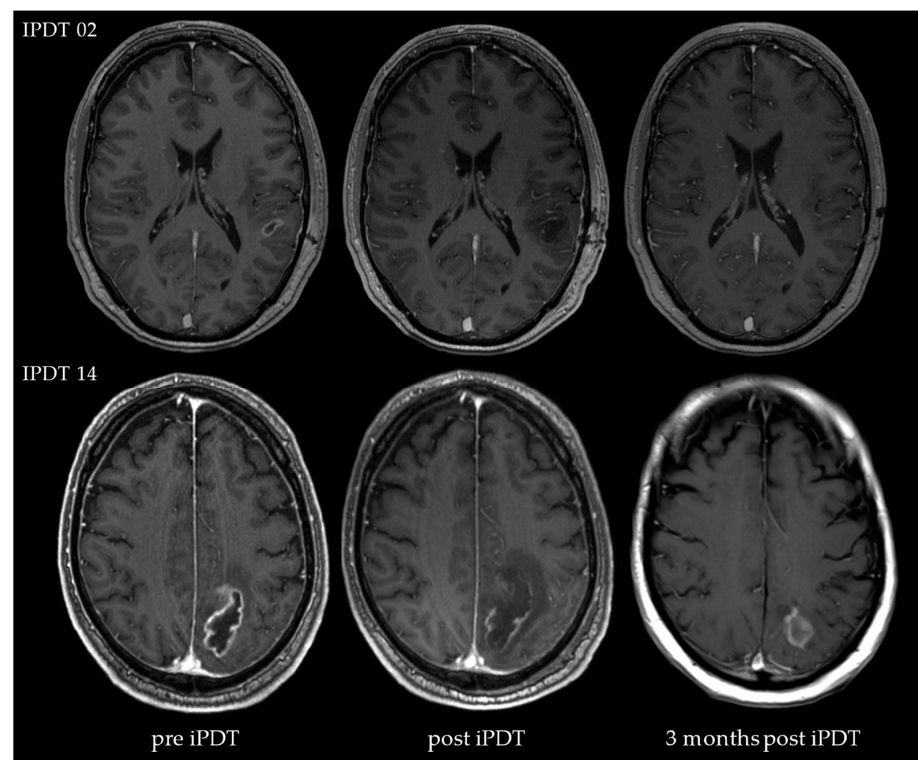


Figure 3. Two exemplary courses of MR images (T1-weighted with contrast agent) recorded before iPDT, twenty-four hours after iPDT, and three months after iPDT (patient IPDT 02 and IPDT 14).

Table 5. Course of different tumor-related volumes of interest for the iPDT-treated patient cohort (values rounded to full mm²).

Volume	Tumor Pre iPDT (mm ³)	CE Pre iPDT (mm ³)	Necrosis Pre iPDT (mm ³)	CE 1 Day Post iPDT (mm ³)	iPDT Remnant 1 Day Post iPDT (mm ³)	iPDT Remnant 3 Months Post iPDT (mm ³)	iPDT Remnant 3 Months Pre Recurrence (mm ³)	iPDT Remnant at Recurrence (mm ³)	Recurrent Tumor at Recurrence (mm ³)
Median	6063	3533	1350	535	12,426	5585	4036	3914	5893
Average	7622	5180	2442	1108	19,166	7151	4474	4556	6645
Max	21,825	12,362	9463	4720	66,857	20,027	12,254	9607	17,177
Min	1362	878	118	0	2062	370	305	157	6
SD	5849	3761	2579	1463	16,571	5395	3188	2917	6115

CE = contrast enhancement; SD = standard deviation.

The median tumor volume to be treated was 6063 mm³ (range: [1362; 21,825] mm³), consisting of a contrast-enhancing region (median volume of 3533 mm³; range of [878; 12,362] mm³) and a necrotic region (median volume of 1350 mm³; range of [118; 9463] mm³). At 24 h after iPDT, 13 patients showed residual CE. Collectively, over all 15 evaluable cases, the median volume of residual CE was 535 mm³ (range: [0; 4720] mm³). In seven patients, residual CE at the former tumor location was still present after three months.

In the MR images recorded 24 h after iPDT, morphological changes appeared in the native T1- and T2-weighted images around the former tumor location (labelled as volume “4” in Figure 1). The affected region (presenting as circumscribed predominantly T1 hypointensity and T2 hyperintensity) was defined as an “iPDT remnant”, representing the devitalized tumor residing in situ. This region featured a median volume of 12,426 mm³ (range: [2062; 66,857] mm³). In 14 patients, the iPDT remnant was larger than the original tumor; in 1 patient, the remnant was smaller.

At the first follow-up (typically 3 months after iPDT), the median iPDT remnant volume decreased to 5585 mm³ (range: [370; 20,027] mm³). In four cases, the remnant

remained larger than the original tumor. In eight cases, the remnant shrank to a volume smaller than the original tumor. In the remaining four cases, no MRI data were available at this point of time. Among the 12 patients who experienced a recurrence, 3 months prior to the relapse, the median iPDT remnant volume decreased even further to 4036 mm³ (range: [305; 12,254] mm³). In 2 of these 12 cases, the remnant was larger than the original tumor; in 7 cases, the remnant was smaller. The median iPDT remnant volume at the time of recurrence amounted to 3914 mm³ (range: [157; 9607] mm³). In three cases, the iPDT remnant at this time point was found to be bigger than the original tumor; in the remaining nine cases, the remnant was smaller.

The median volume of the 12 recurrent tumors was 5893 mm³ (range: [6; 17,177] mm³), consisting of 8 local and 4 distant relapses. The distant recurrences had a median distance of 29.5 mm to the margin of the iPDT-treated tumor (IPDT 06: 39 mm) (IPDT 08: 31 mm) (IPDT 13: 26 mm) (IPDT 14: 28 mm) (values rounded).

3.3. Relations between Observations

In Figure 4, the selected graphs are displayed to illustrate the possible relations between the different parameters and observations. For further information, see Tables 1,2 and S1 (for univariate Cox regression results, see Supplementary Table S2).

Figure 4a (for numeric values, see Table 1) displays the *age at diagnosis* vs. OS. Prolonged OS was seen in all the patients with an age under 60. For patients older than 60 years, three of nine cases still showed prolonged OS. ($p = 0.067$; HR = 1.038; 95% CI = [0.997; 1.080].) Although slightly missing significance, the resulting hazard ratio still suggests a worse OS prognosis for patients with a higher age at diagnosis.

Figure 4b (for numeric data, see Table 2) displays the *number of TMZ cycles after chemoradiation* vs. OS. OS below 24 months was only seen in the case of two or less TMZ cycles (typical cycle period of 1 month). Within this subgroup of two or less cycles, three of eight cases still showed prolonged OS. All the other patients showed prolonged OS ($p = 0.146$; HR = 0.859; 95% CI = [0.700; 1.055]).

Figure 4c (for numeric values, see Supplementary Table S1) displays the *necrosis–tumor ratio (NTR)* vs. OS. No pattern indicating a systematic relation could be derived in this case ($p = 0.540$; HR = 0.279; 95% CI = [0.005; 16.533]). The high p -value and the broad 95% CI also suggest that this cohort shows no correlation between the NTR and OS.

Figure 4d (for numeric values, see Table 1) displays the *PPS* vs. *PFS* values. It was observed that longer PFS was accompanied by longer PPS and vice versa ($p = 0.053$; HR = 0.938; 95% CI = [0.879; 1.001]). It is to be noted that only four of the seven patients with PFS > 24 months are included in this graph because three of them have not experienced progression. No further systematic trends could be found.

Six examples of tumor-related volumes lacking a clear trend in relation to OS are shown in Figure 5 (see also Supplementary Table S2), namely for the *tumor volume* (Figure 5a; $p = 0.653$; HR = 1.020; 95% CI = [0.935; 1.112]) and the *contrast-enhancing volume 24 h after iPDT* (Figure 5b; $p = 0.599$; HR = 1.096; 95% CI = [0.779; 1.541]). In addition, the volumes of the *iPDT remnant* are shown at the time points 24 h after iPDT (Figure 5c; $p = 0.401$; HR = 0.986; 95% CI = [0.954; 1.019]), 3 months after iPDT (Figure 5d; $p = 0.341$; HR = 0.946; 95% CI = [0.845; 1.060]), 3 months before recurrence (Figure 5e; $p = 0.051$; HR = 1.318; 95% CI = [0.998; 1.740]), and at recurrence (Figure 5f; $p = 0.156$; HR = 1.144; 95% CI = [0.950; 1.377]).

In Figure 6 (see also Supplementary Table S2), the distribution of the PFS and OS values is shown, stratified by MGMT promoter methylation and the presence of CE three months after iPDT. No correlation between the presence of CE and survival (PFS and OS) could be discerned (e.g., with regard to OS, $p = 0.223$, HR = 2.259, and 95% CI = [0.610; 8.363]). Additionally, the MGMT methylation status did not show any correlation with CE three months after iPDT.

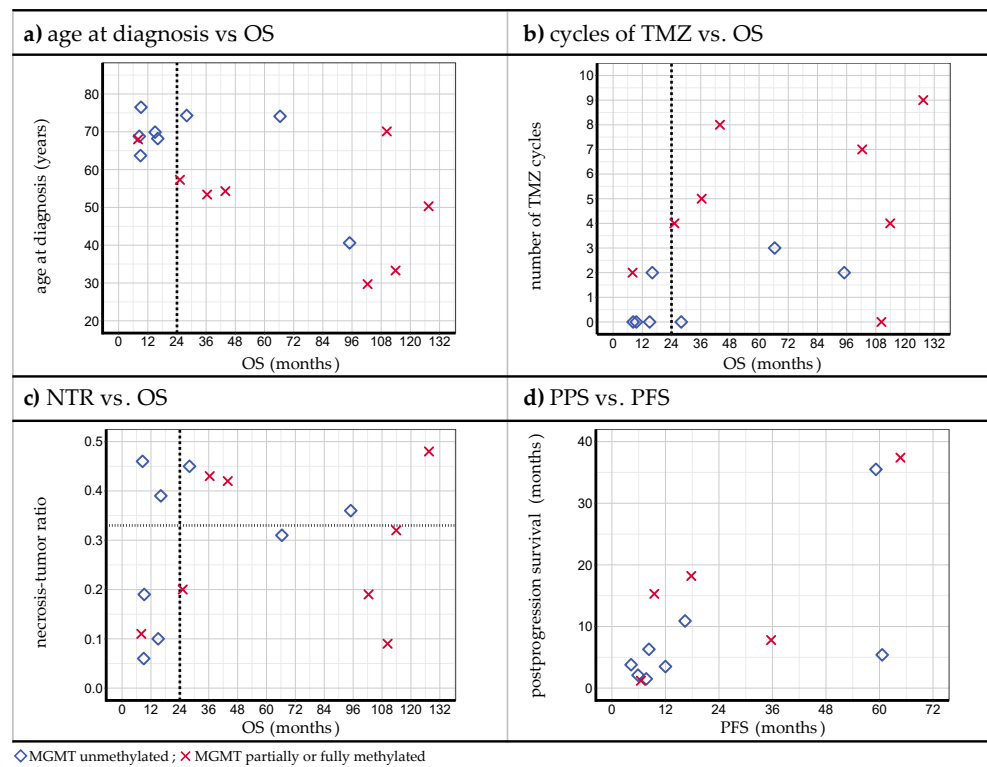


Figure 4. Plots of several parameters for the iPDT cohort vs. OS, (a) age at diagnosis, (b) number of TMZ cycles, and (c) necrosis–tumor ratio (NTR), and vs. PFS, (d) postprogression survival (PPS). The dashed vertical line in panels (a–c) marks the 24-month threshold value introduced to define prolonged OS. The dotted horizontal line in panel (c) represents the lower cutoff NTR value associated with a detrimental influence on survival in standard of care (SOC) as suggested by Henker et al. [43].

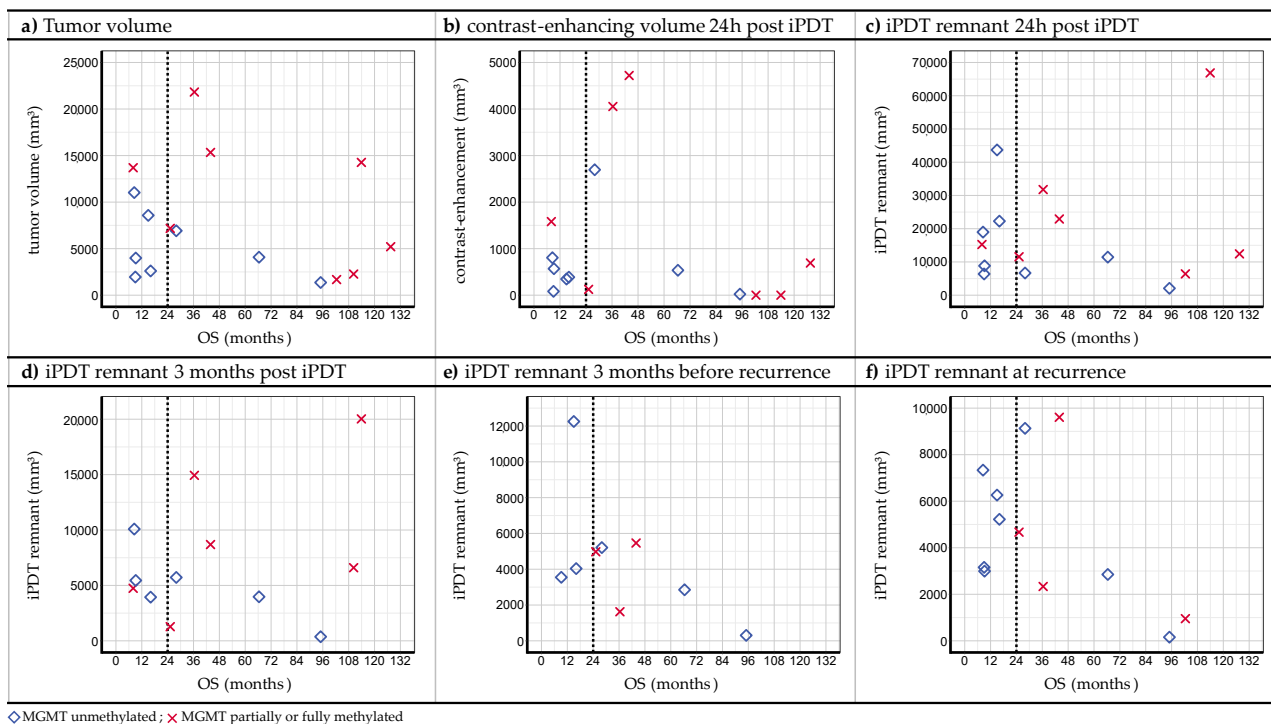


Figure 5. Plots of segmented volumes vs. OS, (a) tumor volume, (b) contrast-enhancing volume, and (c–f) iPDT remnant volume, determined at four different time points. The dashed vertical line marks the 24-month threshold value introduced to define prolonged OS.

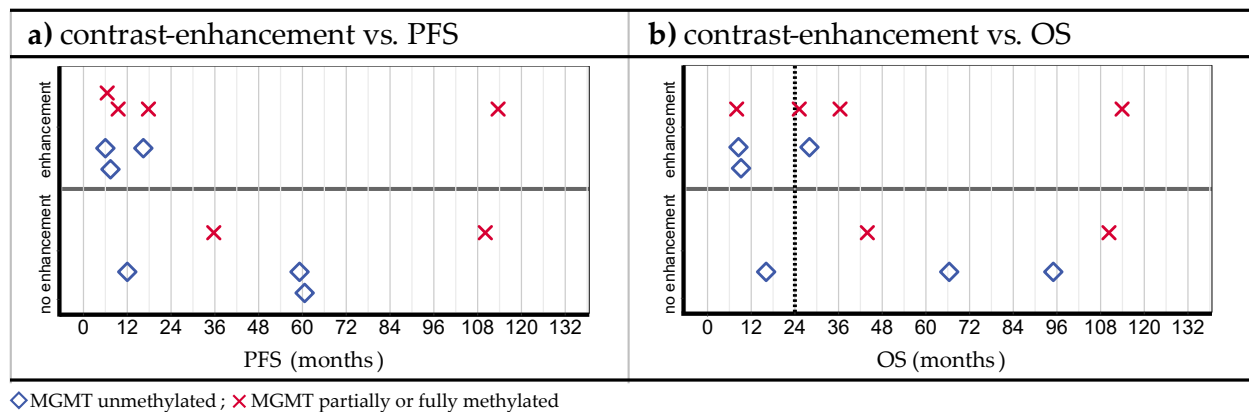


Figure 6. (a) Progression-free survival (PFS) and (b) overall survival (OS) stratified by the presence or absence of contrast enhancement 3 months after iPDT.

4. Discussion

4.1. Survival Comparison

Compared to the cohort of Stupp et al. [2], the iPDT cohort exhibited significantly longer median PFS and OS. This comparison to a prospective study with randomized arms must be interpreted cautiously due to the following limitations: The control of potential confounders was not sufficient in the iPDT cohort (e.g., age, symptomatology, the size of the tumor, and the impact of other molecular biological markers). Treated individuals were not selected randomly, and the overall number of treatments was small. Nonetheless, this comparison can help to estimate the survival outcome of iPDT treatments and motivates further investigations due to these promising results.

In comparison to the *chemoradiation-treated cohort* [10], the iPDT cohort also showed promising results. Again, these results must be interpreted cautiously, as the iPDT study lacked a prospective design. The patients were treated with iPDT due to the nonresectability of their tumors. The promising results after iPDT in this rather desperate clinical situation provide an outlook on the potential of iPDT treatments.

In comparison with *stereotactic radiosurgery* [11], prolonged OS could be confirmed for the iPDT cohort, outliving the SOC comparison cohort by an additional 13.2 months (based on the median OS values). This comparison can be seen as quite meaningful and relevant since both cohorts represent highly selected groups with a small number of cases. Still, the differences in the patient characteristics are apparent and need to be addressed in further studies.

Compared to the *CyberKnife*® treatment, the iPDT cohort outlived the SOC comparison cohort by an additional 10 months (based on the median OS values), although this result did not reach statistical significance. These cohorts did match well since a good overall status, a lack of randomization, and a small number of patients ($n = 12$) were shared by both cohorts.

Overall, it can be concluded that this specific iPDT cohort showed promising survival. This is a favorable fact which is highly worthwhile to be corroborated in further clinical trials such as NCT03897491. In further investigations, other minimally invasive therapy approaches should also be included in the survival comparison. Examples are seed-based brachytherapy [13,50] and laser-induced thermal therapy [51,52]. In contrast to iPDT, these therapies do not comprise tumor selectivity but rely on the optimal tailoring of the therapeutic effect to a predefined treatment volume that is to be destroyed entirely [13,50–52].

The *MGMT status* played a significant role in the treatment outcome of the iPDT cohort [17]. The iPDT patients with a methylated MGMT promoter outlived those with an unmethylated MGMT promoter by an additional 28.9 months (based on the median OS values), and they remained progression-free for an additional 27.4 months (based on the median PFS values).

Such survival advantages in the case of a methylated MGMT promoter have been reported for many other treatment approaches [10,53–56]. This is commonly attributed to a higher sensitivity of the tumor cells to adjuvant chemotherapy with temozolomide [54,57]. In the case of iPDT-treated recurrent glioblastomas, no survival benefit was found for a methylated MGMT promoter compared to an unmethylated MGMT promoter [16]. This might be due to a higher resistance of these patients' tumors to chemotherapy due to the inhibition of apoptosis [58] or an upregulation of the genes causing multidrug resistance [59,60]. Still, the cohort with recurrent glioblastomas showed promising survival [16]. Additionally, in comparison to the patient cohort suffering from newly diagnosed glioblastomas and being treated with chemoradiation as reported by Hegi et al. [56] (see Table 6), the iPDT cohort reported here showed superior survival both for methylated and unmethylated MGMT promoters. In conclusion, it seems that iPDT shows promising survival with an even stronger improvement in prognosis when the tumor has a higher sensitivity to temozolomide.

Table 6. Median survival values obtained separately for unmethylated and methylated MGMT promoters for iPDT in this study and for sole chemoradiation treatment [56] (values rounded).

	iPDT		Chemoradiation [56]	
	MGMT Unmethylated	MGMT Methylated	MGMT Unmethylated ^e	MGMT Methylated ^e
PFS median (months)	8.3	35.7	5.3	10.3
OS median (months)	15.0	43.9	12.7	21.7

PFS = progression-free survival, OS = overall survival, and ^e = values from publication.

4.2. Posttreatment CE

For the evaluation of the standard therapies, the course of posttreatment CE was an important aspect [61,62]. First, the observation that, 24 h after iPDT, CE was apparent in some patients is discussed with regard to its impact on the survival of the iPDT-treated patients and in relation to the common findings after the SOC.

After the SOC, the residual CE in the MRI data recorded within the first 72 h after open resection is associated with remaining vital tumor tissue [63]. This indicates an incomplete resection, suggesting that the complete resection of contrast-enhancing tumors (CRET) failed, which is associated with a significant reduction in OS [64–68]. Likewise, in case of iPDT, the residual CE in the early imaging after iPDT may, at first sight, be interpreted as an incomplete response, which, in turn, is generally considered as a negative predictive factor for survival [23]. However, no correlation of this observation in the MRI data with the therapy outcome could be derived from the present study (see Figure 5b), which is contrary to the respective statements in the review by Leroy et al. [23]. In the iPDT patient cohort of the present study, residual CE less than 72 h after iPDT was not significantly associated with inferior survival. This suggests that residual CE may not necessarily indicate residual vital tumor tissue but rather some remaining disturbance of the vasculature and the blood–brain barrier (BBB) after iPDT. This assumption relies on the core principle of the contrast agent that various conditions (e.g., tumors, ischemia, and autoimmune diseases) affect the BBB, thus allowing the agent to emerge [69,70]. In the case of residual CE after iPDT, it might indicate a remaining local alteration of the BBB in the treated tissue volume. This hypothesis is affirmed by the knowledge that 5-ALA mediated PDT has the potential to temporarily disrupt the BBB [71]. This may possibly help to enable immunogenic effects. The general role of the involvement of the immune system is known from other applications of the PDT [24–30]. The affected BBB might support or even enable the immune system to react on the glioblastoma tissue. A detailed understanding of this complex topic requires further investigation.

In any case, it must be concluded that the presence of CE 24 h after treatment is not well suited as a predictor of the completeness of response in the case of iPDT, at least not in the case of this particular iPDT-treated patient cohort. This can be seen as a paradigm shift for physicians and radiologists since a formerly clearly negative predictor is now to be interpreted more carefully.

Three months after iPDT, CE was found in seven patients around the former location of the tumor. Generally, CE beyond the 72-h threshold can either be associated with a reaction to the treatment or can indicate residing/progressive tumor tissue. This complicates the differentiation between a therapy reaction and tumor progression by means of conventional MRI sequences [63]. Similarly, in 20% to 30% of the SOC-treated patients, small changes in the contrast-enhancing regions or the edema were observed within the first 3 to 6 months after treatment [72]. This phenomenon of pseudoprogression is supposed to be based on postsurgical changes, radiation necrosis [73], and/or inflammation [74]. To differentiate these changes from a progressive disease, response assessment criteria for high-grade gliomas were developed based on the SOC data [61,62]. Since the role of CE after iPDT remains uncertain, an adjustment of the evaluation criteria for the case of iPDT should be pursued.

The role of residual CE after iPDT should also be examined regarding the supposed immunogenic response as observed in other applications of PDT [24–30].

4.3. iPDT Remnant

The composition of the iPDT remnant will remain unclear as long as the systematic analyses of posttreatment biopsies are lacking. Generally, it was found that the PDT treatment induces a mixture of apoptosis and necrosis [29,30,75–77]. Consequently, signatures of both processes may be expected in the iPDT remnant region. Investigating the iPDT remnant for apoptosis- and necrosis-related effects would be desirable for an enhanced understanding of the involved processes.

4.4. Recurrence Patterns

According to the literature, 90–95% of all glioblastomas reoccur within 2 cm from the primary tumor's margin as observed in a plenitude of other glioblastoma cohorts [78–82]. The remaining 5–10% of recurrences outside of that 2 cm margin may be termed distant recurrences. The high number of local recurrences might be due to insufficient local tumor cell eradication. One explanation could be that the tumor margins apparent in conventional MRI do not include the tumor cells spread into the local environment [83]. In the analyzed iPDT-treated cohort, 4 of the 12 recurrences (33%) were distant recurrences according to the criterion mentioned above. It may be concluded that a smaller fraction of local recurrences is observed after iPDT compared to other treatments. This suggests a superior sustained local tumor control (the permanent absence of vital tumor cells within the former tumor location and its surroundings) compared to other approaches. No correlation between the distance of the recurrence from the primary tumor and any other evaluated parameter could be found in this study. Potential reasons would need to be further investigated, for example, a better (or even complete) eradication of tumor cells due to the induction of an immunogenic response [24–30]. Besides the involvement of the immune system, there might be another explanation: Due to the oral application of 5-ALA, the photosensitizer PpIX could accumulate in all the tumor cells regardless of their location [18]. An uptake of the photosensitizer outside of the CE-based tumor margins, indicated by photosensitizer-specific fluorescence, was also observed in fluorescence-guided resection [84]. This means that the tumor cells in the surrounding of the MRI-based tumor volume also accumulated the photosensitizer, which made them vulnerable to illumination, while the physiological cells were preserved [22]. Although the used target fluence (18.72 J/mm^2 [15]) may not be reached in that tissue region, the photosensitizer may still become activated and cause cell damage and/or death to some extent. These two aspects may mutually reinforce each other. A detailed assessment and analysis of the immunogenic response to iPDT would be

desirable, especially in combination with examining other parameters, e.g., the supposedly compromised BBB (see Section 4.2).

4.5. Examination of Possibly Survival-Related Factors

In the case of resection, the following aspects are considered to be of prognostic importance: the patient's age, tumor volume, extent or completeness of tumor resection, degree of necrosis, involvement of the eloquent cortex or a deep structure, and pretreatment uptake of the contrast agent [68,85,86]. Additionally, the necrosis–tumor ratio (NTR) was also regarded as relevant for the prognosis [43].

For iPDT, a preoperative Karnofsky performance scale (KPS) score over 70, a well circumscribed roughly spherical lesion, and strong PpIX accumulation were seen as favorable factors [23]. Additionally, a complete response according to early posttreatment brain imaging (a major reduction in CE 24 h after iPDT) and a small tumor volume before treatment ($<5000\text{ mm}^3$) were reported to be beneficial to survival [23].

In the analyzed iPDT cohort, it was seen in Figure 4a that a *younger age at diagnosis* (<60 years) led to prolonged OS in all cases. This suggests that a younger age is a favorable predictive factor, which is consistent with the equivalent findings of the SOC [68,85,86]. Nonetheless, 3/9 patients (33%) with an age over 60 years experienced long-term survival. It can be concluded that an age <60 is a positive predictive factor, but a higher age still does not rule out a prolonged OS. Thus, iPDT seems to provide a favorable survival perspective for all age groups.

Concerning the number of *TMZ cycles* after iPDT (see Figure 4b), a higher number of cycles also seems to have a positive influence on the outcome. Here, longer OS might be confounded by an otherwise good health status and a correspondingly better toleration for chemotherapy. However, prolonged survival was also seen in combination with a low number of TMZ cycles, affirming considerable tumor eradication with iPDT by itself.

Surprisingly, the *necrosis–tumor ratio (NTR)* (see Figure 4c) does not seem to have any influence on the outcome. This observation is contrary to the SOC, where an NTR above 0.33 is seen as a negative predictor regarding OS [43]. As an explanation, a higher NTR is supposed to be associated with a more invasive and more resistant type of glioblastoma [43]. However, the NTR does not seem to be relevant to iPDT, at least for the present patient cohort. This, again, suggests good local tumor control with iPDT, even in the case of more invasive tumors.

Patients with long *progression-free survival (PFS)* (see Figure 4d) also tended to show long *postprogression survival (PPS)*, which might be explainable by a better overall health state and/or good tumor control in the respective cases.

The *tumor volume* (Figure 5a) showed no correlation with OS. This is in contradiction to common experiences in the treatment of glioblastomas. However, it has to be kept in mind that the tumor diameter was limited to 4 cm by the inclusion criteria for the iPDT cohort (see Quach et al. [17]). Specifically, a tumor volume $<5000\text{ mm}^3$ was postulated to be a favorable factor for prolonged OS after iPDT [23]. When comparing this value to the median tumor volume of the present iPDT cohort of 6063 mm^3 (range: $[1362; 21,825]\text{ mm}^3$), the suggested threshold was clearly exceeded. Nevertheless, a large fraction of the patients showed prolonged OS (10/16 patients overall (62.5%) and 6/9 patients with a tumor volume $>5000\text{ mm}^3$ (67%). The postulated threshold tumor volume of 5000 mm^3 was apparently based on the research of Kaneko et al. [87]. This work did not involve dosimetry calculations, so an incomplete illumination of the tumor tissue cannot be ruled out. As a consequence, the iPDT effects may have been triggered insufficiently, particularly in the case of larger tumors. Hence, a nonnegligible number of vital tumor cells may have survived the therapeutic intervention, resulting in a situation comparable to an incomplete resection in the SOC. Therefore, it is crucial that the iPDT procedure is well planned to properly illuminate the target volume [88] since iPDT relies on the interaction of light with the photosensitizing drug [89]. The obtained results suggest that thorough treatment planning allows one to avoid a deterioration of iPDT's success with increasing tumor

volume [90,91]. Additionally, advances in dosimetry planning [92–94] and intraoperative monitoring [21] should make it possible to treat larger tumors in the future.

Like the primary tumor volume, the *volume of the iPDT remnant* (Figure 5c–f) also did not show any correlation with survival. Despite the low *p*-value in the univariate Cox regression analysis three months before recurrence, a causal relationship with survival in this case seems unlikely. Considering that no significant correlation of OS was found with respect to the iPDT remnant volume shortly after iPDT treatment and three months after iPDT treatment, the low *p*-value might be explained by the time-dependent decrease in the iPDT remnant: the longer overall survival is, the longer the iPDT remnant volume can decrease. This would result in a smaller remnant if recurrence occurred after a long survival period. This implies a correlation but not causality.

Furthermore, no connection with OS was found for the CE volume 24 h after iPDT (Figure 5b) or for the observation of CE 3 months after iPDT (Figure 6).

All in all, these results for iPDT differ in several ways from the common experience in resection, where the complete resection of the contrast-enhancing tumor volume (i.e., vanished CE in postoperative imaging) is a well-accepted predictor of prolonged OS [68,86,95]. In conclusion, the reactions to the iPDT intervention seem to be different from the reactions to the other therapy approaches.

4.6. Quality Assessment of the Performed Treatment

It appears trivial that the quality of the iPDT treatment must have a crucial influence on survival. From this study, no specific quality criterium can be derived. Further research is needed to define specific criteria for a deeper evaluation in that respect. For now, spectral online monitoring allows for the measuring of PpIX-fluorescence within the tumor volume to confirm the availability of the photosensitizer at the start of the iPDT-illumination process [21,96].

4.7. Discussion of Materials and Methods

When critically evaluating the used materials and methods, establishing an artificial-intelligence-based segmentation method would be desirable to facilitate the evaluation of larger patient cohorts in future studies. Additionally, a larger patient cohort would have been helpful for testing the statistical significance of the more survival-related factors. As further means to evaluate and potentially improve the success of iPDT, advanced MRI techniques (e.g., diffusion-weighted imaging (DWI), MR perfusion imaging, and MR spectroscopy) as well as positron emission tomography (PET) imaging may be helpful, as they allow one to assess tumor spreading and to identify the regions associated with a high risk of tumor recurrence and progression [97].

4.8. Limitations

Although the median tumor volume of the iPDT cohort was comparatively small, this does not necessarily reduce the relevance of the general success of the performed iPDT treatments. It is to be noted that the presented iPDT cohort was a highly-selected cohort, especially in comparison to the patient cohorts treated according to the Stupp protocol [2] or with chemoradiation [10]. Nonetheless, without iPDT, the treated individuals, with their nonresectable tumors, would have had a daunting prognosis [10,85,86]. With iPDT, 10/16 patients (62.5%) experienced prolonged OS, suggesting that the treated individuals strongly benefitted from the offered salvage treatment.

Despite the truly encouraging outcome in this small patient cohort, the potential pitfalls of iPDT in general might contribute to the fact that early recurrence was still observed, especially in the cases with an unmethylated MGMT promoter. PDT induces hypoxia, which stimulates the proliferation of glioblastoma stem cells [98] and might activate angiogenic factors [99]. It is well established that PpIX is a substrate for some of the multidrug-resistance-associated membrane transporters, such as ABCB1 [100] or ABCG2 [101,102]. As the expression of these transporters is associated with the stemness

of cells, PDT might, therefore, lead to the preferential survival of glioblastoma stem cells, although it has been shown that glioblastoma stem cells are susceptible to 5-ALA based treatment [103]. Nitric oxide (NO) production was observed in glioma cells treated with a sublethal dose of 5-ALA-PDT [104], which led to increased proliferation and migration. As far as resistance to repetitive PDT is concerned, the reports are controversial: while Madson et al. [105] did not find a buildup of 5-ALA-PDT resistance in glioma spheroids, PDT-resistant cells could be induced with multiple PDT treatments as found by Casas et al. [106]. More caveats to consider in GBM-PDT have recently been reviewed by Miretti et al. [107]. It appears worthwhile to investigate which of the above-mentioned potential restrictions are clinically relevant in order to develop targeted mitigation strategies that might improve the clinical outcome of 5-ALA based iPDT even further.

This investigation was intentionally focused on volumetric MRI analyses during longtime follow-ups. Priority was given to the clinically relevant *Response Assessment in Neuro-Oncology* (RANO) criteria, such as the contrast-enhancing volume and necrosis post-iPDT [97]. Advanced MRI techniques (e.g., quantitative analyses of contrast-enhanced T1 signal intensities and diffusion-weighted imaging (DWI) with a quantitative evaluation of the apparent diffusion coefficient) were not part of the present nonexhaustive analysis but might depict significant correlations with the overall outcome or at least with local tumor control [108].

4.9. Recapitulation and Outlook

1. The presented data indicate that the first results obtained through the iPDT-treatment of patients with de novo glioblastomas are promising, e.g., in terms of OS. The possibility of treating nonresectable tumors should especially be highly appreciated, as it would greatly improve the prognosis of the affected patients. For recurrent glioblastomas, iPDT was already tested on a larger number of patients, showing the feasibility and safety of the treatment [16].
2. It appears that the good performance of iPDT regarding survival is not only due to a good local tumor-debulking effect but is also based on immunogenic effects. This can be concluded from the observed unusual recurrence pattern characterized by a lower rate of local recurrence than that seen in a plenitude of other glioblastoma patient cohorts [78–82].
3. The confirmation of the importance of the MGMT methylation status [17] can be seen as an important step in the improvement of the patient selection of iPDT for de novo glioblastomas.
4. The assessment of MRI data showed peculiarities compared to the SOC treatment. In the case of residual or increasing CE after iPDT, advanced imaging techniques (e.g., DWI, MR perfusion and spectroscopy, PET) should be considered to enable better differentiation between vital tumor reactions and tissue reactions/pseudoprogression.

In the future, iPDT could also be combined with other therapies to eliminate as many neoplastic cells as possible and to initiate a broad variety of processes that can help to combat this invasive malignancy. To improve the distant tumor control, a combination with a sonodynamic approach might be interesting to better eliminate disseminated tumor cells [109–113].

In glioblastomas, the first trials of the therapies with immune checkpoint inhibitors did not show very encouraging outcomes [114,115]. However, in the other applications, a combination of 5-ALA-mediated PDT with immune checkpoint inhibitors revealed promising results [116]. This could lead to an enhanced response of glioblastoma cells to these new treatment drugs. Likewise, the variety of glioblastomas' therapeutic resistances may be addressable by combining the current iPDT protocol with chemoradiation-enhancing substances [117]. These approaches are to be tested in future studies.

To improve the perspectives for glioblastoma patients, a large repertoire of therapies should be provided against the burden of glioblastomas in the future. This study explored the potential of iPDT to contribute to the fight against this deadly disease and to provide

motivation for scientists and physicians all over the world to further investigate this promising therapy option.

5. Conclusions

In this study, iPDT has shown its potential based on a large fraction of patients (63%) experiencing prolonged OS, although this patient cohort was faced with an a priori very daunting prognosis due to the nonresectability of their tumors. In these individuals, the treatment was capable of debulking the tumor burden while only causing transient morbidity.

Furthermore, this investigation demonstrated that survival-related parameters could be derived from commonly available patient data. However, it is to be noted that some of these parameters may need to be interpreted differently compared to the standard treatment. Likewise, a paradigm shift seems to be required with regard to the established interpretation of imaging data since the known predictive factors suitable for other treatments do not seem to be directly transferable to the case of iPDT.

In conclusion, iPDT presents promising survival perspectives and broad applicability, even in the case of problematic tumor locations. With its minimally invasive nature, iPDT carries a notable potential to contribute to the combat against glioblastomas. This potential should certainly be explored further.

Supplementary Materials: The following supporting information can be downloaded at <https://www.mdpi.com/article/10.3390/cancers15092603/s1>, Supplementary Figure S1: Kaplan–Meier plots for comparative outcome evaluation; Supplementary Table S1: Individual tumor-related volumes and volume ratios; Supplementary Table S2: Univariate Cox regression analysis of possibly survival-related factors; and Supplementary Table S3: Survival value comparison of published values and calculated values.

Author Contributions: Conceptualization, M.A., M.F., A.R., R.S. and H.S.; methodology, M.A., M.F. and A.R.; validation, K.B., A.B. and R.F.; formal analysis, A.B., M.F. and M.E.F.; investigation, M.A., M.F., A.R., R.S. and H.S.; resources, K.B. and R.F.; data curation, M.F. and M.E.F.; writing—original draft preparation, M.F. and A.R.; writing—review and editing, M.A., K.B., A.B., M.F., R.F., S.Q., A.R., R.S. and N.T.; visualization, A.B., M.F., A.R. and R.S.; supervision, A.B., A.R., R.S. and N.T.; project administration, A.R. and R.S.; funding acquisition, A.R. and R.S. All authors have read and agreed to the published version of the manuscript.

Funding: We greatly thank the German Research Foundation (DFG) for the financial support from the research training group (RTG) GRK2274.

Institutional Review Board Statement: The study was organized in accordance with the guidelines of the Declaration of Helsinki and was approved by the Ethics Committee of Ludwig–Maximilian–Universität München, Munich, Germany (UE No. 335–16).

Informed Consent Statement: All patients treated at the Department of Neurosurgery of the Ludwig Maximilian University of Munich give their consent to participate in retrospective studies through a local prospective tumor registry.

Data Availability Statement: No new data were created or analyzed in this study. Data sharing is not applicable to this article.

Acknowledgments: We gratefully acknowledge Robert Stahl for his technical assistance and Christian Heckl for his additional input on the methods and research.

Conflicts of Interest: The authors declare no conflict of interest. The funders did not participate in the design of the study; in the collection, analysis, or interpretation of the data; in the writing of the manuscript; or in the decision to publish the results.

Abbreviations

5-ALA represents 5-aminolevulinic acid, CE represents contrast enhancement, CI represents confidence interval, DWI represents diffusion-weighted imaging, iPDT represents interstitial photodynamic therapy, MGMT represents O(6)-methylguanine-DNA methyltransferase, OS represents overall survival, PDT represents photodynamic therapy, PFS represents progression-free survival, PpIX represents protoporphyrin IX, PPS represents postprogression survival, SOC represents standard of care, and NTR represents necrosis–tumor ratio.

References

- Ostrom, Q.T.; Price, M.; Neff, C.; Cioffi, G.; Waite, K.A.; Kruchko, C.; Barnholtz-Sloan, J.S. CBTRUS Statistical Report: Primary Brain and Other Central Nervous System Tumors Diagnosed in the United States in 2015–2019. *Neuro-oncology* **2022**, *24* (Suppl. 5), v1–v95. [\[CrossRef\]](#) [\[PubMed\]](#)
- Stupp, R.; Mason, W.P.; Van den Bent, M.J.; Weller, M.; Fisher, B.; Taphoorn, M.J.; Belanger, K.; Brandes, A.A.; Marosi, C.; Bogdahn, U.; et al. Radiotherapy plus concomitant and adjuvant temozolomide for glioblastoma. *N. Engl. J. Med.* **2005**, *352*, 987–996. [\[CrossRef\]](#) [\[PubMed\]](#)
- Friedmann-Morvinski, D. Glioblastoma heterogeneity and cancer cell plasticity. *Crit. Rev. Oncog.* **2014**, *19*, 327–336. [\[CrossRef\]](#)
- Orzan, F.; De Bacco, F.; Crisafulli, G.; Pellegatta, S.; Mussolin, B.; Siravegna, G.; D’Ambrosio, A.; Comoglio, P.M.; Finocchiaro, G.; Boccaccio, C. Genetic Evolution of Glioblastoma Stem-Like Cells from Primary to Recurrent Tumor. *Stem Cells* **2017**, *35*, 2218–2228. [\[CrossRef\]](#)
- Lara-Velazquez, M.; Al-Kharboosh, R.; Jeanneret, S.; Vazquez-Ramos, C.; Mahato, D.; Tavanaiepour, D.; Rahmathulla, G.; Quinones-Hinojosa, A. Advances in Brain Tumor Surgery for Glioblastoma in Adults. *Brain Sci.* **2017**, *7*, 166. [\[CrossRef\]](#)
- Venkataramani, V.; Yang, Y.; Schubert, M.C.; Reyhan, E.; Tetzlaff, S.K.; Wißmann, N.; Botz, M.; Soyka, S.J.; Beretta, C.A.; Pramatarov, R.L.; et al. Glioblastoma hijacks neuronal mechanisms for brain invasion. *Cell* **2022**, *185*, 2899–2917.e2831. [\[CrossRef\]](#) [\[PubMed\]](#)
- Fisher, J.P.; Adamson, D.C. Current FDA-Approved Therapies for High-Grade Malignant Gliomas. *Biomedicines* **2021**, *9*, 324. [\[CrossRef\]](#)
- Sun, R.; Cuthbert, H.; Watts, C. Fluorescence-Guided Surgery in the Surgical Treatment of Gliomas: Past, Present and Future. *Cancers* **2021**, *13*, 3508. [\[CrossRef\]](#)
- Wilson, B.C.; Eu, D. Optical spectroscopy and imaging in surgical management of cancer patients. *Transl. Biophotonics* **2022**, *4*, e202100009. [\[CrossRef\]](#)
- Thon, N.; Thorsteinsdottir, J.; Eigenbrod, S.; Schüller, U.; Lutz, J.; Kreth, S.; Belka, C.; Tonn, J.C.; Niyazi, M.; Kreth, F.W. Outcome in unresectable glioblastoma: MGMT promoter methylation makes the difference. *J. Neurol.* **2017**, *264*, 350–358. [\[CrossRef\]](#)
- Azoulay, M.; Chang, S.D.; Gibbs, I.C.; Hancock, S.L.; Pollom, E.L.; Harsh, G.R.; Adler, J.R.; Harraher, C.; Li, G.; Hayden Gephart, M.; et al. A phase I/II trial of 5-fraction stereotactic radiosurgery with 5-mm margins with concurrent temozolomide in newly diagnosed glioblastoma: Primary outcomes. *Neuro-oncology* **2020**, *22*, 1182–1189. [\[CrossRef\]](#)
- Oermann, E.; Collins, B.T.; Erickson, K.T.; Yu, X.; Lei, S.; Suy, S.; Hanscom, H.N.; Kim, J.; Park, H.U.; Eldabh, A.; et al. CyberKnife enhanced conventionally fractionated chemoradiation for high grade glioma in close proximity to critical structures. *J. Hematol. Oncol.* **2010**, *3*, 22. [\[CrossRef\]](#)
- Barbarite, E.; Sick, J.T.; Berchmans, E.; Bregy, A.; Shah, A.H.; Elsayyad, N.; Komotar, R.J. The role of brachytherapy in the treatment of glioblastoma multiforme. *Neurosurg. Rev.* **2017**, *40*, 195–211. [\[CrossRef\]](#) [\[PubMed\]](#)
- Stummer, W.; Beck, T.; Beyer, W.; Mehrkens, J.H.; Obermeier, A.; Etminan, N.; Stepp, H.; Tonn, J.C.; Baumgartner, R.; Herms, J.; et al. Long-sustaining response in a patient with non-resectable, distant recurrence of glioblastoma multiforme treated by interstitial photodynamic therapy using 5-ALA: Case report. *J. Neurooncol.* **2008**, *87*, 103–109. [\[CrossRef\]](#) [\[PubMed\]](#)
- Beck, T.J.; Kreth, F.W.; Beyer, W.; Mehrkens, J.H.; Obermeier, A.; Stepp, H.; Stummer, W.; Baumgartner, R. Interstitial photodynamic therapy of nonresectable malignant glioma recurrences using 5-aminolevulinic acid induced protoporphyrin IX. *Lasers Surg. Med.* **2007**, *39*, 386–393. [\[CrossRef\]](#) [\[PubMed\]](#)
- Lietke, S.; Schmutzer, M.; Schwartz, C.; Weller, J.; Siller, S.; Aumiller, M.; Heckl, C.; Forbrig, R.; Niyazi, M.; Egensperger, R.; et al. Interstitial Photodynamic Therapy Using 5-ALA for Malignant Glioma Recurrences. *Cancers* **2021**, *13*, 1767. [\[CrossRef\]](#) [\[PubMed\]](#)
- Quach, S.; Schwartz, C.; Aumiller, M.; Foglar, M.; Schmutzer, M.; Katzendobler, S.; Forbrig, R.; Bochmann, K.; Egensperger, R.; Sroka, R.; et al. Interstitial photodynamic therapy for newly diagnosed glioblastoma. *J. Neuro-Oncol.* **2023**, ahead of print. [\[CrossRef\]](#)
- Traylor, J.I.; Pernik, M.N.; Sternisha, A.C.; McBrayer, S.K.; Abdullah, K.G. Molecular and Metabolic Mechanisms Underlying Selective 5-Aminolevulinic Acid-Induced Fluorescence in Gliomas. *Cancers* **2021**, *13*, 580. [\[CrossRef\]](#)
- Malik, Z. Fundamentals of 5-aminolevulinic acid photodynamic therapy and diagnosis: An overview. *Transl. Biophotonics* **2020**, *2*, e201900022. [\[CrossRef\]](#)

20. Kiening, M.; Lange, N. A Recap of Heme Metabolism towards Understanding Protoporphyrin IX Selectivity in Cancer Cells. *Int. J. Mol. Sci.* **2022**, *23*, 7974. [CrossRef]
21. Aumiller, M.; Heckl, C.; Quach, S.; Stepp, H.; Ertl-Wagner, B.; Sroka, R.; Thon, N.; Rühm, A. Interrelation between Spectral Online Monitoring and Postoperative T1-Weighted MRI in Interstitial Photodynamic Therapy of Malignant Gliomas. *Cancers* **2021**, *14*, 120. [CrossRef] [PubMed]
22. Stepp, H.; Stummer, W. 5-ALA in the management of malignant glioma. *Lasers Surg. Med.* **2018**, *50*, 399–419. [CrossRef] [PubMed]
23. Leroy, H.A.; Guérin, L.; Lecomte, F.; Baert, G.; Vignion, A.S.; Mordon, S.; Reyns, N. Is interstitial photodynamic therapy for brain tumors ready for clinical practice? A systematic review. *Photodiagn. Photodyn. Ther.* **2021**, *36*, 102492. [CrossRef] [PubMed]
24. Nkune, N.W.; Simelane, N.W.N.; Montaseri, H.; Abrahamse, H. Photodynamic Therapy-Mediated Immune Responses in Three-Dimensional Tumor Models. *Int. J. Mol. Sci.* **2021**, *22*, 2618. [CrossRef]
25. Donohoe, C.; Senge, M.O.; Arnaut, L.G.; Gomes-da-Silva, L.C. Cell death in photodynamic therapy: From oxidative stress to anti-tumor immunity. *Biochim. Biophys. Acta Rev. Cancer* **2019**, *1872*, 188308. [CrossRef]
26. Hamblin, M.R.; Abrahamse, H. Factors Affecting Photodynamic Therapy and Anti-Tumor Immune Response. *Anticancer Agents Med. Chem.* **2021**, *21*, 123–136. [CrossRef]
27. Yu, X.; Zheng, H.; Chan, M.T.V.; Wu, W.K.K. Immune consequences induced by photodynamic therapy in non-melanoma skin cancers: A review. *Environ. Sci. Pollut. Res. Int.* **2018**, *25*, 20569–20574. [CrossRef]
28. Gollnick, S.O.; Brackett, C.M. Enhancement of anti-tumor immunity by photodynamic therapy. *Immunol. Res.* **2010**, *46*, 216–226. [CrossRef]
29. Castano, A.P.; Mroz, P.; Hamblin, M.R. Photodynamic therapy and anti-tumour immunity. *Nat. Rev. Cancer* **2006**, *6*, 535–545. [CrossRef]
30. Li, F.; Cheng, Y.; Lu, J.; Hu, R.; Wan, Q.; Feng, H. Photodynamic therapy boosts anti-glioma immunity in mice: A dependence on the activities of T cells and complement C3. *J. Cell. Biochem.* **2011**, *112*, 3035–3043. [CrossRef]
31. Louis, D.N.; Perry, A.; Wesseling, P.; Brat, D.J.; Cree, I.A.; Figarella-Branger, D.; Hawkins, C.; Ng, H.K.; Pfister, S.M.; Reifenberger, G.; et al. The 2021 WHO Classification of Tumors of the Central Nervous System: A summary. *Neuro-oncology* **2021**, *23*, 1231–1251. [CrossRef] [PubMed]
32. Louis, D.N.; Perry, A.; Reifenberger, G.; Von Deimling, A.; Figarella-Branger, D.; Cavenee, W.K.; Ohgaki, H.; Wiestler, O.D.; Kleihues, P.; Ellison, D.W. The 2016 World Health Organization Classification of Tumors of the Central Nervous System: A summary. *Acta Neuropathol.* **2016**, *131*, 803–820. [CrossRef]
33. Smoll, N.R.; Schaller, K.; Gautschi, O.P. Long-term survival of patients with glioblastoma multiforme (GBM). *J. Clin. Neurosci.* **2013**, *20*, 670–675. [CrossRef] [PubMed]
34. Krex, D.; Klink, B.; Hartmann, C.; Von Deimling, A.; Pietsch, T.; Simon, M.; Sabel, M.; Steinbach, J.P.; Heese, O.; Reifenberger, G.; et al. Long-term survival with glioblastoma multiforme. *Brain* **2007**, *130*, 2596–2606. [CrossRef] [PubMed]
35. Jovčevska, I. Genetic secrets of long-term glioblastoma survivors. *Bosn. J. Basic. Med. Sci.* **2019**, *19*, 116–124. [CrossRef] [PubMed]
36. Gately, L.; McLachlan, S.A.; Philip, J.; Ruben, J.; Dowling, A. Long-term survivors of glioblastoma: A closer look. *J. Neurooncol.* **2018**, *136*, 155–162. [CrossRef] [PubMed]
37. Johnson, D.R.; Ma, D.J.; Buckner, J.C.; Hammack, J.E. Conditional probability of long-term survival in glioblastoma: A population-based analysis. *Cancer* **2012**, *118*, 5608–5613. [CrossRef] [PubMed]
38. Anselmo, P.; Maranzano, E.; Selimi, A.; Lupattelli, M.; Palumbo, I.; Bini, V.; Casale, M.; Trippa, F.; Bufi, A.; Arcidiacono, F.; et al. Clinical characterization of glioblastoma patients living longer than 2 years: A retrospective analysis of two Italian institutions. *Asia Pac. J. Clin. Oncol.* **2021**, *17*, 273–279. [CrossRef]
39. Gately, L.; McLachlan, S.A.; Dowling, A.; Philip, J. Life beyond a diagnosis of glioblastoma: A systematic review of the literature. *J. Cancer Surviv.* **2017**, *11*, 447–452. [CrossRef]
40. Poon, M.T.C.; Sudlow, C.L.M.; Figueroa, J.D.; Brennan, P.M. Longer-term (≥ 2 years) survival in patients with glioblastoma in population-based studies pre- and post-2005: A systematic review and meta-analysis. *Sci. Rep.* **2020**, *10*, 11622. [CrossRef]
41. Avants, B.; Tustison, N.; Song, G. Advanced normalization tools (ANTS). *Insight J.* **2008**, *2*, 1–35.
42. Yushkevich, P.A.; Piven, J.; Hazlett, H.C.; Smith, R.G.; Ho, S.; Gee, J.C.; Gerig, G. User-guided 3D active contour segmentation of anatomical structures: Significantly improved efficiency and reliability. *Neuroimage* **2006**, *31*, 1116–1128. [CrossRef] [PubMed]
43. Henker, C.; Hiepel, M.C.; Kriesen, T.; Scherer, M.; Glass, Ä.; Herold-Mende, C.; Bendszus, M.; Langner, S.; Weber, M.A.; Schneider, B.; et al. Volumetric assessment of glioblastoma and its predictive value for survival. *Acta Neurochir.* **2019**, *161*, 1723–1732. [CrossRef] [PubMed]
44. IBM Corp. *IBM SPSS Statistics for Windows, Version 29*; IBM Corp: Armonk, NY, USA, 2022.
45. R Core Team. *R: A Language and Environment for Statistical Computing*; R Core: Vienna, Austria, 2022.
46. Wickham, H. Data analysis. In *ggplot2*; Springer: Berlin/Heidelberg, Germany, 2016; pp. 189–201.
47. Mitchell, M.; Muftakhidinov, B.; Winchen, T. Engauge Digitizer Software. 2019. Available online: <https://markummittell.github.io/engauge-digitizer> (accessed on 5 February 2023).
48. Schwartz, C.; Rühm, A.; Tonn, J.-C.; Kreth, S.; Kreth, F.-W. Surg-25interstitial Photodynamic Therapy of De-Novo Glioblastoma Multiforme Who IV. *Neuro-Oncology* **2015**, *17*, v219. [CrossRef]
49. Epstein, N.E. A review of the risks and benefits of differing prophylaxis regimens for the treatment of deep venous thrombosis and pulmonary embolism in neurosurgery. *Surg. Neurol.* **2005**, *64*, 295–301; discussion 302. [CrossRef]

50. Bartek, J., Jr.; Alattar, A.A.; Dhawan, S.; Ma, J.; Koga, T.; Nakaji, P.; Dusenbery, K.E.; Chen, C.C. Receipt of brachytherapy is an independent predictor of survival in glioblastoma in the Surveillance, Epidemiology, and End Results database. *J. Neurooncol.* **2019**, *145*, 75–83. [\[CrossRef\]](#)
51. Norred, S.E.; Johnson, J.A. Magnetic resonance-guided laser induced thermal therapy for glioblastoma multiforme: A review. *Biomed. Res. Int.* **2014**, *2014*, 761312. [\[CrossRef\]](#)
52. Traylor, J.I.; Patel, R.; Muir, M.; De Almeida Bastos, D.C.; Ravikumar, V.; Kamiya-Matsuoka, C.; Rao, G.; Thomas, J.G.; Kew, Y.; Prabhu, S.S. Laser Interstitial Thermal Therapy for Glioblastoma: A Single-Center Experience. *World Neurosurg.* **2021**, *149*, e244–e252. [\[CrossRef\]](#)
53. Binabaj, M.M.; Bahrami, A.; ShahidSales, S.; Joodi, M.; Joudi Mashhad, M.; Hassanian, S.M.; Anvari, K.; Avan, A. The prognostic value of MGMT promoter methylation in glioblastoma: A meta-analysis of clinical trials. *J. Cell. Physiol.* **2018**, *233*, 378–386. [\[CrossRef\]](#)
54. Weller, M.; Tabatabai, G.; Kästner, B.; Felsberg, J.; Steinbach, J.P.; Wick, A.; Schnell, O.; Hau, P.; Herrlinger, U.; Sabel, M.C.; et al. MGMT Promoter Methylation Is a Strong Prognostic Biomarker for Benefit from Dose-Intensified Temozolomide Rechallenge in Progressive Glioblastoma: The DIRECTOR Trial. *Clin. Cancer Res.* **2015**, *21*, 2057–2064. [\[CrossRef\]](#)
55. Fuster-Garcia, E.; Lorente Estellés, D.; Álvarez-Torres, M.D.M.; Juan-Albarracín, J.; Chelebian, E.; Rovira, A.; Acosta, C.A.; Pineda, J.; Oleaga, L.; Mollá-Olmos, E.; et al. MGMT methylation may benefit overall survival in patients with moderately vascularized glioblastomas. *Eur. Radiol.* **2021**, *31*, 1738–1747. [\[CrossRef\]](#)
56. Hegi, M.E.; Diserens, A.C.; Gorlia, T.; Hamou, M.F.; De Tribolet, N.; Weller, M.; Kros, J.M.; Hainfellner, J.A.; Mason, W.; Mariani, L.; et al. MGMT gene silencing and benefit from temozolomide in glioblastoma. *N. Engl. J. Med.* **2005**, *352*, 997–1003. [\[CrossRef\]](#)
57. Gerson, S.L. MGMT: Its role in cancer aetiology and cancer therapeutics. *Nat. Rev. Cancer* **2004**, *4*, 296–307. [\[CrossRef\]](#) [\[PubMed\]](#)
58. Dean, M.; Fojo, T.; Bates, S. Tumour stem cells and drug resistance. *Nat. Rev. Cancer* **2005**, *5*, 275–284. [\[CrossRef\]](#) [\[PubMed\]](#)
59. Liu, G.; Yuan, X.; Zeng, Z.; Tunici, P.; Ng, H.; Abdulkadir, I.R.; Lu, L.; Irvin, D.; Black, K.L.; Yu, J.S. Analysis of gene expression and chemoresistance of CD133+ cancer stem cells in glioblastoma. *Mol. Cancer* **2006**, *5*, 67. [\[CrossRef\]](#)
60. Salmaggi, A.; Boiardi, A.; Gelati, M.; Russo, A.; Calatuzzolo, C.; Ciusani, E.; Sciacca, F.L.; Ottolina, A.; Parati, E.A.; La Porta, C.; et al. Glioblastoma-derived tumorspheres identify a population of tumor stem-like cells with angiogenic potential and enhanced multidrug resistance phenotype. *Glia* **2006**, *54*, 850–860. [\[CrossRef\]](#)
61. Chinot, O.L.; Macdonald, D.R.; Abrey, L.E.; Zahlmann, G.; Kerloëguen, Y.; Cloughesy, T.F. Response assessment criteria for glioblastoma: Practical adaptation and implementation in clinical trials of antiangiogenic therapy. *Curr. Neurol. Neurosci. Rep.* **2013**, *13*, 347. [\[CrossRef\]](#)
62. Wen, P.Y.; Macdonald, D.R.; Reardon, D.A.; Cloughesy, T.F.; Sorensen, A.G.; Galanis, E.; Degroot, J.; Wick, W.; Gilbert, M.R.; Lassman, A.B.; et al. Updated response assessment criteria for high-grade gliomas: Response assessment in neuro-oncology working group. *J. Clin. Oncol.* **2010**, *28*, 1963–1972. [\[CrossRef\]](#)
63. Albert, F.K.; Forsting, M.; Sartor, K.; Adams, H.P.; Kunze, S. Early postoperative magnetic resonance imaging after resection of malignant glioma: Objective evaluation of residual tumor and its influence on regrowth and prognosis. *Neurosurgery* **1994**, *34*, 45–60; discussion 60–61. [\[CrossRef\]](#) [\[PubMed\]](#)
64. Han, Q.; Liang, H.; Cheng, P.; Yang, H.; Zhao, P. Gross Total vs. Subtotal Resection on Survival Outcomes in Elderly Patients With High-Grade Glioma: A Systematic Review and Meta-Analysis. *Front. Oncol.* **2020**, *10*, 151. [\[CrossRef\]](#)
65. Sanai, N.; Polley, M.Y.; McDermott, M.W.; Parsa, A.T.; Berger, M.S. An extent of resection threshold for newly diagnosed glioblastomas. *J. Neurosurg.* **2011**, *115*, 3–8. [\[CrossRef\]](#)
66. Stummer, W.; Reulen, H.J.; Meinel, T.; Pichlmeier, U.; Schumacher, W.; Tonn, J.C.; Rohde, V.; Oppel, F.; Turowski, B.; Woiciechowsky, C.; et al. Extent of resection and survival in glioblastoma multiforme: Identification of and adjustment for bias. *Neurosurgery* **2008**, *62*, 564–576; discussion 564–576. [\[CrossRef\]](#)
67. Kreth, F.W.; Thon, N.; Simon, M.; Westphal, M.; Schackert, G.; Nikkhah, G.; Hentschel, B.; Reifenberger, G.; Pietsch, T.; Weller, M.; et al. Gross total but not incomplete resection of glioblastoma prolongs survival in the era of radiochemotherapy. *Ann. Oncol.* **2013**, *24*, 3117–3123. [\[CrossRef\]](#)
68. Lacroix, M.; Abi-Said, D.; Fourney, D.R.; Gokaslan, Z.L.; Shi, W.; DeMonte, F.; Lang, F.F.; McCutcheon, I.E.; Hassenbusch, S.J.; Holland, E.; et al. A multivariate analysis of 416 patients with glioblastoma multiforme: Prognosis, extent of resection, and survival. *J. Neurosurg.* **2001**, *95*, 190–198. [\[CrossRef\]](#) [\[PubMed\]](#)
69. Zhou, Z.; Lu, Z.R. Gadolinium-based contrast agents for magnetic resonance cancer imaging. *Wiley Interdiscip. Rev. Nanomed. Nanobiotechnol.* **2013**, *5*, 1–18. [\[CrossRef\]](#) [\[PubMed\]](#)
70. Kiviniemi, A.; Gardberg, M.; Ek, P.; Frantzén, J.; Bobacka, J.; Minn, H. Gadolinium retention in gliomas and adjacent normal brain tissue: Association with tumor contrast enhancement and linear/macrocyclic agents. *Neuroradiology* **2019**, *61*, 535–544. [\[CrossRef\]](#) [\[PubMed\]](#)
71. Hirschberg, H.; Uzal, F.A.; Chighvinadze, D.; Zhang, M.J.; Peng, Q.; Madsen, S.J. Disruption of the blood-brain barrier following ALA-mediated photodynamic therapy. *Lasers Surg. Med.* **2008**, *40*, 535–542. [\[CrossRef\]](#) [\[PubMed\]](#)
72. Brandsma, D.; Van den Bent, M.J. Pseudoprogression and pseudoresponse in the treatment of gliomas. *Curr. Opin. Neurol.* **2009**, *22*, 633–638. [\[CrossRef\]](#)



73. Kumar, A.J.; Leeds, N.E.; Fuller, G.N.; Van Tassel, P.; Maor, M.H.; Sawaya, R.E.; Levin, V.A. Malignant gliomas: MR imaging spectrum of radiation therapy- and chemotherapy-induced necrosis of the brain after treatment. *Radiology* **2000**, *217*, 377–384. [\[CrossRef\]](#)
74. Brandsma, D.; Stalpers, L.; Taal, W.; Sminia, P.; Van den Bent, M.J. Clinical features, mechanisms, and management of pseudoprogression in malignant gliomas. *Lancet Oncol.* **2008**, *9*, 453–461. [\[CrossRef\]](#)
75. Dolmans, D.E.; Fukumura, D.; Jain, R.K. Photodynamic therapy for cancer. *Nat. Rev. Cancer* **2003**, *3*, 380–387. [\[CrossRef\]](#)
76. Schwake, M.; Nemes, A.; Dondrop, J.; Schroeteler, J.; Schipmann, S.; Senner, V.; Stummer, W.; Ewelt, C. In-Vitro Use of 5-ALA for Photodynamic Therapy in Pediatric Brain Tumors. *Neurosurgery* **2018**, *83*, 1328–1337. [\[CrossRef\]](#)
77. Karmakar, S.; Banik, N.L.; Patel, S.J.; Ray, S.K. 5-Aminolevulinic acid-based photodynamic therapy suppressed survival factors and activated proteases for apoptosis in human glioblastoma U87MG cells. *Neurosci. Lett.* **2007**, *415*, 242–247. [\[CrossRef\]](#) [\[PubMed\]](#)
78. De Bonis, P.; Anile, C.; Pompucci, A.; Fiorentino, A.; Balducci, M.; Chiesa, S.; Lauriola, L.; Maira, G.; Mangiola, A. The influence of surgery on recurrence pattern of glioblastoma. *Clin. Neurol. Neurosurg.* **2013**, *115*, 37–43. [\[CrossRef\]](#) [\[PubMed\]](#)
79. Hou, L.C.; Veeravagu, A.; Hsu, A.R.; Tse, V.C. Recurrent glioblastoma multiforme: A review of natural history and management options. *Neurosurg. Focus* **2006**, *20*, E5. [\[CrossRef\]](#) [\[PubMed\]](#)
80. Gaspar, L.E.; Fisher, B.J.; Macdonald, D.R.; LeBer, D.V.; Halperin, E.C.; Schold, S.C., Jr.; Cairncross, J.G. Supratentorial malignant glioma: Patterns of recurrence and implications for external beam local treatment. *Int. J. Radiat. Oncol. Biol. Phys.* **1992**, *24*, 55–57. [\[CrossRef\]](#) [\[PubMed\]](#)
81. Hess, C.F.; Schaaf, J.C.; Kortmann, R.D.; Schabet, M.; Bamberg, M. Malignant glioma: Patterns of failure following individually tailored limited volume irradiation. *Radiother. Oncol.* **1994**, *30*, 146–149. [\[CrossRef\]](#)
82. Lee, S.W.; Fraass, B.A.; Marsh, L.H.; Herbolt, K.; Gebarski, S.S.; Martel, M.K.; Radany, E.H.; Lichter, A.S.; Sandler, H.M. Patterns of failure following high-dose 3-D conformal radiotherapy for high-grade astrocytomas: A quantitative dosimetric study. *Int. J. Radiat. Oncol. Biol. Phys.* **1999**, *43*, 79–88. [\[CrossRef\]](#)
83. Lohmann, P.; Stavrinou, P.; Lipke, K.; Bauer, E.K.; Ceccon, G.; Werner, J.M.; Neumaier, B.; Fink, G.R.; Shah, N.J.; Langen, K.J.; et al. FET PET reveals considerable spatial differences in tumour burden compared to conventional MRI in newly diagnosed glioblastoma. *Eur. J. Nucl. Med. Mol. Imaging* **2019**, *46*, 591–602. [\[CrossRef\]](#)
84. Schucht, P.; Knittel, S.; Slotboom, J.; Seidel, K.; Murek, M.; Jilch, A.; Raabe, A.; Beck, J. 5-ALA complete resections go beyond MR contrast enhancement: Shift corrected volumetric analysis of the extent of resection in surgery for glioblastoma. *Acta Neurochir.* **2014**, *156*, 305–312; discussion 312. [\[CrossRef\]](#)
85. Laws, E.R.; Parney, I.F.; Huang, W.; Anderson, F.; Morris, A.M.; Asher, A.; Lillehei, K.O.; Bernstein, M.; Brem, H.; Sloan, A.; et al. Survival following surgery and prognostic factors for recently diagnosed malignant glioma: Data from the Glioma Outcomes Project. *J. Neurosurg.* **2003**, *99*, 467–473. [\[CrossRef\]](#) [\[PubMed\]](#)
86. Li, S.W.; Qiu, X.G.; Chen, B.S.; Zhang, W.; Ren, H.; Wang, Z.C.; Jiang, T. Prognostic factors influencing clinical outcomes of glioblastoma multiforme. *Chin. Med. J. Engl.* **2009**, *122*, 1245–1249. [\[PubMed\]](#)
87. Kaneko, S. Photodynamic therapy for human malignant gliomas. *J. Jpn. Soc. Laser Surg. Med.* **2011**, *32*, 131–138. [\[CrossRef\]](#)
88. Van Veen, R.L.P.; Robinson, D.J.; Sterenborg, H.; Aans, J.B.; Tan, I.B.; Vrieze, O.H.; Hoebbers, F.; Witjes, M.J.H.; Levendag, P.C. Treatment planning for Interstitial Photodynamic Therapy for head and neck cancer. *Head Neck Oncol.* **2010**, *2*, O45. [\[CrossRef\]](#)
89. Leroy, H.A.; Baert, G.; Guerin, L.; Delhem, N.; Mordon, S.; Reyns, N.; Vignion-Dewalle, A.S. Interstitial Photodynamic Therapy for Glioblastomas: A Standardized Procedure for Clinical Use. *Cancers* **2021**, *13*, 5754. [\[CrossRef\]](#) [\[PubMed\]](#)
90. Dupont, C.; Betrouni, N.; Mordon, S.; Reyns, N.; Vermandel, M. 5-ALA Photodynamic Therapy in Neurosurgery, Towards the Design of a Treatment Planning System: A Proof of Concept. *Innov. Res. BioMed. Eng.* **2016**, *38*, 34–41. [\[CrossRef\]](#)
91. Shafirstein, G.; Bellnier, D.; Oakley, E.; Hamilton, S.; Potasek, M.; Beeson, K.; Parilov, E. Interstitial Photodynamic Therapy—A Focused Review. *Cancers* **2017**, *9*, 12. [\[CrossRef\]](#)
92. Yassine, A.A.; Lilge, L.; Betz, V. Optimizing interstitial photodynamic therapy with custom cylindrical diffusers. *J. Biophotonics* **2019**, *12*, e201800153. [\[CrossRef\]](#)
93. Yassine, A.A.; Lilge, L.; Betz, V. Optimizing Interstitial Photodynamic Therapy Planning with Reinforcement Learning-Based Diffuser Placement. *IEEE Trans. Biomed. Eng.* **2021**, *68*, 1668–1679. [\[CrossRef\]](#)
94. Yassine, A.A.; Kingsford, W.; Xu, Y.; Cassidy, J.; Lilge, L.; Betz, V. Automatic interstitial photodynamic therapy planning via convex optimization. *Biomed. Opt. Express* **2018**, *9*, 898–920. [\[CrossRef\]](#)
95. Molinaro, A.M.; Hervey-Jumper, S.; Morshed, R.A.; Young, J.; Han, S.J.; Chunduru, P.; Zhang, Y.; Phillips, J.J.; Shai, A.; Lafontaine, M.; et al. Association of Maximal Extent of Resection of Contrast-Enhanced and Non-Contrast-Enhanced Tumor with Survival Within Molecular Subgroups of Patients With Newly Diagnosed Glioblastoma. *JAMA Oncol.* **2020**, *6*, 495–503. [\[CrossRef\]](#) [\[PubMed\]](#)
96. Rühm, A.; Stepp, H.; Beyer, W.; Hennig, G.; Pongratz, T.; Sroka, R.; Schnell, O.; Tonn, J.-C.; Kreth, F.-W. 5-ALA based photodynamic management of glioblastoma. *SPIE* **2014**, *8928*, 69–75.
97. Leao, D.J.; Craig, P.G.; Godoy, L.F.; Leite, C.C.; Policeni, B. Response Assessment in Neuro-Oncology Criteria for Gliomas: Practical Approach Using Conventional and Advanced Techniques. *AJNR Am. J. Neuroradiol.* **2020**, *41*, 10–20. [\[CrossRef\]](#) [\[PubMed\]](#)
98. Bar, E.E.; Lin, A.; Mahairaki, V.; Matsui, W.; Eberhart, C.G. Hypoxia increases the expression of stem-cell markers and promotes clonogenicity in glioblastoma neurospheres. *Am. J. Pathol.* **2010**, *177*, 1491–1502. [\[CrossRef\]](#) [\[PubMed\]](#)

99. Jung, H.S.; Han, J.; Shi, H.; Koo, S.; Singh, H.; Kim, H.-J.; Sessler, J.L.; Lee, J.Y.; Kim, J.-H.; Kim, J.S. Overcoming the Limits of Hypoxia in Photodynamic Therapy: A Carbonic Anhydrase IX-Targeted Approach. *J. Am. Chem. Soc.* **2017**, *139*, 7595–7602. [\[CrossRef\]](#)
100. Chelakkot, V.S.; Liu, K.; Yoshioka, E.; Saha, S.; Xu, D.; Licursi, M.; Dorward, A.; Hirasawa, K. MEK reduces cancer-specific PpIX accumulation through the RSK-ABCB1 and HIF-1 α -FECH axes. *Sci. Rep.* **2020**, *10*, 22124. [\[CrossRef\]](#)
101. Müller, P.; Abdel Gaber, S.A.; Zimmermann, W.; Wittig, R.; Stepp, H. ABCG2 influence on the efficiency of photodynamic therapy in glioblastoma cells. *J. Photochem. Photobiol. B* **2020**, *210*, 111963. [\[CrossRef\]](#)
102. Abdel Gaber, S.A.; Müller, P.; Zimmermann, W.; Hüttenberger, D.; Wittig, R.; Abdel Kader, M.H.; Stepp, H. ABCG2-mediated suppression of chlorin e6 accumulation and photodynamic therapy efficiency in glioblastoma cell lines can be reversed by KO143. *J. Photochem. Photobiol. B* **2018**, *178*, 182–191. [\[CrossRef\]](#)
103. Schimanski, A.; Ebbert, L.; Sabel, M.C.; Finocchiaro, G.; Lamszus, K.; Ewelt, C.; Etminan, N.; Fischer, J.C.; Sorg, R.V. Human glioblastoma stem-like cells accumulate protoporphyrin IX when subjected to exogenous 5-aminolaevulinic acid, rendering them sensitive to photodynamic treatment. *J. Photochem. Photobiol. B* **2016**, *163*, 203–210. [\[CrossRef\]](#)
104. Fahey, J.M.; Emmer, J.V.; Korytowski, W.; Hogg, N.; Girotti, A.W. Antagonistic Effects of Endogenous Nitric Oxide in a Glioblastoma Photodynamic Therapy Model. *Photochem. Photobiol.* **2016**, *92*, 842–853. [\[CrossRef\]](#)
105. Madsen, S.J.; Sun, C.H.; Tromberg, B.J.; Hirschberg, H. Repetitive 5-aminolevulinic acid-mediated photodynamic therapy on human glioma spheroids. *J. Neurooncol.* **2003**, *62*, 243–250. [\[CrossRef\]](#) [\[PubMed\]](#)
106. Casas, A.; Perotti, C.; Ortel, B.; Di Venosa, G.; Saccoliti, M.; Batlle, A.; Hasan, T. Tumor cell lines resistant to ALA-mediated photodynamic therapy and possible tools to target surviving cells. *Int. J. Oncol.* **2006**, *29*, 397–405. [\[CrossRef\]](#) [\[PubMed\]](#)
107. Miretti, M.; González Graglia, M.A.; Suárez, A.I.; Puccia, C.G. Photodynamic therapy for glioblastoma: A light at the end of the tunnel. *J. Photochem. Photobiol.* **2023**, *13*, 100161. [\[CrossRef\]](#)
108. Fujita, Y.; Nagashima, H.; Tanaka, K.; Hashiguchi, M.; Itoh, T.; Sasayama, T. Hyperintense signal on diffusion-weighted imaging for monitoring the acute response and local recurrence after photodynamic therapy in malignant gliomas. *J. Neurooncol.* **2021**, *155*, 81–92. [\[CrossRef\]](#) [\[PubMed\]](#)
109. Sheehan, K.; Sheehan, D.; Sulaiman, M.; Padilla, F.; Moore, D.; Sheehan, J.; Xu, Z. Investigation of the tumoricidal effects of sonodynamic therapy in malignant glioblastoma brain tumors. *J. Neurooncol.* **2020**, *148*, 9–16. [\[CrossRef\]](#) [\[PubMed\]](#)
110. Wu, T.; Liu, Y.; Cao, Y.; Liu, Z. Engineering Macrophage Exosome Disguised Biodegradable Nanoplatfor for Enhanced Sonodynamic Therapy of Glioblastoma. *Adv. Mater.* **2022**, *34*, e2110364. [\[CrossRef\]](#)
111. Zhang, C.; Wu, J.; Liu, W.; Zheng, X.; Zhang, W.; Lee, C.S.; Wang, P. A novel hypocrellin-based assembly for sonodynamic therapy against glioblastoma. *J. Mater. Chem. B* **2021**, *10*, 57–63. [\[CrossRef\]](#)
112. Guo, Q.L.; Dai, X.L.; Yin, M.Y.; Cheng, H.W.; Qian, H.S.; Wang, H.; Zhu, D.M.; Wang, X.W. Nanosensitizers for sonodynamic therapy for glioblastoma multiforme: Current progress and future perspectives. *Mil. Med. Res.* **2022**, *9*, 26. [\[CrossRef\]](#)
113. Suehiro, S.; Ohnishi, T.; Yamashita, D.; Kohno, S.; Inoue, A.; Nishikawa, M.; Ohue, S.; Tanaka, J.; Kunieda, T. Enhancement of antitumor activity by using 5-ALA-mediated sonodynamic therapy to induce apoptosis in malignant gliomas: Significance of high-intensity focused ultrasound on 5-ALA-SDT in a mouse glioma model. *J. Neurosurg.* **2018**, *129*, 1416–1428. [\[CrossRef\]](#)
114. Omuro, A. Immune-checkpoint inhibitors for glioblastoma: What have we learned? *Arq. Neuropsiquiatr.* **2022**, *80*, 266–269. [\[CrossRef\]](#)
115. Medikonda, R.; Dunn, G.; Rahman, M.; Fecci, P.; Lim, M. A review of glioblastoma immunotherapy. *J. Neurooncol.* **2021**, *151*, 41–53. [\[CrossRef\]](#) [\[PubMed\]](#)
116. Zeng, Q.; Yang, J.; Ji, J.; Wang, P.; Zhang, L.; Yan, G.; Wu, Y.; Chen, Q.; Liu, J.; Zhang, G.; et al. PD-L1 blockade potentiates the anti-tumor effects of ALA-PDT and optimizes the tumor microenvironment in cutaneous squamous cell carcinoma. *Oncoimmunology* **2022**, *11*, 2061396. [\[CrossRef\]](#) [\[PubMed\]](#)
117. Werner, M.; Lyu, C.; Stadlbauer, B.; Schrader, I.; Buchner, A.; Stepp, H.; Sroka, R.; Pohla, H. The role of Shikonin in improving 5-aminolevulinic acid-based photodynamic therapy and chemotherapy on glioblastoma stem cells. *Photodiagn. Photodyn. Ther.* **2022**, *39*, 102987. [\[CrossRef\]](#) [\[PubMed\]](#)

Disclaimer/Publisher's Note: The statements, opinions and data contained in all publications are solely those of the individual author(s) and contributor(s) and not of MDPI and/or the editor(s). MDPI and/or the editor(s) disclaim responsibility for any injury to people or property resulting from any ideas, methods, instructions or products referred to in the content.

Article

Interrelation between Spectral Online Monitoring and Postoperative T1-Weighted MRI in Interstitial Photodynamic Therapy of Malignant Gliomas

Maximilian Aumiller ^{1,2,*} , Christian Heckl ^{1,2}, Stefanie Quach ³, Herbert Stepp ^{1,2} , Birgit Ertl-Wagner ⁴, Ronald Sroka ^{1,2}, Niklas Thon ³ and Adrian Rühm ^{1,2}

¹ Laser-Forschungslabor, LIFE Center, University Hospital, LMU Munich, 82152 Planegg, Germany; christianheckl1@web.de (C.H.); herbert.stepp@med.uni-muenchen.de (H.S.); ronald.sroka@med.uni-muenchen.de (R.S.); adrian.ruehm@med.uni-muenchen.de (A.R.)

² Department of Urology, University Hospital, LMU Munich, 81377 Munich, Germany

³ Department of Neurosurgery, University Hospital LMU Munich, 81377 Munich, Germany; Stefanie.Quach@med.uni-muenchen.de (S.Q.); Niklas.Thon@med.uni-muenchen.de (N.T.)

⁴ Department of Medical Imaging, The Hospital for Sick Children, University of Toronto, Toronto, ON M5G 1X8, Canada; birgitbetina.ertl-wagner@sickkids.ca

* Correspondence: max.aumiller@med.uni-muenchen.de; Tel.: +49-89-44000



Citation: Aumiller, M.; Heckl, C.; Quach, S.; Stepp, H.; Ertl-Wagner, B.; Sroka, R.; Thon, N.; Rühm, A. Interrelation between Spectral Online Monitoring and Postoperative T1-Weighted MRI in Interstitial Photodynamic Therapy of Malignant Gliomas. *Cancers* **2022**, *14*, 120. <https://doi.org/10.3390/cancers14010120>

Academic Editor: Fiona Lyng

Received: 8 November 2021

Accepted: 22 December 2021

Published: 27 December 2021

Publisher's Note: MDPI stays neutral with regard to jurisdictional claims in published maps and institutional affiliations.



Copyright: © 2021 by the authors. Licensee MDPI, Basel, Switzerland. This article is an open access article distributed under the terms and conditions of the Creative Commons Attribution (CC BY) license (<https://creativecommons.org/licenses/by/4.0/>).

Simple Summary: Treatment monitoring is highly important for the delivery and control of brain tumor therapy. For interstitial photodynamic therapy (iPDT), an intraoperative spectral online monitoring (SOM) setup was established in former studies to monitor photosensitizer fluorescence and treatment light transmission during therapy. In this work, data from patients treated with iPDT as the initial treatment for newly diagnosed glioblastoma ($n = 11$) were retrospectively analyzed. Observed changes in treatment light transmission were assessed, and changes in optical tissue absorption were calculated out of these. In addition, magnetic resonance imaging (MRI) data were recorded within 48 h after therapy and showed intrinsic T1 hyperintensity in the treated area in non-contrast-enhanced T1-weighted sequences. A 3D co-registration of intrinsic T1 hyperintensity lesions and the light transmission zones between cylindrical diffuser fiber pairs showed that reduction in treatment light transmission corresponding to increased light absorption had a spatial correlation with post-therapeutic intrinsic T1 hyperintensity ($p \leq 0.003$).

Abstract: In a former study, interstitial photodynamic therapy (iPDT) was performed on patients suffering from newly diagnosed glioblastoma ($n = 11$; 8/3 male/female; median age: 68, range: 40–76). The procedure includes the application of 5-ALA to selectively metabolize protoporphyrin IX (PpIX) in tumor cells and illumination utilizing interstitially positioned optical cylindrical diffuser fibers (CDF) (2–10 CDFs, 2–3 cm diffuser length, 200 mW/cm, 635 nm, 60 min irradiation). Intraoperative spectral online monitoring (SOM) was employed to monitor treatment light transmission and PpIX fluorescence during iPDT. MRI was used for treatment planning and outcome assessment. Case-dependent observations included intraoperative reduction of treatment light transmission and local intrinsic T1 hyperintensity in non-contrast-enhanced T1-weighted MRI acquired within one day after iPDT. Intrinsic T1 hyperintensity was observed and found to be associated with the treatment volume, which indicates the presence of methemoglobin, possibly induced by iPDT. Based on SOM data, the optical absorption coefficient and its change during iPDT were estimated for the target tissue volumes interjacent between evaluable CDF-pairs at the treatment wavelength of 635 nm. By spatial comparison and statistical analysis, it was found that observed increases of the absorption coefficient during iPDT were larger in or near regions of intrinsic T1 hyperintensity ($p = 0.003$). In cases where PpIX-fluorescence was undetectable before iPDT, the increase in optical absorption and intrinsic T1 hyperintensity tended to be less. The observations are consistent with in vitro experiments and indicate PDT-induced deoxygenation of hemoglobin and methemoglobin formation. Further investigations are needed to provide more data on the time course of the observed changes, thus paving the way for optimized iPDT irradiation protocols.

Keywords: malignant glioma; glioblastoma; photodynamic therapy; interstitial photodynamic therapy; 5-ALA; protoporphyrin IX; online monitoring; fluorescence; T1 hyperintensity; methemoglobin

1. Introduction

The standard of care for treating newly diagnosed malignant gliomas comprises surgical resection, when feasible, followed by radiochemotherapy. Unfortunately, the median survival for patients suffering from high grade gliomas continues to be low [1,2]. In an attempt to improve this dismal prognosis, the feasibility of photodynamic therapy (PDT) has been investigated since the 1980s [3,4]. So far, several clinical trials using different photosensitizers have been published (for an overview, see [5]). Several clinical studies have explored the use of 5-aminolevulinic acid (5-ALA) as a photosensitizer precursor [6–10], which has some intriguing advantages over other photosensitizers for treating high grade gliomas:

- There is much less concern about unspecific photosensitization during circulation and tissue distribution, as 5-ALA itself is not photoactive [11].
- Clinically approved, 5-ALA is also widely used for protoporphyrin IX (PpIX)-based fluorescence-guided resection of malignant gliomas [11–13].
- The photosensitizer PpIX is produced in the mitochondria of malignant glioma cells with a high selective accumulation compared to adjacent tissue [11].
- Due to the relatively fast photobleaching of PpIX, any low PpIX concentration metabolized in adjacent tissue will be used up before cell death is induced [14–16].

There are two different approaches to deliver 5-ALA-based PDT for malignant gliomas: as an adjuvant treatment after surgical resection in order to destroy residual PpIX-containing diffusely infiltrating glioma cells [17,18] or as a primary treatment in a stereotactic interstitial approach by inserting cylindrical diffuser fibers (CDF) into the glioma tissue, named interstitial PDT (iPDT) [6,10,14].

In any approach, sufficient light needs to be delivered throughout the relevant tissue volumes. Light penetration depends on the wavelength-dependent optical tissue parameters governing light absorption and scattering. Utilizing Monte Carlo simulations, it was shown that inside the tissue the light fluence rate around a CDF used during iPDT typically decays exponentially to $1/e$ (37%) within less than 3 mm for red light [6,19]. At 635 nm, the iPDT treatment wavelength used for excitation of the 5-ALA-induced PpIX, blood is still the dominant absorber. Therefore, the absorption depends, critically, also on the blood oxygenation level, as the absorption coefficient of deoxygenated blood is about 8.5 times higher than that of oxygenated blood at this specific wavelength [20]. As PDT consumes tissue oxygen, the oxygenation status of hemoglobin—and thus its absorption coefficient—may dynamically vary during treatment as reported [21,22]. It can be hypothesized that intracerebral hemorrhages induced by the implantation procedure may, therefore, have a rather complex impact on treatment success. To elucidate the involved processes, the effects of 5-ALA-PDT on hemoglobin absorption were experimentally assessed in an artificial liquid tissue phantom model in a prior study [23]. In artificial samples containing intact erythrocytes, almost no change in optical parameters was observed when the illumination started and PpIX photobleaching occurred continuously. If lysed erythrocytes were used in the liquid phantom, however, a change in treatment light transmission was observed immediately after initiating treatment. Comparing these two experiments shows that some time is needed for the erythrocyte cell membrane to rupture under laser irradiation, plus further time for the hemoglobin to be deoxygenated. Once the erythrocyte cell membrane ruptured, rapid deoxygenation of the hemoglobin occurred, and, in addition, met-hemoglobin (MetHb) was formed. As the absorption of deoxy-hemoglobin (Hb) and, even more so, of MetHb at 635 nm is much stronger than the absorption of oxy-hemoglobin (HbO₂) (about 8.5 and 33 times higher, respectively), this has an immediate effect on the light distribution [23].

Clinically, intercranial hemorrhages are visualized and controlled using CT and MRI. In case of an intracerebral hemorrhage, the MRI signal characteristics depend on the cellular location and the different types of hemoglobin produced during the breakdown and removal of blood [24]. Typically, in the acute setting after intracerebral hemorrhage, intracellular HbO₂ or, later, Hb appears largely isointense to the surrounding brain parenchyma in non-enhanced T1-weighted MR imaging. Two to three days after PDT illumination, the formation of intracellular MetHb is usually seen as intrinsic signal hyperintensity on T1-weighted images [24–28]. Whether and how these changes are seen after PDT treatment, and whether and how they may be related to the PDT procedure, has not been systematically investigated so far.

Therefore, in this investigation, intraoperative changes in treatment light transmission and PpIX fluorescence are assessed, based on measurements before and after iPDT according to the spectral online monitoring (SOM) procedure described in [7,10,29], retrospectively analyzed for a number of patients with high grade glioma undergoing iPDT [8]. A further aim was the investigation of potential relations between changes in light absorption within the tissue and intrinsic T1 hyperintensity visible on early postoperative MRI within 48 h after treatment. To this end, the appearance, strength, as well as 3D positional relations of increased light absorption within the tissue and intrinsic T1 hyperintensity in early postoperative MRI data were analyzed.

2. Materials and Methods

2.1. Data Acquisition

Ethical approval for the retrospective analysis of the collected data was obtained from the institutional review board (University Hospital LMU Munich ethics protocol: UE no. 335–16). SOM and MRI data were obtained from patients suffering from de novo GBM treated with salvage iPDT [8] and were analyzed retrospectively ($n = 11$; 8/3 male/female; median age: 68, range: 40–76). Relevant irradiation and spectral online monitoring characteristics are listed in Table 1. In one case, the entire tumor could not be treated in one single treatment session due to its localization. Therefore, iPDT was applied in two successive treatment sessions: iPDT cases #4a and #4b. The iPDT treatment was performed as earlier described [6,8]. The number of CDFs and the insertion coordinates for stereotactic placement of the fibers were determined by careful 3D treatment planning (target 1.19 software, Brain LAB AG, Munich, Germany), with the number of CDFs employed per iPDT ranging from 2 to 10. Parallel placement of the CDFs is favored but not always possible due to the shape of the target volume or other restrictions to be considered during the treatment planning. Treatment light with a wavelength of 635 nm was delivered by a 4-port diode laser system (Ceralas PDT Diode Laser, biolitec AG, Jena, Germany). The CDFs (outer diameter 1.56 mm; Light Guide Optics, Rheinbach, Germany) with a 20 or 30 mm diffuser length were connected to the laser ports via short connecting fibers. To perform SOM measurements, all treatment fibers, except the one for illumination and excitation for the desired measurement, were temporarily disconnected from the short connecting fibers and instead connected to the inputs of a fiber switch (MPM-2000, Mikropack, Ostfildern, Germany) [10,29]. The output of the fiber switch was guided to a spectrometer (USB2000+, Ocean Insight, former Ocean Optics, Ostfildern, Germany) with a long pass inline filter (RG645, Schott Glas, Mainz, Germany) at the spectrometer entrance. PDT illumination was conducted with a 200 mW/cm diffuser length for 1 h as standard-setting [30], if not indicated otherwise in Table 1. It was shown that, for comparable scenarios, this power setting limits the tissue heating to below 42 °C [6]. A minimum target light dose of 18.7 J/mm² was used for treatment planning, as previously calculated based on the concept of “complete” photobleaching [31]. In cases where interfiber distances below 9 mm had to be chosen due to restrictions in the treatment planning (e.g., blood vessels near the trajectories), the power was reduced and the irradiation time prolonged to prevent thermal damage. SOM was performed twice, immediately before (pre) and after (post) iPDT illumination, thus receiving the pre and post iPDT spectra, exemplarily illustrated in Figure 1. The

transmitted treatment light is visible in the wavelength range of 626–642 nm. The PpIX fluorescence signal is in the range of 650–750 nm. In total, 320 spectra (pre plus post iPDT) were recorded and analyzed (range: 2–36 per iPDT case, median: 24), representing about 41% of all possibilities of measurable spectra (784 for 392 CDF-pair combinations).

Table 1. Irradiation and spectral online monitoring characteristics, displaying the number of measured spectra and used cylindrical diffuser fibers (CDFs) with the irradiation parameters during the treatment.

iPDT Case	Total Number of Measured Spectra	CDFs Used	Median Interfiber Distance	CDF Power	Irradiation Time	Total Applied Light Dose
			[mm]	[mW/cm]	[s]	[J]
1	12	4	10.0	200	3600	8640
2	28	7	13.2	200	5400	20,520
3	30	6	10.5	200	3600	8640
4a	12	4	10.2	200	3600	8640
4b	2	2	10.0	200	3600	2880
5	20	5	11.0	100	7200	7200
6	20	5	12.3	150	7200	10,800
7	42	7	10.6	200	3600	12,960
8	72	9	13.0	200	3600	15,120
9	30	6	11.0	200	3600	12,960
10	32	10	13.2	200	3600	18,720
11	20	5	11.4	133	5400	8694

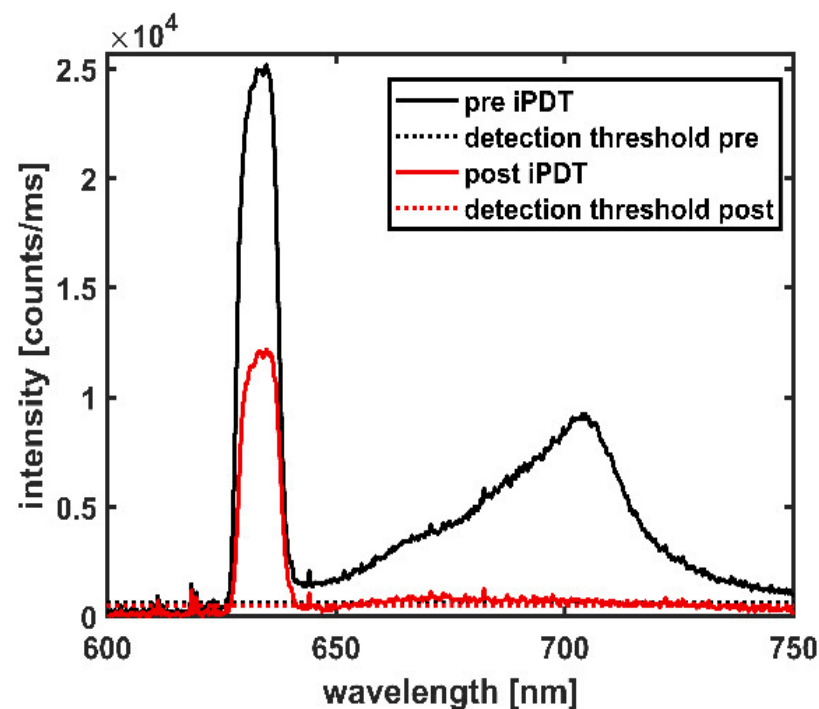


Figure 1. Spectral online monitoring data of a CDF-pair shown at iPDT start (pre iPDT, solid black line) and iPDT end (post iPDT, solid red line). Dotted lines indicate the detection thresholds.

2.2. Spectral Data Assessment

The spectra measured during the SOM procedure were assessed regarding treatment light transmission around 635 nm and PpIX fluorescence around 705 nm (see Figure 1). The transmitted treatment light was analyzed concerning its integral signal intensity I_t

(in counts/ms), recorded within the wavelength interval of 626–642 nm according to Equation (1).

$$I_t = \int_{626 \text{ nm}}^{642 \text{ nm}} I(\lambda) d\lambda \quad (1)$$

where $I(\lambda)d\lambda$ is the intensity measured within a wavelength interval $d\lambda$. The PpIX fluorescence was assessed by fitting a normalized pure PpIX fluorescence spectrum $I_{\text{PpIX}}(\lambda)$ and a normalized auto-fluorescence spectrum $I_{\text{auto}}(\lambda)$ to the recorded data $I_{\text{rec}}(\lambda)$ in the wavelength range of 650–750 nm:

$$I_{\text{rec}}(\lambda) = a I_{\text{PpIX}}(\lambda) + b I_{\text{auto}}(\lambda) \quad (2)$$

with adjustable weighting factors a and b . The first addend in Equation (2) represents the fitted PpIX spectrum contained in the recorded spectra. This fluorescence was analyzed based on its maximum signal intensity value I_f (in counts/ms) recorded within the wavelength range 702–708 nm:

$$I_f = \max\{a I_{\text{PpIX}}(\lambda) \mid 702 \text{ nm} \leq \lambda \leq 708 \text{ nm}\} \quad (3)$$

The signal intensities I_t and I_f given by Equations (1) and (3) were considered detectable (above detection threshold) if the maximum signal intensities $I(\lambda)$ within the specified wavelength intervals were higher than three times the noise level, which was determined individually for each spectrum from the spectral range of 500–550 nm, outside the ranges of transmitted treatment light and fluorescence. To obtain a measure for the change of treatment light transmission during iPDT, the intra-operative pre versus post iPDT treatment light transmission ratio $R_{\text{pre/post}}$ is calculated using Equation (4):

$$R_{\text{pre/post}} = \frac{I_{t,\text{pre}}}{I_{t,\text{post}}} \quad (4)$$

If $I_{t,\text{pre}}$ was below the detection threshold, $R_{\text{pre/post}}$ was defined as 0. Multiple measurements on tissue phantoms showed that the statistical uncertainty of the signal intensities I_t and I_f given by Equations (1) and (3) was not more than 8%. Propagation of uncertainty with the variance formula yields an uncertainty <20% for $R_{\text{pre/post}}$.

2.3. Calculation of Intensities and Optical Tissue Properties

Diffusion approximation was used for all calculations to derive the absorption coefficient μ_a of the tissue at the treatment wavelength of 635 nm using the measured treatment light transmission signal intensities I_t between the CDF-pairs. It was assumed that the CDFs emit and detect light homogeneously. The active CDF-sections were approximated as linear arrays of isotropically emitting point sources or isotropically collecting point detectors (five sources or detectors per mm diffuser length, each contributing with the same weight). The photon fluence rate Φ_{ij} generated for each photon emitted from one point source i on the emitting CDF at the location of one point detector j on the detecting CDF is given by [32,33]:

$$\Phi_{ij}(r_{ij}, \mu_a, \mu'_s) = \frac{1}{4 \pi r_{ij}} 3(\mu_a + \mu'_s) \exp\left(-r_{ij} \sqrt{3\mu_a(\mu_a + \mu'_s)}\right) \quad (5)$$

where r_{ij} is the distance between an emitting and a detector point and μ'_s the reduced scattering coefficient of the tissue. The double sum over Equation (5) for all emitting points i and detector points j includes all point-to-point combinations between the two CDFs and is proportional to the theoretically expected value of the transmitted treatment light intensity $I_{t,\text{theo}}$ for the CDF-pair [34]. As for constant emission power per active CDF length,

the total power emitted by a CDF scales with the length of its light-emitting section; L_E , $I_{t,theo}$ is described by Equation (6):

$$I_{t,theo} = \frac{P_0 \cdot L_E}{N} \sum_i \sum_j \Phi_{ij}(r_{ij}, \mu_a, \mu'_s) \quad (6)$$

where N is the number of point combinations. The constant calibration factor P_0 (in $\text{cm} \cdot \text{counts}/\text{ms}$) includes the emitted photon rate per cm diffuser length and the conversion factor from photon fluence rate at the detecting CDF-section to measured intensity. To note, Equation (6) is independent of the length of the active CDF section of the detector, which relies on the assumptions that the detection efficiency is homogeneous and the total detection efficiency is independent of the diffuser length. P_0 was determined experimentally by fitting Equation (6) to transmitted laser intensities acquired from measurements with the iPDT SOM setup in liquid artificial tissue phantoms with pre-characterized optical properties made from ink (brilliant black, Pelikan 4011, Pelikan Group GmbH, Berlin, Germany), Lipovenös® (Lipovenös MCT 20%, Fresenius, Bad Homburg, Germany), and distilled water. The measurements were performed between CDF-pairs with various active diffuser lengths in a distance-dependent manner.

To determine an average absorption coefficient μ_a at 635 nm for the tissue volume surrounding the CDF-pair in the clinical case, the integral transmitted treatment light intensity I_t obtained from the spectral measurements is compared to $I_{t,theo}(\mu_a, \mu'_s)$ (see Equation (6)). During this comparison, the absorption coefficient μ_a in Equation (6) is adjusted, and the reduced scattering coefficient μ'_s is kept constant at 2 mm^{-1} [6]. The distance values r_{ij} inserted in Equations (5) and (6) were calculated using the coordinates of the active CDF-sections defined in the treatment plan. These coordinates further define the coordinates of the emitter and detector points of each CDF-pair. From these calculations, the minimum distance was derived as a distance classifier for each CDF-pair, as the CDFs often cannot be placed perfectly in parallel to each other. For each CDF-pair, a lookup table of intensity values $I_{t,theo}(\mu_a)$ according to Equation (6) was calculated for a set of μ_a values from 0.0001 to 0.75 mm^{-1} with a resolution of 0.0001 mm^{-1} . The μ_a value leading to the best match between the calculated intensity $I_{t,theo}(\mu_a)$ and the intraoperatively measured intensity I_t was selected and defined as the representative absorption coefficient for the tissue volume surrounding the specified CDF-pair.

For CDF-pairs with no transmission (transmitted treatment light intensity below detection threshold) pre or post iPDT, the minimally needed μ_a to obtain a signal intensity equal to the detection threshold was determined, using the same procedure. From the μ_a values obtained from the pre and post iPDT spectra, the difference $\Delta\mu_a$ induced during the iPDT illumination was calculated. For iPDT case #1, $\Delta\mu_a$ was calculated based on $R_{pre/post}$, but not the two μ_a values themselves, because an individual optical filter was used, which was different from the filter used for the SOM procedure in all other iPDT cases, so the predetermined P_0 value was not suitable.

In addition, forward calculations were performed with Equation (6) to examine the influence of different blood volume fractions (bvf) and hemoglobin species in tumor tissue on I_t . As blood is the main absorber in tissue at 635 nm [35], the μ_a values inserted into Equation (6) were set to those of the respective hemoglobin species multiplied with the assumed bvf, while the absorption of all other tissue constituents was assumed to be neglectable. The following absorption coefficients at 635 nm were used for the different pure hemoglobin species: HbO_2 : $\mu_a = 0.2477 \text{ mm}^{-1}$; Hb : $\mu_a = 2.1149 \text{ mm}^{-1}$ and MetHb : $\mu_a = 8.1073 \text{ mm}^{-1}$ [20,36]. The average oxygen saturation of normal capillary blood is assumed to be 85% [37]. Therefore, a mixture of 85% HbO_2 and 15% Hb is used in the calculations for this case. To sum up, this resulted in the following absorption coefficients of the tissue per % bvf: $0.0053 \text{ mm}^{-1}/\%$ for capillary blood, $0.0211 \text{ mm}^{-1}/\%$ bvf for Hb , and $0.0811 \text{ mm}^{-1}/\%$ bvf for MetHb .

2.4. CT and MRI-Protocol

A contrast-enhanced CT was acquired for treatment planning after the induction of anesthesia and assembly of the stereotactic frame. MR images were acquired within 14 days before iPDT for treatment planning and on the day after iPDT for treatment assessment (median: 22 h after the end of therapy; range: 15–29 h). Pre- and postoperative MRI was performed with a GE SIGNA HDxt 3T scanner (GE Healthcare, General Electric, Chicago, IL, USA). T1-weighted sequences (Repetition time TR = 6.5 ms; Echo time TE = 3.15 ms) were recorded before (3D; resolution $0.4297 \times 0.4297 \times 3.5 \text{ mm}^3$) and after (3D; resolution $0.4297 \times 0.4297 \times 0.7 \text{ mm}^3$) administration of a Gadolinium-based contrast agent (GBCA).

2.5. MRI Analysis

By affine transformation using mutual information, MR images were co-registered with the CT scan in the stereotactic frame [38]. For this purpose, all images were resampled to the lowest image resolution ($0.4297 \times 0.4297 \times 0.5 \text{ mm}^3$) via 3D extrapolation. The resampling and automatic co-registration of the MR and CT images were performed using Advanced Normalization Tools (ANTs; version 2.3.2, University of Pennsylvania, Philadelphia, PA, USA, University of Virginia, Charlottesville, VA, USA and University of Iowa, Iowa City, IA, USA) [39]. The co-registration was visually verified and, if necessary, adjusted manually using ITK-Snap (version 3.8, University of Pennsylvania, Philadelphia, USA) [40]. The tumor volume was defined in the pre-therapeutic contrast-enhanced T1-weighted MR images. The T1 hyperintensity structure was segmented in the post-therapeutic non-contrast enhanced T1-weighted MRI. T1 hyperintensity structures were defined as regions where the intensity was higher than in the directly surrounding tissue in the post-therapeutic dataset but not in the pre-therapeutic dataset. The segmentation of all structures was performed manually and was independently reviewed by two medical doctors (S.Q., neurosurgeon with more than 5 years experience; and B.E-W., neuroradiologist with more than 15 years of post-fellowship experience in interpreting MRI). To characterize the spatial relation of the tumor volume (V_T) and the intrinsic T1 hyperintensity (V_{hyp}) structures, the Dice similarity coefficient (DSC, Equation (7)), and the Jaccard similarity coefficient (JSC, Equation (8)), as well as the overlap volume (OV, Equation (9)), were calculated [41–44].

$$DSC = \frac{2 |V_T \cap V_{hyp}|}{|V_T| + |V_{hyp}|} \quad (7)$$

$$JSC = \frac{|V_T \cap V_{hyp}|}{|V_T \cup V_{hyp}|} \quad (8)$$

$$OV = \frac{|V_T \cap V_{hyp}|}{\min(|V_T|, |V_{hyp}|)} \quad (9)$$

A DSC or JSC value of 1 indicates identical volumes in shape, localization, and size. An OV of 1 indicates that the smaller volume is fully included in the larger volume. DSC, JSC, and OV values of 0 all indicate disjunct volumes without any overlap. In addition to the overlap parameters, the volume ratios V_{hyp}/V_T and $(V_T \cap V_{hyp})/V_T$ were calculated.

For the intrinsic T1 hyperintensity analysis, a normalized value of the MRI signal intensity within the intrinsic T1 hyperintensity region (I_{T1}) is calculated. I_{T1} provides at least a rough estimate of the degree of T1 hyperintensity. It further considers different gain settings of the images, allowing comparability between the different iPDT cases.

$$I_{T1} = \frac{\bar{I}_{T1}}{\bar{I}_{WM}} \quad (10)$$

According to Equation (10), I_{T1} is defined as the ratio of the mean image intensity within the intrinsic T1 hyperintensity (\bar{I}_{T1}) and the mean image intensity of white matter regions (\bar{I}_{WM}). For this purpose, seven isotropic spheres (diameter 8 mm) containing only white matter were drawn in the brain hemisphere unaffected by the tumor, and their overall mean image intensity was calculated. In this calculation, background intensity was neglected, as it was less than 1% of the image intensity.

2.6. Overlap Calculation between T1 Hyperintensity and CDF-Pairs

For further assessment of the obtained MRI and SOM results, the spatial relation between intrinsic T1 hyperintensity and the positions of the CDFs placed in the tumor was examined. To determine whether the T1 hyperintensity is located between a CDF-pair and how much it may have affected the light transmission, a 3D volume of simple geometrical shape (see Figure 2) was defined around the active sections of each CDF-pair. That volume roughly represents the region in which most light propagation occurs from one to the other CDF. This “light transmission zone” is a volume with standardized shape which was intersected with the intrinsic T1 hyperintensity, as shown in Figure 2. For the positional analysis, the coordinates of the stereotactic CDF trajectory were transformed to CT image coordinates, using a linear coordinate transformation, and the image coordinates of the active CDF-section along the trajectory were determined. Based on these coordinates, the predominant light transmission zone surrounding a CDF-pair was defined by fluence calculations between two parallel line sources placed at a 10 mm distance. Assuming tumor-like tissue optical properties ($\mu_a = 0.02 \text{ mm}^{-1}$, $\mu_s' = 2 \text{ mm}^{-1}$ [6]), Equations (5) and (6) were used to determine the two light fluence rates that would be generated in every voxel (size $0.1 \times 0.1 \times 0.1 \text{ mm}^3$) of a large discretized volume surrounding the CDF-pair if one or the other active CDF-section would emit light, respectively. By multiplication of these fluence rates (Equation (11)), an estimate measure for the contribution of a voxel with coordinates (x, y, z) to the treatment light transmission signal expected for this CDF-pair is obtained.

$$I_{\text{voxel}}(x, y, z) \sim \Phi_1(x, y, z) \cdot \Phi_2(x, y, z) \quad (11)$$

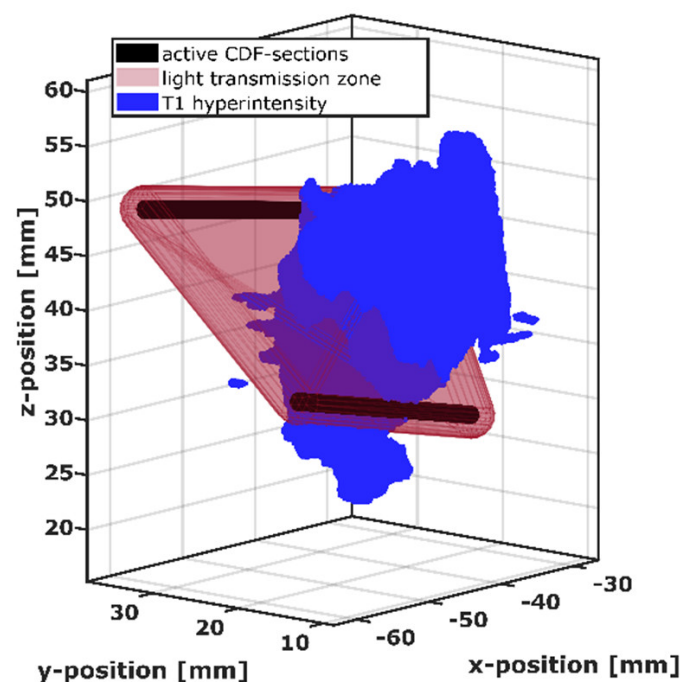


Figure 2. Visualization of the intersection between the light transmission zone (red) of the active cylindrical diffuser fiber (CDF) sections of one CDF-pair (black) and the intrinsic T1 hyperintensity volume (blue).

Using this estimation, the light transmission zone was defined by combining the voxels with the strongest contributions, up to a total contribution of 2/3 (67%) compared to the sum over all voxels. The size of this combined volume corresponds to a convex hull surrounding two capsules of radius 2.1 mm constructed around the two active sections of the CDF-pair. The definition of the light transmission zone was standardized in this way for all CDF-pairs, i.e., by the construction of capsule-shaped volumes with radius 2.1 mm around the active CDF-sections and the subsequent construction of the convex hull around these two capsule-shaped volumes. For the 3D analysis, the capsule-shaped volumes are built up employing a computer aided design program (FreeCAD version 0.18.16117 © Juergen Riegel, Werner Mayer, Yorik van Havre 2001–2019), and the convex hull around them is computed automatically with Matlab R2018b (MathWorks Inc., Natick, MA, USA) during the intersection process. For the positional analysis of the volumes illustrated in Figure 2, the T1 hyperintensity volume was transformed into a tetrahedral mesh with an average tetrahedron size of 0.02 mm³ (min: 0.0004 mm³, max: 0.06 mm³) using a mesh tool based on the computational geometry algorithms library (CGAL) [45]. For each tetrahedron, it was checked whether it was within the light transmission zone of a CDF-pair, and the overlap volume was determined by summing those tetrahedron volumes. In case of a non-zero overlap volume, the CDF-pair was regarded as affected by T1 hyperintensity.

2.7. Data Evaluation and Statistics

Descriptive p-values were calculated using the Mann–Whitney U test and the two-sided Spearman test (alpha = 0.05; power = 0.8). Statistical comparisons were performed using IBM SPSS Statistics for Windows, version 25 (IBM Corp., Armonk, NY, USA). Mathematical calculations and data fitting procedures were implemented in MATLAB R2018b (MathWorks Inc., Natick, MA, USA). The 3D visualizations and further 3D analysis were completed using Paraview version 5.6.0 (Kitware, Inc., Clifton Park, NY, USA, [46]).

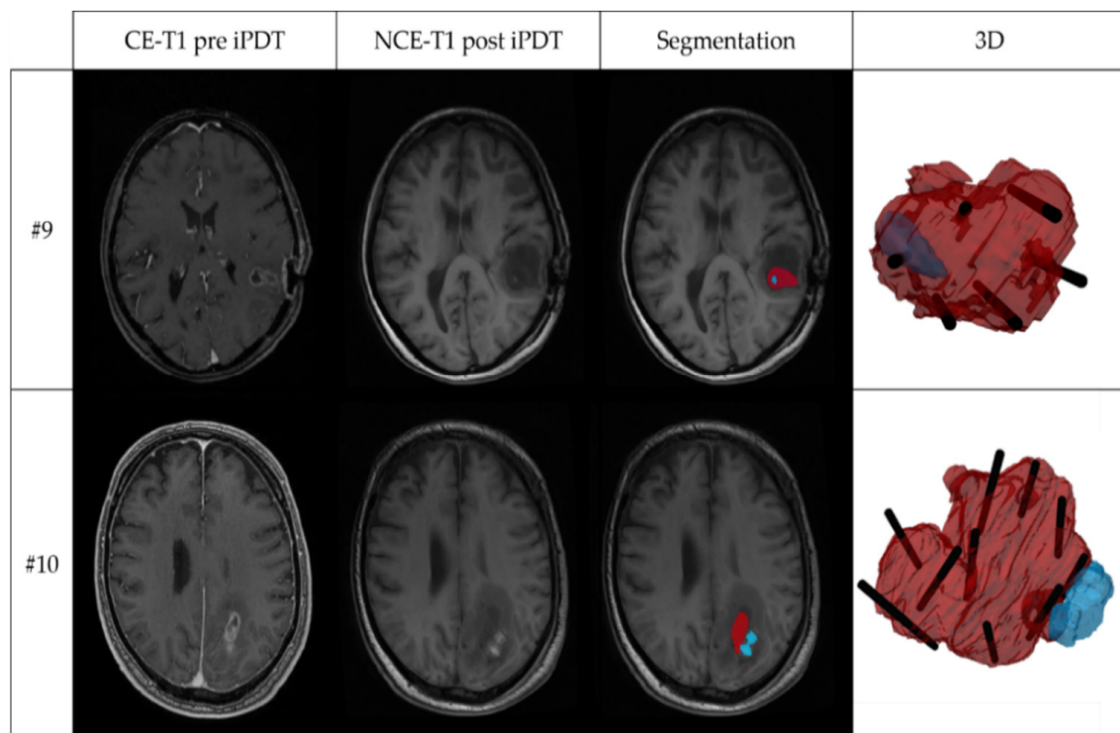
3. Results

3.1. T1 Hyperintensity in Early Postoperative MRI and 3D Superimposition

Intrinsic T1 hyperintensity was visible in early postoperative MRI (median: 22 h after the end of therapy; range: 15–29 h) after iPDT. The calculated geometric and overlay measures of the tumor volume (V_T) and the intrinsic T1 hyperintensity volume (V_{hyp}) are listed in Table 2. While the median T1 hyperintensity volume (V_{hyp}) was 790.1 mm³, there was one case with V_{hyp} less than 100 mm³ and two cases with V_{hyp} larger than 1500 mm³. The maximum diameter of the intrinsic T1 hyperintensity ranged between 3 mm and 19.1 mm (median: 8.45 mm). The comparison between V_{hyp} and the tumor volume V_T based on V_{hyp}/V_T shows that in 7/12 patients, the intrinsic T1 hyperintensity volume after treatment was larger than 5% of the tumor volume. In only three cases was it larger than 30%. With regard to $(V_{hyp} \cap V_T)/V_T$, in only 5/12 cases more than 5% (max 28%) of the tumor volume was covered by T1 hyperintensity. In 11/12 cases V_{hyp} was smaller than V_T so that $OV = (V_{hyp} \cap V_T)/V_{hyp}$. Thereof, in 7/11 cases, at least 60% of the intrinsic T1 hyperintensity are localized within the tumor (median: 0.61). In 3/12 cases, the volume of intrinsic T1 hyperintensity was almost completely located within the tumor volume ($OV > 0.90$). This is demonstrated in Figure 3, showing in the upper panel the T1-weighted MR images and segmentations for case #9 with the largest overlap, $OV = 0.99$. The 3D superimposition shows that the intrinsic T1 hyperintensity region (blue) is almost completely located within the contrast enhancing tumor region (red) and crossing one of the CDF sections (black). In the lower panel of Figure 3, case #10 with the smallest overlap, $OV = 0.02$, is shown. Here, the 3D superimposition shows that the intrinsic T1 hyperintensity volume is located almost entirely outside the segmented tumor volume, but next to two CDFs.

Table 2. Tumor volume (V_T) and properties of the intrinsic T1 hyperintensity volume (V_{hyp}) of the different iPDT cases and the calculated Overlap (OV), Dice (DSC), and Jaccard (JSC).

iPDT Case	V_T (mm ³)	V_{hyp} (mm ³)	Max. Diameter V_{hyp} (mm)	I_{T1} a.u.	$\frac{V_{hyp}}{V_T}$ (%)	$\frac{V_{hyp} \cap V_T}{V_T}$ a.u.	OV a.u.	DSC a.u.	JSC a.u.
1	1382	50	4.6	0.67	3.7	0.02	0.42	0.03	0.02
2	8574	3928	19.1	1.45	45.8	0.28	0.62	0.39	0.24
3	1955	544	9.6	0.80	27.8	0.01	0.03	0.01	0.01
4a	2269	1740	12.0	0.56	76.7	0.22	0.29	0.25	0.14
4b	537	978	15.0	0.91	182.1	0.03	0.03	0.02	0.01
5	4079	137	4.5	0.59	3.4	0.02	0.66	0.04	0.02
6	6920	152	4.4	0.71	2.2	0.02	0.96	0.04	0.02
7	11,020	361	3.0	0.73	3.3	0.03	0.94	0.06	0.03
8	13,650	1374	10.0	0.81	10.1	0.08	0.79	0.14	0.08
9	7176	115	5.1	0.73	1.6	0.02	0.99	0.03	0.02
10	15,340	1065	13.1	1.19	6.9	0.00	0.02	0.00	0.00
11	3990	603	7.3	0.74	15.1	0.09	0.60	0.16	0.09
median	6064	790	8.45	0.74	12.8	0.05	0.61	0.09	0.05

**Figure 3.** Two examples of MRI and 3D superimposition visualization, showing: contrast-enhanced T1-weighted MRI before iPDT (CE-T1 pre iPDT); non-contrast-enhanced T1-weighted MRI after iPDT (NCE-T1 post iPDT); segmentation of the tumor volume (red) and intrinsic T1 hyperintensity (blue) based on the CE-T1 pre iPDT and NCE-T1 post iPDT images; and 3D superimposition of tumor volume (red), intrinsic T1-hyperintensity volume (blue), and planned localization of irradiating tips of cylindrical diffuser fibers (black). The upper panel shows iPDT case #9 with the largest overlap coefficient (OV = 0.99); the lower panel iPDT case #10 with smallest overlap coefficient (OV = 0.02).

In total, 5/11 patients had an OV < 0.5, but the volume of intrinsic T1 hyperintensity was still located in close proximity to the contrast-enhancing tumor region. DSC and JSC show the positional agreement between tumor and T1 hyperintensity to be 0.39 or 0.24 at most, respectively (median: 0.09/0.05). A higher OV than DSC or JSC further indicates the high volume differences between V_T and V_{hyp} . Further comparison of the intrinsic

T1 hyperintensity and the position of CDF-pairs demonstrated that 298/392 CDF-pairs (76%) had a local intrinsic T1 hyperintensity involvement within the light transmission zone surrounding the CDF-pair. The residual 94/392 CDF-pairs (24%) showed no local intrinsic T1 hyperintensity involvement. Of all CDF-pairs, 108/392 (27.6%, or 36.2% of all 298 CDF-pairs with T1 hyperintensity) had >5% T1 hyperintensity volume in the light transmission zone surrounding the CDF-pairs.

3.2. Effects of Different Blood Volume Fractions on Laser Light Transmission at 635 nm

As intrinsic T1 hyperintensity in early postoperative MRI may be associated with blood degradation products, theoretical calculations were made to illustrate the effects of increasing blood volume fraction (bvf) and different hemoglobin species on the detected light intensities. The results shown in Figure 4 represent the calculated dependency of the treatment light transmission on the interfiber distance between two parallel CDFs with 20 mm diffuser length. The shown intensity values are normalized to the intensity in tumor tissue with optical parameters $\mu_a = 0.02 \text{ mm}^{-1}$; $\mu'_s = 2 \text{ mm}^{-1}$ (bvf = 3.8%, red solid line) at 10 mm interfiber distance indicated by a red circle in Figure 4. These values are compared to the detection threshold of the SOM setup obtained from the intraoperative data marked by a horizontal dashed line. A slightly increased bvf (7.5% or 15%, cyan curves), potentially induced by a hemorrhage, would reduce the signal intensity. However, transmitted laser light would still be detectable at interfiber distances up to at least 17 mm. In case the bvf increases further, e.g., if a hemorrhage is induced during fiber placement before iPDT illumination, the absorption increases further and leads to a steeper signal decay (brown dashed curve). According to the calculations and assumptions, a bvf of at least 40% accounts for absorption, making it impossible to detect a transmitted light signal for interfiber distances larger than 10 mm (brown square). In addition to changes in bvf, spectral changes of the absorbing molecules may occur. For example, with ongoing iPDT and deoxygenation of the blood, Hb might become the relevant absorber. With Hb as the absorber, the effect of the increase on μ_a would rise by a factor of four, resulting in a further reduction of transmitted light intensity, as shown by the dark blue lines (Hb = 7.5%/15%). A fraction of about 10% Hb would have a similar effect as a hemorrhage with 40% bvf. The occurrence of methemoglobin would lead to a further drastic reduction of signal intensity (violet curves). A MetHb fraction of 15% in tissue (μ_a (15% MetHb) = 1.2 mm^{-1}) would lead to a complete loss of detectable laser light for CDF separations larger than 4 mm (violet dashed curve). Calculations show that 1% bvf of MetHb would lead to an absorption of $\mu_a \sim 0.08 \text{ mm}^{-1}$, which is four times higher than the preset 'normal' tumor absorption of $\mu_a = 0.02 \text{ mm}^{-1}$ with a bvf of 3.8%. Thus two different changes must be considered for interpretation of measured SOM data: changes in the bvf and changes in the absorption spectrum due to photo-induced molecular processes.

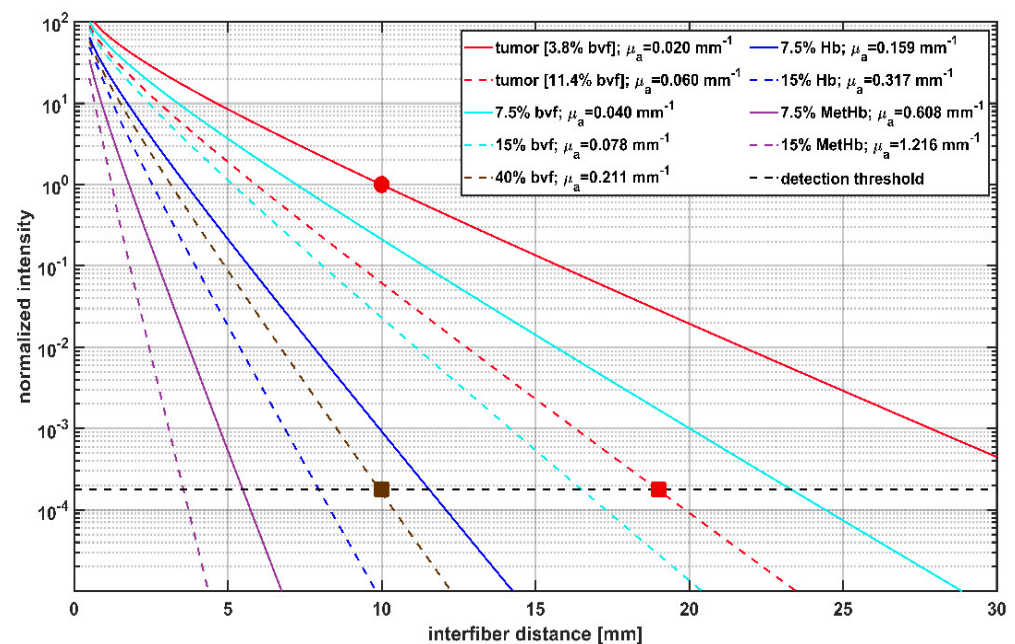


Figure 4. Calculation of transmitted light intensity at 635 nm between cylindrical diffuser fibers (CDFs) with a 2 cm diffuser length, and its dependency on the interfiber distances for different blood volume fractions (bvf) and hemoglobin species. Blood is approximated to contain 85% HbO₂ and 15% Hb. Transmitted light intensities are normalized to tumor ($\mu_a = 0.02 \text{ mm}^{-1}$, $\mu_s' = 2 \text{ mm}^{-1}$) at 10 mm interfiber distance (red circle). The legend shows the different blood volume fractions of hemoglobin species and the resulting μ_a assumed for the calculation with μ_s' set constant to 2 mm^{-1} . The horizontal dashed line at 1.9×10^{-4} shows the estimated detection threshold of the iPDT SOM setup. The red square indicates that in case of a tumor with 11.4% bvf the detection threshold is reached at an interfiber distance of 19 mm. The brown square shows that for 40% bvf the detection threshold is already reached at an interfiber distance of 10 mm.

3.3. Intraoperative Transmission Intensity Change and Its Comparison to Intrinsic T1 Hyperintensity

Intraoperative SOM data were acquired for 160 CDF-pairs. For 132/160 CDF-pairs, the interfiber distance was less or equal to 19 mm, the distance at which a signal should be detectable even with the highest absorption measured for undisturbed “brain adjacent tumor” tissue ($\mu_a = 0.06 \text{ mm}^{-1}$, red square in Figure 4) [47]. Table 3 shows the numbers of CDF-pairs with detectable transmitted laser light and PpIX fluorescence pre and post iPDT and with or without local intrinsic T1 hyperintensity in the light transmission zone surrounding a CDF-pair. As CDF-pairs with interfiber distances larger than 19 mm may have no or very low laser light transmission even at ‘normal’ optical tissue properties, only CDF-pairs with interfiber distances ≤ 19 mm were included in the statistical evaluations (132/160). Of these 132 CDF-pairs, 17 showed no detectable laser light transmission at iPDT start. The 17 CDF-pairs divide into 14 cases with and 3 cases without local intrinsic T1 hyperintensity in early postoperative MRI, with a significantly higher number of those with local intrinsic T1 hyperintensity ($p = 0.008$). After iPDT, additional 25 CDF-pairs (increase from 39 to 64) had no detectable laser light transmission, which includes additional 20 CDF-pairs with interfiber distance ≤ 19 mm (increase from 17 to 37). Thereof 1 CDF-pair had no local intrinsic T1 hyperintensity, and 19 had local intrinsic T1 hyperintensity involvement. When considering CDF-pairs with interfiber distance ≤ 19 mm, PpIX fluorescence could be measured for 95/115 CDF-pairs pre iPDT, of which 72/95 had a local intrinsic T1 hyperintensity. After iPDT, residual PpIX fluorescence was observed in neither iPDT case nor for any CDF-pair. Two iPDT cases (#6 and #11) unite 19/20 (95%) of all CDF-pairs without detectable PpIX fluorescence pre-iPDT, corresponding to all CDF-pairs of these two cases. In Figure 5a, the calculated intra-operative pre versus post iPDT treatment light

transmission ratio $R_{\text{pre/post}}$ is plotted against the interfiber distance. The data are grouped by CDF-pairs with local intrinsic T1 hyperintensity involvement (red and black symbols) and those without (blue and cyan symbols). $R_{\text{pre/post}}$ values larger than 50 were observed only for CDF-pairs with detectable laser light transmission signal before but not after iPDT and with local intrinsic T1 hyperintensity in early postoperative MRI (black symbols). In total, 9/160 (6%) CDF-pairs had a $R_{\text{pre/post}}$ smaller than 0.8 (increase of $I_t > 20\%$; maximum error of $R_{\text{pre/post}}$ is 20%). For 98/160 CDF-pairs, $R_{\text{pre/post}}$ was larger than 1.20 (decrease of $I_t > 20\%$). The comparison of CDF-pairs with detectable transmission pre iPDT in Figure 5b shows that the ratio $R_{\text{pre/post}}$ is larger for CDF-pairs with local intrinsic T1 hyperintensity than for those without (median/interquartile range: 4.5/[2.3, 13.3] versus 2.3/[1.2, 4.1], $p = 0.001$).

Table 3. Overview of evaluated CDF-pairs and observed detectability of treatment light transmission intensity (transmission) or PpIX fluorescence signal before (pre iPDT) and after (post iPDT) conducted iPDTs.

Number of CDF-Pairs	Total	Transmission Detectable				Fluorescence Detectable			
		Pre iPDT		Post iPDT		Pre iPDT		Post iPDT	
		yes	no	yes	no	yes	no	yes	no
All interfiber distances	160	121	39	96	64	114	46	0	160
Interfiber distance ≤ 19 mm ¹	132	115	17	95	37	95 ²	20 ²	0	115 ²
With local intrinsic T1 hyperintensity	102	88	14	69	33	72 ²	16 ²	0	88 ²
Without local intrinsic T1 hyperintensity	30	27	3	26	4	23 ²	4 ²	0	27 ²

¹ Only CDF-pairs with interfiber distance ≤ 19 mm were included in statistical evaluations to avoid bias by spectra with undetectable transmission at “normal” optical tissue properties ($\mu_a \leq 0.06$ mm⁻¹). ² Transmission signal detectable pre iPDT (in total 115 CDF-pairs).

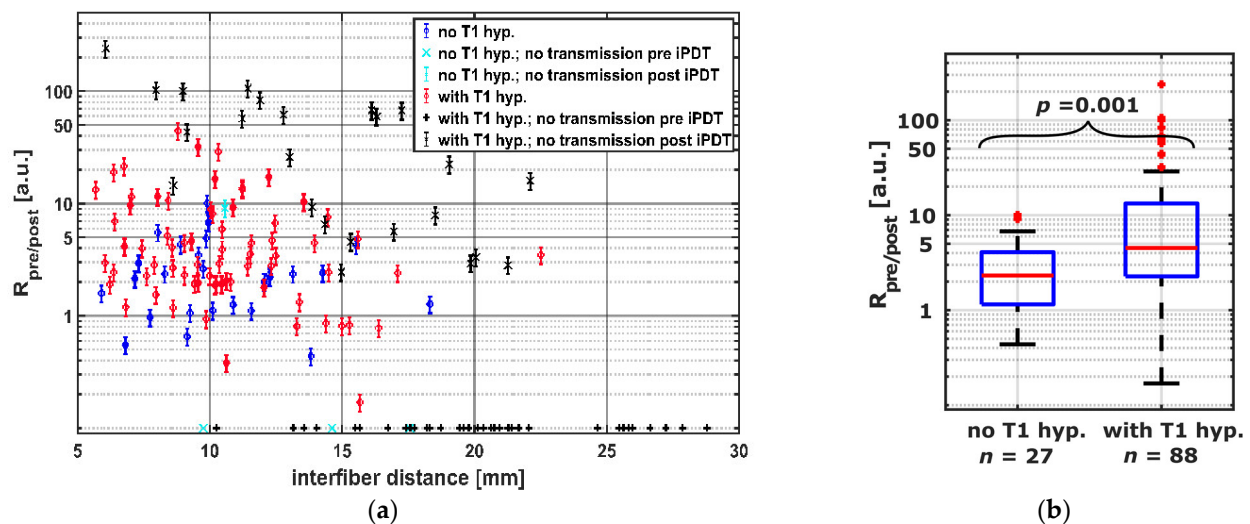


Figure 5. (a) Transmission ratios $R_{\text{pre/post}}$ for all CDF-pairs compared to interfiber distance. The colors and symbols indicate whether transmission was detectable post iPDT and whether T1 hyperintensity was observed (see legend). Crosses near the x-axis indicate CDF-pairs with no detectable treatment light transmission at iPDT start, for which $R_{\text{pre/post}}$ is defined as 0. (b) Comparison of CDF-pairs with and without local intrinsic T1 hyperintensity, considering only CDF-pairs with detectable transmission pre iPDT and interfiber distance ≤ 19 mm.

The average μ_a of the tissue between two CDFs, calculated from the SOM measurements pre iPDT, are shown in Figure 6 as a function of the interfiber distance. The median μ_a pre iPDT determined from all SOM measurements with detectable transmission signals

(blue and red symbols) was 0.068 mm^{-1} (interquartile range: $[0.045, 0.093]$). There was no significant difference between the μ_a values for CDF-pairs with and without intrinsic T1 hyperintensity (red versus blue symbols): 0.069 mm^{-1} vs. 0.070 mm^{-1} ; $p = 0.37$.

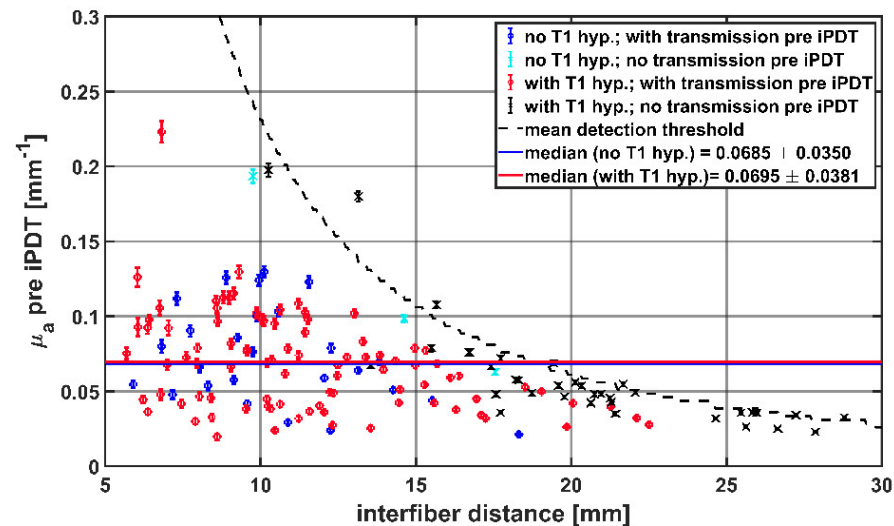


Figure 6. Calculated μ_a values before start of iPDT compared to interfiber distance. The colors and symbols indicate whether transmission was detectable pre iPDT and whether intrinsic T1 hyperintensity was observed (see legend). The dashed line represents the mean detection threshold of the SOM setup.

The calculation of $\Delta\mu_a$ showed (see Figure 7a) that only for CDF-pairs with local intrinsic T1 hyperintensity involvement (red, black), a $\Delta\mu_a$ greater than 0.054 mm^{-1} was observed. A decrease in μ_a was seen for 12 CDF-pairs. Of these, 8 had local intrinsic T1 hyperintensity involvement. Considering only CDF-pairs with an interfiber distance $\leq 19 \text{ mm}$, $\Delta\mu_a$ was higher when intrinsic local T1 hyperintensity was observed (median/interquartile range in mm^{-1} : $0.025/[0.012, 0.052]$ versus $0.0134/[0.0022, 0.030]$, $p = 0.003$, Figure 7b). CDF-pairs with no detectable treatment light transmission at iPDT start were not considered, as no $\Delta\mu_a$ could be calculated.

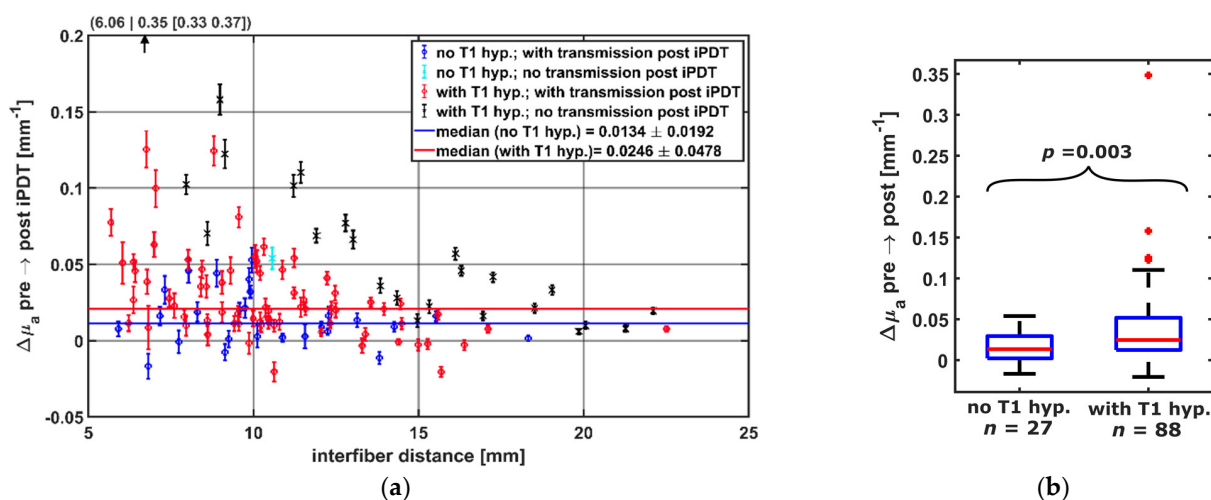


Figure 7. (a) Calculated $\Delta\mu_a$ dependent on the interfiber distance between CDF-pairs. Colors indicate whether transmission was detectable post iPDT and whether intrinsic T1 hyperintensity was observed (see legend). For better visibility, the data point at $(6.06 | 0.35)$ is omitted. (b) Comparison of $\Delta\mu_a$ of CDF-pairs with and without local intrinsic T1 hyperintensity, considering only pairs with transmission pre iPDT and interfiber distance $\leq 19 \text{ mm}$.

3.4. Comparing Intrinsic T1 Hyperintensity Strength

The signal intensity of the intrinsic T1 hyperintensity and the degree of overlap between intrinsic T1 hyperintensity and light transmission zone were evaluated to investigate whether a stronger involvement of T1 hyperintensity for a given CDF-pair leads to a stronger influence on the observed absorption change $\Delta\mu_a$. For this purpose, the fraction of T1 hyperintensity within the light transmission zone between a CDF-pair was multiplied by I_{T1} . The resulting T1 hyperintensity strength was compared to $\Delta\mu_a$ in Figure 8, separately for each CDF-pair and with respect to detectable laser light transmission at the end of iPDT. The linear two-sided Spearman regression ($R^2 = 0.66$, $p < 0.001$, $N = 115$) indicates that for higher $\Delta\mu_a$ values, a higher intrinsic T1 hyperintensity strength can be expected in the light transmission zone. From CDF-pairs without local intrinsic T1 hyperintensity (blue and cyan symbols, T1 hyperintensity strength = 0), the degree of T1 hyperintensity strength that leads to a significant increase in $\Delta\mu_a$ can be deduced. According to Figure 8, a T1 hyperintensity strength of approximately 0.20 leads to an average $\Delta\mu_a$ of 0.05 mm^{-1} .

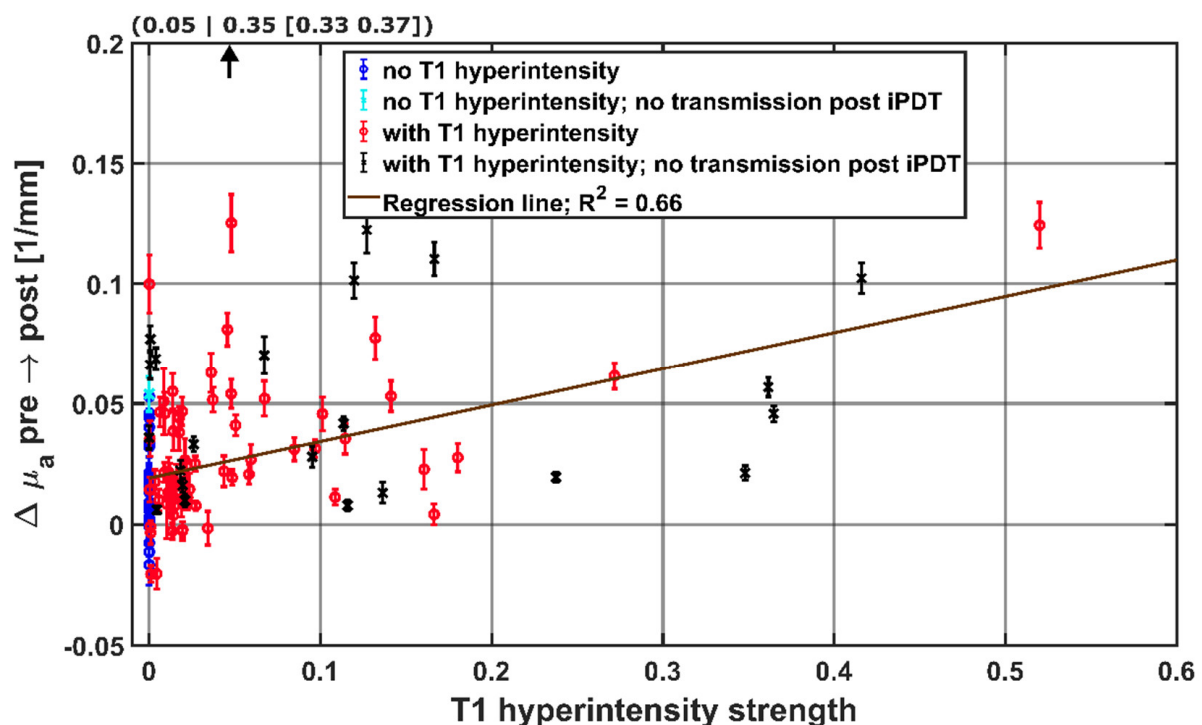


Figure 8. Hyperintensity strength in the light propagation volume surrounding CDF-pairs, with the calculated regression line obtained by the Spearman test. For better visibility, the data point at (0.05 | 0.35) is not shown. The colors and symbols indicate whether transmission was detectable post iPDT and whether intrinsic T1 hyperintensity was observed (see legend).

3.5. Analysis of PpIX Fluorescence

Analyzing $\Delta\mu_a$ in relation to the occurrence of PpIX fluorescence between a CDF-pair showed, for the 20 CDF-pairs without local fluorescence before iPDT, that either an increase (11/20) or a decrease (9/20) in μ_a could be observed ($\Delta\mu_a$ range: -0.021 mm^{-1} to 0.125 mm^{-1}). A $\Delta\mu_a < -0.005 \text{ mm}^{-1}$ only occurred for CDF-pairs with no PpIX fluorescence before iPDT. Overall, for CDF-pairs without detectable fluorescence, the median $\Delta\mu_a$ is more than 2.7 times smaller compared to CDF-pairs with detectable fluorescence before iPDT. This indicates a possible relationship between higher $\Delta\mu_a$ and the occurrence of fluorescence, but the difference is not statistically significant (0.0098 mm^{-1} vs. 0.0265 mm^{-1} , $p = 0.063$). Only CDF-pairs with detectable PpIX fluorescence had intrinsic T1 hyperintensity strengths larger than 0.14.

4. Discussion

Analyzing intraoperative SOM measurements from patients receiving iPDT for high grade glioma, a decrease in transmitted treatment light related to an increase in tissue absorption for 85% of the evaluated CDF-pairs could be observed for the treatment wavelength of 635 nm. On postoperative MRI, areas with intrinsic T1 hyperintensity in the treatment area were identified and analyzed with respect to their location relative to the iPDT treatment volume. A stronger increase in μ_a correlates significantly with the occurrence of intrinsic T1 hyperintensity in the light transmission zone surrounding a CDF-pair. No correlation between tissue absorption at iPDT start and intrinsic T1 hyperintensity in early postoperative MRI was observed. Further SOM analysis demonstrated a tendency towards higher $\Delta\mu_a$ related to if PpIX fluorescence was observed between a CDF-pair.

Intercranial intrinsic T1 hyperintensity may be caused by different substances, including MetHb, melanin, lipids, proteins, minerals, and others [48]. MetHb is a blood degradation product that could be procedure-related, produced with a potentially accelerated conversion due to iPDT [49].

High-grade gliomas form an especially pronounced capillary system with thinner vessel walls than normal blood vessels [50]. Silent, asymptomatic hemorrhages are reported in 20–60% of biopsies [51,52], albeit before MRI was readily available for trajectory planning. A small proportion of these silent hemorrhages were distant from the biopsy location itself and, therefore, described as trajectory-related. The occurrence of trajectory-related hemorrhages was confirmed by Casanova et al. [53,54], who even described injuries occurring at some distance from the trajectory. The diameters of intrinsic T1 hyperintensities found in the case of this study (3 mm to 19 mm) were of similar size to that of the silent hemorrhages found for biopsies (diameters < 5 mm to 40 mm) [51,52]. Clinically silent hemorrhages may have been treatment-related during iPDT and become visible as intrinsic T1 hyperintensity in early postoperative T1-weighted MRI due to the accelerated conversion of Hb species to MetHb by iPDT illumination. This accelerated conversion would be well consistent with findings in liquid tissue phantoms [23].

Some intrinsic T1 hyperintensity was found in every post iPDT non-enhanced T1-weighted sequence analyzed in the presented cohort. In most iPDT cases, either the overlap (OV) of the intrinsic T1 hyperintensity with the tumor volume was high (above median), or the volume of intrinsic T1 hyperintensity was very small (below median). Therefore, the observed T1 hyperintensity was mainly confined within the tumor volume or directly adjacent to the contrast enhancing tumor margin. Unfortunately, the contrast enhancement in MRI does not fully represent the actual tumor volume, as contrast enhancement is mainly related to the breakdown of the blood brain barrier but does not cover the infiltration zone [44,55]. It is known that FET-PET allows better visualization of the metabolically active tumor, and, in most cases, high-grade gliomas show a larger volume in FET-PET imaging compared to MRI [56]. This is consistent with reports stating that PpIX is also accumulated in the diffuse infiltration zone or peritumoral zone with metabolically active tumor cells [31,57]. To take into account that MRI does not display the full tumor volume, the iPDT treatment planning is carried out in such a way that the PDT effect is extended into the PpIX-accumulating infiltration zone. For this purpose, the peripheral CDFs are placed within the contrast-enhanced tumor volume but close to the tumor margin. Taking both aspects into account, it can be assumed that the OV coefficients between the T1 hyperintensity volume and the real tumor volume, including the infiltration zone not visible in contrast-enhanced MRI, are larger than those OV coefficients calculated only based on the contrast-enhanced MRI. Thus, it can be concluded that all T1 hyperintensity volumes observed in this work are located within the full tumor volume, including the infiltration zone, and within the intended iPDT treatment volume. A notable exception was iPDT case #4, which was treated twice. In the second treatment, case #4b, a four-fold smaller tumor volume was targeted compared to the first treatment. About 2/3 of the intrinsic T1 hyperintensity volume recorded after the second iPDT overlapped with the tumor volume treated in the first iPDT session. In this case, the formation of an additional

fraction of MetHb or another intrinsically T1 hyperintense substrate between the two iPDT sessions can be assumed.

The occurrence of a hemorrhage may by itself immediately cause an absorption increase due to the increased bvf in the tissue. However, as observed in the results, this would probably not lead to a complete loss of transmission between some CDF-pairs. In case of a reference interfiber distance of 10 mm, capillary blood would need to occupy 40% of the tissue volume to reduce the light transmission to below the detection limit. As a further effect, spectral changes due to potentially photo-induced molecular changes must be taken into account. If oxygen consumption by the iPDT procedure led to the formation of deoxygenated hemoglobin, a bvf of about 10% would be sufficient for a total loss of transmission. The formation of MetHb would further increase the absorption coefficient at an iPDT treatment wavelength of 635 nm, and even small bvf would have a severe effect on transmission. Deoxygenation of blood is well consistent with previous findings on liquid phantoms [23]. In addition, a directly ROS-induced MetHb formation has indeed been reported [36,58–60]. PDT-induced hemoglobin deoxygenation may be the probable cause in all instances, where a high increase in tissue absorption was observed, and ROS-induced MetHb-formation can also not be excluded.

By calculating the intrinsic T1 hyperintensity strength, better quantification of the local T1 hyperintensity volume's influence on the light propagation between a CDF-pair should be achieved to correlate it with a potentially iPDT-induced absorption change. This was only partly successful, as the conclusion that a strong and large T1 hyperintensity is only observed when the absorption increase during iPDT was high is not very well-founded with $R^2 = 0.66$. Furthermore, it was observed that the T1 hyperintensity strength was relatively small between many CDF-pairs, although a high $\Delta\mu_a$ was calculated. With the observed $\Delta\mu_a$ being higher than expected if only induced by oxygenated blood, hemoglobin deoxygenation, or even MetHb production by iPDT have to be considered.

Assuming that CDF insertion leads to an intercranial hemorrhage, this would usually be followed by a hyperacute stage, during which predominantly HbO_2 is expected in the tissue, followed by an acute stage, where Hb is formed within 24–48 h after onset of the hemorrhage. Only after 2–7 days, intrinsic T1 hyperintensity is usually expected as a consequence of the MetHb formation [24,61]. Due to oxygen consumption during the iPDT procedure, hemoglobin deoxygenation may occur more rapidly, and MetHb formation may be accelerated. Thus, the intrinsic T1 hyperintensity occurring already one day after iPDT could be explained.

With the observed intrinsic T1 hyperintensity and increase in tissue absorption, possible detrimental effects on the iPDT efficacy need to be addressed. With increasing tissue absorption, the initial light dosimetry may become invalid, potentially leading to under-treatment. While increased absorption leads to decreased light penetration depth, the implications for the treatment depth are not so clear because photobleaching of PpIX is a further decisive factor. Due to the high light dose applied, complete photobleaching—and, thus, induced tissue damage—can be achieved. Indeed, there is no case in the performed SOM measurements where residual fluorescence was found after iPDT—independent of CDF separation, pre iPDT absorption, or absorption change. Of course, when there is no detectable treatment light transmission signal before iPDT, a lack of fluorescence signal cannot be interpreted as a lack of PpIX. However, in all cases with a detectable treatment light transmission signal after iPDT, complete PpIX photobleaching could be confirmed. In the cases with treatment light transmission signal before but without treatment light transmission signal after iPDT, more detailed time-dependent SOM recordings would be required to unravel when during the treatment absorption increase and fluorescence decrease occurred. Overall, it can be expected that there will be an effective light dose applied throughout the entire contrast enhanced tumor volume. However, as far as penetration into the infiltration zone outside the contrast-enhanced tumor volume is concerned, higher absorption would lead to a smaller necrosis depth.

The induction of necrosis requires PpIX activation and oxygen consumption for ROS generation. One may speculate that the estimated absorption increase in tissue should be higher for CDF-pairs with detectable PpIX fluorescence signal at iPDT start and subsequent local intrinsic T1 hyperintensity. Indeed a tendency towards a stronger absorption increase in the tissue for these CDF-pairs could be observed. Furthermore, the results also indicated that for CDF-pairs with no PpIX fluorescence, the increase in tissue absorption is smaller, or even a decrease may happen. Undetectable PpIX fluorescence does not necessarily mean that no PpIX was accumulated in the tumor, as the detected PpIX fluorescence signal depends on the localization of the PpIX relative to the CDF-pair and on tissue inhomogeneities inducing inhomogeneous optical tissue properties. So, there is the possibility of a sufficient PpIX amount present in the tumor for iPDT but not causing detectable PpIX fluorescence pre iPDT.

For the quantitative analysis of optical tissue properties, absolute values of the absorption coefficient μ_a were calculated based on the diffusion approximation of the radiative transfer equation. Unlike the directly measured treatment light transmission signals, the computed values for μ_a are independent of interfiber separation. The applied diffusion approximation assumes homogeneous optical tissue properties, so the possibility of individual μ_a values in different tissue regions is disregarded. Thus, only an averaged μ_a value could be computed for the volume surrounding a CDF-pair [33]. This affects the comparability of the obtained μ_a values (range: 0.02–0.22 mm^{−1}) with optical properties of brain tissue (white matter, grey matter, glioblastoma) in the literature (range 0.02–0.08 mm^{−1}) [62–64]. Therefore, the obtained results might be overestimated due to the assumption of a constant $\mu_s' = 2$ mm^{−1}, so differing μ_s' values for brain tissue (range 1.0–6.0 mm^{−1}) are neglected.

Finally, it must be mentioned that the data amount was limited due to the low number of iPDT cases. Further data had to be excluded due to sophisticated technical demands issues for this analysis, e.g., incorrectly measured spectral data or MRI sequences that were not comparable to the others. In some iPDT cases, SOM was only performed for a selection of CDF-pairs, to decrease measurement time and, therefore, minimize patient load. A revised, dedicated iPDT protocol with optimized equipment might allow to speed up the SOM data acquisition process and increase the available data amount. In addition, these technical and clinical constraints limit the statistical power of the data. The calculated p-values, even if they are low, should be carefully interpreted as only indicating tendencies. To obtain results with stronger significance, future analyses on larger patient collectives are necessary, ideally using improved automated SOM concepts.

The overall aim of the presented investigation and future work should be to derive additional information from different monitoring applications (e.g., SOM, MRI, PET) by combining them and comparing abnormalities to further improve iPDT procedure, both clinically and technically. This also contributes to gain more detailed insight into the phototoxic reactions in the target tissue. With enhanced interpretation of the recorded spectral and MRI data sets, the benefit of the patients suffering from this kind of cancer with a bad prognosis may be further improved.

5. Conclusions

SOM measurements enable an individual intra-operative assessment of absorption and fluorescence. With calibrated detectors, known trajectory coordinates, and laser light powers, one can calculate optical parameters of perfused viable tumor tissue in situ, at least in the form of mean values, albeit their detailed spatial distribution cannot be derived. This should lead to a much more reliable database of optical properties of GBM tissue, in particular for in vivo interventions. If optical parameters in individual patients or locations should turn out to strongly deviate from the mean values, a personalized irradiation time might at least partly compensate for this condition.

Frequently, an increase in absorption between measurements before and after iPDT was observed, which correlated with early postoperative intrinsic T1 hyperintensity in non-contrast-enhanced T1-weighted MRI data. This may indicate that clinically silent

hemorrhage was induced during cylindrical diffuser fiber insertion. During iPDT, a ROS-driven accelerated hemoglobin deoxygenation and conversion to MetHb may then occur and may impair the irradiation efficacy. However, the fraction of tumor volume affected by T1 hyperintensity was below 28% in all cases (<10% in most cases). Substantial PDT-related effects will thus be induced in the tumor region, even in non-ideal situations.

On the basis of these results, additional evaluations and research should allow for further elucidation on the mechanisms of iPDT-related changes in tissue absorption and intrinsic T1 hyperintensity.

Author Contributions: Conceptualization, M.A., C.H., H.S. and A.R.; methodology, M.A., C.H., H.S. and B.E.-W.; software, M.A. and A.R.; validation, S.Q., B.E.-W. and A.R.; formal analysis, M.A. and B.E.-W.; investigation, M.A., C.H. and S.Q.; resources N.T. and A.R.; data curation, R.S., H.S. and A.R.; writing—original draft preparation, M.A. and H.S.; writing—review and editing, C.H., S.Q., B.E.-W., R.S., N.T. and A.R.; visualization, M.A.; supervision, R.S., N.T. and A.R.; project administration, R.S., N.T. and A.R.; funding acquisition, R.S. and A.R. All authors have read and agreed to the published version of the manuscript.

Funding: This research was funded by the German Research Foundation (DFG) in terms of the research training group (RTG) GRK2274.

Institutional Review Board Statement: The study was conducted according to the guidelines of the Declaration of Helsinki and approved by the Ethics Committee of Ludwig-Maximilians-University, Munich, Germany (reference number 335-16).

Informed Consent Statement: Informed consent was obtained from all subjects involved in the study.

Data Availability Statement: No new data were created or analyzed in this study. Data sharing is not applicable to this article.

Acknowledgments: We gratefully acknowledge Alexander Buchner for assistance with statistical questions and Christoph Barth for technical assistance.

Conflicts of Interest: The authors declare no conflict of interest. The funders had no role in the design of the study; in the collection, analyses, or interpretation of data; in the writing of the manuscript; or in the decision to publish the results.

References

1. Stupp, R.; Hegi, M.E.; Mason, W.P.; van den Bent, M.J.; Taphoorn, M.J.B.; Janzer, R.C.; Ludwin, S.K.; Allgeier, A.; Fisher, B.; Belanger, K.; et al. Effects of radiotherapy with concomitant and adjuvant temozolomide versus radiotherapy alone on survival in glioblastoma in a randomised phase III study: 5-year analysis of the EORTC-NCIC trial. *Lancet Oncol.* **2009**, *10*, 459–466. [\[CrossRef\]](#)
2. Stupp, R.; Mason, W.P.; van den Bent, M.J.; Weller, M.; Fisher, B.; Taphoorn, M.J.B.; Belanger, K.; Brandes, A.A.; Marosi, C.; Bogdahn, U.; et al. Radiotherapy plus concomitant and adjuvant temozolomide for glioblastoma. *N. Engl. J. Med.* **2005**, *352*, 987–996. [\[CrossRef\]](#) [\[PubMed\]](#)
3. Muller, P.J.; Wilson, B.C. Photodynamic therapy: Cavitory photoillumination of malignant cerebral tumours using a laser coupled inflatable balloon. *Can. J. Neurol. Sci. J. Can. Des. Sci. Neurol.* **1985**, *12*, 371–373. [\[CrossRef\]](#) [\[PubMed\]](#)
4. Kostron, H.; Fritsch, E.; Grunert, V. Photodynamic therapy of malignant brain tumours: A phase I/II trial. *Br. J. Neurosurg.* **1988**, *2*, 241–248. [\[CrossRef\]](#) [\[PubMed\]](#)
5. Stepp, H.; Stummer, W. 5-ALA in the management of malignant glioma: 5-ala in malignant gliomas. *Lasers Surg. Med.* **2018**, *50*, 399–419. [\[CrossRef\]](#) [\[PubMed\]](#)
6. Beck, T.J.; Kreth, F.W.; Beyer, W.; Mehrkens, J.H.; Obermeier, A.; Stepp, H.; Stummer, W.; Baumgartner, R. Interstitial photodynamic therapy of nonresectable malignant glioma recurrences using 5-aminolevulinic acid induced protoporphyrin IX. *Lasers Surg. Med.* **2007**, *39*, 386–393. [\[CrossRef\]](#)
7. Johansson, A.; Faber, F.; Kniebühler, G.; Stepp, H.; Sroka, R.; Egensperger, R.; Beyer, W.; Kreth, F.-W. Protoporphyrin IX Fluorescence and Photobleaching During Interstitial Photodynamic Therapy of Malignant Gliomas for Early Treatment Prognosis: Fluorescence for Treatment Prognosis in Glioma pdt. *Lasers Surg. Med.* **2013**, *45*, 225–234. [\[CrossRef\]](#)
8. Schwartz, C.; Stepp, H.; Rühm, A.; Tonn, J.-C.; Kreth, S.; Kreth, F.-W. Interstitial Photodynamic Therapy for De-Novo Glioblastoma Multiforme WHO IV: A Feasibility Study. In Proceedings of the 66th Annual Meeting of the German Society of Neurosurgery (DGNC), Karlsruhe, Germany, 7–10 June 2015.

9. Vermandel, M.; Dupont, C.; Lecomte, F.; Leroy, H.A.; Tuleasca, C.; Mordon, S.; Hadjipanayis, C.G.; Reyns, N. Standardized intraoperative 5-ALA photodynamic therapy for newly diagnosed glioblastoma patients: A preliminary analysis of the INDYGO clinical trial. *J. Neurooncol.* **2021**, *152*, 501–514. [CrossRef] [PubMed]
10. Lietke, S.; Schmutzer, M.; Schwartz, C.; Weller, J.; Siller, S.; Aumiller, M.; Heckl, C.; Forbrig, R.; Niyazi, M.; Egensperger, R.; et al. Interstitial Photodynamic Therapy Using 5-ALA for Malignant Glioma Recurrences. *Cancers* **2021**, *13*, 1767. [CrossRef]
11. Collaud, S.; Juzeniene, A.; Moan, J.; Lange, N. On the selectivity of 5-aminolevulinic acid-induced protoporphyrin IX formation. *Curr. Med. Chem. Anticancer Agents* **2004**, *4*, 301–316. [CrossRef]
12. Stummer, W.; Pichlmeier, U.; Meinel, T.; Wiestler, O.D.; Zanella, F.; Reulen, H.J.; Group, A.L.-G.S. Fluorescence-guided surgery with 5-aminolevulinic acid for resection of malignant glioma: A randomised controlled multicentre phase III trial. *Lancet Oncol.* **2006**, *7*, 392–401. [CrossRef]
13. Malik, Z. Fundamentals of 5-aminolevulinic acid photodynamic therapy and diagnosis: An overview. *Transl. Biophotonics* **2020**, *2*, e201900022. [CrossRef]
14. Johansson, A.; Kreth, F.-W.; Stummer, W.; Stepp, H. Interstitial Photodynamic Therapy of Brain Tumors. *IEEE J. Sel. Top. Quantum Electron.* **2010**, *16*, 841–853. [CrossRef]
15. Potter, W.R.; Mang, T.S.; Dougherty, T.J. The theory of photodynamic therapy dosimetry: Consequences of photo-destruction of sensitizer. *Photochem. Photobiol.* **1987**, *46*, 97–101. [CrossRef] [PubMed]
16. Mang, T.S.; Dougherty, T.J.; Potter, W.R.; Boyle, D.G.; Somer, S.; Moan, J. Photobleaching of porphyrins used in photodynamic therapy and implications for therapy. *Photochem. Photobiol.* **1987**, *45*, 501–506. [CrossRef] [PubMed]
17. Dupont, C.; Vermandel, M.; Leroy, H.-A.; Quidet, M.; Lecomte, F.; Delhem, N.; Mordon, S.; Reyns, N. INtraoperative photo-DYnamic Therapy for GliOblastomas (INDYGO): Study Protocol for a Phase I Clinical Trial. *Neurosurgery* **2019**, *84*, E414–E419. [CrossRef]
18. Schipmann, S.; Mütter, M.; Stögbauer, L.; Zimmer, S.; Brokinkel, B.; Holling, M.; Grauer, O.; Suero Molina, E.; Warneke, N.; Stummer, W. Combination of ALA-induced fluorescence-guided resection and intraoperative open photodynamic therapy for recurrent glioblastoma: Case series on a promising dual strategy for local tumor control. *J. Neurosurg.* **2020**, *134*, 426–436. [CrossRef]
19. Baran, T.M.; Foster, T.H. New Monte Carlo model of cylindrical diffusing fibers illustrates axially heterogeneous fluorescence detection: Simulation and experimental validation. *J. Biomed. Opt.* **2011**, *16*, 085003. [CrossRef]
20. Prah, S. Optical Absorption of Hemoglobin. Available online: <https://omlc.org/spectra/hemoglobin/index.html> (accessed on 30 March 2021).
21. Johansson, A.; Johansson, T.; Thompson, M.S.; Bendsoe, N.; Svanberg, K.; Svanberg, S.; Andersson-Engels, S. In vivo measurement of parameters of dosimetric importance during interstitial photodynamic therapy of thick skin tumors. *J. Biomed. Opt.* **2006**, *11*, 34029. [CrossRef]
22. Heckl, C.; Eisel, M.; Lang, A.; Homann, C.; Paal, M.; Vogeser, M.; Rühm, A.; Sroka, R. Spectroscopic methods to quantify molecules of the heme-biosynthesis pathway: A review of laboratory work and point-of-care approaches. *Transl. Biophotonics* **2021**, *3*, e202000026. [CrossRef]
23. Heckl, C.; Aumiller, M.; Rühm, A.; Sroka, R.; Stepp, H. Fluorescence and Treatment Light Monitoring for Interstitial Photodynamic Therapy. *Photochem. Photobiol.* **2020**, *96*, 388–396. [CrossRef]
24. Bradley, W.G. MR appearance of hemorrhage in the brain. *Radiology* **1993**, *189*, 15–26. [CrossRef] [PubMed]
25. Federica, M.; Maurizio, P.; Giancarlo, A.; Valeria, C. Neuroimaging in Intracerebral Hemorrhage. *Stroke* **2014**, *45*, 903–908. [CrossRef]
26. Kidwell, C.S.; Wintermark, M. Imaging of intracranial haemorrhage. *Lancet Neurol.* **2008**, *7*, 256–267. [CrossRef]
27. Saad, A.F.; Chaudhari, R.; Fischbein, N.J.; Wintermark, M. Intracranial Hemorrhage Imaging. *Semin. Ultrasound CT MRI* **2018**, *39*, 441–456. [CrossRef] [PubMed]
28. Siddiqui, F.M.; Bekker, S.V.; Qureshi, A.I. Neuroimaging of Hemorrhage and Vascular Defects. *Neurother. J. Am. Soc. Exp. Neurother.* **2011**, *8*, 28–38. [CrossRef] [PubMed]
29. Rühm, A.; Stepp, H.; Beyer, W.; Hennig, G.; Pongratz, T.; Sroka, R.; Schnell, O.; Tonn, J.-C.; Kreth, F.-W. 5-ALA based photodynamic management of glioblastoma. In Proceedings of the SPIE, Optical Techniques in Neurosurgery, Neurophotonics, and Optogenetics, SPIE BiOS, San Francisco, CA, USA, 1–6 February 2014; 89280E. [CrossRef]
30. Powers, S.K.; Cush, S.S.; Walstad, D.L.; Kwock, L. Stereotactic intratumoral photodynamic therapy for recurrent malignant brain tumors. *Neurosurgery* **1991**, *29*, 688–696. [CrossRef]
31. Stepp, H.; Beck, T.; Pongratz, T.; Meinel, T.; Kreth, F.W.; Tonn, J.; Stummer, W. ALA and malignant glioma: Fluorescence-guided resection and photodynamic treatment. *J. Environ. Pathol. Toxicol. Oncol.* **2007**, *26*, 157–164. [CrossRef]
32. Martelli, F. *Light Propagation through Biological Tissue and Other Diffusive Media: Theory, Solutions, and Software*; SPIE Press: Bellingham, WA, USA, 2009; Chapter 2–4; pp. 9–89. ISBN 978-0-8194-7658-6.
33. Wang, L.V.; Wu, H.-I. *Biomedical Optics: Principles and Imaging*; Wiley-Interscience, John Wiley & Sons: Hoboken, NJ, USA, 2012; Chapter 5; pp. 83–118. ISBN 978-0-471-74304-0.
34. Dupont, C.; Vignion, A.-S.; Mordon, S.; Reyns, N.; Vermandel, M. Photodynamic therapy for glioblastoma: A preliminary approach for practical application of light propagation models: Photodynamic Therapy for Glioblastoma. *Lasers Surg. Med.* **2018**, *50*, 523–534. [CrossRef]

35. Jacques, S.L. Optical properties of biological tissues: A review. *Phys. Med. Biol.* **2013**, *58*, R37–R61. [\[CrossRef\]](#)
36. Randeberg, L.L.; Bonesrønning, J.H.; Dalaker, M.; Nelson, J.S.; Svaasand, L.O. Methemoglobin formation during laser induced photothermolysis of vascular skin lesions: Methemoglobin Formation. *Lasers Surg. Med.* **2004**, *34*, 414–419. [\[CrossRef\]](#) [\[PubMed\]](#)
37. Hennig, G.; Homann, C.; Teksan, I.; Hasbargen, U.; Hasmüller, S.; Holdt, L.M.; Khaled, N.; Sroka, R.; Stauch, T.; Stepp, H.; et al. Non-invasive detection of iron deficiency by fluorescence measurement of erythrocyte zinc protoporphyrin in the lip. *Nat. Commun.* **2016**, *7*, 10776. [\[CrossRef\]](#)
38. Maes, F.; Collignon, A.; Vandermeulen, D.; Marchal, G.; Suetens, P. Multimodality image registration by maximization of mutual information. *IEEE Trans. Med. Imaging* **1997**, *16*, 187–198. [\[CrossRef\]](#)
39. Avants, B.B.; Tustison, N.; Johnson, H. Advanced Normalization Tools (ANTs). *Insight J.* **2009**, *2*, 1–35.
40. Yushkevich, P.A.; Piven, J.; Hazlett, H.C.; Smith, R.G.; Ho, S.; Gee, J.C.; Gerig, G. User-guided 3D active contour segmentation of anatomical structures: Significantly improved efficiency and reliability. *NeuroImage* **2006**, *31*, 1116–1128. [\[CrossRef\]](#)
41. Dice, L.R. Measures of the Amount of Ecologic Association Between Species. *Ecology* **1945**, *26*, 297–302. [\[CrossRef\]](#)
42. Jaccard, P. The Distribution of the Flora in the Alpine Zone.1. *New Phytol.* **1912**, *11*, 37–50. [\[CrossRef\]](#)
43. Besemer, A.E.; Titz, B.; Grudzinski, J.J.; Weichert, J.P.; Kuo, J.S.; Robins, H.I.; Hall, L.T.; Bednarz, B.P. Impact of PET and MRI threshold-based tumor volume segmentation on patient-specific targeted radionuclide therapy dosimetry using CL1404. *Phys. Med. Biol.* **2017**, *62*, 6008–6025. [\[CrossRef\]](#) [\[PubMed\]](#)
44. Lohmann, P.; Stavrinou, P.; Lipke, K.; Bauer, E.K.; Ceccon, G.; Werner, J.-M.; Neumaier, B.; Fink, G.R.; Shah, N.J.; Langen, K.-J.; et al. FET PET reveals considerable spatial differences in tumour burden compared to conventional MRI in newly diagnosed glioblastoma. *Eur. J. Nucl. Med. Mol. Imaging* **2019**, *46*, 591–602. [\[CrossRef\]](#)
45. Cassidy, J.; Nouri, A.; Betz, V.; Lilge, L. High-performance, robustly verified Monte Carlo simulation with FullMonte. *J. Biomed. Opt.* **2018**, *23*, 1. [\[CrossRef\]](#)
46. Ahrens, J.; Geveci, B.; Law, C. ParaView: An End-User Tool for Large-Data Visualization. In *Visualization Handbook*; Elsevier: Amsterdam, The Netherlands, 2005; pp. 717–731.
47. Beck, T.J.; Beyer, W.; Pongratz, T.; Stummer, W.; Stepp, H.; Wagner, S.; Baumgartner, R. Clinical Determination of Tissue Optical Properties in vivo by Spatially Resolved Reflectance Measurements. In Proceedings of the SPIE, European Conference on Biomedical Optics, Munich, Germany, 22 June 2003; p. 5138_96. [\[CrossRef\]](#)
48. Ginat, D.T.; Meyers, S.P. Intracranial Lesions with High Signal Intensity on T1-weighted MR Images: Differential Diagnosis. *RadioGraphics* **2012**, *32*, 499–516. [\[CrossRef\]](#) [\[PubMed\]](#)
49. Ginat, D.T.; Schaefer, P.W.; Moisi, M.D. Imaging the Intraoperative and Postoperative Brain. In *Atlas of Postsurgical Neuroradiology: Imaging of the Brain, Spine, Head, and Neck*; Ginat, D.T., Westesson, P.-L.A., Eds.; Springer International Publishing: Cham, Switzerland, 2017; pp. 183–258.
50. Kane, J.R. The Role of Brain Vasculature in Glioblastoma. *Mol. Neurobiol.* **2019**, *56*, 6645–6653. [\[CrossRef\]](#) [\[PubMed\]](#)
51. Kreth, F.W.; Muacevic, A.; Medele, R.; Bise, K.; Meyer, T.; Reulen, H.J. The risk of haemorrhage after image guided stereotactic biopsy of intra-axial brain tumours—A prospective study. *Acta Neurochir.* **2001**, *143*, 539–545. [\[CrossRef\]](#) [\[PubMed\]](#)
52. Kulkarni, A.V.; Guha, A.; Lozano, A.; Bernstein, M. Incidence of silent hemorrhage and delayed deterioration after stereotactic brain biopsy. *J. Neurosurg.* **1998**, *89*, 31–35. [\[CrossRef\]](#)
53. Casanova, F.; Carney, P.R.; Sarntinoranont, M. Effect of needle insertion speed on tissue injury, stress, and backflow distribution for convection-enhanced delivery in the rat brain. *PLoS ONE* **2014**, *9*, e94919. [\[CrossRef\]](#)
54. Casanova, F.; Carney, P.R.; Sarntinoranont, M. In vivo evaluation of needle force and friction stress during insertion at varying insertion speed into the brain. *J. Neurosci. Methods* **2014**, *237*, 79–89. [\[CrossRef\]](#)
55. Wen, P.Y.; Macdonald, D.R.; Reardon, D.A.; Cloughesy, T.F.; Sorensen, A.G.; Galanis, E.; Degroot, J.; Wick, W.; Gilbert, M.R.; Lassman, A.B.; et al. Updated response assessment criteria for high-grade gliomas: Response assessment in neuro-oncology working group. *J. Clin. Oncol.* **2010**, *28*, 1963–1972. [\[CrossRef\]](#)
56. Unterrainer, M.; Fleischmann, D.F.; Diekmann, C.; Vomacka, L.; Lindner, S.; Vettermann, F.; Brendel, M.; Wenter, V.; Ertl-Wagner, B.; Herms, J.; et al. Comparison of (18)F-GE-180 and dynamic (18)F-FET PET in high grade glioma: A double-tracer pilot study. *Eur. J. Nucl. Med. Mol. Imaging* **2019**, *46*, 580–590. [\[CrossRef\]](#)
57. Schucht, P.; Knittel, S.; Slotboom, J.; Seidel, K.; Murek, M.; Jilch, A.; Raabe, A.; Beck, J. 5-ALA complete resections go beyond MR contrast enhancement: Shift corrected volumetric analysis of the extent of resection in surgery for glioblastoma. *Acta Neurochir.* **2014**, *156*, 305–312. [\[CrossRef\]](#)
58. Andrade, C.T.d.; Nogueira, M.S.; Kanick, S.C.; Marra, K.; Gunn, J.; Andreozzi, J.; Samkoe, K.S.; Kurachi, C.; Pogue, B.W. Optical Spectroscopy of Radiotherapy and Photodynamic Therapy Responses in Normal Rat Skin Shows Vascular Breakdown Products. In Proceedings of the Optical Methods for Tumor Treatment and Detection: Mechanisms and Techniques in Photodynamic Therapy XXV, SPIE BiOS, San Francisco, CA, USA, 13–18 February 2016; p. 969410. [\[CrossRef\]](#)
59. Hamada, R.; Ogawa, E.; Arai, T. Continuous Optical Monitoring of Red Blood Cells During a Photosensitization Reaction. *Photobiomodul. Photomed. Laser Surg.* **2019**, *37*, 110–116. [\[CrossRef\]](#)
60. Larsen, E.L.P.; Randeberg, L.L.; Gederaas, O.A.; Krokan, H.E.; Hjelle, D.R.; Svaasand, L.O. In Vitro Study on Methemoglobin Formation in Erythrocytes Following Hexyl-Aminolevulinic Acid Induced Photodynamic Therapy. In Proceedings of the Optical Methods for Tumor Treatment and Detection: Mechanisms and Techniques in Photodynamic Therapy XVI, San Jose, CA, USA, 20–25 January 2007; p. 642719-3. [\[CrossRef\]](#)

61. Anzalone, N.; Scotti, R.; Riva, R. Neuroradiologic differential diagnosis of cerebral intraparenchymal hemorrhage. *Neurol. Sci.* **2004**, *25*, s3–s5. [[CrossRef](#)] [[PubMed](#)]
62. Gebhart, S.C.; Lin, W.C.; Mahadevan-Jansen, A. In vitro determination of normal and neoplastic human brain tissue optical properties using inverse adding-doubling. *Phys. Med. Biol.* **2006**, *51*, 2011–2027. [[CrossRef](#)] [[PubMed](#)]
63. Yaroslavsky, A.N.; Schulze, P.C.; Yaroslavsky, I.V.; Schober, R.; Ulrich, F.; Schwarzmaier, H.-J. Optical properties of selected native and coagulated human brain tissues in vitro in the visible and near infrared spectral range. *Phys. Med. Biol.* **2002**, *47*, 2059–2073. [[CrossRef](#)] [[PubMed](#)]
64. Bevilacqua, F.; Piguet, D.; Marquet, P.; Gross, J.D.; Tromberg, B.J.; Depeursinge, C. In vivo local determination of tissue optical properties: Applications to human brain. *Appl. Opt.* **1999**, *38*, 4939. [[CrossRef](#)] [[PubMed](#)]